



The  
University  
Of  
Sheffield.

## Access to Electronic Thesis

Author: Juanjuan Zhu  
Thesis title: Simulation Model and Ultrasound Study for Engineering Interfaces  
Qualification: PhD

**This electronic thesis is protected by the Copyright, Designs and Patents Act 1988. No reproduction is permitted without consent of the author. It is also protected by the Creative Commons Licence allowing Attributions-Non-commercial-No derivatives.**

If this electronic thesis has been edited by the author it will be indicated as such on the title page and in the text.

# **Simulation Model and Ultrasound Study for Engineering Interfaces**

**JUANJUAN ZHU**

**Thesis submitted for the Degree of Doctor of Philosophy**

**Department of Mechanical Engineering**

**The University of Sheffield**

**May, 2012**

# Abstract

Friction and wear are experienced both in terms of machine operation and finance. They impact, amongst other things, energy consumption and material loss, product manufacture and component maintenance. Liquid lubrication is widely used on machinery interfaces to separate the loaded surfaces, with the ultimate aim of reducing friction and wear from direct metallic contacts. However, in most engineering applications, the lubricant film thickness is not thick enough to fully separate matching surfaces because of too high loads or low speeds. Therefore, the interface contains isolated asperity contacts with the surrounding gaps filled by liquid, which is known as mixed lubrication. The aim of this project is to investigate engineering interfaces using both theoretical and experimental approaches.

A statistical mixed lubrication model has been built in this study. The friction force, load sharing proportions, film formation and normal contact stiffness can be simulated for engineering interfaces under varying operating conditions. The model was applied to a greased contact of a landing gear articulating pin joint and an oil lubricated contact of a ball-on-disc. Friction forces, load sharing ratios, contact stiffness, and mean film thickness from asperity contact and lubricant layer have been predicted and compared with experimental measurements.

The ultrasonic method was applied to the greased pin joint contact and the oil lubricated ball-on-disc contact. Reflection measurements have been linked to the interface characteristics, including contact pressure, lubricating film thickness and contact stiffness. A start-up process of a ball sliding on disc was studied to extract contributions from asperity interaction and trapped lubricant on the interface. Finally, a shear study on a dry Perspex contact was carried out using the ultrasonic technique. The shear stiffness in the stationary and stick-slip process was studied which presents the shear performance of contacting asperities under normal pressure.

Results of these investigations show that the mixed lubrication model and the ultrasonic technique could be used to accurately determine the interfacial characteristics for real engineering contacts. Agreement between analytical model and ultrasonic measurement is found to be good, indicating the applicability of the technique for analysis of contact size, contact pressure and interfacial stiffness.

# Content

Abstract

Content

Nomenclature

Acknowledgements

Chapter 1 Introduction

1.1 Statement of the Problem .....	1
1.2 Aims and Objectives .....	3
1.3 Layout of the Thesis.....	3

Chapter 2 Background

2.1 Rough Surface Contact .....	5
2.2 Mixed Lubrication.....	8
2.3 Ultrasonic Method.....	12
2.4 Interface Stiffness .....	15
2.4.1 Contact Stiffness.....	15
2.4.2 Contact Stiffness of a Fluid Film.....	17
2.4.3 Contact Stiffness in the Mixed Regime .....	17
2.4.4 Shear Stiffness .....	19
2.5 Summary .....	20

Chapter 3 Mixed Lubrication Model

3.1 Introduction.....	22
3.2 Mixed Lubrication Contact .....	23
3.2.1 Load Sharing Concept .....	24
3.2.2 Scaling Factors.....	25
3.2.3 Shear Force on a Mixed Lubrication Contact.....	26
3.2.3.1 Shear Force of a Lubricant Film .....	27
3.2.3.2 Shear Force for Metallic Contact .....	29
3.2.3.3 Friction Coefficient.....	30
3.3 Mixed Lubrication Model .....	30
3.3.1 Asperity Contact Component.....	30

3.3.2	Elastohydrodynamic Lubrication Component .....	31
3.3.3	Formulation and MathCAD Solution .....	32
3.5	Conclusions.....	32
<b>Chapter 4 Mixed Lubrication in an EHL Contact</b>		
4.1	Introduction.....	34
4.2	Experimental Benchmark.....	35
4.3	Mixed Lubrication Model for Contact Stiffness .....	38
4.3.1	Stiffness of Static Dry Contact .....	38
4.3.1.1	GW Model .....	39
4.3.1.2	WAO Model.....	40
4.3.1.3	BGT Model .....	41
4.3.2	Stiffness of a Fluid Film .....	43
4.3.3	Stiffness of Static Wet Contact .....	45
4.3.4	Stiffness of Mixed Lubrication Contact.....	46
4.4	Model Inputs and Simulation Results .....	47
4.4.1	Input Parameters of Ball and Disc Contact.....	47
4.4.2	Simulation Results .....	48
4.4.3	Contact Stiffness .....	52
4.5	Comparison between Experiment and Simulation .....	55
4.5.1	Stiffness Varying with Sliding Speed .....	55
4.5.2	Stiffness in the Start-up Sequence .....	57
4.5.3	Lubricating Film Thickness .....	59
4.6	Conclusions.....	60
<b>Chapter 5 Mixed Lubrication in a Pin Joint</b>		
5.1	Background of Landing Gear Pin Joints .....	61
5.2	Experimental Apparatus and Method.....	63
5.2.1	Pin Joint Function Tester .....	63
5.2.2	Specimens and Operating Conditions.....	64
5.2.3	Instrumentation .....	65
5.3	Mixed Lubrication Model for Pin Joint .....	67
5.3.1	Pin Joint Friction.....	67
5.3.2	Pin Joint Mixed Lubrication Model.....	69
5.3.2.1	Load Sharing .....	69

5.3.2.2 Asperity Contact .....	70
5.3.2.3 Fluid Film Formation .....	72
5.3.3 Input Parameters .....	73
5.4 Numerical Simulation Results.....	76
5.5 Comparison between Simulation and Experiment .....	79
5.6 Conclusions .....	82
<b>Chapter 6 Contact Pressure and Friction in a Landing Gear Pin Joint</b>	
6.1 Introduction.....	84
6.2 Experimental Measurement .....	86
6.2.1 Ultrasonic Reflection and Contact Stiffness .....	86
6.2.2 Calculation of Contact Pressure.....	89
6.3 Theoretical Modelling.....	91
6.3.1 Contact Pressure Distribution .....	91
6.3.2 Contact Size .....	96
6.3.3 Nominal and True Frictional Torque in Pin Joint .....	98
6.4 Comparison between Simulation and Experiment .....	100
6.4.1 Contact Pressure and Size.....	100
6.4.2 Frictional Torque.....	103
6.4.3 Estimation of Friction Coefficient .....	106
6.5 Conclusions .....	107
<b>Chapter 7 Shear Study on a Sliding Contact</b>	
7.1 Introduction.....	109
7.2 Experimental Details.....	112
7.2.1 Specimen Preparation .....	112
7.2.2 Sliding Test Rig .....	115
7.2.3 Ultrasonic Apparatus and Data Processing.....	116
7.3 Ultrasonic Measurement .....	117
7.3.1 Reflection Dependence on Frequency .....	117
7.3.2 Loading/Unloading Cycles .....	120
7.3.3 Reflection Measurement during Stick-slip .....	124
7.3.4 Interfacial Shear Stiffness Varying with Traction Force.....	130
7.3.5 Effect of the Sliding Speed .....	133
7.3.6 Effect of the Normal Load .....	137

7.4 Real Contact Area from Ultrasonic Measurement .....	140
7.4.1 Formula Derivation.....	140
7.4.2 Real Contact Area Evolution in Hysteresis Cycles.....	141
7.4.3 Real Contact Area in Stick-slip Process .....	143
7.5 Conclusions.....	147
<b>Chapter 8 General Discussion</b>	
8.1 Characterisation of an Engineering Interface.....	149
8.2 Statistical Contact Model.....	151
8.3 Ultrasonic Measurement .....	152
8.4 Mixed Solid-liquid Contact.....	154
<b>Chapter 9 Conclusions and Recommendation</b>	
9.1 Mixed Lubrication Model .....	158
9.2 Mixed EHL Contact.....	158
9.3 Pin Joint Contact .....	159
9.4 Ultrasonic Investigation for Static/Dynamic Interfaces .....	160
9.5 Future Work .....	161
9.6 Publications Arising from this Work .....	163
<b>Reference</b>	
<b>Appendix</b>	
Appendix A: MathCAD Program for Ball on Disc Contact .....	175
A.1 Formulation and Solution .....	175
A.2 Stribeck Parameter and Friction Coefficient.....	176
A.3 Calculation of Static Contact Stiffness .....	178
Appendix B: MathCAD Program for Pin Joint.....	181
Appendix C: Influence of Speed on Reflection .....	183
Appendix D: Influence of Load on Reflection.....	187

# Nomenclature

$a$	Average half width of Hertzian contact
$a_{1,2,3,4}$	Constants in Equation 5.13
$\langle a \rangle$	Radii of asperity contact spot
$A$	Contact area
$A_0$	Nominal contact area
$b$	Half contact width in Persson's model
$B$	Lubricant bulk modulus
$B_0$	Bulk modulus at zero pressure
$B_0'$	Pressure rate of change of $B$ at zero pressure
$B_{00}$	Constant in Equation 4.14
$c$	Ultrasound wave speed
$c_p$	Constant in Roelands's formula
$d_d$	Distance between mean line of asperities and mean line of surface
$D_p$	Density of asperities per unit length
$D_s$	Density of asperities per unit area
$E_{1,2}$	Elastic modulus
$E_p$	Elastic modulus of pin
$E_b$	Elastic modulus of bush
$E'$	Reduced elastic modulus
$f$	Frequency
$F_n(t)$	Integral of summit height distribution
$G$	Shear modulus
$h$	Mean surface separation/mean film thickness
$h_c$	Central film thickness
$H$	Hardness
$K$	Stiffness
$K_a$	Asperity contact stiffness
$K_l$	Lubricant layer stiffness
$K_s$	Shear stiffness



$L$	Length of contact
$L_{1,2,3,4}$	Length of each bush
$m$	Slope of pressure and stiffness
$m_{2,4}$	Second and fourth spectral moments of roughness profile
$N$	Number of contact spots
$n$	Total asperity number
$p$	Contact pressure
$p_0$	Peak contact pressure
$p_a$	Asperity contact pressure
$p_h$	Maximum Hertzian pressure of line contact
$p_l$	Lubricant pressure
$p_m$	Mean contact pressure
$p_{nom}$	Nominal contact pressure
$P$	Load
$P_a$	Load supported by asperity contact
$P_l$	Load supported by lubricant layer
$P_L$	Projected load
$P_t$	Total load
$P'$	Load per unit length
$q$	Shear stress
$Q_a$	Friction force from asperity contact
$Q_l$	Shear force from lubricant layer
$Q_t$	Total shear force on interface
$R$	Ultrasonic reflection coefficient
$R_a$	Surface roughness
$R_{ab}$	Surface roughness of ball
$R_{ad}$	Surface roughness of disc
$R_{ba}$	Radius of ball
$R_b$	Radius of bush
$R_p$	Radius of pin
$R_q$	Root mean square roughness
$R_{qb}$	Root mean square roughness of ball

$R_{qd}$	Root mean square roughness of disc
$R_{qbu}$	Root mean square roughness of bush
$R_{qp}$	Root mean square roughness of pin
$R_s$	Average asperity radius
$R'$	Reduced radius of contact bodies
$\Delta R$	Radial clearance
$S$	Sommerfeld number
$t$	Normalized surface separation
$T$	Friction torque
$T'$	Nominal torque
$T^*$	Ratio between true and nominal torque
$u$	Velocity of contacting surfaces
$z_{1,2}$	Acoustic impedances
$Z$	Roelands' pressure-viscosity index
$\alpha$	Half contact angle
$\alpha'$	Pressure-viscosity index
$\beta_0$	Slope of the limiting shear stress-pressure relation
$\beta_k$	Constant in Equation 4.14
$\gamma_{1,2}$	Scaling factors
$\dot{\gamma}$	Lubricant shear rate
$\varepsilon$	Shear strain
$\eta$	Lubricant dynamic viscosity
$\eta_0$	Lubricant viscosity at zero pressure and 40°C temperature
$\eta_\infty$	Constant in Roelands's formula
$\lambda$	Film thickness parameter
$\lambda'$	Dimensionless shear rate
$\mu$	Friction coefficient
$\mu_a$	Friction coefficient of asperity contact
$\rho$	Density of material
$\sigma$	Shear stress of asperity contact
$\sigma_s$	Standard deviation of asperity summit heights
$\sigma_T$	Torque deviation

$\sigma_Y$	Yield stress of material
$\sigma_\mu$	Friction coefficient deviation
$\tau_l$	Lubricant shear stress
$\tau_L$	Lubricant limiting shear stress
$\tau_{L0}$	Lubricant limiting shear stress at ambient pressure
$\tau_y$	Limiting shear stress
$\nu_{1,2}$	Poisson's ratio
$\nu_b$	Poisson's ratio of bush
$\nu_p$	Poisson's ratio of pin
$\phi(z)$	Asperity height distribution function
$\omega$	Angular frequency

# Acknowledgements

The author would like to acknowledge the encouragement, inspiration and guidance given by Prof. Rob Dwyer-Joyce throughout the duration of this project. Without his help, it would not be possible to complete the work in this thesis. The attitude towards the scientific research that the author has learned from him will benefit her for a lifetime.

The author would also like to thank the University of Sheffield and the China Scholarship Council for the financial support.

Thanks to Mr. David Butcher for his technical assistance.

Thanks also go to all PhDs in 133A. A supportive research atmosphere makes a positive PhD daily life. Thanks to Dr Ezequiel Alberto Gallardo Hernandez, who encouraged the author in the beginning of the PhD. Thanks to Mr. Emin Yusuf Avan, who offered impassioned communication throughout the work. Thanks to Mr. Robin Mills, who is always helpful to all group members. Thanks to Mr. Steve Lewis, Mr. Steven Pugh, Mr. Dedison Gasni, Mr. Henry Brunskill, and Mr. Kamel Wan Ibrahim, who have given a grateful friendship to the author. Thanks to new group members, Mr. Lu Zhou, Miss Wenqu Chen, Mr. Hiroyuki Suzuki, and Mr. Dlair Ramadan for giving the great joy at the end of the PhD. Especially thanks to Mr. Luke Buckley-Johnstone for thesis grammar checking.

Finally, the author would like to dedicate this work to her parents, Mrs. Chuanlan Tian, Mr. Zengjun Zhu, to her husband, Mr. Xijin Hua, to her sisters and brother, Mrs. Lianying Zhu, Mrs. Linlin Zhu and Mr. Fei Zhu, who have always been supporting and encouraging the author.

# Chapter 1 Introduction

## 1.1 Statement of the Problem

Friction waste has been reported to cause as much as one third of the global energy consumption. In addition, extra cost is needed for the manufacture and replacement of failed components (Williams, 2005). Other than a few exceptions where friction is needed such as clutches and brakes, engineering designers have always tried to make use of mechanical power with lowest friction loss. For example, the articulating pin joint on the aircraft landing gear: lower friction force between the pin and bush allows smaller actuators, therefore saving weight. In order to improve lubrication and reduce friction, each pin joint is regularly maintained with a hand-delivered fill of grease. This is not only a costly maintenance, but also could be hazardous if not performed correctly.

Lubrication plays an important role in reducing friction and wear. It is widely used on machinery interfaces in order to separate the loaded surfaces, with the ultimate aim of removing directly metallic contact. For the full film lubricated interface, energy loss is associated with the shear in viscous lubricant, rather than solid sliding which is deemed to be much higher. However, due to low sliding speed or high supporting load, frequently the hydrodynamic action is insufficient to generate a thick enough fluid film to separate surface asperities. The interface then contains isolated asperity contacts with the surrounding gaps filled by liquid. This is known as mixed lubrication. In the last three decades, mixed lubrication has drawn a considerable amount of attention from tribologists. Unlike hydrodynamic lubrication, the contact mechanics on mixed lubricated interface has not been well understood. How the lubrication film is breaking

down, what the proportions of load sharing by liquid and asperities, how the contact pressure distributes on the interface, how the physical interaction is taking place, how much the real contact area becomes, as well as what is the deformation state of interacting asperities, are still challenges for mixed lubrication.

In-situ investigation of contact parameters have been carried out using electrical, optical or neutro-graphic techniques. Recently, the ultrasound method has received more attention. The contact pressure distribution and contact size depends on the number, as well as the size, of individual contact spots (asperity contact junction). Hence, the interfacial properties are well suited to be investigated by an ultrasonic reflection which depends on the interfacial characteristics. A useful parameter, contact stiffness, can also be easily obtained through ultrasonic reflection measurement using a simple spring model. This method can also be potentially considered as means of validating theoretical investigations as well as a helpful tool for the engineer to design machinery component.

Most of the current analyses of the contact mechanism are based on static contacts, where there is no relative movement of mating surfaces. However, most of engineering contacts fall in dynamic cases. The real contact area, contact stress distribution and contact stiffness are of importance for disclosing characteristic features of the contact, which are critical for understanding the mechanism of friction and wear. The investigation of a sliding contact between solids is a major objective in this research.

Therefore, in this study, there are three problems which will be dealt with. The first is the development of a mixed lubrication model and its application to a greased landing gear pin joint and a sliding ball-on-disc. The friction force, film formation and normal contact stiffness are simulated and verified by experimental measurements. The second part is the investigation of the pressure distribution, contact size and friction for a landing gear pin and bush contact. Theoretical results were compared to experimental measurements. The final piece of work is the investigation of a stick-slip using the ultrasonic method: shear stiffness, friction and real contact area evolution have been studied.

## **1.2 Aims and Objectives**

The aim of this thesis is the development of a combined modelling and ultrasonic experimental method for sliding mixed lubrication regime contacts, and to apply this approach to study the performance of aircraft landing gear pin joints. Specific objectives are summarized as:

1. Develop a statistical mixed lubrication model which can predict: load sharing proportions between asperity contact and liquid action, mean lubricant film thickness, and friction coefficient at an interface.
2. Apply the model to a sliding ball-on-disc configuration (circular point contact). Investigate mean film thickness, load sharing proportions and normal contact stiffness. Compare model predictions with ultrasonic measurements.
3. Apply the mixed lubrication model to the landing gear pin joint (line contact). Carry out friction experiments and compare with simulations.
4. Investigate the contact pressure distribution, contact size and normal contact stiffness by using ultrasonic measurements for the pin and bush contact. Compare with theoretical predictions.
5. Investigate the onset of sliding by carrying out ultrasonic shear and friction measurements during the stick-slip process. Analyse interfacial parameters, such as static friction, shear stiffness and real contact area. Investigate the onset of sliding, and the mechanism of stick-slip.

## **1.3 Layout of the Thesis**

In Chapter 2, the background of the rough surface contact was presented, along with mixed lubrication regimes and interfacial parameters. The ultrasonic method was reported, and the simple spring model was explained.

Chapter 3 presents the development process of a mixed lubrication model. In the mixed

lubrication regime, the shear force generated at the interface is contributed by asperity shear stress, and lubricant shear force. The model contains friction force/coefficient, frictional torque for line contact, contact stiffness, and mean film thickness. In Chapter 4, the model was used to analyse a sliding point contact taking place between a sliding ball and a stationary disc. The model simulation results were compared to the ultrasonic measurements (a journal paper has been published on this work). Later, the model was applied to a greased articulating landing gear pin joint in Chapter 5, where friction coefficient and torque were predicted and compared with experimental records (a journal paper has been published on this investigation).

Chapter 6 deals with the contact pressure, normal interfacial stiffness and contact size for the pin and bush contact by analysing the ultrasonic measurement (a journal paper has been published based on these results). Meanwhile, the contact pressure and size were also studied by elastic Hertzian theory and Persson's model, which is specified for conformal contact. The nominal and real friction torque/coefficient was analysed.

In previous chapters, normal contact mechanics was addressed by studying the pin joint contact and the ball sliding on the disc contact. The normal interfacial properties due to asperity interaction have been studied. How the micro-contact junctions deform along the tangential direction was investigated in Chapter 7. An ultrasonic shear study for a Perspex-Perspex contact was performed. The ultrasonic reflection was recorded during the stick-slip process, while the friction evolution was measured as well. The interfacial shear stiffness and real contact area were analysed from reflection measurements under varying loads and speeds. Static reflection measurements were also carried out which were used to investigate the hysteresis phenomenon at the interface.

Chapter 8 is a brief discussion of the study with comments of application and limitation of both theoretical and experimental methods. Chapter 9 contains general conclusions and recommendations for the further study arising from this work.



# Chapter 2 Background

In this chapter, features of a mixed regime lubricated interface were described. Firstly, the rough surface contact model used in this study was addressed. Secondly, characteristics of mixed lubrication regime were presented. The main principle of load sharing for establishing the mixed lubrication model was explained. The interface stiffness, which plays an important role in disclosing the nature of interface, was then presented, including the normal stiffness and the shear stiffness. Finally, the ultrasonic technique, which has been proven to be a helpful tool in analysing engineering interfaces, was introduced in this study.

## 2.1 Rough Surface Contact

When two solids come into contact, the initial touch takes place at a point or along a line. While the load is increased and transmitted gradually through the contact zone, the contact area will be enlarged due to the deformation of the surface material. Due to the size of acting force or relative movement, interface phenomenon known as contact mechanics takes place and draws considerable interest of researchers. Central aspects in contact mechanics are: pressure distribution, contact area, contact stiffness, and the frictional stresses acting tangentially between the surfaces if relative movement exists.

Figure 2.1 shows an elastic ball compressed under a certain load  $P$  on a plane. Elastic deformation is expected to take place first on the interface. The nominal contact area should be a circle with a radius of  $a$ , given by Hertz (Hertz, 1885), who originally analysed the elastic contact problem:

$$a = \left( \frac{3PR}{2E'} \right)^{1/3} \quad (2.1)$$

Where  $P$  is the applied normal load,  $R$  is the radius of elastic ball,  $E'$  is the reduced elastic modulus which depends on Young's modulus and Poisson's ratio of two contacting materials. It is defined in Hertzian theory as:

$$\frac{1}{E'} = \frac{1}{2} \left( \frac{1-\nu_1^2}{E_1} + \frac{1-\nu_2^2}{E_2} \right) \quad (2.2)$$

Subscript number 1 and 2 refer to two contacting bodies respectively.

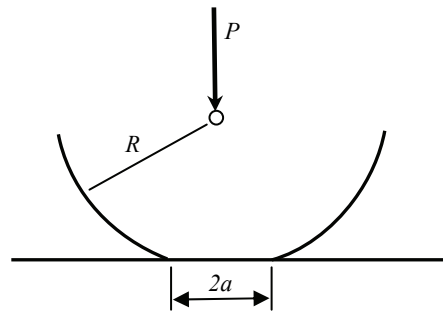


Figure 2.1. Elastic contact between a sphere of radius  $R$  and a plane under a load of  $P$ .

However, there are no ideally “smooth” engineering surfaces at the microscopic level. Figure 2.2 shows the property of a typical machined surface. When two rough surfaces are compressed against each other under a gentle load, the initial contact takes place on a few rough spots. Increasing load brings more contact points and greater contact size due to the elastic deformation of rough asperities. The real contact area is the sum of these microscopic spots. It is usually a small fraction of the nominal or apparent contact size (McCool, 1986).

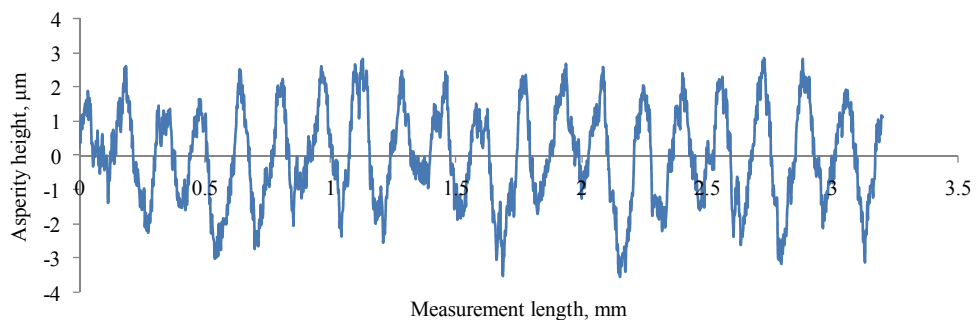


Figure 2.2. Rough surface profile of an engineering surface.

Many models have been developed for theoretical analysis of a rough surface interface since 1970s. They can be classified into two types based on how the roughness parameter

is generated; stochastic models and deterministic models. Some typical stochastic models were built by Christensen (1969), Elrod (1973), Patir and Cheng (1978), Zhu and Cheng (1988). Statistical parameters of rough surfaces are used to represent the characteristics in stochastic models. The deterministic models are based on the geometric topography and surface profile of the real surface. The relevant research has been done by Kweh *et al.* (1989), Ai and Cheng (1996), Venner and Lubrecht (1996), Zhu and Ai (1997), Wang and Zhu (2005). However, the real engineering surface structure is very complicated. The consideration of real texture brings challenges in profile measuring and difficulty in computing work, especially for problems of large geometric contact. Conversely stochastic models use selected statistical parameters to represent the characteristics. It provides a simplified mathematical tool to deal with rough surface contact. It is therefore widely adopted even in the research nowadays.

One of the first statistical theories based on the stochastic model of roughness for the rough surface contact was presented in the Greenwood and Williamson model (GW model) (1966). Rough surfaces were assumed to be composed of asperities with a simple shape and a fixed curvature. This model has been widely used to estimate the number of contact asperities, real contact area fraction and nominal contact pressure (McCool, 1986), which are given by the following equations:

Number of contact spots:

$$N = D_s A_0 F_0(t) \quad (2.3)$$

Total real contact area:

$$A = \pi D_s A_0 R_s \sigma_s F_1(t) \quad (2.4)$$

Nominal contact pressure:

$$p_a = \frac{4}{3} D_s E' R_s^{1/2} \sigma_s^{3/2} F_{3/2}(t) \quad (2.5)$$

Where  $D_s$  is the asperity density per unit area,  $A_0$  is the nominal contact area,  $R_s$  is the average radius of the asperity tips,  $\sigma_s$  is the standard deviation of the height distribution of

the summits,  $t$  is the normalized separation (equal to  $h/\sigma_s$ ),  $h$  is the gap between two contacting surfaces, which is defined as the distance from two mean levels of the surfaces, and  $F_n(t)$  is integral of summit height distribution. For Gaussian distribution of asperity heights the expression of  $F_n(t)$  becomes:

$$F_n(t) = \frac{1}{\sqrt{2\pi}} \int_t^{\infty} (s-t)^n e^{-s^2/2} ds \quad (2.6)$$

The GW model is based on elastic deformation of rough surfaces. However, if the load reaches a certain level, some high rough peaks tend to undergo plastic deformation. In 1987, Chang *et al.* (1987) developed an elasto-plastic contact model (CEB model) for circular asperity contact. Horng (1998) expanded this model for an elliptic elasto-plastic asperity contact more recently. Further research relating to elasto-plasticity of asperities has been carried out by Horng (1998), Zhao *et al.* (2000), Liu (2001), Kogut and Etsion (2002), and Pei *et al.* (2005).

## 2.2 Mixed Lubrication

Lubrication is widely used in engineering components in order to control friction and wear, and prolong the lifetime of the machinery. Ideally these lubricated contacts should be operating in the regime referred to as hydrodynamic lubrication, for example, the contacts between gear teeth in the gear transmissions, between journal bearing and shaft, between rolling elements and the inner or outer raceway in rolling bearings, between rolling balls and screw or between a cam and follower. The ideal operation is that the solid surfaces are completely separated by intervening fluid film, shown by Figure 2.3.

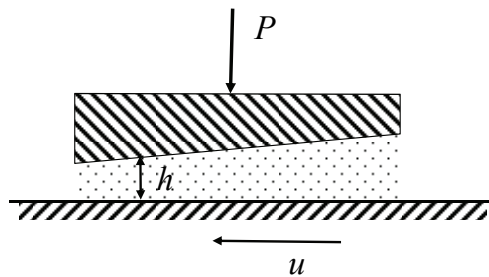


Figure 2.3. Hydrodynamic lubrication between two surfaces.

However, due to operating conditions, e.g. applied load, relative movement speed and

lubricant properties, the hydrodynamic action is insufficient to generate a fluid film thick enough to completely separate the contacting surfaces. As a consequence, the pressed liquid film thickness is of the similar order to the micro surface roughness. Solid contact may occur on the failure of the lubricant film, in which case the asperities interact and support part of the load. The interface then consists of isolated asperity contacts with the surrounding gaps filled by liquid, shown by Figure 2.4. The load is shared between direct solid to solid contact and a liquid film. This is known as the mixed lubrication, which has been recognized as a common regime in engineering lubrication applications.

*“If the lubricating film separating the surfaces is such that it allows some contact between the deformed asperities, then this type of lubrication is considered in the literature as 'mixed' or 'partial lubrication' (Stachowiak and Batchelor, 2005).”*

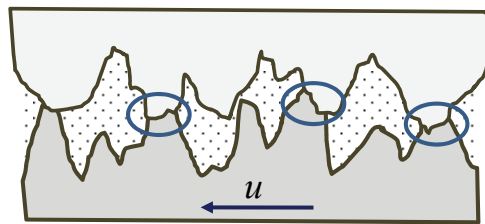


Figure 2.4. Asperity interaction in the mixed lubrication.

Three following methods are usually used to determine the lubrication regime for an engineering contact (Dowson, 2001).

- a) *Friction coefficient ( $\mu$ )*. As shown in Table 2.1, each lubrication regime is associated with ranges of the friction coefficient.
- b) *The Stribeck curve*. Stribeck (1901; 1902) first systematically carried out experimental studies and found a clear view of the characteristic curve of friction coefficient against speed. The  $x$ -axis was later extended to an integrated parameter containing information of lubricant, speed and load, shown in Figure 2.5. It has been proven to be very useful for determining the lubrication regime of a contact. Barring solid contacts, lubrication regimes fall into four different types; from severe to mild, boundary lubrication, mixed lubrication, elastohydrodynamic lubrication (EHL), and hydrodynamic lubrication.
- c) *Film thickness parameter*. Film thickness parameter,  $h/R_q$  is shown as well for each

lubrication regimes, where  $R_q$  is known as the root mean square roughness.  $h/R_q$  has been considered to be a useful parameter in characterisation of lubrication layer, shown in Figure 2.5.

Table 2.1. Representative friction coefficient for various lubrication regimes (Dowson, 2001).

Lubrication regimes	Friction coefficient
Dry	0.1-2
Boundary	0.07-0.15
Mixed	0.01-0.1
Fluid film	0.001-0.02

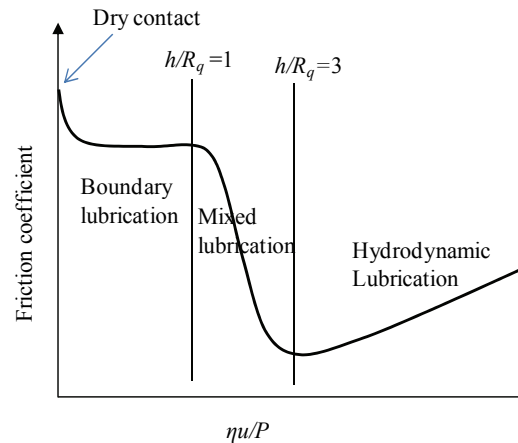


Figure 2.5. Stribeck curve and lubrication regimes,  $\eta$  refers to viscosity of lubricant,  $u$  refers to speed, and  $P$  is the load at the interface.

A number of numerical models have been developed for studying the mixed-EHL contact based on the deterministic models (Jiang *et al.*, 1999; Hu and Zhu, 2000; Zhao *et al.*, 2001; Redlich *et al.*, 2003; Wang *et al.*, 2004; Holmes *et al.*, 2005; Ichimaru, 2005). These analyses are all based on deterministic models with a common feature of using the coupled approach to simultaneously solve both fluid film lubrication in the hydrodynamic lubricated area, and direct asperity contacts when the lubricating film thickness was reduced to a similar height of asperities. In solving the Reynolds equation, elastic deformation equation, asperity contact pressure, and operation conditions, the numerical method has been found to be much more complex and demanding higher ability of the computational server.

A simple concept for load sharing has been chosen for the study of the mixed lubrication in this thesis. It is assumed that the separation between two surfaces is governed by the deformation of asperities, as both compressed lubricant and interacting asperities support normal load. If the total load on the contact is  $P_t$ , the load supported by asperities is  $P_a$ , and the load lifted by liquid is  $P_l$ , the following expression arises:

$$P_t = P_l + P_a \quad (2.7)$$

Figure 2.6 shows the total contact pressure is shared between direct solid to solid contact and a liquid film.

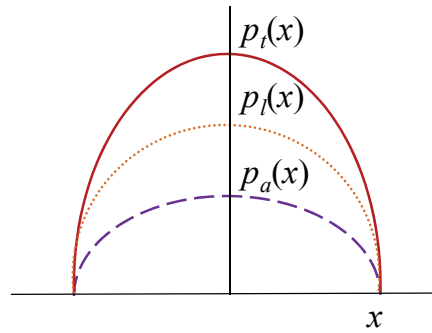


Figure 2.6. Pressure sharing in the mixed lubrication regime.

Johnson *et al.* (1972) introduced the scaling factor  $\gamma$  to define these two parts:

$$\frac{1}{\gamma_1} + \frac{1}{\gamma_2} = 1 \quad (2.8)$$

Where,  $1/\gamma_1$  and  $1/\gamma_2$  refer to the sharing proportions for lubricant action and asperity interaction respectively. In this model, it is assumed that hydrodynamic film formation and solid contact are mutually independent, so that the film formation is not affected by the presence of roughness.

The concept of load sharing is widely used for modelling mixed lubrication problems (Tsao, 1975; Soda, 1985; Yamaguchi and Matsuoka, 1992). Combining the classical contact theory from Greenwood and Williamson (1966) and the Moes's film thickness function (Moes, 1992), a similar approach was adopted by Gelinck and Schipper and used to predict film thickness and friction for line contact problems (Gelinck and Schipper, 1999; 2000).

Later, Lu carried out experimental study on a mixed lubrication line contact (Lu *et al.*, 2006; Lu and Khonsari, 2007). The Stribeck curve was presented and compared with the simulation results using Gelinck and Schipper's model (1999; 2000), which shows good agreement. Figure 2.7 shows part of Lu's work; friction coefficient and film thickness parameter varying with Sommerfeld number (explained in Chapter 5).

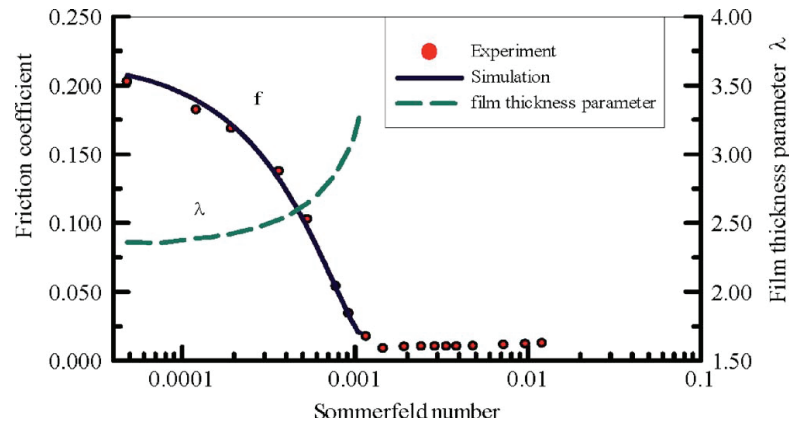


Figure 2.7. The film thickness parameter and friction coefficient as a function of the Sommerfeld number (Lu *et al.*, 2006).

## 2.3 Ultrasonic Method

Ultrasonic waves have a wide variety of applications over an extended range of intensity, including cutting, cleaning and medical applications. The application of ultrasound to non-destructive testing was first made possible with the discovery of the piezoelectric effect by the brothers Pierre and Jacques Curie in 1880. It is currently most widely used as a testing method. Furthermore, due to the reducing cost and increasing capabilities of pulsing and digitizing equipment, the use of ultrasonic testing method is becoming increasingly widespread.

The ultrasonic method used to study a contact was first proposed by Kendall and Tabor (1971) and Manolov (1970). They found the reflection/transmission of ultrasonic waves from/through a contact interface was influenced by the contact stiffness. Tattersall (1973) gave the following relationship between ultrasonic reflection coefficient and the stiffness per unit area,  $K$ :



$$R = \frac{z_1 - z_2 + i\omega(z_1 z_2 / K)}{z_1 + z_2 + i\omega(z_1 z_2 / K)} \quad (2.9)$$

Where,  $z_1$  and  $z_2$  are the acoustic impedances of two host mediums, 1 and 2 denotes the materials above and below the interface respectively, and  $\omega$  is the angular frequency of the ultrasound wave ( $\omega=2\pi f$ ),  $f$  is the frequency of ultrasound waves.

Kendall and Tabor's work was later followed by some theoretical work (Schoenberg, 1980; Baik, 1984; Temple, 1985). Haines (1980) combined the Kendall-Tabor model (1971) with the Tsukizoe-Hisakado model of contact of rough surfaces (Tsukizoe and Hisakado, 1965; 1968). Their results showed a theoretical dependence of the reflection/transmission coefficient of ultrasonic waves on the nominal contact pressure and the surface parameters. This provides a method to calculate contacting pressure distribution at an interface by studying ultrasonic reflection from the interface.

Figure 2.8 shows four contact cases studied by ultrasonic method in this work. For static dry contact, nominal normal pressure,  $p_{nom}$ , is supported by contacting asperities. When ultrasound is projected onto the interface, some of it,  $T$ , is transmitted through to the second material and some of it,  $R$ , is reflected back at air gaps, shown by Figure 2.8 (a). If the interface is wetted but still static, some ultrasound is reflected back from the wet layer, shown by Figure 2.8 (b). Figure 2.8 (c) shows the mixed lubrication case, where the nominal pressure is shared by asperity interaction and lubricant action. Some ultrasound is transmitted through asperity contact but some is reflected from liquid layer. If a full lubricant layer is formed to separate two contacting surfaces; all reflected ultrasound is from the liquid layer, shown by Figure 2.8 (d). This provides a method for determining the lubricating film thickness through the ultrasonic measurement.

As the reflection/transmission coefficient of ultrasonic waves from/through a contact interface refers to the nominal contact pressure and other surface parameters, it is widely used to characterise different contacts (Manolov, 1970; Kendall and Tabor, 1971; Arakawa, 1983; Minakuchi *et al.*, 1985; Królikowski and Szczepek, 1991; Berthoud and Baumberger, 1998; Dwyer-Joyce *et al.*, 2001).

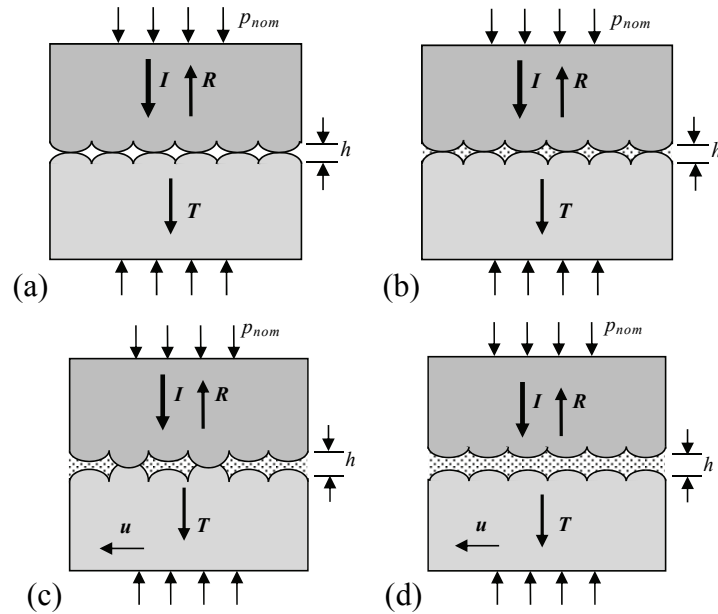


Figure 2.8. Ultrasonic reflection for four contact cases, (a) dry static contact, (b) wet static contact, (c) mixed lubrication contact, and (d) hydrodynamic lubrication.

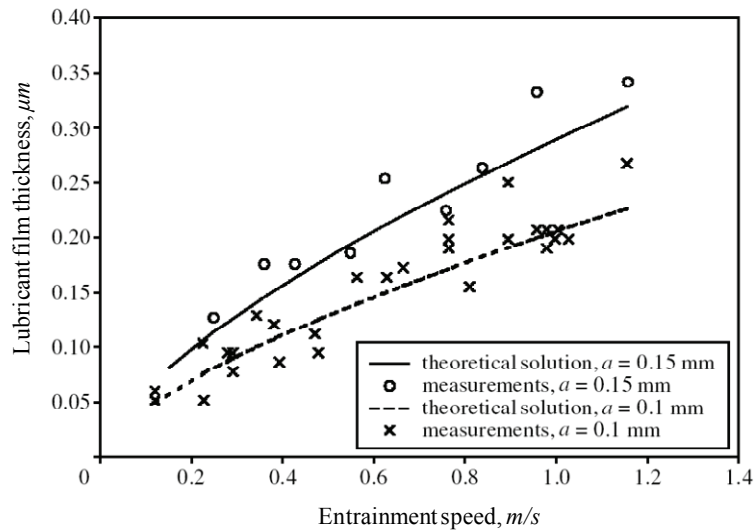


Figure 2.9. EHL lubricant film thickness variation with ball-sliding speed ( $a$  is contact radii), Ultrasonic reflection measurements are compared with a theoretical solution (Dwyer-Joyce *et al.*, 2003).

The ultrasonic technique has been used for the measurement of thin oil films in machine components (Dwyer-Joyce *et al.*, 2003; Harper *et al.*, 2005; Reddyhoff *et al.*, 2008; Zhang and Drinkwater, 2008; Dwyer-Joyce *et al.*, 2011). When ultrasonic pulses are incident at a rough surface contact or a thin liquid layer, they are partially reflected and partially transmitted, shown in Figure 2.8 (c) and (d). The more contact that exists so the thinner the oil film, the less the reflection. Figure 2.9 shows lubrication film thickness

from ultrasonic measurement for an EHL contact (Dwyer-Joyce *et al.*, 2003).

## 2.4 Interface Stiffness

### 2.4.1 Contact Stiffness

Normal contact between elastic bodies has always been a hot topic among researchers. Much theoretical work has been carried out in order to calculate elastic and plastic deformation of contacting surfaces with the characteristics of surface asperities, to show the factors affecting the deformation (Tsukizoe and Hisakado, 1965; Greenwood and Williamson, 1966; Tsukizoe and Hisakado, 1968; Hisakado, 1969, 1970; Pullen and Williamson, 1972; Tsukada *et al.*, 1972; Tsukada and Anno, 1972; Uppal and Probert, 1972; Nuri and Halling, 1975). A term that determines the relationship between applied pressure and approach of contacting surfaces is called contact stiffness. It is therefore related to the deformation of asperity/surface and the friction at the interface, and considered to be one of the key parameters in studying contact dynamics and modelling interfaces.

The earlier exploration of contact stiffness was carried out by Kendall and Tabor (1971), Tattersall (1973), and Thomas and Sayles (1977). In order to represent the compliance or stiffness at the interface, which will be used to define the usual boundary conditions that displacement and stress are continuous, Tattersall (1973) introduced a ‘spring’ concept for modelling the contact between two isotropic elastic mediums. The following sketch was used to model the contact between two isotropic elastic mediums, body 1 and 2, shown in Figure 2.10 (a).

A density of springs was used to express the interfacial forces between two mediums. When external pressure is applied on the interface, the properties of these springs will give the displacement of the coupling surfaces of two host bodies. The strength of these springs is called interfacial contact stiffness (normal to the contact) and is defined by:

$$K = \frac{\textit{increase in stress on the adjacent surfaces}}{\textit{increase in separation between adjacent surfaces}}$$

Namely,

$$K = -\frac{dp_{nom}}{dh} \quad (2.10)$$

Where,  $h$  is the separation of the mean lines of the two contacting surfaces, and  $p_{nom}$  is the nominal contact pressure given by the applied load divided by the nominal contact area. It should be noted that the interfacial stiffness is not like spring stiffness (a constant in Hooke's law) but a non-linear parameter. When the contact area is low, the separation will be easily decreased under little applied load. Conversely, if the contact area is high, a larger load is needed to get the surfaces to approach by the same amount.

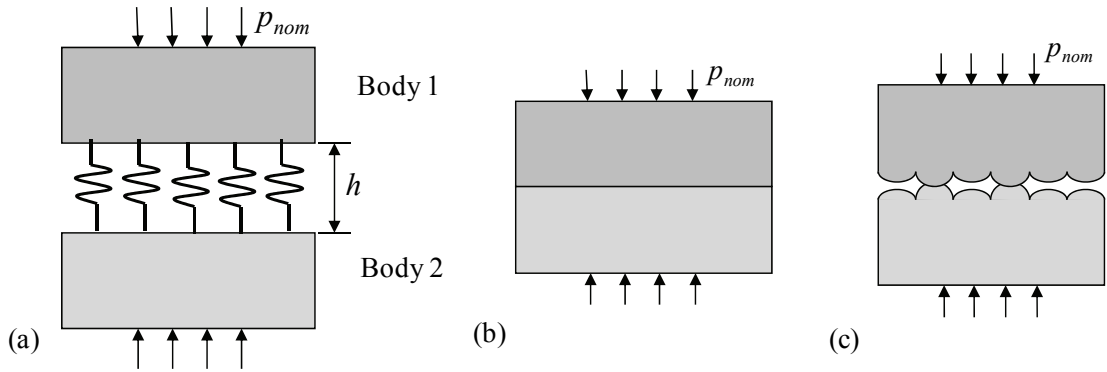


Figure 2.10. (a) Sketch of contact between two bodies, (b) perfectly smooth surfaces contact, and (c) rough surfaces contact.

The springs transmit stress instantaneously across the boundary, so that the stress at the boundary of medium 1 is always equal to the stress at the boundary of medium 2. Obviously, if two materials are perfectly smooth, shown by Figure 2.10 (b), the contact tends to infinitely rigid ( $K \rightarrow \infty$ ). Whereas, if the coupling bodies have rough surfaces, the springs are finitely, shown by Figure 2.10 (c). The top medium (body 1) has a completely free boundary; there is no energy transmitted into the second medium (body 2).

For a loaded interface under the nominal pressure,  $p$ , McCool (1986) deduced the following expression for asperity contact stiffness based on the GW model (1966).

$$K = \frac{p}{\sigma_s} \left[ 2.05 - 1.24 \log_e \left( \frac{p/E'}{0.57 D_s R_s^{1/2} \sigma_s^{3/2}} \right) \right]^{1/2} \quad (2.11)$$

Where  $p$  is expressed by Equation (2.5).

For Gaussian of summit height distribution, McCool tabulated, with a good approximation, the following expression in analytical form as:

$$F_{3/2}(t) = 0.43 \exp(-0.31t^2 - 1.43t) \quad (2.12)$$

## 2.4.2 Contact Stiffness of a Fluid Film

An ultrasonic wave will also be reflected back from a thin oil film between two solid surfaces, shown by Figure 2.8 (d). Both the interfaces at the front and back of the oil film will act to reflect the wave. In most lubricated machinery the oil film is thin, so these two reflections cannot be spatially separated. In this case, when the wavelength is large compared to the thickness of the interface, it behaves as a single reflector.

The same spring model approach, as used for rough surface contacts, can be applied to the measurement of lubricant films. A lubricant film acts as a compliant layer between the two mating surfaces. Rokhlin and Wang (2002) addressed the ultrasonic interaction and spring stiffness for thin viscoelastic fluid films. Dwyer-Joyce *et al.* (2004) showed that the oil films formed in conventional elastohydrodynamic and hydrodynamic regimes are also governed by the spring model. It is the stiffness of the liquid layer that controls the ultrasonic reflection and the spring model, Equation (2.9), applies.

The oil film is considered as a fluid of bulk modulus,  $B$ , between two infinite flat half spaces. The ultrasonic wave is again assumed to be large compared with the gap thickness,  $h$ . This means that the film is constrained to deformation in the through thickness direction only. The stiffness of a liquid film is related to its thickness. Hosten (1991) gave the following expression for the stiffness of the liquid layer:

$$K_l = \frac{B}{h} \quad (2.13)$$

## 2.4.3 Contact Stiffness in the Mixed Regime

At values of the film thickness greater than the surface roughness the interacting surfaces

are fully separated by the lubricant and the fluid supports the total load, shown schematically in Figure 2.8 (d). As the film thickness reduces due to high loads or slow speeds, the contacting asperities become more significant, shown in Figure 2.8 (c). In a mixed regime contact the interface consists of both liquid and solid bridges. The spring concept is introduced for this interface, the total interfacial contact stiffness (total normal stiffness),  $K_t$  is contributed from both asperity contact,  $K_a$ , and compressed lubricant,  $K_l$ , shown by Figure 2.11(b) (Dwyer-Joyce *et al.*, 2011):

$$K_t = K_l + K_a \quad (2.14)$$

So combining equations (2.10), (2.13) and (2.14) gives:

$$K_t = \frac{B}{h} - \frac{dp}{dh} \quad (2.15)$$

In this way the mixed regime interface is represented by two springs in parallel, shown in Figure 2.11. At greater surface separation, the asperity contact is negligible and, the  $dp/dh$  term falls to zero, the load is entirely carried by the liquid spring. For this reason the asperity spring is drawn not in contact with the lower surface. As the film thickness reduces, a limiting value similar to the height of asperities is reached, and solid asperities come to contact, giving the spring a finite stiffness, shown in Figure 2.11 (b). Conversely, at low separation both the stiffness of the thin liquid film and the asperity spring contribute to the solid stiffness.

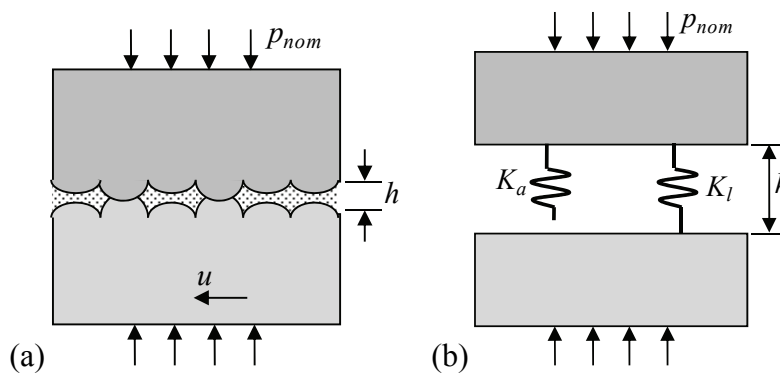


Figure 2.11. (a) Sketch of the mixed lubrication, and (b) concept of 'spring' for the mixed lubrication contact.

## 2.4.4 Shear Stiffness

Shear stiffness is defined as the ratio of applied shear stress to shear deformation. It has been known that the interface consists of independent micro-contacts. This configuration is referred to as a multi-contact interface (Berthoud and Baumberger, 1998). Under applied normal load, these multi-contact spots will undergo the shear stress caused by a sliding movement. The friction behavior is found to be governed by the material properties of load-bearing asperities. The statistical parameters, e.g. micro-contact size and multi-contact number, provide a method to study the shear property of the sliding interface. The shear stiffness shows the ability of the interface to resist the shear deformation. It is not an inherent property, but one determined by the strength of the multi-contact junctions which are undergoing interlock, elasto-plastic deformation, and friction dissipation for a sliding contact.

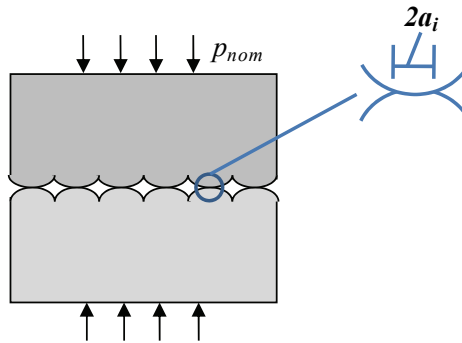


Figure 2.12. Multi-contact interface and micro-contact size,  $a_i$  is the radii of the  $i^{\text{th}}$  contact spot.

Figure 2.12 shows an interface characterised by a distribution  $\{a_i\}$  of the spot radii of the  $N$  micro-contacts for a given nominal pressure. For a single contact, the local shear stress,  $\sigma_i$ , induces a strain,  $\varepsilon_i = \sigma_i/G$ , within a volume of order of  $a_i^3$  (Timoshenko and Goodier, 1982).  $G$  is the shear modulus of material. If the relative displacement is set as  $x$  between the slider and the track, and the bulk deformation is neglected, the strain is:

$$\varepsilon_i \cong x / a_i \quad (2.16)$$

The symbol  $\cong$  stands for equality within a multiplicative geometry-dependent constant. Assuming all the contacts are independent with an average size of  $\langle a \rangle$ , then the friction force,  $F$ , is the integration of all micro-contacts:

$$F = \sum_{1 \leq i \leq N} \sigma_i a_i^2 \cong Gx \sum_{1 \leq i \leq N} a_i \quad (2.17)$$

According to the stiffness definition, the interfacial shear stiffness is given as (Johnson, 1985):

$$K_s \cong NG \langle a \rangle \quad (2.18)$$

With, the shear modulus of material,  $G$ , and the number of contacts,  $N$ , are given as:

$$G = \frac{E}{2(1+\nu)} \quad (2.19)$$

$$N = n \int_h^{+\infty} \phi(z) dz \quad (2.20)$$

$E$  and  $\nu$  are the elastic modulus and Poisson ratio of the material respectively,  $n$  is the total number of asperities,  $h$  is separation of contacting surfaces, and  $\phi(z)$  is a function of asperity height distribution.

## 2.5 Summary

The multi-contact interface between nominally smooth engineering surfaces has been presented. Due to the asperity interaction on a given interface, the real area of contact is significantly less than the apparent area of contact. The statistical asperity contact model presented by Greenwood and Williamson has been introduced. It represents an analytical solution for calculation of interface parameters, e.g. asperity interacting force, real contact area and interfacial stiffness.

For lubricated interfaces, hydrodynamic lubrication is not always possible due to severe operating conditions. Asperities contact takes place where the lubricant film breaks down. A mixed lubrication regime is formed at the interface. It is characterised for the presence of solid contact, with a proportion of the pressure remaining supported by a partial hydrodynamic film. Based on this concept, the Greenwood and Williamson will be adopted for developing a mixed lubrication model for a ball sliding on disc and a pin rotating inside bush contacting configurations. Load sharing proportions will obtained,



which presents contributions from the solid contact and the liquid layer for supporting the nominal pressure.

The concept and definition of normal and shear contact stiffness have been presented. Macroscopically, contact stiffness refers to the ability of interface to resist deformation and can currently be obtained through the ultrasonic method. While microscopically the multi-contact stiffness relates to the interface characteristics, e.g. contact stress distribution, multi-contact size and number, which can be analysed using a theoretical model. This provides a way to validate theoretical modelling for the investigation of an engineering interface.

# Chapter 3 Mixed Lubrication Model

In this chapter, a mixed lubrication model for a lubricated interface was developed based on a load sharing concept. Analysis of sharing factors and shear stress from asperity contact and liquid layer has been presented in the first part of this chapter. The formulation and solution of the model was introduced in the second part. Finally, some simulation results were presented for a ball-on-disc contact using this model. Scaling factors, film thickness, friction force and friction coefficient are presented.

## 3.1 Introduction

Figure 3.1 shows the hydraulic lubrication between two mating surfaces under a load of  $P$  and a moving speed  $u$ . In most cases, lower load and higher speed are wanted for thicker film layer,  $h$ , and hence lower friction on the interface. If a full film is formed, the lubrication regime is known as the hydrodynamic lubrication. However in many engineering applications, due to high load or low speed, film thickness has the similar order with surface roughness. Both the rough asperities and hydraulic lubricant support the applied load. This is called mixed lubrication. If operating conditions are too severe, asperity interaction support most of the load, and the lubrication regime falls to boundary lubrication. They are shown on the “Stribeck curve”, presented by Figure 2.5.

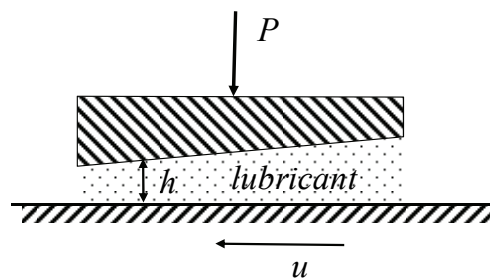


Figure 3.1. Sketch of a full film lubricated contact.

Mixed lubrication is a transition stage between boundary and hydrodynamic lubrication. It is a type of lubrication in which bearing surfaces support the load partially with asperity interaction and partially with the lubricant film. The modelling of mixed lubrication was carried out by Parir and Cheng (1978) to calculate pressure distribution and film thickness of rough surfaces contact. The modelling of load sharing between lubricant film and interacting asperities was first studied by Johnson *et al.* (1972) and Tallian (1972).

Much experimental and theoretical work has been done on mixed lubrication regime (Tsao and Tong, 1975; Soda, 1978, 1985; Yamaguchi and Matsuoka, 1992). Combining the classical contact theory from Greenwood and Williamson (1966) and the Moes's film thickness function, the Stribeck curve for line contact was predicted by Gelinck and Schipper (2000) and verified by Lu (2006, 2007) through experiments. In this section, mixed lubrication modelling for a point contact was developed and discussed. Load sharing proportions were predicted which give the contribution of lubricant layer and asperity interaction. Film thickness and friction coefficient in the contact were simulated against speed, load or integrated value, Stribeck parameter,  $\eta u/P$ . More theoretical results can be found in Chapter 4, 5 and 6. Experiments were carried out to verify modelling predictions for line and point contact respectively, which were presented in the later chapters.

### **3.2 Mixed Lubrication Contact**

In mixed lubrication regime, the pressure in the lubricant is not high enough to support the applied load. The separation between two contacting surfaces is of a similar height to the surface asperities. As a result, the breakdown of a lubricating film must be taking place and is associated, in some way, with contact between the asperities on the two solid surfaces when relative movement exists. The approach used here is based on the work of Johnson *et al.* (1972), which introduced the concept of load sharing between pressed lubrication liquid and interacting asperities.

### 3.2.1 Load Sharing Concept

In mixed lubrication regime, both asperity contact and lubricant support exist. The total load  $P$  is assumed to be shared by contacting asperities and compressed lubricant. This concept of load sharing relationship,  $P_t = P_l + P_a$ , is widely used for modelling mixed lubrication problems (Tsao and Tong, 1975; Soda, 1978; Yamaguchi and Matsuoka, 1992). It was assumed that hydrodynamic film formation and solid contact are mutually independent, so that the film formation is not affected by the presence of roughness (Johnson *et al.*, 1972). A statistical model of rough surface contact was combined with a solution for smooth surface elastohydrodynamic film thickness. A similar approach was adopted by Gelinck and Schipper (2000) who combined the solid contact equations and lubrication theory to predicted film thickness and friction for line contact problems.

Figure 3.2 illustrates a rough surface contact (Johnson *et al.*, 1972). The two surfaces have a random distribution of asperity heights. A large number of asperity contacts might be expected within the nominal contact area so that, although the pressure on single contact spots vary, it can be assumed that a constant average pressure distribution occurs, this is called the apparent asperity pressure,  $P_a$ . This pressure, together with the pressure in the lubricant film,  $P_l$ , makes up the total pressure,  $P_t$ , which gives rise to the bulk elastic deformation of the two surfaces. So, the pressure is contributed by part from compressed liquid and metallic contact, shown by the following expression:

$$p_t = p_l + p_a \quad (3.1)$$

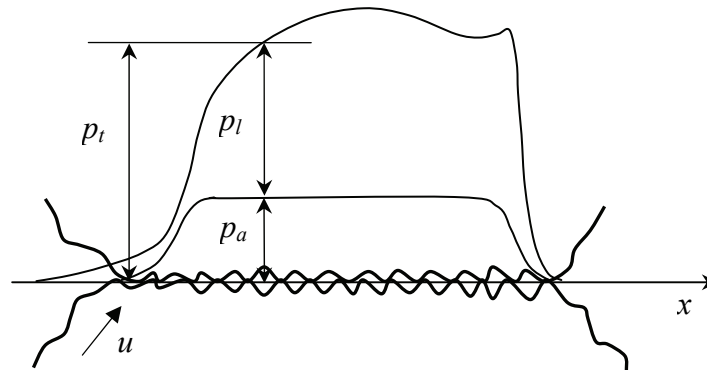


Figure 3.2. An EHL contact with rough surfaces: the total pressure  $p_t$  is made up of the fluid pressure  $p_l$  and the asperity contact pressure  $p_a$  (Johnson *et al.*, 1972).

It has been discussed that the nominal contact pressure of asperities is expressed as Equation 2.5. Meanwhile, the pressure in lubricating liquid cannot be calculated directly but can be related to the film thickness from a fitting equation developed by Hamrock and Dowson (1976, 1977). When the film thickness is obtained through theoretical or experimental method, the pressure in compressed lubricant can be computed by the following equation:

$$H = 2.69U^{0.67}G^{0.53}W^{-0.067}(1 - 0.61e^{-0.73}) \quad (3.2)$$

Where  $H$ ,  $W$ ,  $U$ , and  $G$  are a set of dimensionless parameters defined by:

$$H = \frac{h}{R'}, \quad W = \frac{P_l}{2E'R'^2}, \quad U = \frac{\eta_0 u}{2E'R'}, \quad G = 2\alpha'E'$$

The explanations of parameters in the above expressions were detailed in Section 3.3.2.

### 3.2.2 Scaling Factors

Figure 3.3 shows the concept of pressure sharing in a contact between two elastic bodies. The exertion of the load  $P$  causes the bulk deformation of the two solids and gives rise to the nominal contact area. The spring  $K_h$  represents the bulk Hertz deformation of both bodies. For a lubricated contact, both oil film and asperities exist, the total contact pressure  $p_t$ , are shared by oil and asperities which are represented by the parallel springs  $K_l$ , and  $K_a$  respectively. The proportion of the load carried by each spring depends upon the relative uncompressed length and the stiffness. Thus for an ideal smooth surface operating with lubricant, the whole load is taken by the oil film as the “asperity spring” whose uncompressed length does not fill the gap whereupon. Conversely rough surfaces operating in conditions of inadequate or starved lubrication would be represented by an “asperity spring” which carries the entire load and a “fluid spring” which hardly fills the gap. Therefore, the condition of mixed lubrication could be represented by two compressed springs, referring to asperities and lubricant film respectively.

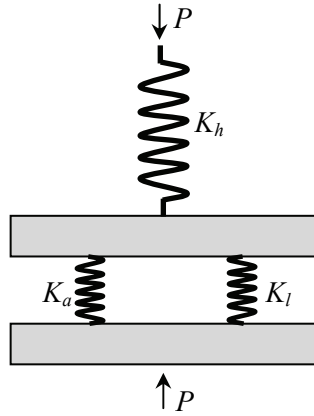


Figure 3.3. A diagrammatic representation of the flexible elements in an EHL contact (Johnson *et al.*, 1972).

$\gamma_1$  and  $\gamma_2$  were introduced in Johnson's model (Johnson *et al.*, 1972) to represent the proportions of hydrodynamic lifting force and the force from surface asperities interaction. They are written as:

$$\gamma_1 P_t = P_l \quad (3.3)$$

$$\gamma_2 P_a = P_t \quad (3.4)$$

As the total normal load,  $P_t$ , is shared by the hydrodynamic lifting force,  $P_l$ , and the asperity contact force,  $P_a$ , namely:

$$P_t = P_l + P_a \quad (3.5)$$

So, combining equations (3.3)-(3.5), the following expression is obtained,

$$\frac{1}{\gamma_1} + \frac{1}{\gamma_2} = 1 \quad (3.6)$$

Where  $1/\gamma_1$  represents the proportion of load supported by compressed lubricant, and  $1/\gamma_2$  represents the proportion of load supported by compressed asperities.

### 3.2.3 Shear Force on a Mixed Lubrication Contact

The friction force at asperity contacts is due to the tangential interaction of asperity summits. Similarly, a viscous friction is generated in lubricant liquid if tangential movement taking place between mating surfaces. Figure 3.4 shows how shear forces

from asperity contact and liquid layer contribute to the entire friction force,  $Q_t$ .

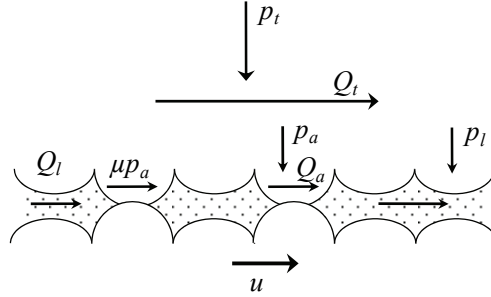


Figure 3.4. A sketch of shear forces taking place on a mixed lubrication interface.

$$Q_t = Q_l + Q_a \quad (3.7)$$

Entire shear force,  $Q_t$ , is the integration of asperity interacting force,  $Q_a$ , expressed by dry friction coefficient,  $\mu$ , multiplying normal force,  $p_a$ , and liquid shear force,  $Q_l$ .

### 3.2.3.1 Shear Force of a Lubricant Film

The hydrodynamic shear force,  $Q_l$ , is given by the following expression,

$$Q_l = \iint_{A_l} \tau_l dA_l \quad (3.8)$$

Where  $\tau_l$  represents the shear stress and  $A_l$  is the contact area of the fluid.

The Bair-Winer model (1979) is used to deduce the lubricant shear force,  $Q_l$ . In their model, the shear rate,  $\dot{\gamma}$ , is expressed as:

$$\dot{\gamma} = -\frac{\tau_L}{\eta} \ln\left(1 - \frac{\tau_l}{\tau_L}\right) \quad (3.9)$$

Where  $\eta$  represents the lubricant viscosity and  $\tau_L$  is the limiting shear stress and is expressed as (Bair and Winer, 1979, 1990; Jacobson and Kalker, 2000; Ståhl and Jacobson, 2003; Hamrock *et al.*, 2004):

$$\tau_L = \tau_{L0} + \beta_0 p_m \quad (3.10)$$

Where  $\tau_{L0}$  is the limiting shear stress at ambient pressure,  $\beta_0$  is the slope of the limiting shear stress-pressure relation; both are constants unique to specified oil. And  $p_m$  represents the mean contact pressure from Hertzian theory.

A dimensionless shear rate parameter,  $\lambda'$ , was introduced by Khonsari and Hua (1993) which has the following form:

$$\lambda' = \eta \frac{|\dot{\gamma}|}{\tau_L} \quad (3.11)$$

By combining equations (3.9)-(3.11), the expression for shear stress in lubricant can be obtained as:

$$\tau_l = \tau_L (1 - e^{-\lambda'}) \quad (3.12)$$

The traction force per unit length of contact  $Q_L$  is determined by integrating the shear stress along the movement direction:

$$Q_L = \int \tau_l dx = \int \tau_L (1 - e^{-\lambda'}) dx \quad (3.13)$$

A laminar Newtonian fluid is assumed in this model and there is no slip at either contact surface. The relative motion between two contacting surfaces can be shown by Figure 3.5.

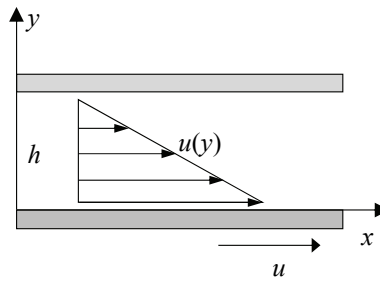


Figure 3.5. Sketch of the flow of lubricant at the interface.

So the shear rate is written as:

$$\dot{\gamma} = \frac{\partial u}{\partial y} = \frac{u}{h} \quad (3.14)$$

Where  $u$  is the speed of the lower surface, and  $h$  represents the separation of two rough surfaces, which is assumed to be constant and equal to the central film thickness  $h_c$ .

Substituting equations (3.11), and (3.14) into (3.13), and taking the positive traction force,



the total hydrodynamic friction force is expressed as:

$$Q_t = \tau_L \left(1 - e^{-\eta u / h_c \tau_L}\right) \cdot A_0 \quad (3.15)$$

Where  $A_0$  is the nominal contact area.

The lubricant viscosity  $\eta$  is assumed to obey the Roelands's formula (Roelands, 1966),

$$\eta = \eta_0 \left( \frac{\eta_\infty}{\eta_0} \right)^{\left[ 1 - \left( 1 + \frac{P_m}{c_p} \right)^Z \right]} \quad (3.16)$$

Where  $\eta_0$  is the lubricant dynamic viscosity at zero pressure and inlet temperature, for most of oil lubricants, its value can be found in (Raimondi and Szeri, 1984).  $\eta_\infty$  and  $c_p$  are two constants in the function with the values of  $6.315 \times 10^{-5}$  Pa·s and  $1.962 \times 10^8$  Pa respectively (Hamrock *et al.*, 2004). The Roelands's pressure-viscosity index  $Z$  can be estimated from the lubricant's viscosity (dynamic viscosity, in centipoises) at 40°C and 100°C through the following equation (Fein, 1997),

$$Z = \left[ 7.81(H_{40} - H_{100}) \right]^{1.5} (F_{40}) \quad (3.17)$$

Where

$$H_{40} = \log \left[ \log(\mu_{40}) + 1.2 \right]$$

$$H_{100} = \log \left[ \log(\mu_{100}) + 1.2 \right]$$

$$F_{40} = 0.885 - 0.864H_{40}$$

### 3.2.3.2 Shear Force for Metallic Contact

The friction force is the integration of all single asperity contacts, shown in Figure 3.4. So the entire friction force for metallic contact,  $Q_a$ , is the integration of each shear force element (Gelinck and Schipper, 2000):

$$Q_a = \sum_{i=1}^N \iint \mu_{ai} P_{ai} dA_{ai} \quad (3.18)$$

Where  $N$ ,  $\mu$ ,  $P_a$ , and  $A_a$  are the number of asperity contacts, friction coefficient, mean contact pressure, and contact area respectively, and  $i$  refers to the  $i^{th}$  asperity contact.

The friction coefficient,  $\mu_a$ , is assumed to be constant, over all asperity contacts:

$$Q_a = \mu_a \sum_{i=1}^N \iint p_{ai} dA_{ai} \quad (3.19)$$

The pressure from each contacting spot contributes to the total load,  $P_a$  supported by the interacting asperities:

$$P_a = \sum_{i=1}^N \iint p_{ai} dA_{ai} \quad (3.20)$$

Therefore, the total tangential force from metallic contact is written as:

$$Q_a = \mu_a P_a \quad (3.21)$$

### 3.2.3.3 Friction Coefficient

It has been shown in Figure 3.4 that the total friction force,  $Q_t$ , produced at the interface is composed of two parts: one is the hydrodynamic friction force,  $Q_l$ , which mostly relies on lubricant viscosity, and the other is asperity interacting shear stress,  $Q_a$ , which is influenced mostly by the morphology of the mating surfaces. The whole friction force is the sum of these two parts:

$$Q_t = Q_l + Q_a \quad (3.22)$$

Friction coefficient is defined as friction force divided by external normal load. So the apparent friction coefficient of mixed lubrication contact is expressed as:

$$\mu = \frac{Q_t}{P_t} = \frac{Q_l + Q_a}{P_t} \quad (3.23)$$

## 3.3 Mixed Lubrication Model

### 3.3.1 Asperity Contact Component

The rough surface contact the GW model (1966) has been adopted in this study. In this model, the load supported by asperities is:

$$P_a = p_a A_0 \quad (3.24)$$

Where  $p_a$  is the nominal contact pressure, and  $A_0$  is the nominal contact area. Greenwood and Williamson gave the contact pressure in a rough surface interface as:

$$p_a = \frac{2}{3} D_s E' R_s^{1/2} \sigma_s^{3/2} F_{3/2}(t) \quad (3.25)$$

Combining equations (3.24) and (3.25), the load supported by asperities becomes:

$$P_a = \frac{2}{3} A_0 \pi D_s E' R_s^{1/2} \sigma_s^{3/2} F_{3/2}(t) \quad (3.26)$$

As it is known that the load sharing proportion of metallic contact part is set as  $1/\gamma_2$ . In Equation (3.26), replacing  $P_a$  by  $P_t/\gamma_2$ ,  $E'$  by  $E'/\gamma_2$ , and  $D_s$  by  $D_s/\gamma_2$  (Gelinck and Schipper, 2000) gives:

$$\frac{P_t}{\gamma_2} = \frac{2}{3} \pi D_s E' R_s^{1/2} \sigma_s^{3/2} \left( \frac{3P_t R'}{4E'} \right)^{2/3} F_{3/2}(t) \quad (3.27)$$

### 3.3.2 Elastohydrodynamic Lubrication Component

The load lifted by lubricant can be related to film thickness by using the film thickness equation for an EHL point contact developed by Hamrock and Dowson (1976, 1977):

$$H = 2.69 U^{0.67} G^{0.53} W^{-0.067} (1 - 0.61 e^{-0.73}) \quad (3.28)$$

Where  $H$ ,  $W$ ,  $U$ , and  $G$  are a set of dimensionless parameters are defined as follows:

$$H = \frac{h}{R'}, \quad W = \frac{P_l}{2E'R'^2}, \quad U = \frac{\eta_0 u}{2E'R'}, \quad G = 2\alpha'E'$$

where  $\eta_0$  is the inlet viscosity at ambient pressure,  $u$  is sliding speed, and  $\alpha'$  is the pressure-viscosity coefficient, which can be obtained by plotting the natural logarithm of dynamic viscosity versus pressure. The slope of the graph is the pressure-viscosity coefficient.

Similarly, the scaling factor,  $\gamma_1$  is used to express the load supported by the hydrodynamic film. Substituting  $E'/\gamma_1$  for  $E'$  and  $P_t/\gamma_1$  for  $P$ , again following the method of Gelinck and Schipper (2000), the film thickness equation for mixed lubrication can be rewritten as:

$$\frac{h}{R'} = 1.899 \left( \frac{\eta_0 u \gamma_1}{2E'R'} \right)^{0.67} \left( \frac{2\alpha'E'}{\gamma_1} \right)^{0.53} \left( \frac{P_t}{2E'R'^2} \right)^{-0.067} \quad (3.29)$$

### 3.3.3 Formulation and MathCAD Solution

Equation (3.6) defines the load sharing proportions  $1/\gamma_1$  and  $1/\gamma_2$ . Equation (3.27) relates  $1/\gamma_2$  to the surface separation,  $h$ . The third Equation, (3.29) relates the lubricant layer thickness to  $1/\gamma_1$ . Hence, a set of equations containing three un-known reads:

$$\begin{cases} \frac{1}{\gamma_1} + \frac{1}{\gamma_2} = 1 \\ \frac{P_t}{\gamma_2} = \frac{2}{3} \pi D_s E' R_s^{1/2} \sigma_s^{3/2} \left( \frac{3P_t R'}{4E'} \right)^{2/3} F_{3/2}(t) \\ \frac{h}{R'} = 1.899 \left( \frac{\eta_0 u \gamma_1}{2E'R'} \right)^{0.67} \left( \frac{2\alpha'E'}{\gamma_1} \right)^{0.53} \left( \frac{P_t}{2E'R'^2} \right)^{-0.067} \end{cases} \quad (3.30)$$

A MathCAD program was written to solve this set of simultaneous equations for given input conditions. Once scaling factors  $1/\gamma_1$ ,  $1/\gamma_2$  and film thickness  $h$  are solved, then load sharing, shear forces, and friction coefficient can be calculated using equations (3.3), (3.4), (3.15), (3.21) and (3.23). More details about calculation process can be found in Appendix A-1.

## 3.5 Conclusions

In this chapter, a mixed lubrication model has been developed to determine load sharing factors and lubrication film thickness. Programs have been written using MathCAD for solving the mixed lubrication model.

In Chapter 4, a ball-on-disc contact has been simulated using the mixed lubrication model. The load sharing parameters and liquid layer thickness, friction force from asperity and liquid were obtained as well as the apparent friction coefficient at the interface. The model was further used for the determination of the interfacial stiffness. And the predictions were compared to ultrasonic measurements. In Chapter 5, the model was revised for predicting friction coefficient (frictional torque) for a landing gear pin joint contact.

# Chapter 4 Mixed Lubrication in an EHL Contact

In this chapter an EHL contact (Elastohydrodynamic lubrication) between a lubricated sliding ball and a disc was investigated. First, the contact stiffness for static dry/wet contact was studied using different statistical models. Then, for the dynamic contact, the mixed lubrication model discussed in Chapter 3 was applied to predict the stiffness of asperity contact and liquid layer. Simulations were compared to ultrasonic measurements. Finally, the oil film thickness was analysed by studying the contact stiffness calculated from ultrasonic reflection.

## 4.1 Introduction

EHL is a common lubrication case taking place on counter-formal surfaces. Ideally, when two deformable mediums come into contact, it is theoretically possible to capture a hydrodynamic film between two faces thus there is no metallic contact occurring. This requires the surfaces to be extremely smooth and carefully aligned. However, frequently the hydrodynamic action is insufficient to generate a fluid film thick enough to separate rough asperities distributed on mating surfaces.

Figure 4.1 shows four contact cases between a steel ball and disc: (a) static dry contact under the normal load of  $P_t$ , which is supported by interacting asperities randomly distributed on the rough surface of contact bodies; (b) static contact wetted by lubricating oil; (c) mixed lubrication contact, where normal load is shared by interacting asperity summits and the compressed oil film; (d) hydrodynamic lubrication, where a full oil film is formed, which lifts the entire normal load.

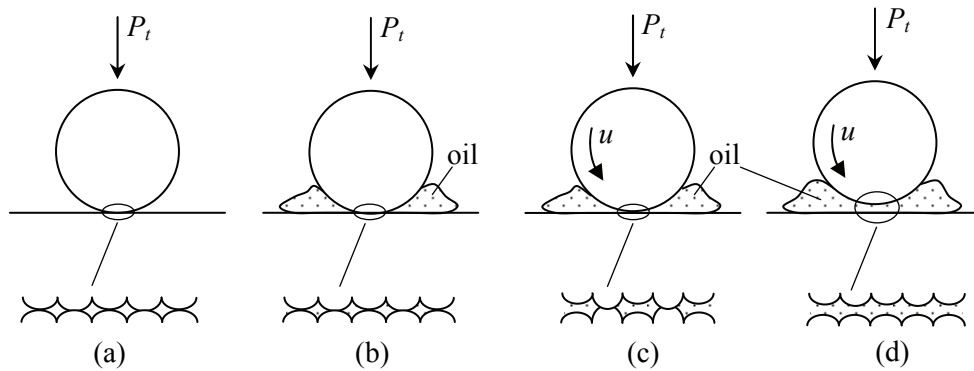


Figure 4.1. Sketch of a ball and disc contact, (a) static dry contact, (b) static wet contact, (c) mixed lubrication contact, (d) full film separation.

Ultrasonic experiment of the steel ball sliding on disc was carried out to study the contact stiffness for above contact cases by Reddyhoff (2006). However, ultrasonic reflection yields only a combined stiffness from the interface, which is composed of both liquid stiffness and asperity contact stiffness. It is impossible to extract the individual stiffness using experimental method. In this work, the mixed lubrication model was used to predict individual stiffness. A good agreement between theoretical simulations and ultrasonic measurements were observed for dynamic contacts. Then, load sharing proportions, predicted in the model, was used to separate liquid layer stiffness from total interfacial stiffness, and hence determine the oil film thickness. This demonstrates an approach by which this model can be used to extract useful information from the ultrasonically measured data. Details were presented in the later sections.

## 4.2 Experimental Benchmark

Ultrasonic measurements on the ball-on-disc contact were carried out under varying mean Hertzian pressures (Reddyhoff, 2006). Figure 4.2 (a) shows the configuration of the contact, where ultrasound is reflected and measured to determine contact stiffness. A water bath was used to enable focusing of the ultrasonic pulse. The ball was half submerged in the lubricant oil and rotating, hence a film layer was formed between the ball and the disc. The contact between ball and disc was pure sliding and the sliding speed of the ball was recorded. Surface speed was set from zero to 0.5 m/s during all tests. The load, in the range of 20 to 80 N, was applied on the sliding ball by a hydraulic jacking

system below the ball. According to an elastic calculation, this corresponded to contact radii from 0.11 to 0.174 mm, and mean contact pressures in the range of 0.53 to 0.84 GPa.

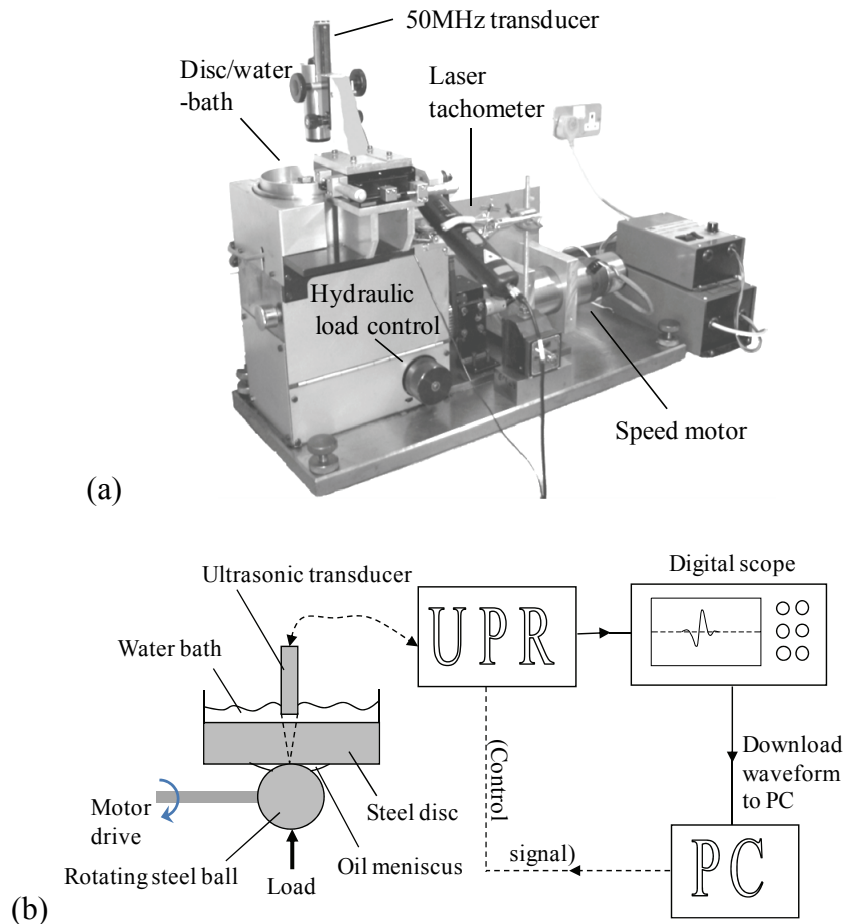


Figure 4.2. (a) Photo of the ultrasonic test rig, and (b) schematic diagram of elastohydrodynamic test apparatus.

Figure 4.2 (b) shows the schematic diagram of ultrasonic test apparatus. A bespoke 50 MHz piezoelectric transducer was commissioned (from NDT Systems Ltd) for this test case. The test lubricant was a VG68 mineral oil (Shell Turbo T68). Both the ball (19mm in diameter) and disk were ground and lapped to give surface finishes of RMS roughness  $R_q = 0.256 \mu\text{m}$ , and  $R_q = 0.339 \mu\text{m}$  respectively.



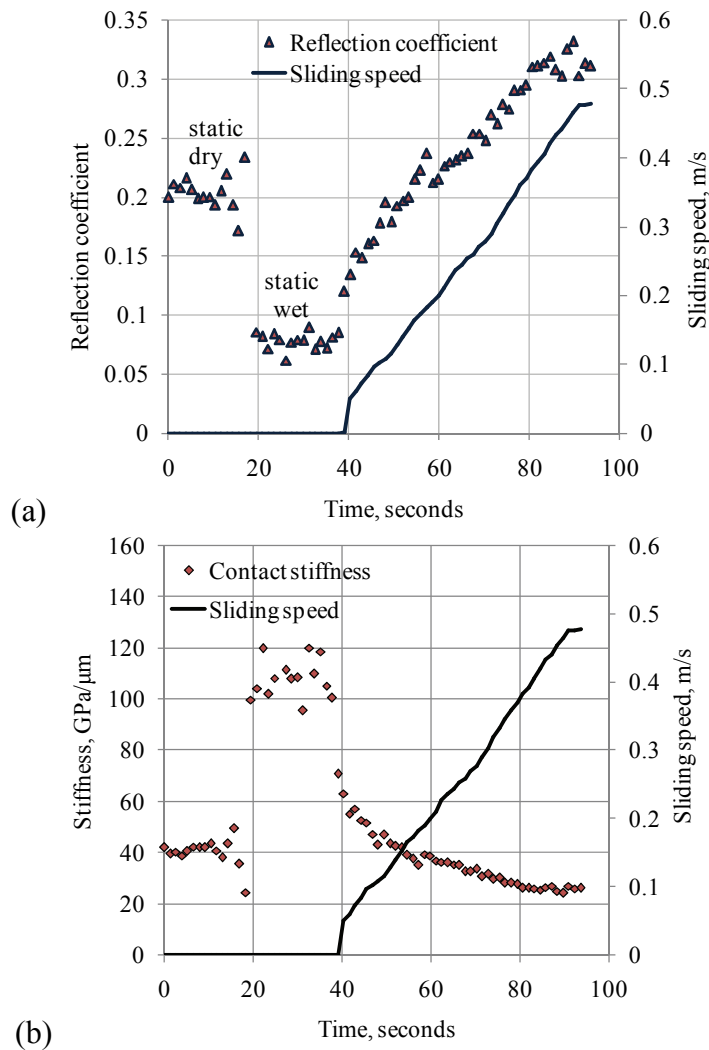


Figure 4.3. Ultrasound reflection measurement for a start-up sequence of ball-on-disc contact under the mean contact pressure of 0.76 GPa, (a) reflection coefficient and ball sliding speed varying with time, (b) contact stiffness calculated from measured reflection coefficient.

Figure 4.3 (a) shows the reflection coefficient measured in a start-up sequence for the ball and disc contact. The first stage in the test was shown as ‘static dry’ on the figure, which corresponds to Figure 4.1 (a). The ultrasound was reflected from the interface composed of interacting asperities. The lubricating oil was then added to the contact and the ball was turned a few cycles before kept stationary to wet the interface, which corresponds to Figure 4.1 (b). This time ultrasonic waves were reflected both from metallic contact spots and the thin oil film. Reflection coefficient was found to decrease to around 0.07 from 0.2 for the static dry case. After that the sliding speed of ball increased gradually to 0.46 m/s. The reflection coefficient was increased with speed to 0.33. Figure 4.3 (b) is the interfacial stiffness calculated from reflection coefficient using ultrasonic spring model,

Equation (2.10) in Chapter 2. Contact stiffness was found to be around 40 GPa/ $\mu\text{m}$  at the dry stationary stage. After lubricant oil was added to the interface, it increased significantly to 110 GPa/ $\mu\text{m}$ . It can be seen that the lubricant oil trapped in the asperity gaps contributed greatly to the ultrasonic reflection and hence the interfacial stiffness. In the dynamic stage, the stiffness was found to decrease with increasing sliding speed. At the highest speed, the interfacial stiffness reached the lowest value of around 25 GPa/ $\mu\text{m}$ .

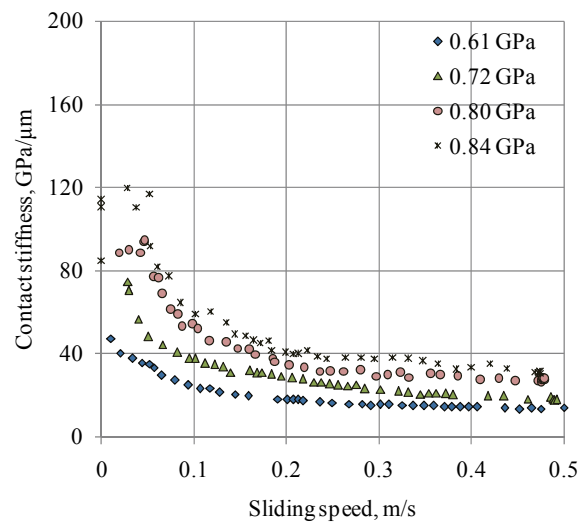


Figure 4.4. Interfacial stiffness of ball-on-disc contact against sliding speed under varying nominal pressures.

Figure 4.4 shows how oil lubricated contact stiffness calculated from measured reflection coefficient vary with sliding speed for a range of contact pressures. Higher pressure leads to better bonded interface and less ultrasound wave reflection. Therefore greater stiffness was obtained using the spring model. In the later section, the interfacial stiffness was analysed using the mixed lubrication model. Comparison between simulations and experimental results were presented.

## 4.3 Mixed Lubrication Model for Contact Stiffness

### 4.3.1 Stiffness of Static Dry Contact

The contact between rough surfaces has been investigated by many researchers. Three typical models of rough surface contact are: (i) the Greenwood-Williamson model (1966);

(ii) the Whitehouse-Archard-Onions model (Whitehouse and Archard, 1970; Onions and Archard, 1973); (iii) the Bush-Gibson-Thomas model (1975), which are referred as GW, WAO and BGT model respectively.

#### 4.3.1.1 GW Model

The GW model is based on purely elastic deformation of contacting asperities. Under all the contacting conditions, the deformation of asperities on the rough surfaces is assumed not to exceed the elastic regime. All the asperities are uniformly distributed on the contacting surfaces with the density per unit area,  $D_s$ . They are presumed to follow a normal probability law with a standard deviation,  $\sigma_s$ , and their summits are of spherical shape with the same radius of curvature,  $R_s$ .

In this model, the contacting parameters are obtained as:

The real contact area (total contact area of asperities):  $A = \pi D_s A_0 R_s \sigma_s F_1(t)$ ;

The nominal contact pressure:  $p = \frac{2}{3} D_s E' R_s^{1/2} \sigma_s^{3/2} F_{3/2}(t)$ ;

Number of contact spots:  $N = D_s A_0 F_0(t)$ .

Where  $N$  is the number of asperity contacting pairs,  $D_s$  is the asperity distribution density per unit area,  $A_0$  is the nominal contact area,  $A$  is the total contact area of the summits,  $R_s$  is the mean radius of the summits,  $\sigma_s$  is the variance of the summit height distribution,  $p$  is the nominal contact pressure,  $E'$  is the reduced elastic modulus of Hertzian contact,  $t$  is the standardized separation of surfaces,  $t = h/\sigma_s$ ,  $h$  is the separation of the mean lines of two rough surfaces, and  $F_n(t)$  is integral of summit height distribution, for Gaussian distribution of asperity heights it is expressed as Equation (2.6).

According to the definition of contact stiffness:

$$K = -\frac{dp}{dh} \quad (4.1)$$

McCool (1986) deduced the following expression for asperity contact stiffness:

$$K_a = \frac{p}{\sigma_s} \left[ 2.05 - 1.24 \log_e \left( \frac{p/E'}{0.57 D_s R_s^{1/2} \sigma_s^{3/2}} \right) \right]^{1/2} \quad (4.2)$$

It is clear that the contact stiffness is a function of contact pressure, and the asperity contact pressure is related to the integral parameter  $F_{3/2}(t)$ . For Gaussian distribution of summit height, McCool tabulated, with a good approximation, the following expression in analytical form, as:

$$F_{3/2}(t) = 0.43 \exp(-0.31t^2 - 1.43t) \quad (4.3)$$

#### 4.3.1.2 WAO Model

In this model, similar to the GW model, the contacting asperity summits are assumed to be hemispherical. Therefore the total real contact area is composed of many of circular spots. There are two main differences in the WAO model compared to GW model: firstly, the asperity height distribution in WAO model is not Gaussian but is a distribution function derived from the assumed Gaussian distribution; secondly, the radius of asperity summit is not assumed to be constant, but following the higher asperities have sharper peaks (smaller radius). The WAO model gives the following expressions for the real contact area and the relationship between the nominal contact pressure and the approach of the two surface mean lines:

The real contact area (total contact area of asperities):  $A = \pi D_s A_0 (2.3 R_s)^2 F_A(t)$ ;

The nominal contact pressure:  $p = \frac{4}{15} (5 D_s)^{1/2} E' \sigma_s F_p(t)$ ;

Number of contact spots:  $N = D_s A_0 F_n(t)$ .

$F_n(t)$ ,  $F_A(t)$  and  $F_p(t)$  are functions of the dimensionless separation between contacting surfaces. Whitehouse and Archard (1970) tabulated the following expressions for them with a quite good approximation in analytical form:

$$F_A(t) = 0.3885 \exp(-0.4t^2 - 1.3t) \quad (4.4)$$

$$F_p(t) = 0.612 \exp(-0.4t^2 - 1.3t) \quad (4.5)$$

$$F_n(t) = 2.6 \exp(-0.53t^2 - 0.24t) \quad (4.6)$$

Correspondingly, the real contact area, the nominal contact pressure and the contacting spot number are as follows:

The real contact area (total contact area of asperities):

$$A = 6.46D_s A_0 R_s^2 \exp(-0.4t^2 - 1.3t);$$

The nominal contact pressure:  $p = 1.877D_s E' \sigma_s R_s \exp(-0.4t^2 - 1.3t)$ ;

Number of contact spots:  $N = 2.6D_s A_0 \exp(-0.53t^2 - 0.24t)$ .

According to the definition of contact stiffness, Królikowski and Szczepiek (1991) used the WAO model to predict the interface stiffness. They gave an analytical curve fit to the data:

$$K_a = \frac{p}{\sigma_s} \left[ 1.7 - 1.6 \log_e \left( \frac{2.7p}{E'D_s^{1/2} \sigma_s} \right) \right]^{1/2} \quad (4.7)$$

#### 4.3.1.3 BGT Model

Bush, Gibson and Thomas (BGT) developed an elastic contact model for isotropic surfaces by adopting the Nayak (1973) micro-geometry assumptions. Different from above two models, the contacting tips on the rough surface are considered to be elliptical, so three parameters are needed to define the tip shape: the height of the summit and two principal radius of curvature. Figure 4.5 shows the random distribution of elliptical contacts. In the calculation of real contact area and nominal contact pressure for GW model, only the distribution of the summit height is required. However, the corresponding calculation under BGT model requires multidimensional integration of the joint distribution of summit height. The following asymptotic solutions were given for BGT model (McCool, 1986):

The real contact area (total contact area of asperities):  $A = \frac{1}{2(2\pi)^{1/2}} \frac{A_0}{t} \exp(-0.5t^2)$ ;

The nominal contact pressure:  $p = \frac{E'}{2\pi} \left(\frac{m_2}{2}\right)^{1/2} \frac{1}{t} \exp(-0.5t^2)$ ;

Number of contact spots:  $N = \frac{A_0}{6\sqrt{3}\pi(m_4/m_2)} F_0(t)$ .

Where  $m_2$  and  $m_4$  are the second and fourth spectral moments of the profile (Nayak, 1971; O'Callaghan and Probert, 1987). The relationship between  $m_4$  and the mean radius of asperities,  $R_s$ , was given as (Longuet-Higgins, 1957):

$$R_s = \frac{3}{8} \left(\frac{\pi}{m_4}\right)^{1/2} \quad (4.8)$$

The ratio between  $m_2$  and  $m_4$  was deduced as :

$$m_4 / m_2 = 6\pi\sqrt{3}D_s \quad (4.9)$$

Królikowski & Szczepek (1991) gave the following expression for the normal asperity contact stiffness based on the definition of contact stiffness:

$$K_a = -\frac{dp}{dh} = \frac{p}{\sigma_s} \left(t + \frac{1}{t}\right) \quad (4.10)$$

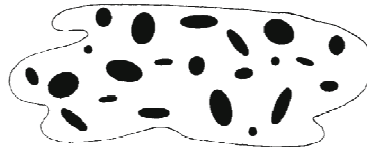


Figure 4.5. Randomly distribution of elliptical contact spots in BGT model.

Figure 4.6 (a) shows contact stiffness varying with nominal contact pressure for GW, WAO and BGT model using the material properties and surface properties of ball and disc, which will be detailed in Section 4.4. For the same pressure, BGT model predicts the highest stiffness with GW model giving the lowest value. WAO model predicts the highest real contact area and the greatest number of contact spots, shown in Figure 4.6 (b)

and (c). Among three models, the GW model predicts the lowest contact area, shown in Figure 4.6 (b). The interface stiffness should therefore be the lowest. This is confirmed by the Figure 4.6 (a), in which the GW model presents the smallest contact stiffness. Detailed calculation process for these three models can be found in Appendix A-3.

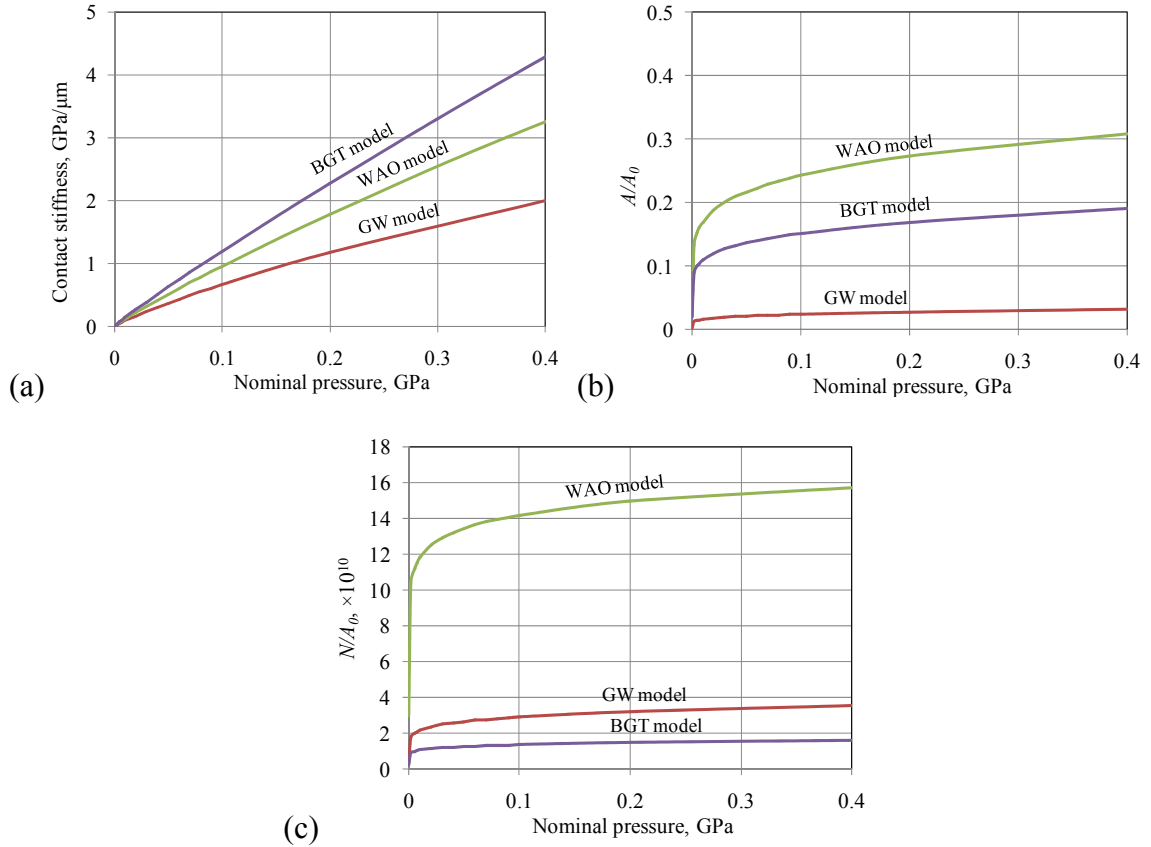


Figure 4.6. Comparison among GW, WAO and BGT model, (a) Contact stiffness, (b) real contact area, and (c) contact spots number.

### 4.3.2 Stiffness of a Fluid Film

The stiffness of a lubricant layer was derived as Equation 2.13 (Hosten, 1991). It is the bulk modulus, at the appropriate contact pressure, divided by the oil film thickness. The bulk modulus can be determined from its acoustic properties according to (Yarwood, 1953):

$$c = \sqrt{\frac{B}{\rho}} \quad (4.11)$$

Where  $c$  is the speed of sound through the liquid, and  $\rho$  is its density. The speed of sound in a sample of oil can readily be measured (using a time of flight method) and the bulk modulus deduced. This is quite satisfactory for application in low pressure hydrodynamic cases (Dwyer-Joyce *et al.*, 2003). However, in EHL the oil is subject to high pressure and so its bulk modulus changes significantly.

Measuring the bulk modulus under such conditions is difficult. Normally this would require a high pressure chamber (Jacobson and Pascal, 1987; Jacobson, 2006). An ultrasonic approach has been used on an EHL contact where an optical interference method was used to determine the film thickness independently (Kondo *et al.*, 2006). This can then be used in Equation (4.11) to determine the bulk modulus.

In this study, the analysis from Bair (2007) is used to calculate the bulk modulus of the compressed lubricant, it is expressed as:

$$B = \left\{ 1 - \frac{1}{1 + B_0'} \log_e \left[ 1 + \frac{p}{B_0} (1 + B_0') \right] \right\} \left[ B_0 + p (1 + B_0') \right] \quad (4.12)$$

Where  $p$  is the pressure in liquid,  $B_0$  is the bulk modulus at ambient pressure ( $p = 0$ );  $B_0'$  is the pressure rate of change of  $B$  at ambient pressure, which is approximately 11.  $B_0$  is described as (Fakhreddine and Zoller, 1990):

$$B_0 = B_{00} \exp(-\beta_k T) \quad (4.13)$$

Where  $B_{00}$  is approximately 9 GPa,  $\beta_k$  is approximately  $6.5 \times 10^{-3} K^{-1}$ , and  $T$  is the absolute temperature. This equation is considered to be the most accurate (Hirschfelder *et al.*, 1954) and even accurate for extrapolation to very high pressures (Millat *et al.*, 1996). It has been used successfully in a free volume pressure-viscosity correlation (Cook *et al.*, 1994). The nominal pressures of ball and disc contact were used in Equation (4.12) for lubricant bulk modulus. The ultrasonic vibration is very low amplitude and high speed. It is therefore an isentropic process and so it is the adiabatic bulk modulus that is the relevant fluid property. Table 4.1 shows the bulk modulus calculated in this study.



Table 4.1. Lubricant bulk modulus with varying test pressures.

<b>Load, <math>N</math></b>	<b>Nominal contact pressure, <math>GPa</math></b>	<b>Bulk modulus, <math>GPa</math></b>
0	0	1.339
10	0.420	5.546
20	0.529	6.565
30	0.605	7.269
40	0.666	7.823
50	0.718	8.287
60	0.763	8.691
70	0.803	9.049
80	0.839	9.374

### 4.3.3 Stiffness of Static Wet Contact

If the interface is submerged in oil, surface tension, or a small relative movement between the contacting surfaces, will draw in liquid to fill the pockets between the asperity contacts. If the load increases, the two interfaces approach and extrude a finite but very small volume of lubricant (Figure 4.1 (b)). When ultrasonic waves strike this interface some will pass through the asperity contact and others are reflected back from the lubricant pockets. Therefore, for a wet interface the total interfacial stiffness has two components: the solid stiffness arising from the mechanical asperity interaction, and the lubricant stiffness attributable to the lubricant pockets.

The surface roughness has a random distribution, and the real area of contact is relatively small compared to the apparent area. It is therefore reasonable to assume that the lubricant can freely flow between the valleys (i.e. there are no trapped and isolated pockets of lubricant). This means that the oil is under ambient atmospheric pressure, even though asperities contacts are under a very much greater pressure. The stiffness of the asperity contacts can be determined from GW model using Equation (4.2).

The total stiffness is the sum of liquid stiffness and asperity contact stiffness:

$$K_t = K_a + K_l \quad (4.14)$$

So the interfacial stiffness for static wet case should be written as:

$$K_t = K_a + K_l = \frac{p}{\sigma_s} \left[ 1.7 - 1.6 \log_e \left( \frac{2.7p}{E'D_s^{1/2}\sigma_s} \right) \right]^{1/2} + \frac{B_0}{h} \quad (4.15)$$

Where the bulk modulus for the oil at ambient pressure,  $B_0$  is used, Equation (4.13) is used to calculate  $B_0$  as 1.339 GPa (see Table 4.1).

#### 4.3.4 Stiffness of Mixed Lubrication Contact

In the case of a sliding contact, oil is entrained between the surfaces and a hydrodynamic pressure is generated. If the sliding speed is sufficiently high then a full film occurs and there is no asperity contact. Equation (2.13) can then be used to determine the stiffness of the contact which is now entirely supported by liquid.

If however the lubricant film thickness is less than the surface roughness then both the hydrodynamic film and the asperity contacts contribute to the total stiffness according to Equation (4.14). In this section, an equation set was built to predict the load sharing proportions and surface separation. From these predictions,  $K_a$  and  $K_l$  can be calculated from equations (4.2) and (2.13). The method follows the approach of Gelinck and Schipper (2000), in which the film formation was modelled independently of asperity contact.

From Equation (3.30), three unknown variables,  $\gamma_1$ ,  $\gamma_2$  and  $h$  can be obtained and used to calculate asperity contact stiffness and lubricant stiffness using equations (4.2) and (2.13) separately. Then the total interfacial contact stiffness can be determined by using Equation (4.14).

## 4.4 Model Inputs and Simulation Results

### 4.4.1 Input Parameters of Ball and Disc Contact

The steel ball and disc were machined with high-quality finish surfaces. Characteristics and working conditions of the contact between the ball and disc are shown in Table 4.2.

Table 4.2. Characteristics and operating conditions of ball and disc contact.

Parameter	Symbol	Value
Elastic modulus of steel ball and disc	$E$	200 <i>GPa</i>
Poisson's ratio of steel ball and disc	$\nu$	0.31
Radius of ball	$R_{ba}$	19 <i>mm</i>
Normal load	$P_t$	30,40...80 <i>kN</i>
Sliding speed	$u$	up to 2 <i>m/s</i>

Table 4.3. Surface parameters of ball and disc.

Parameter	Symbol	Value
Asperity density	$D_s$	$1.97 \times 10^{10} \text{ m}^{-2}$
Mean radius of asperity summits	$R_s$	2.7 $\mu\text{m}$
Standard deviation of asperity summit heights	$\sigma_s$	0.3 $\mu\text{m}$
Surface roughness of ball	$R_{ab}$	0.218 $\mu\text{m}$
Surface roughness of disc	$R_{ad}$	0.291 $\mu\text{m}$
Root mean square roughness of ball	$R_{qb}$	0.256 $\mu\text{m}$
Root mean square roughness of disc	$R_{qd}$	0.339 $\mu\text{m}$

The asperity parameters shown in Table 4.3 were obtained from profiles of the ball and disk surfaces measured by a Mitutoyo stylus profilometer. The recorded surface profile was put in MathCAD. By counting the number of asperity summits for the studied profile, a scanning step was set as length of measured profile divided by summit number. A MathCAD program was written for scanning along the profile until three points on one asperity arc can be used for calculation of mean summit radius,  $R_s$ . Meanwhile, the

number of asperity per unit length,  $D_p$ , was recorded. The asperity distribution density per unit area,  $D_s$ , is then determined through  $D_s=1.8 D_p^2$  (Williams, 2005). For  $D_s$ ,  $R_s$ , and  $\sigma_s$ , the average value of two surfaces were used for further analysis.

In this study, Shell Turbo Oil T 68 was used to lubricate the ball and disc contact. Lubricant properties are shown in Table 4.4.

Table 4.4. Properties of lubricant oil used in this study.

Parameter	Symbol	Value
Lubricant dynamic viscosity at zero pressure and 40°C temperature	$\eta_0$	0.095 Pa·s
Pressure-viscosity coefficient	$\alpha'$	25.1 GPa <sup>-1</sup>
Density of the oil at 15°C	$\rho$	0.876 kg/L

#### 4.4.2 Simulation Results

All the parameters in the above section were inputted into a MathCAD program for solving the equation set (Equation (3.30)). Scaling factors and film thickness were predicted from the program under varying operating conditions. Processing details in MachCAD have been described in Chapter 3. More details can be found in Appendix A-1.

Figure 4-7 shows the predicted scaling factors varying with contact pressure. For the speed range of 0.01-4m/s, the lubricant layer was found to bear more than 50% of the normal load. It can be concluded that substantial hydrodynamic action of lubrication layer is taking place on the contacting interface, especially under higher speeds. Even though higher loads lead to more severe metallic contact, the load sharing ratio of lubricant,  $1/\gamma_1$  was found greater than that of the asperities,  $1/\gamma_2$  for all simulated pressures.

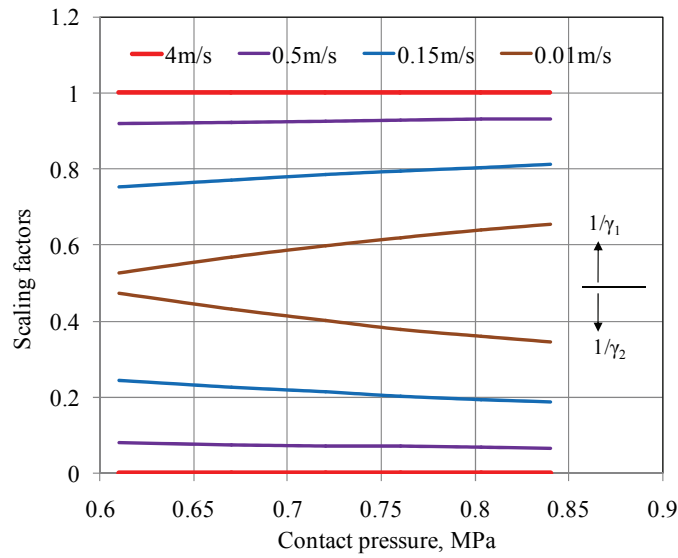


Figure 4-7. Scaling factors  $\gamma_1$  and  $\gamma_2$  varying with mean Hertzian pressure for four speed cases.

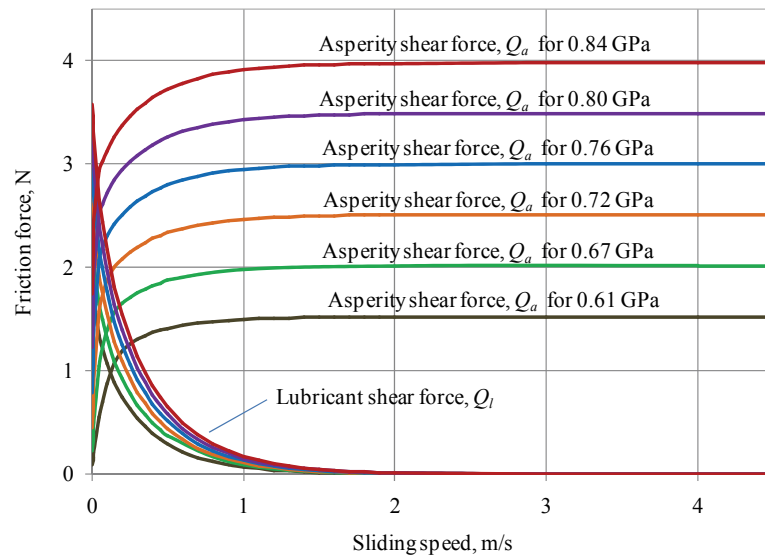


Figure 4-8. Shear forces of liquid and asperity varying with sliding speed.

Figure 4-8 shows the friction force on the interface. Shear forces for asperity contact,  $Q_a$  and shear force from the liquid film,  $Q_l$  are simulated and presented in the figure. It was found that the asperity shear force was much higher than the lubricant shear force. The shear force of liquid layer has an opposite varying trend compared to metallic contact. It decreased dramatically with increasing speeds. No full separation between contacting surfaces was observed during the whole speed range.

Figure 4-9 shows predicted Stribeck curves for varying pressures. In order to show the results clearly, Stribeck parameter  $\eta u/P_t$  was made logarithmic. As expected, mixed

lubrication regime were observed for all pressures. It shows the consistency to the load sharing concept of the model. It can be seen that Stribeck curves didn't show a flat under lower Stribeck parameter,  $\log(\eta u/P_t) < 0.1$ . This is due to the shear force of asperity contact that increases with sliding speed much quicker than initially compared with the decrease of lubricant shear force, shown in Figure 4-8. The calculation process for Figure 4-8 and Figure 4-9 can be found in Appendix A-2.

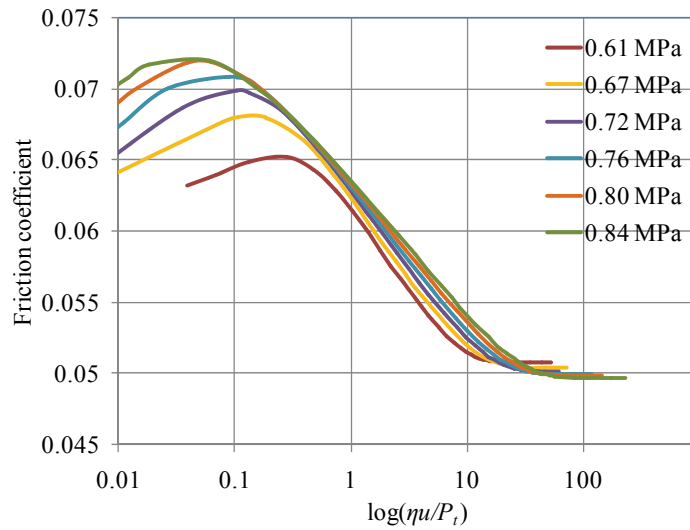


Figure 4-9. Simulation Stribeck curves for varying loads.

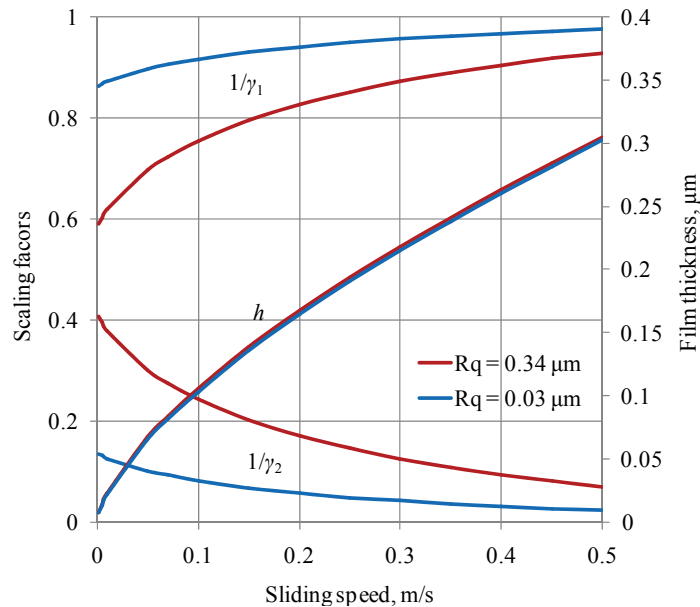


Figure 4.10. Scaling factors and film thickness for two surface finishes under a pressure of 0.76 GPa.

Figure 4.10 shows the prediction of a standard rough surface ( $R_q = 0.34 \mu\text{m}$ ) compared

with a polished surface ( $R_q = 0.03 \mu\text{m}$ ), both under a pressure of 0.76 GPa (60 kN). The scaling factors show significant difference but the film thicknesses are almost the same for both surfaces. For smooth surface, asperity interaction contributes little to load supporting. More than 60% of the load was supported by the liquid layer. Above sliding speed of 0.3m/s, film thickness was found to be in the range of 0.2-0.31 $\mu\text{m}$ , which was the typical EHL film thickness range (0.2-0.4  $\mu\text{m}$ ) and similar to those findings for ground surfaces (Stachowiak and Batchelor, 2005). However, in the whole speed range,  $1/\gamma_1$  was found to be less than 100%, which means the load was not wholly supported by the lubricant, asperity interaction existed. Therefore, in evaluating EHL contact, the asperity interaction should be considered as the film thickness is usually in a similar order of surface roughness. Even so, smoother surfaces produce better tribological properties as more conformable surfaces are essential for lubrication formation.

A parameter known as lambda ratio is usually used to express the comparison between the film thickness and the surface roughness. It shows the ratio between film thickness and the composite roughness from two surfaces in contact. The definition is given as (Tallian, 1967):

$$\lambda = \frac{h}{\sqrt{R_{qb}^2 + R_{qd}^2}} \quad (4.16)$$

Where  $h$  is the film thickness, and  $R_{qb}$  and  $R_{qd}$  are the root mean square roughness of two contacting bodies, here they refer to the ball and disc respectively. It has been found that if the lambda ratio is lower than 1, asperity interaction is quite severe (Stachowiak and Batchelor, 2005), and the contacting surfaces are operating in the mixed lubrication regime. When  $\lambda$  is greater than 4, full separation film is formed between contacting surfaces.

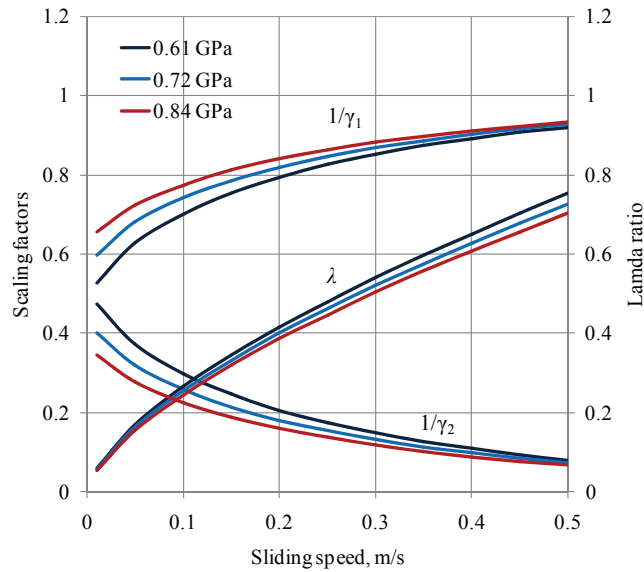


Figure 4.11. Scaling factors and lambda ratio against sliding speed under varying pressures.

Figure 4.11 shows scaling factors and lambda ratio varying with sliding speed for three pressures, 0.61 GPa, 0.72 GPa and 0.84 GPa. The proportions of hydrodynamic action (expressed as  $1/\gamma_1$ ) and the lubricant film thickness were found to increase with velocity. This confirms that speed plays an important part in film formation. At the speed of 0.5 m/s, more than 90% of the total load is supported by liquid layer. However, when the sliding speed was below 0.1 m/s, Appreciable solid contact was still observed as  $1/\gamma_2$  was found to be between 20% and 50%. In the whole speed range, the lambda ratio,  $\lambda$ , was shown to be lower than 0.8. It means there was no full separation between ball and disc surfaces within the simulated speed, up to 0.5 m/s. Interacting asperities and lubricating film share the total applied load.

### 4.4.3 Contact Stiffness

When scaling factors were obtained from the MathCAD program, pressures shared by the lubricating film and asperities can be separated from each other. They were later used in Equation (4.2) for solving asperity contact stiffness, and Equation (4.12) for solving lubricant bulk modulus respectively. Liquid stiffness can be determined from equation (2.13) using the bulk modulus divided by the film thickness. Therefore, the total contact stiffness is the sum of asperity stiffness and liquid stiffness through Equation (4.14). A MathCAD program has been written for solving the asperity contact stiffness, details



can be found in Appendix A-3.

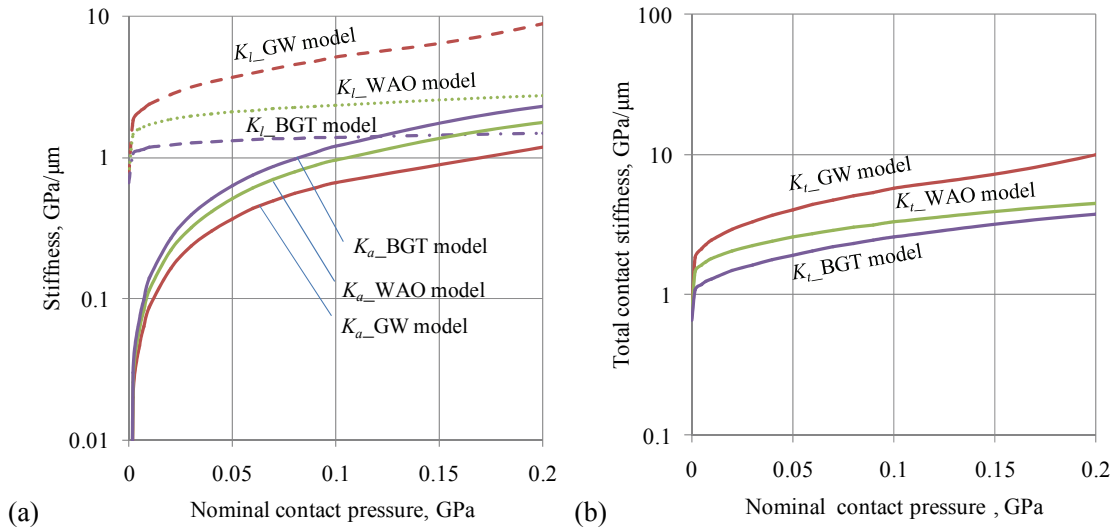


Figure 4.12. Static contact stiffness against nominal contact pressure, (a) asperity contact stiffness,  $K_a$  and liquid layer stiffness,  $K_l$ , and (b) integration stiffness,  $K_t$ .

Figure 4.12 shows theoretical simulations of contact stiffness varying with nominal pressure up to 0.2 GPa. The liquid layer stiffness,  $K_l$ , was found to be much higher than that of asperity contact,  $K_a$ . In order to show both on one plot, logarithmic coordinate was used for y-axis. From Figure 4.12 (a), it can be seen that the GW model predicts the lowest  $K_a$ , with the BGT model predicting the highest. This agrees with Figure 4.6 (a). But for liquid layer, the GW model predicts the greatest among three models. This is because the GW model predicts the lowest surface separation,  $h$ . But the bulk modulus was the same among three models as the trapped lubricant was assumed to be under ambient pressure. At a certain pressure,  $K_l$  was found to be almost twenty times higher than asperity stiffness. The total interfacial stiffness mostly relies on the lubricant component, which can be seen in Figure 4.12 (b). Among these three models, the GW model has been widely used in contact modelling due to its simplification. In this work, it was adopted for further study.

Figure 4.13 shows predicted interfacial stiffness varying with sliding speed using the mixed lubrication model. Higher nominal contact pressure produced greater interfacial stiffness between the ball and the disc. For each pressure, the contact stiffness was found to drop greatly with sliding speed and tend to be a constant: 10 GPa/μm. Lower speeds lead to a thin film so the mixed lubrication dominates on the interface. With increasing

speed, contact stiffness decreases. Thus, hydrodynamic lubrication was expected as a thicker film was formed.

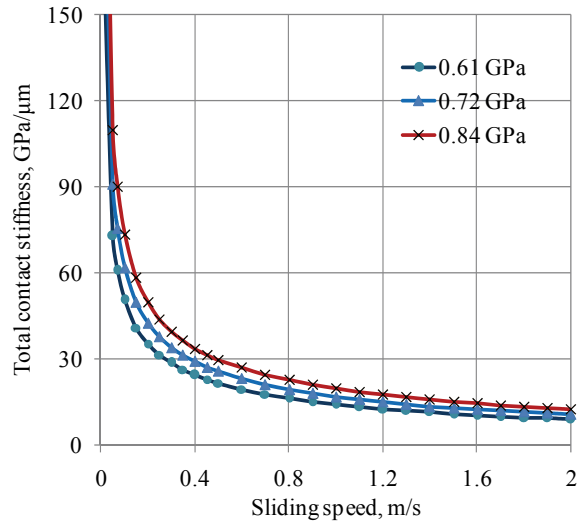


Figure 4.13. Total contact stiffness varying with sliding speed for different pressures.

Figure 4.14 demonstrates how the stiffness varies using the mixed lubrication model. It was evident that the liquid component of stiffness was very much higher than the solid part. Essentially this is because whilst the modulus of a liquid is lower, the layer thickness is very much thinner, and so it is inherently stiffer. Therefore the thin layer has a lower ability to move or deform.

The effect of pressure on the total and asperity stiffness is shown in Figure 4.14 (a). The locations of lambda ratio 0.5, 1 and 1.5 were also plotted in this figure to show the increasing contribution of lubricant to the load sharing. In all cases as the sliding speed reached 1.5m/s, lambda was greater than 1.5 and the asperity stiffness fell closely to zero.

Comparison between the lubricant stiffness,  $K_l$ , and asperity contact stiffness,  $K_a$ , are shown in Figure 4.14 (b), (c) and (d). The ratio of  $K_l / K_a$  varying with sliding speed and nominal pressure were simulated and shown in Figure 4.14 (c) and (d) individually. The inversion in Figure 4.14 (c) is caused by the faster rate of reduction in stiffness as the film tends to zero. Liquid stiffness was inversely proportional to thickness and therefore  $K_l$  tends rapidly to infinity. The reduction in solid stiffness as the surfaces approach was gentler. It is clear that in all cases compressed liquid played the main part in supporting the applied load.

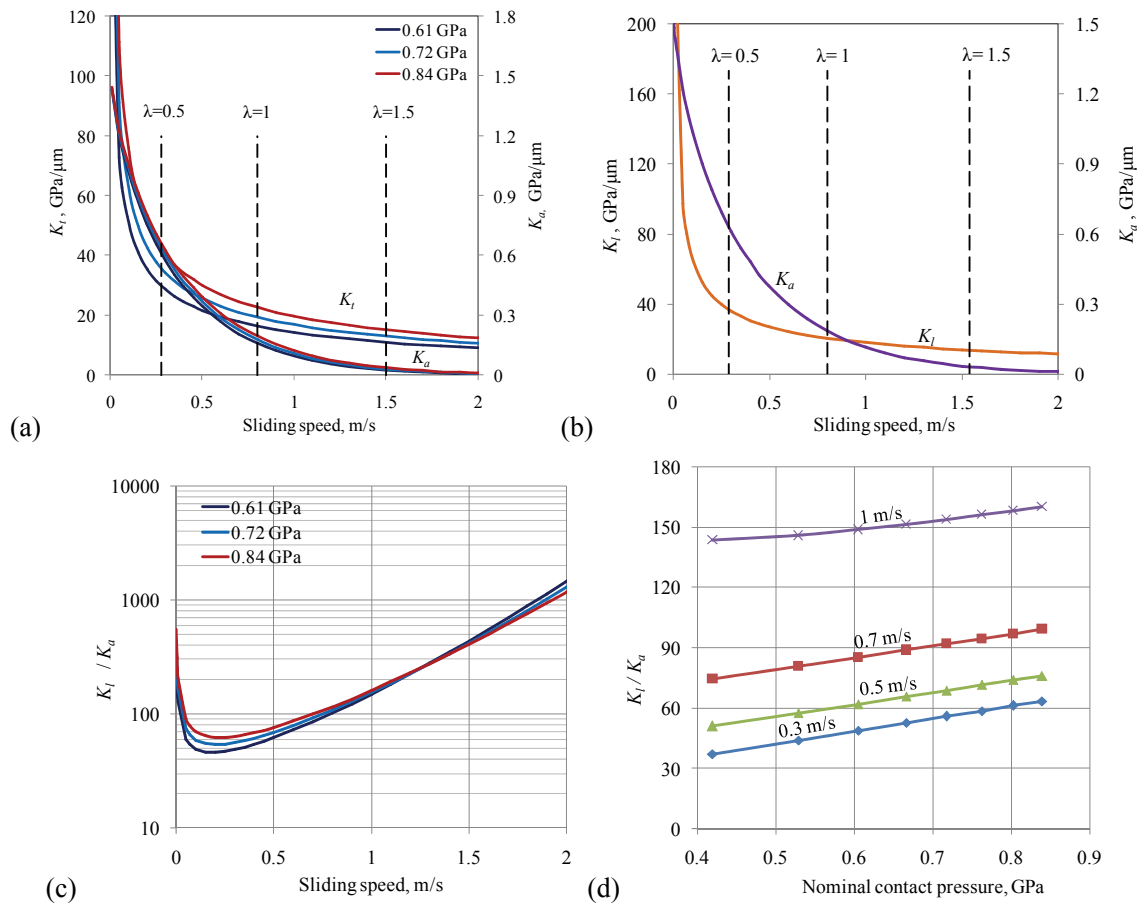


Figure 4.14. Comparison of stiffness,  $K_l$ ,  $K_a$  and  $K_t$  (a) total and asperity stiffness variation with load and speed, (b) liquid and asperity stiffness variation with speed under 0.61GPa, (c) ratio of liquid to asperity stiffness variation with speed, (d) ratio of liquid to asperity stiffness variation with load.

## 4.5 Comparison between Experiment and Simulation

### 4.5.1 Stiffness Varying with Sliding Speed

Figure 4.15 shows the predicted stiffness from the mixed lubrication model compared with experimental data for six load cases. Simulations of dynamic stiffness for different pressures showed a good agreement with experimental measurements, especially for higher pressures. As the sliding speed increases, the separation increased, the proportion of load shared by asperity contacts decreased, thus asperity stiffness decreased based on Equation (4.2). At higher speeds the total interfacial stiffness was mostly contributed by compressed liquid.

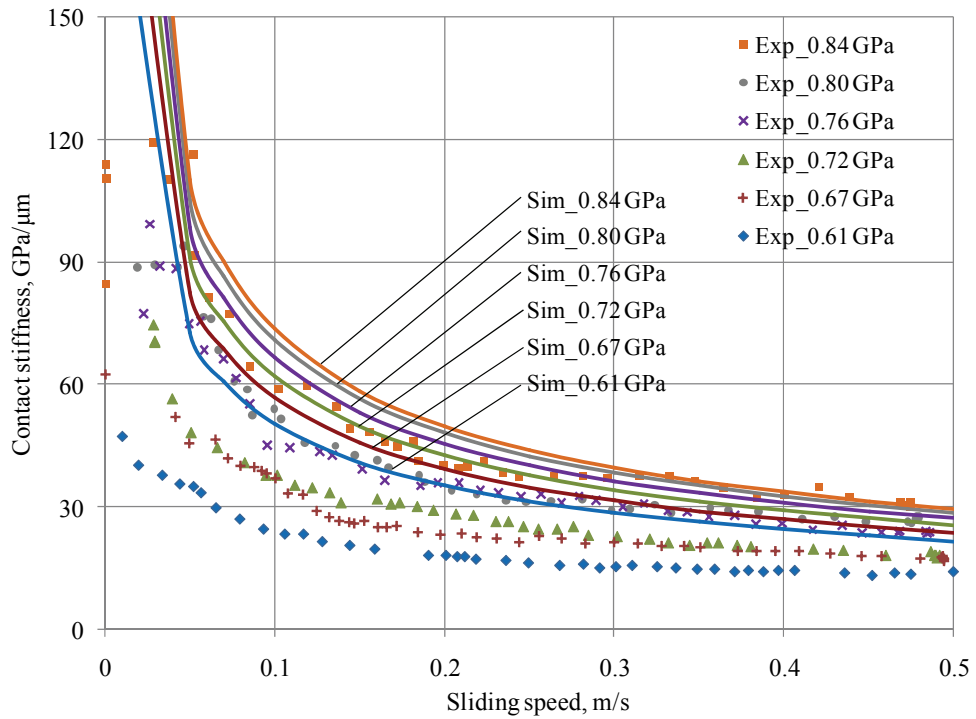


Figure 4.15. Comparison of measured stiffness and simulation stiffness varying with sliding speed for a series of different contact loads.

The mixed lubrication model was used to determine the ratio of liquid stiffness to asperity stiffness at each speed data point for the contact pressures of 0.61, 0.72 and 0.84 GPa (loads of 30, 50 and 80 N). This ratio was then used with the experimental data to separate stiffness contributions from compressed liquid and asperity contact respectively (Dwyer-Joyce *et al.*, 2011). Figure 4.16 shows the calculation results. Again, it can be seen that the lubricant stiffness is massively greater the asperity contact stiffness.

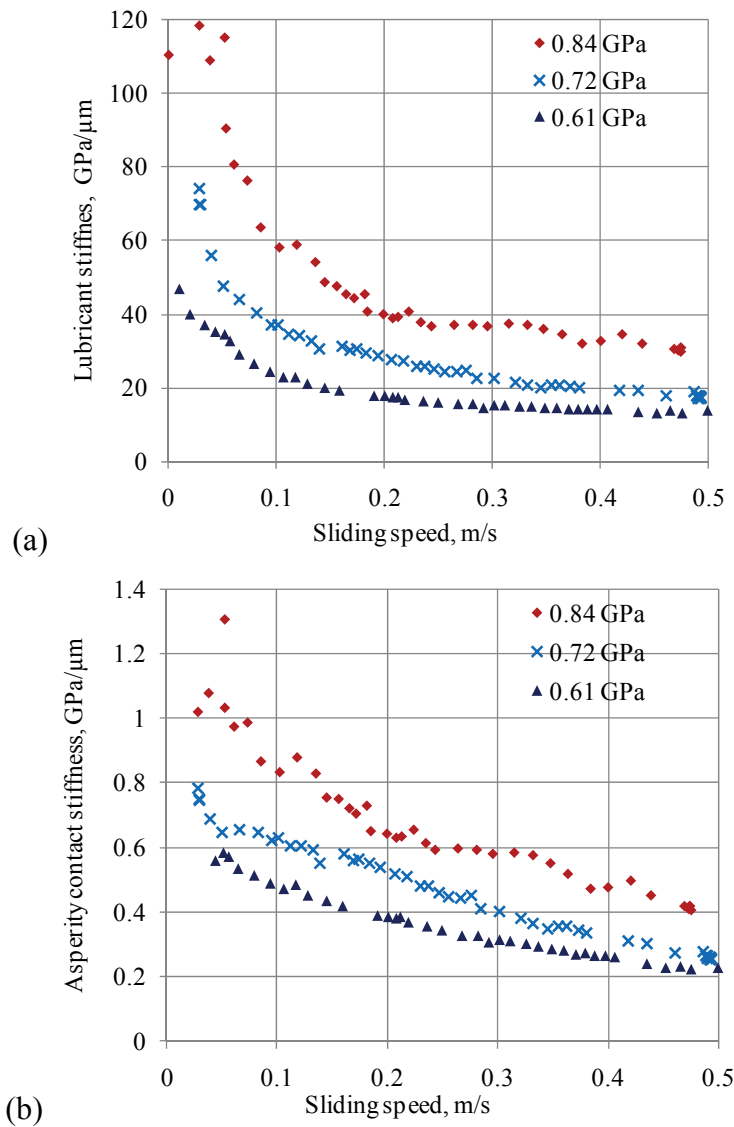


Figure 4.16. Experimental stiffness of mixed regime contact, (a) the stiffness of lubricant film, and (b) stiffness of asperity contact, from the measured combined stiffness (data from Figure 4.15).

## 4.5.2 Stiffness in the Start-up Sequence

Figure 4.17 shows the mixed regime model, and the static dry and wet stiffness models compared with experiment results during a start-up process. The prediction of the full film model, Hamrock and Dowson model (1976, 1977) was shown as well (the stiffness becomes infinite when the speed and film thickness tend to zero). As expected, the dynamic lubrication part agrees well. It was apparent that in the  $40 < t < 100$  seconds region on the graph, a continuous film was formed; and the fluid film stiffness shows

close agreement with the mixed lubrication prediction. At around 40 seconds, as the speed tends to be zero, the predicted oil film stiffness rises to infinity as  $h \rightarrow 0$ . The measured value tends to a finite stiffness of  $\sim 120 \text{ GPa}/\mu\text{m}$  as the contact consists of rough asperity interactions and a thin layer.

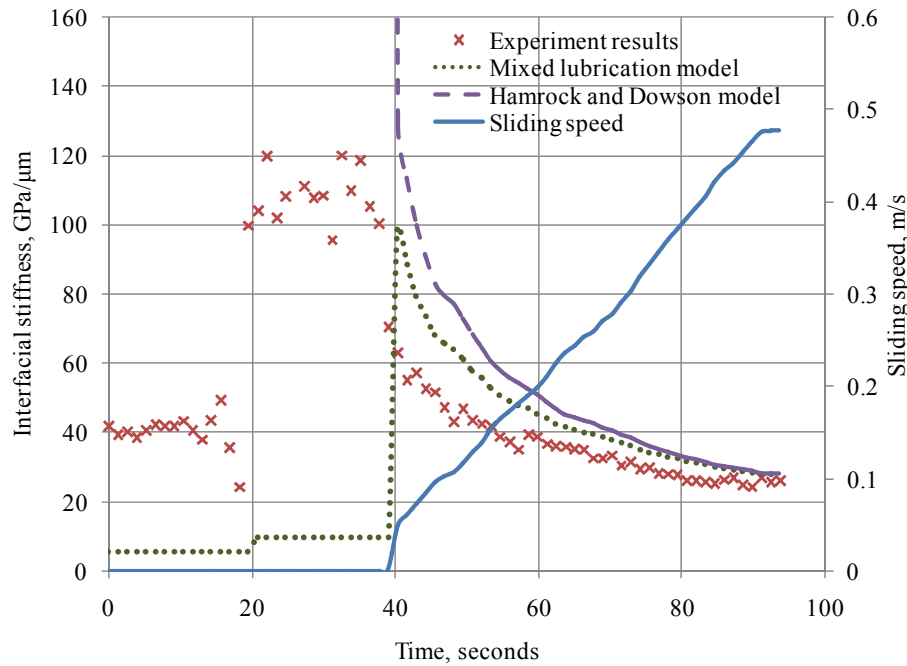


Figure 4.17. Comparison of interface contacting stiffness for a start-up sequence of ball and disc contact under the mean contact pressure of 0.76 GPa.

The simulation gives the dry contact stiffness of  $5.6 \text{ GPa}/\mu\text{m}$ , which was some eight times lower than the measured value. A similar large discrepancy was observed for the wet static contact. The agreement between models of dry asperity contact and ultrasonic data was difficult to achieve. Poor agreement has also been observed in earlier work in this area (Królikowski and Szczepek, 1991; Drinkwater *et al.*, 1996).

Perhaps the source of error was the difficulty in measuring surface roughness. Roughness parameters are dependent on the measurement scale used (Thomas, 1998) and it was likely that the measurement scale imposed by a stylus profilometer differs significantly from that of an ultrasonic wave striking the asperity. This is an issue that remains to be resolved. In previous study, ultrasonic results were complemented with theoretical contact model to deduce roughness parameters (Baltazar *et al.*, 2002; Pecorari and Poznic, 2006). These parameters were then used for further simulation. Therefore,

closer agreement with experimental data for this dry contact was only observed using the modelling approach where roughness data was obtained by fitting ultrasonic data to model predictions.

### 4.5.3 Lubricating Film Thickness

Once the stiffness components have been separated out (as shown in Figure 4.16 (a) and (b)), the oil film thickness were determined using Equation (2.13), shown in Figure 4.18. The non-dimensional speed and load axes,  $U^{0.67}W^{-0.067}$ , corresponding to the Hamrock and Dowson (Equation (3.28)) were used so that the data should all collapse onto one curve if that model holds. In order to make a comparison to a theoretical simulation, the mixed lubrication model was used to predict the lubricating film thickness. Also plotted in Figure 4.18 is the oil film thickness prediction using the standard full film Hamrock and Dowson model. The experimental data at the highest load closely fits the model. At the two lower loads, whilst the slope was similar, the agreement was not so good.

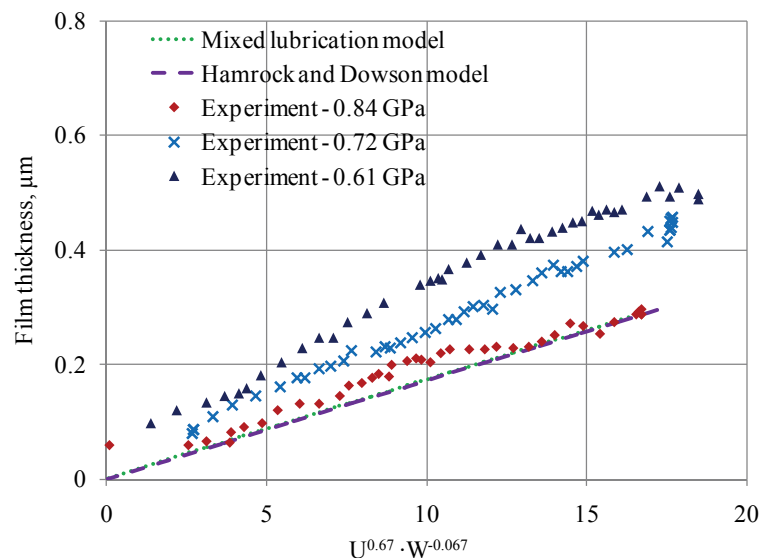


Figure 4.18. Comparison of film thickness against dimensionless parameter for several sets of experimental data.

The film thickness given by the Hamrock and Dowson model was zero when the speed and load parameter approached zero as the surface roughness was not considered in the model. However, from the ultrasonic measurement, the lowest film thickness was higher than zero. This was because the real surface consists of rough asperities. On the static

interface lubricant trapped in asperity valleys reflects ultrasonic pulses that were further used for calculation of film thickness.

## **4.6 Conclusions**

In this chapter, the contact between a steel and disc has been investigated. The normal interfacial stiffness for un-lubricated rough contact has been analysed using three statistical models, GW model, WAO model and BGT model under a certain nominal contact pressure. For lubricating oil, the liquid layer stiffness on the interface was determined by liquid bulk modulus divided by surface separation.

A mixed lubrication model for the contact ball-on-disc has been built to predict contact load sharing parameters and surface separation which were later used for calculation of asperity contact stiffness and lubricant stiffness. A MathCAD program has been written for solving the whole process for contact stiffness. For sliding contact between the steel ball and disc, liquid stiffness was found to be very much greater than asperity contact stiffness. The lubricating film was considered to support most of the applied load.

In the speed range of 0-2 m/s, scaling factors of liquid was found always lower than 1, which mean asperity interaction existed all the time. The contact between the ball and disc was in the mixed lubrication regime. But at higher speeds, most of the load was supported by lubricating film.

Simulation results have been compared to experimental stiffness determined from ultrasonic reflection coefficient. It showed good agreement for dynamic cases for all loads. But for static contact, theoretical prediction gave much lower stiffness compared to test results. Using the predicted scaling factors, asperity stiffness and liquid stiffness were separated from the total measured stiffness. Film thickness was calculated from test data and compared with Hamrock and Dowson's model, which showed acceptable agreement.



# Chapter 5 Mixed Lubrication in a Pin Joint

In this chapter, the contact of an articulating pin joint on the landing gear was studied. The first section describes the test rig and experimental instrumentation. A series of experiments have been carried out on a pin and bush assembly under a range of loads and speeds. Later, the development of a mixed lubrication model for pin joint contact is presented, which predicts load sharing proportions, film thickness and friction at the interface. In the final section a comparison of simulation results and experimental measurements was carried out. From the comparison, the model has been proven to be an acceptable method for predicting frictional performance of low speed and high load cylindrical contacts.

## 5.1 Background of Landing Gear Pin Joints

Figure 5.1 shows an aircraft landing gear on which the articulation system is achieved by the use of a whole system of varied pin type joints. These help complete the extending and retracting movement. The joints consist of a hollow steel pin that is free to reciprocate inside aluminium bronze bushes. The bushes are press fitted into the landing gear members. The joints are lubricated by grease which is replenished manually at regular maintenance intervals. The lubricant film formed separates the surfaces of the pin and bush and reduces metallic contact and wear. There are several aerospace greases used on landing gear, e.g. Aeroshell 7, Aeroshell 22, Aeroshell 33, and NYCO GN 22. The joint in this study was lubricated by Aeroshell 33, which was replenished at regular maintenance intervals. A grease film is formed to separate the surfaces of the pin and bush and reduces metallic contact and wear.

Ideally, the grease lubricant film should be as thick as possible to minimize solid contact and therefore friction. The landing gear joints oscillate, however, under low-speed and heavy-load conditions which are not conducive to lubricant film formation. The grease also has high viscosity and poor flowing ability. It is therefore difficult for full film lubrication to be generated. The pin joints are usually considered to operate in boundary or mixed lubrication regimes. This means that the operating torque depends on the respective proportions of liquid and solid contact between the joint mating faces.

Weight is one of the key factors in aircraft design. Lower friction or less grease leads to significant weight saving advantages as smaller actuators are needed. In this chapter, the main focus concerns aspects of friction and lubrication of pin joint contact. The aim is to offer theoretical support for the joint design and actuator sizing.

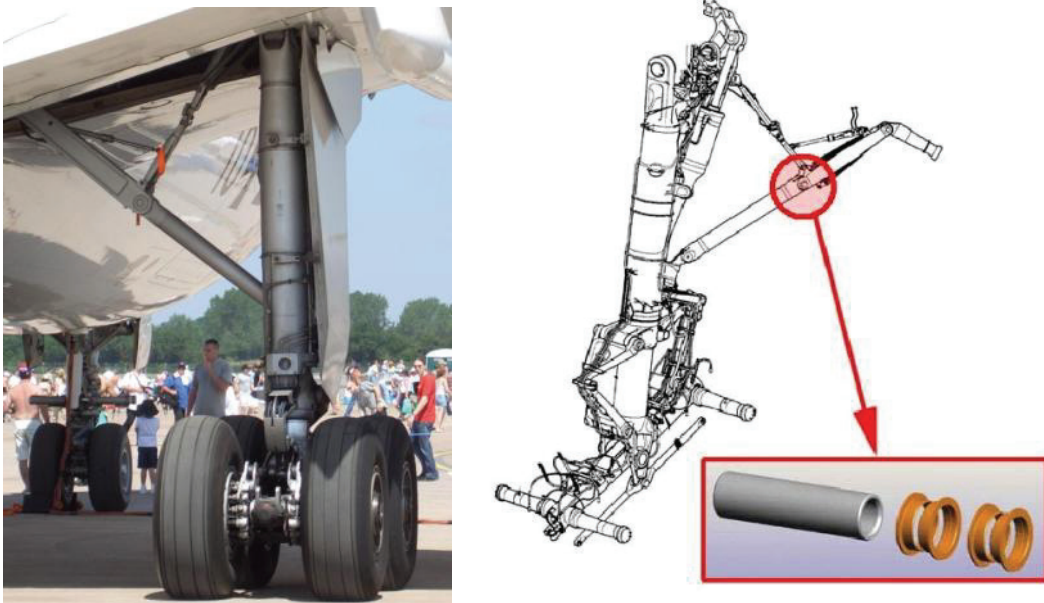


Figure 5.1. Photo and sketch of landing gear from the Airbus A320.

Much experimental work on this kind of joints was conducted by Glaeser and Dufrane (1977). But there are still no theories available to accurately predict friction coefficient for low-velocity, high-load and articulating bearings. In the mixed lubrication regime, both hydrodynamic lubrication and asperity contact exist to support the total load.

In this study, the mixed lubrication model established in Chapter 3 was used for the grease lubricated landing gear joint. The theoretical Stribeck curve, frictional torque and

lubricant film thickness under varying operating conditions were investigated. A series of experiments have been carried out on a sample pin joint with full instrumentation. The friction torque required during articulations were recorded and used for calculation of friction coefficient. Both of them were then compared with theoretical predictions.

## 5.2 Experimental Apparatus and Method

### 5.2.1 Pin Joint Function Tester

A test rig, shown in Figure 5.2, was built by the University of Sheffield for a series of projects. In this study, this test rig has been used for testing the landing gear pin joint. Friction torque produced on the interface during articulation was recorded to determine the frictional performance of pin joint.

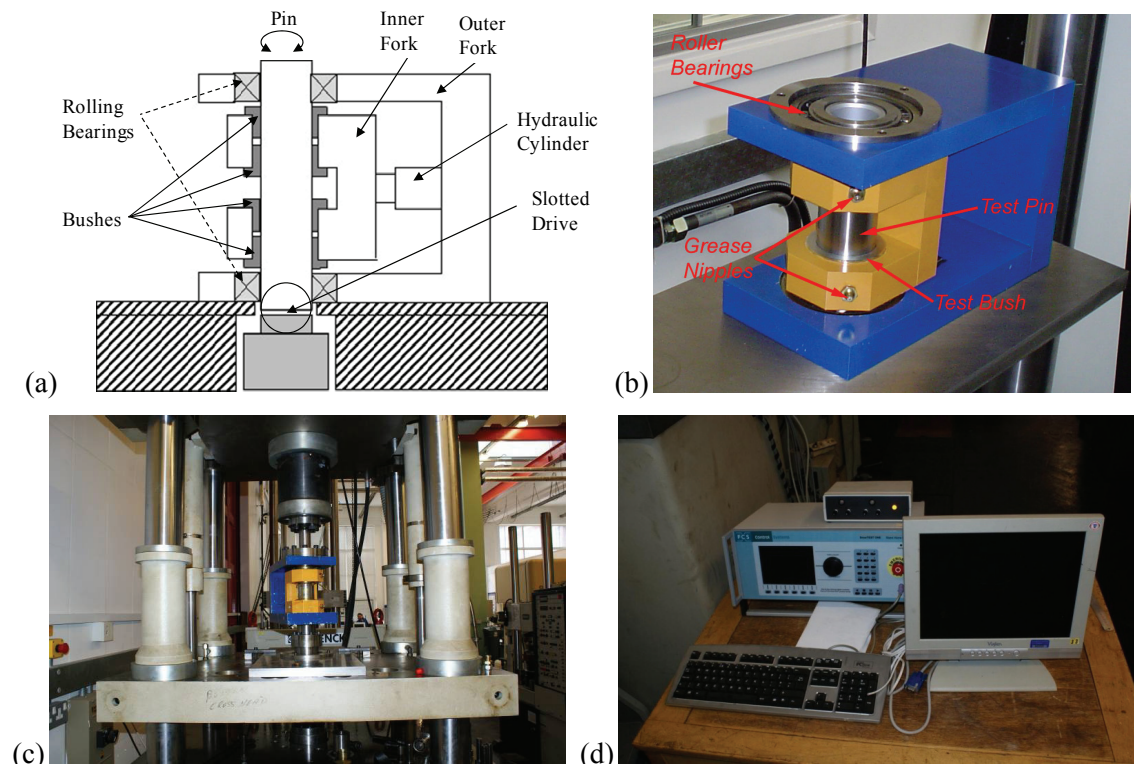


Figure 5.2. Illustration and photos of pin joint test rig, (a) sketch, (b) pin joint assembling housing, (c) photo, and (d) control system.

On this test rig, a double fork arrangement was used to load and support the pin within the test bushes (Figure 5.2 (a) and (b)). The inner fork has four bushes press fitted. The outer

fork has two rolling bearings as shown. A low height hydraulic cylinder was used to load the two forks apart. This double arrangement was geometrically similar to the pin joint arrangement found on the landing gear upper to lower side-stay pin (the joint shown in Figure 5.1). This housing (Figure 5.2 (b)) was then mounted on a torsional servo-hydraulic actuator (Figure 5.2 (c)). Four slots, shown by an illustration in Figure 5.2 (a) and the photo in Figure 5.3, were wire cut at one end, which enabled a direct line axial coupling, via a splined interface, to the torsion drive shaft. The control system (Figure 5.2 (d)) was used to set the pin articulating speed and record displacement, speed and torque.

### 5.2.2 Specimens and Operating Conditions

A pin and four bushes were obtained from an actual upper to lower side-stay pin joint and were used as the test specimens, shown in Figure 5.3. The single pin, OD 56mm, ID  $42\pm 0.2\text{mm}$ , length  $200.5\pm 0.1\text{mm}$  was mated with four bushes with the radial clearance of  $25\mu\text{m}$ . The four aluminium bronze bushes have an inner diameter of 56mm. A grease lubricant was applied with two axial lubrication grooves in each bush.

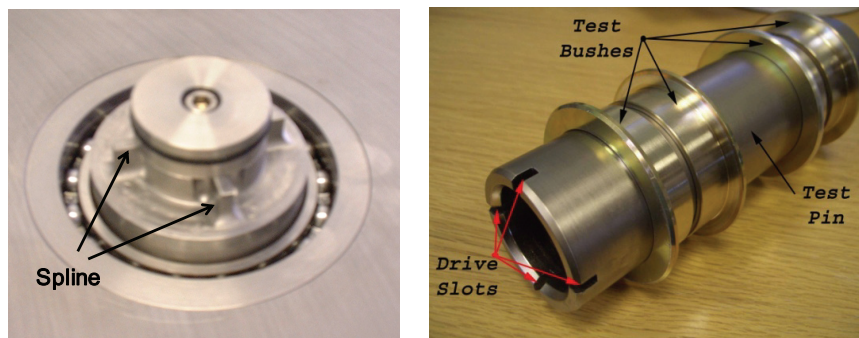


Figure 5.3. Photo of slots and the pin and bush system.

The tests were conducted with a range of radial loads, (from 5 to 60 kN). The torsional actuator of the test rig has a maximum capacity of 200 Nm. The maximum radial load achievable on the pin was therefore a function of the friction coefficient between the pin and bush. The typical rotational speed of pin joint was 0.033 Hz, (12 deg/s, actual main lock stay articulation speed). In this research, experiments at different frequencies of 0.03 Hz, 0.3 Hz and 1 Hz were carried out with pin angular displacement of  $\pm 40^\circ$ .

### 5.2.3 Instrumentation

The servo-hydraulic torsional actuator was fitted with both an angular position sensor and a strain gauge based internal torque sensor. The tension hydraulic actuator could be driven in both torque and angular displacement controls. In this study the displacement control was used via angular control from a function generator. The reacted torque was then recorded during the cycle.

The torque transducer also measured the torque in the two support ball bearings. However, this torque was low compared with the torque from the pin joints. The torque in the ball bearings was measured when unloaded (i.e. the pin not in place) and found to be within the noise range of the transducer.

The overall monitoring, recording and control of the rig was via a PC using a software program written in Labtech Notebook. During testing the duration of each test, the angular position of the pin relative to the start position and the frictional torque were recorded. Figure 5.4 (a) shows the response of the angular displacement sensor for one complete cycle. The rotation was a smooth and continuous sine wave. Recorded position data were then inputted in MathCAD to deduce the velocity characteristic curve, which was an important parameter in determining friction coefficient. This is shown in Figure 5.4 (b).

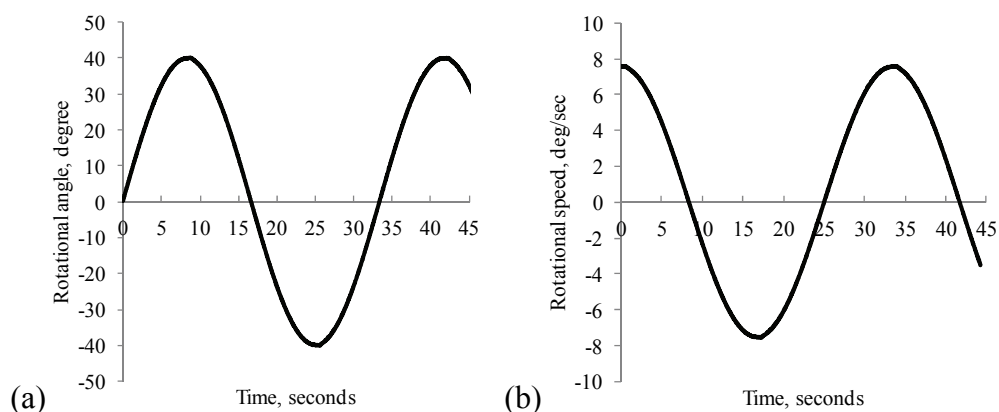


Figure 5.4. Typical cycles of displacement and angular speed on pin joint, (a) angular displacement against time, and (b) angular speed against time.

The frictional torque was also recorded throughout the cycle. Figure 5.5 (a) and (b) show

the torque plotted against time and articulation angle respectively. There were two peaks on the recorded torque cycle as the speed at these points was zero. The high static friction was due to the lack of lubrication as the grease has been squeezed out of the contact. The torque then drops during the articulation. It reaches a minimum at around zero degrees, and then rises towards the next peak. This demonstrates that as the pin joint speed increases, the torque reduces. The sliding motion between pin and bush entrains some grease and generates a thin lubrication film, which leads to the torque reduction.

Thermocouples were imbedded in the housing close to the location of the bushes. Temperature was monitored throughout testing. The tests presented here, however, were of a short duration (a few cycles) and therefore significant heating above room temperature did not occur.

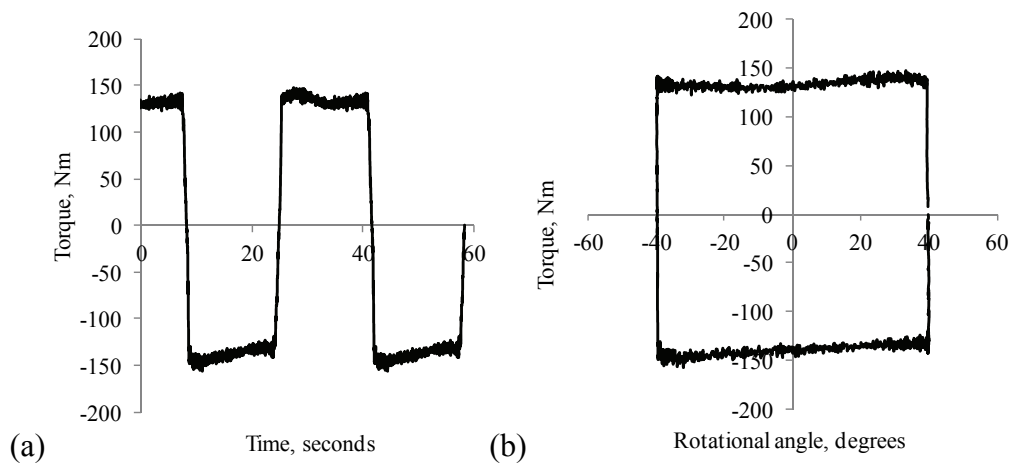


Figure 5.5. Torque cycles against time and angular position on pin joint, (a) torque cycle against time, and (b) torque cycle against rotational angle.

Figure 5.6 shows the recorded data plotted out as torque against time and friction coefficient calculated from torque data against displacement for articulating pin joint. The pin joint was lubricated by Aeroshell 33. Frictional torque increases with radial load. As the movement of the pin was following a sinusoid, rotational speed was varying during articulations. The speed reaches the climax at zero displacement in each articulation (Figure 5.4). Therefore, the frictional torque was not constant with time and had a minimum value at the highest speed point. Friction coefficient against angular displacement obtained from recorded torque is plotted in Figure 5.6 (b). Higher loads lead to a closer approach of mating surfaces. More asperities on the surfaces come to contact

that increases the shear force on the interface. Therefore, the friction coefficient for greater loads was higher compared to lower cases.

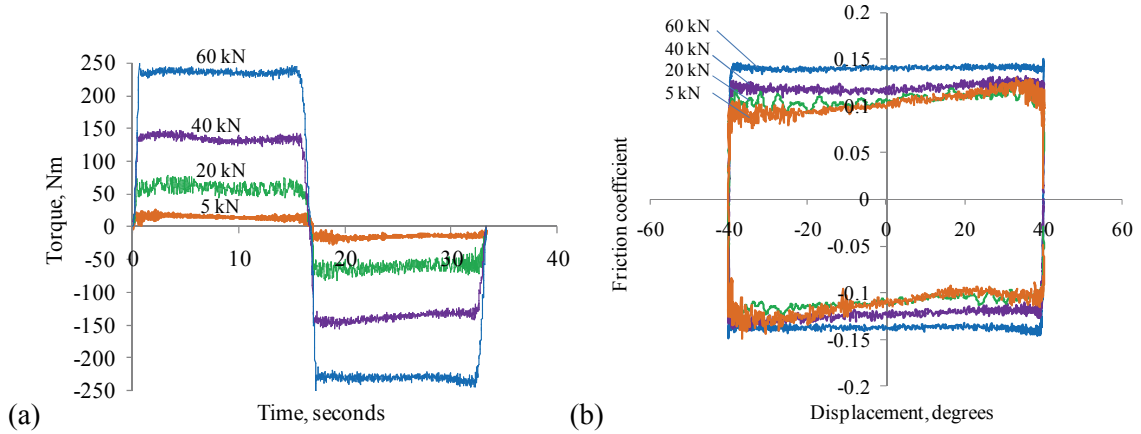


Figure 5.6. Torque and corresponding friction coefficient cycles at  $f=0.033\text{Hz}$ , (a) torque cycles against time, and (b) friction coefficient from torque data against angular displacement.

## 5.3 Mixed Lubrication Model for Pin Joint

As discussed in Chapter 2 and 3, in the mixed lubrication regime, the normal contact pressure was shared by both asperity contact and lubricant action. In this section, the mixed lubrication model was modified for pin and bush contact. Load sharing proportions and individual shear force for asperity interaction and liquid layer were analysed.

### 5.3.1 Pin Joint Friction

Figure 5.7 shows a sketch of the contact between the pin and the bush. In order to simplify the contact, a bush with the length of  $L$  was used instead of 4 separate bushes with the same total length. In this study, the edge of each bush was not considered. The pin was rotating inside under a normal load,  $P_t$ , which produces a torque,  $T$ . The contact size is expressed as  $2a$ , shown by a dashed ellipse. From the right enlarged view of the contact, a mixed lubrication regime is sketched. The total load,  $P_t$ , is equalised by both asperity contact force,  $P_a$ , and the lubricant action force,  $P_l$ . Similarly, the total shear force at the interface contains two components, one is the shear force from asperity interaction,  $Q_a$ , and the other is the shear in the liquid,  $Q_l$ .

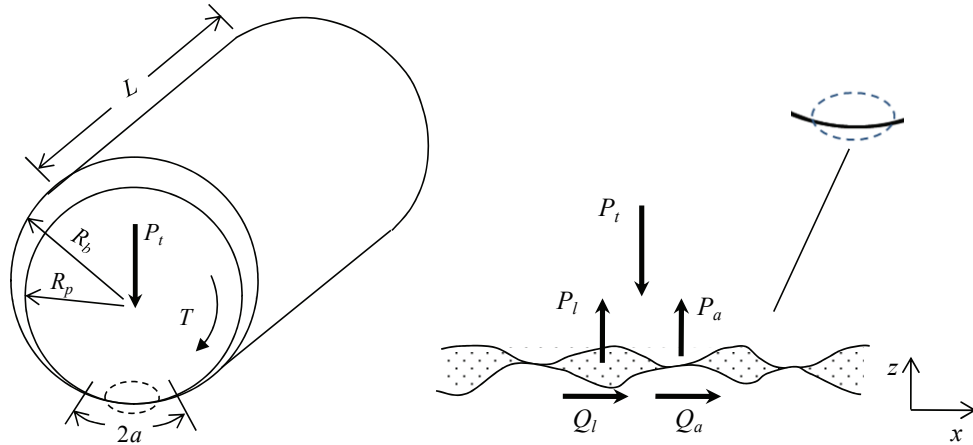


Figure 5.7. Schematic diagram of pin joint and load distribution in the mixed lubrication contact.

Friction coefficient is defined as shear force divided by total normal load. As the shear force is composed of asperity contact,  $Q_a$  and compressed lubricant layer,  $Q_l$ , so:

$$\mu = \frac{Q_l}{P_t} = \frac{Q_l + Q_a}{P_t} \quad (5.1)$$

Where  $P_t$  is the normal load applied at the interface.

When the coefficient is obtained, the frictional torque can be calculated through the linear relationship to normal load:

$$T = \mu R_p P_t \quad (5.2)$$

The friction force of asperity interaction for pin and bush contact is expressed as:

$$Q_a = \mu_a P_a \quad (5.3)$$

Where  $\mu_a$  is friction coefficient of single asperity contact, which is assumed to be the same for all asperity contacting spots.

The shear force from the hydrodynamic lubricant film is expressed as (detailed in Chapter 3):

$$Q_l = \tau_L \left(1 - e^{-\eta u / h_c \tau_L}\right) \cdot A_0 \quad (5.4)$$

In the shear force expressions,  $\tau_L$  is the limiting shear stress,  $\eta$  is the lubricant viscosity, which is assumed to obey Roelands' equation (Roelands, 1966; Hamrock *et al.*, 2004),  $u$



is the effective velocity of contacting surfaces,  $h_c$  is the central film thickness,  $A_0$  is the nominal contact area which can be determined from Hertzian contact theory,  $A_0 = 2aL$ ,  $a$  is the half width of Hertzian contact, and  $L$  is the total length of the four bushes. Both the parameters  $\tau_L$  and  $\eta$  are functions of the pressure in the contact,  $p_m$ , according to equations (3.10) and (3.16).

To simplify this model, the contact between the pin and bush was assumed to follow Hertzian elastic contact analysis. Strictly this kind of contact violates the Hertz principle because the contact area is not small compared with the radius of the contacting bodies. However, an experimental analysis (see Chapter 6) shows that the approximation is not too severe. The mean and peak contact pressures and half contact width are then given by:

$$p_m = \frac{P_t}{2aL}, p_0 = \sqrt{\frac{P_t E'}{2\pi L R'}}, a = \sqrt{\frac{8P_t R'}{\pi E' L}} \quad (5.5)$$

Where  $R'$  is the reduced radius:

$$\frac{1}{R'} = \frac{1}{R_p} - \frac{1}{R_b} \quad (5.6)$$

Where  $R_p$  and  $R_b$  are the outer radius of pin and inner radius of bush respectively,

and  $E'$  is the effective modulus:

$$\frac{1}{E'} = \frac{1}{2} \left( \frac{1 - \nu_b^2}{E_b} - \frac{1 - \nu_p^2}{E_p} \right)$$

In order to get the whole friction coefficient from equations (5.1), (5.3) and (5.4), the individual load sharing loads,  $P_l$ ,  $P_a$ , and film thickness,  $h$ , should be determined first. The following section presents the mixed lubrication model developed for pin joint contact and used for solving the above three unknowns.

## 5.3.2 Pin Joint Mixed Lubrication Model

### 5.3.2.1 Load Sharing

Scaling factors,  $\gamma_1$  and  $\gamma_2$  (Johnson *et al.*, 1972), were used to represent the proportions of

hydrodynamic lifting force,  $P_l$ , and surface asperities contacting force,  $P_a$ , detailed in Chapter 3 . The relationship between them is expressed as:

$$\frac{1}{\gamma_1} + \frac{1}{\gamma_2} = 1 \quad (5.7)$$

### 5.3.2.2 Asperity Contact

The pressure generated by the deformation of the asperities (Greenwood and Williamson, 1966),  $p_a$  is used to analyse the asperity contact, which is expressed as,

$$p_a = \frac{2}{3} D_s R_s \sigma_s \sqrt{\frac{\sigma_s}{R_s} E' F_{3/2}(t)} \quad (5.8)$$

Where  $t$  is dimensionless surface separation,  $t = h/\sigma_s$ ,  $h$  is the separation between the two surfaces. It should be noted that in the calculation of hydrodynamic film thickness,  $h$ , refer to the distance between the two mean levels of surfaces rather than the mean plane through the summit. The difference between the mean plane through the surface heights and the mean plane through the summit heights,  $d_d$  is shown in Figure 5.8. According to the model of Whitehouse and Archard (1970),  $d_d$  is approximately  $1.15\sigma_s$ ,  $D_s$  is the density of the asperities,  $R_s$  is the average radius of the asperities, and  $\sigma_s$  is the standard deviation of the height distribution of the summits. These parameters will be addressed in the following section. Finally,  $F_{3/2}(t)$  follows:

$$F_n(t) = \frac{1}{\sqrt{2\pi}} \int_t^\infty (s-t)^n e^{-s^2/2} ds \quad (5.9)$$

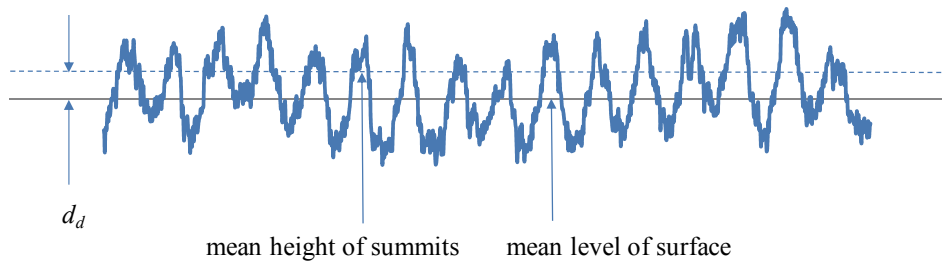


Figure 5.8. The different planes through a rough surface.

Thus, the central contact pressure of asperity contact,  $p_a$ , is a function of the central surface separation,  $h_c$ :

$$p_a = \frac{2}{3} D_s R_s \sigma_s \sqrt{\frac{\sigma_s}{R_s}} E' F_{3/2} \left( \frac{h_c - d_d}{\sigma_s} \right) \quad (5.10)$$

The expression for the statistical function  $F_{3/2}$  depends on the distribution of asperity heights,  $\phi(z)$ , where  $z$  is the height of asperity. In this study, a Gaussian height distribution of the summits was adopted. Hence the expression of  $\phi(z)$  is written as,

$$\phi(z) = \frac{1}{\sqrt{2\pi}} e^{-z^2/2} \quad (5.11)$$

In the rough line contact, the maximum pressure is equal to the central contact pressure. It was reported that the central pressure is a useful parameter to characterise the pressure distribution of a rough line contact (Gelinck and Schipper, 2000). The function fit for the central pressure is in the following expression:

$$p_c = p_h \left[ 1 + \left( a_1 D_s^{a_2} R_s^{\frac{3a_2}{2} - a_3} R_s^{a_2/2} \sigma_s^{a_3} W^{a_2 - a_3} \right)^{a_4} \right]^{1/a_4} \quad (5.12)$$

With  $a_1 = 1.558$ ,  $a_2 = 0.0337$ ,  $a_3 = -0.442$ ,  $a_4 = -1.7$ , and  $p_h$  is the maximum Hertzian pressure of line contact,  $p_h = \sqrt{\frac{P_t E'}{2\pi L R'}}$ .

The two expressions of central contact pressure should be the same, so combining Equation (5.10) from the GW model, and Equation (5.12) from the Gelinck and Schipper (2000) fitted function, it becomes:

$$\frac{2\sqrt{2\pi}}{3} \left( \frac{L R' E'}{P_t} \right)^{1/2} D_s R_s^{1/2} \sigma_s^{3/2} F_{3/2} \left( \frac{h_c - d_d}{\sigma_s} \right) = \left[ 1 + \left( a_1 D_s^{a_2} R_s^{\frac{3a_2}{2} - a_3} R_s^{a_2/2} \sigma_s^{a_3} W^{a_2 - a_3} \gamma_2^{a_2} \right)^{a_4} \right]^{1/a_4} \quad (5.13)$$

This equation describes the relationship between the surface roughness parameters, the geometry of the pin joint contact, the applied load and the separating film thickness.

It has been proven that  $E'$  should be replaced by  $E'/\gamma_2$ ,  $P_t$  by  $P_t/\gamma_2$  and  $D_s$  by  $D_s\gamma_2$  in Equation (5.13) when considering the asperity contact component (Gelinck and Schipper,

2000). So the above equation becomes:

$$\frac{2\sqrt{2\pi}}{3} \left( \frac{LR'E'}{P_t} \right)^{1/2} D_s R_s^{1/2} \sigma_s^{3/2} F^{3/2} \left( \frac{h_c - d_d}{\sigma_s} \right) = \frac{1}{\gamma_2} \left[ 1 + \left( a_1 D_s^{a_2} R_s^{\frac{3a_2}{2} - a_3} R_s^{\frac{a_2}{2}} \sigma_s^{a_3} W^{a_2 - a_3} \gamma_2^{a_2} \right)^{a_4} \right]^{1/a_4} \quad (5.14)$$

### 5.3.2.3 Fluid Film Formation

In this section, the liquid film formation on the interface is examined by using the Moes's model (1992). The assumption here is that the formation of the oil film is unaffected by the presence of the roughness. Then a conventional smooth surface EHL solution was used to determine the load supported by the hydrodynamic film.

The Moes equation is used to predict the central film thickness,

$$H_C = \left[ \left( H_{RI}^{7/3} + H_{EI}^{7/3} \right)^{3s/7} + \left( H_{RP}^{-7/2} + H_{EP}^{-7/2} \right)^{-2s/7} \right]^{1/s} \quad (5.15)$$

With  $s$  is defined as:  $s = \frac{1}{5} \left( 7 + 8e^{(-2H_{EI}/H_{RI})} \right)$ .

Where the dimensionless parameters are defined as follows:

$$\begin{aligned} H_{RI} &= 3M^{-1}, \\ H_{EI} &= 2.621M^{-1/5}, \\ H_{RP} &= 1.287F^{2/3}, \\ H_{EP} &= 1.311M^{-1/8}F^{3/4}, \\ H_C &= h_c' U_\Sigma^{-1/2}, h_c' = \frac{h_c}{R'}, \\ M &= WU_\Sigma^{-1/2}, F = GU_\Sigma^{1/4}, \\ W &= \frac{P_t}{E'R'L}, U_\Sigma = \frac{\eta_0 u}{E'R'}, G = \alpha'E' \end{aligned}$$

Where  $h_c$  is the separation in the center of the contact,  $h_c'$  and  $H_c$  are dimensionless film thicknesses,  $U_\Sigma$  is the dimensionless viscosity,  $M$  and  $W$  are dimensionless load parameters,  $F$  and  $G$  are material parameters, and  $\alpha'$  is the pressure-viscosity coefficient.

Again, in Equation (5.15), by replacing  $E'$  with  $E'/\gamma_1$  and  $P_t$  with  $P_t/\gamma_1$ , the film thickness

equation can be rewritten by:

$$h_c' U_{\Sigma}^{-1/2} = \left[ (\gamma_1)^{s/2} \left( H_{RI}^{7/3} + (\gamma_1)^{-14/15} H_{EI}^{7/3} \right)^{3s/7} + (\gamma_1)^{-s/2} \left( H_{RP}^{-7/2} + H_{EP}^{-7/2} \right)^{-2s/7} \right]^{1/s} (\gamma_1)^{1/2} \quad (5.16)$$

With  $s$  is expressed as:

$$s = \frac{1}{5} \left( 7 + 8e^{\left( -2(H_{EI}/H_{RI}) \gamma_1^{-2/5} \right)} \right) \quad (5.17)$$

The numerical solution of equations (5.7), (5.14) and (5.16) give the mean separation of contacting surfaces and scaling factors. Hence the hydrodynamic lifting force and asperity interaction force can then be calculated respectively. This information allows prediction of the coefficient of friction in the mixed lubrication regime.

### 5.3.3 Input Parameters

A MathCAD program was written to solve this set of equations for a given set of input conditions, detailed in Appendix B. Once the film thickness and load is solved, the friction coefficient can be determined from equations (5.1), (5.3) and (5.4). Frictional torque can then be calculated by Equation (5.2).

The pin being modeled in this study was a high strength corrosive resistant steel (300M) while the four bushes were made of aluminum bronze. All were machined with high-quality finish surfaces. Characteristics and working conditions of the pin joint are shown in Table 5.1.

Surface roughness of pin and bush was measured using a stylus profilometer. Figure 5.9 shows recorded surfaces profiles of pin and bush. A MathCAD program was written for analyzing the asperity distribution density,  $D_s$ , mean summit radius,  $R_s$ , and standard deviation of asperity distribution,  $\sigma_s$ . Details of each parameter are shown in Table 5.2. For the simulation in this study, average values from the pin and the bush were used for  $D_s$ ,  $R_s$  and  $\sigma_s$ .

Table 5.1. Characteristics and operating conditions of pin joint.

Parameter	Symbol	Value
Elastic modulus of pin	$E_p$	205 GPa
Elastic modulus of bush	$E_b$	117 GPa
Poisson's ratio of pin	$\nu_p$	0.28
Poisson's ratio of bush	$\nu_b$	0.34
Radius of pin	$R_p$	28 mm
Radius of bush	$R_b$	28.025 mm
Length of bush	$L$	59.4 mm
Total normal load	$P_t$	5,10,20,40,60 kN
Angular frequency	$\omega$	Varying, in radians/s
Effective velocity of contacting surfaces	$u$	Varying, in m/s
Radial clearance	$\Delta R$	25 $\mu\text{m}$
Rotation frequency of pin	$f$	0.03, 0.3 or 1 Hz

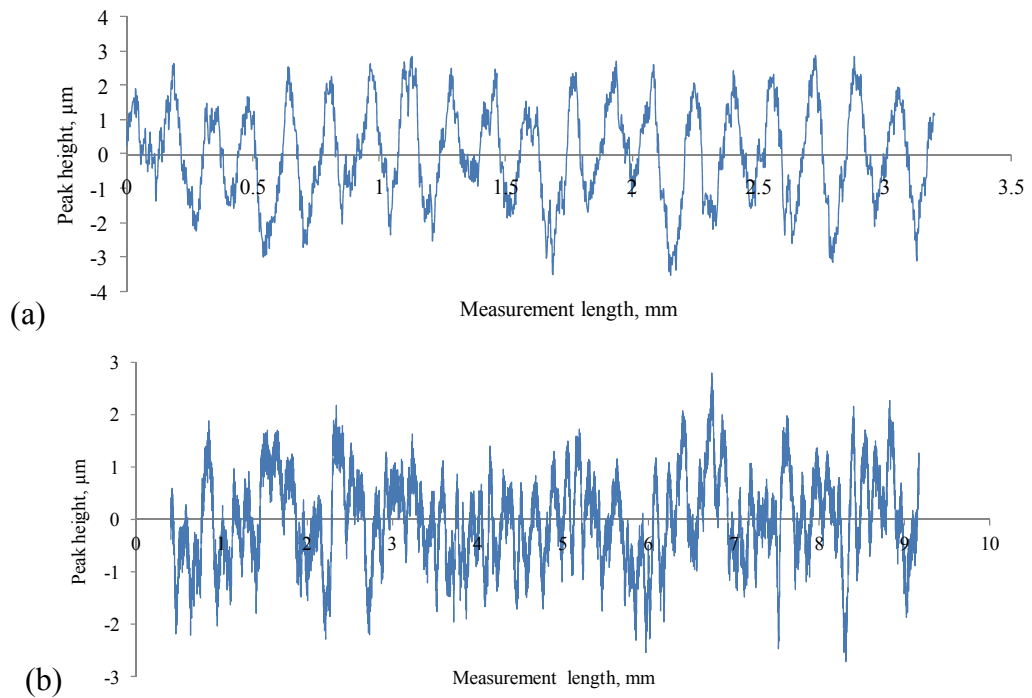


Figure 5.9. Surface profile of pin and bush: (a) bush, and (b) pin.

Table 5.2. Surface parameters of the pin joint used in this study.

Parameter	Symbol	Value
Density of asperities	$D_s$	$7.15 \times 10^9 \text{ m}^{-2}$
Average asperity radius	$R_s$	$3.4 \mu\text{m}$
Standard deviation of asperity height	$\sigma_s$	$1.09 \mu\text{m}$
Root mean square roughness of pin	$R_{qp}$	$0.83 \mu\text{m}$
Root mean square roughness of bush	$R_{qbu}$	$1.35 \mu\text{m}$
Distance between the mean plane through the summits and the mean plane through the surface heights (Figure 5.8)	$d_d$	$1.25 \mu\text{m}$

In this paper Aeroshell 33 was used to lubricate pin joint. The properties shown in Table 5.3 were used for the analysis in this study.

Table 5.3. Parameters of lubricant used in this study.

Parameter	Symbol	Value
Slope of the limiting shear stress-pressure relation	$\beta_0$	0.047
Limiting shear stress at ambient pressure (khonsari and hua, 1993)	$\tau_{L0}$	$2.28 \times 10^6 \text{ Pa}$
Lubricant viscosity at inlet temperature	$\eta_0$	$12.45 \times 10^{-3} \text{ Pa}\cdot\text{s}$
Constant in Roelands' formula (hamrock <i>et al.</i> , 2004)	$\eta_\infty$	$6.31 \times 10^{-5} \text{ Pa}\cdot\text{s}$
Constant in Roelands' formula (hamrock <i>et al.</i> , 2004)	$c_p$	$1.96 \times 10^8 \text{ Pa}$
Roelands' pressure-viscosity index (hamrock <i>et al.</i> , 2004)	$Z$	0.63
Pressure-viscosity coefficient	$\alpha'$	$16.9 \text{ GPa}^{-1}$

A critical unknown in this model is the “dry” friction coefficient,  $\mu_a$ , that exists between the two solid surfaces at the asperity contact points. In the absence of any data for this parameter, a value of 0.12 was used in this study. This value has been proven reasonable in the study of Lunn (1957), Gelinck and Schipper (2000) and Lu *et al.* (2006, 2007).

## 5.4 Numerical Simulation Results

Under varying pin joint operating conditions, numerical solutions for friction coefficient, film thickness, lambda ratio and the scaling factors were solved by using the MathCAD friction model, detailed in Appendix B.

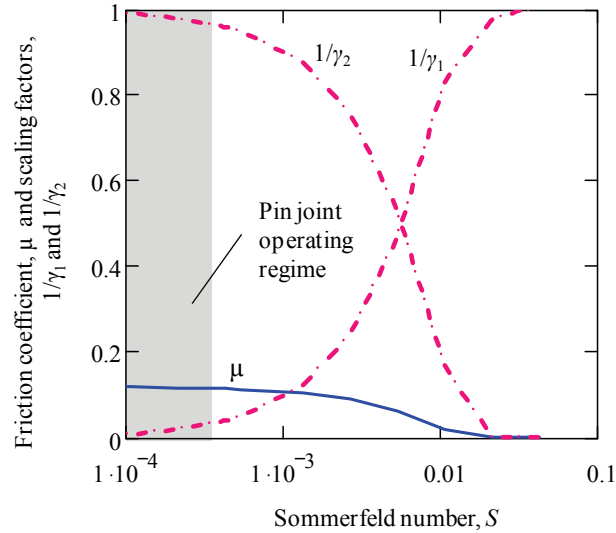


Figure 5.10. Scaling factors and friction coefficient against Sommerfeld number under 20kN.

Figure 5.10 shows the predicted scaling factors and friction coefficient variation with the pin joint operating conditions. The  $x$ -axis on the plot is expressed in terms of the Sommerfeld number defined by (Cameron, 1971):

$$S = \frac{\eta\omega}{2\pi P_L} \left( \frac{R}{\Delta R} \right)^2 \quad (5.18)$$

Where  $\eta$  is the oil viscosity,  $\omega$  is the rotation speed of pin,  $P_L$  is the projected load and  $\Delta R$  is the radial clearance. As the Sommerfeld number increases (by the joint articulation velocity increasing), more lubricant is dragged into pin joint contact to maintain the pressure field. This causes an increase in film thickness, and can be seen in Figure 5.10 as  $1/\gamma_1$  becomes greater. This process agrees with the theory that pressure magnitudes are proportional to the square of the reciprocal of film thickness (Stachowiak and Batchelor, 2005). When the lubricant film supports most of the load, contact between asperities declines. The composite result was that friction coefficient of pin/bush contact decreased



with the Sommerfeld number.

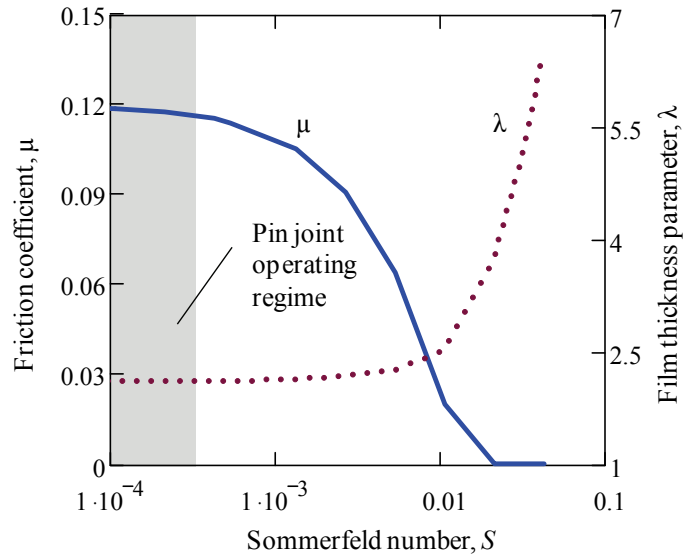


Figure 5.11. Fiction coefficient and Lambda ratio against Sommerfeld number under 20kN.

Figure 5.11 shows the friction coefficient varies with the Sommerfeld number determined, from Equation (5.1). Also shown is the lambda ratio,  $\lambda$ , where:

$$\lambda = h / \sqrt{R_{qp}^2 + R_{qb}^2} \quad (5.19)$$

In the simulation work of this study, the pin joint rotated in the speed range from 1 to 800 rpm under pressure in the range 7 to 23 MPa. This resulted in the Sommerfeld number in the range of 0 - 0.15. For the load of 20 kN (13MPa), this range is marked in Figure 5.10 and Figure 5.11. It shows clearly that the dominant mechanism was of solid contact and hydrodynamic film formation plays little part in friction.

Figure 5.12 shows the relation between lubricant film thickness and friction coefficient for the pin joint contact. Lower friction was obtained when a thicker film was formed, which meant little asperity interaction on the interface.

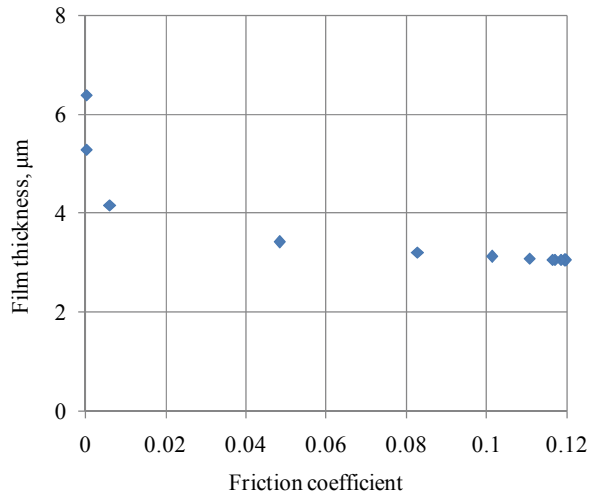


Figure 5.12. Film thickness against friction coefficient under 60 kN.

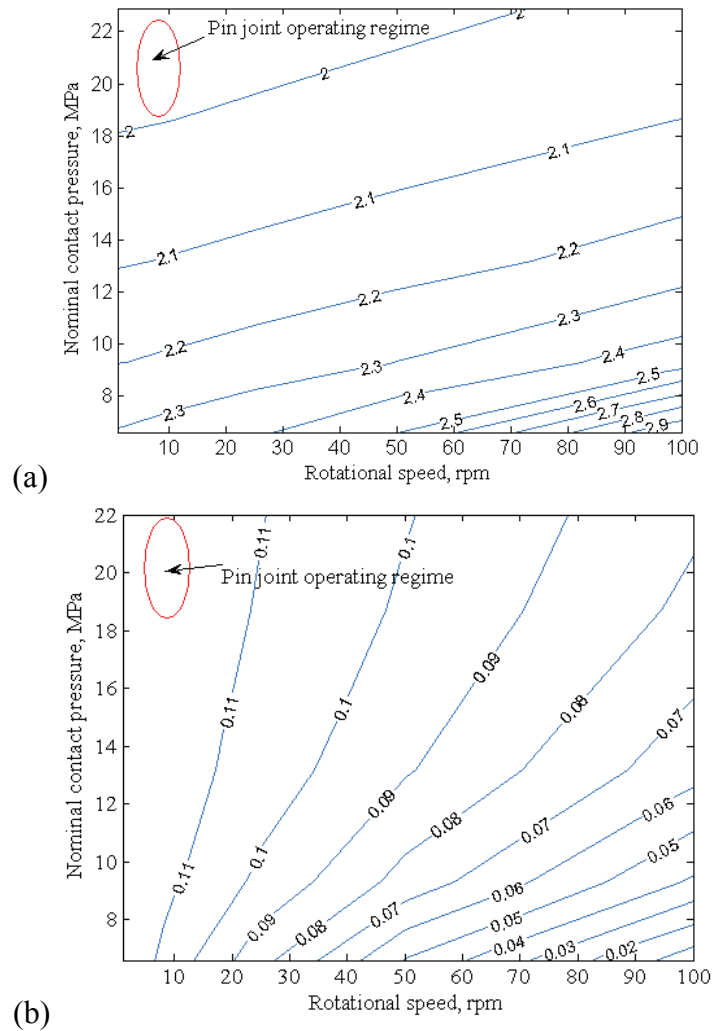


Figure 5.13. (a) Lambda ratio map, and (b) friction coefficient map simulated by the mixed lubrication model.

Figure 5.13 shows maps of the friction coefficient and lambda ratio determined from the model for various pin joint loads and speeds. Again, the operating region for the pin joint was indicated. The data indicated that friction coefficients did not fall below 0.11 as lambda ratios stayed below 2. In this region of operation the prediction friction coefficient was highly dependent on the value selected for the dry friction coefficient,  $\mu_d$ . This was in common with many other models of mixed lubrication, and was a limitation of the model.

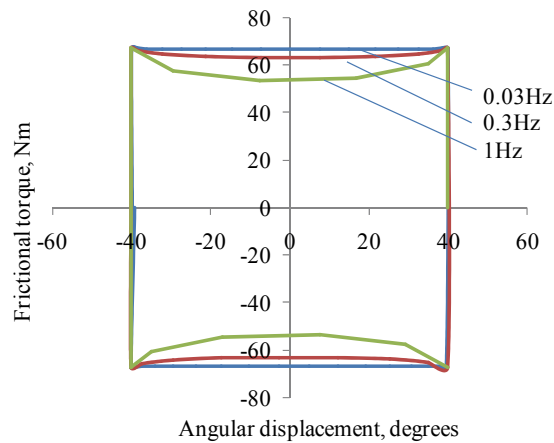


Figure 5.14. Frictional torque against angular displacement for different frequencies under 20N.

Figure 5.14 shows predicted frictional torque on the pin joint varying with rotational speed for different frequencies. The simulated torque was found to decrease with frequency (speed). This was because higher speed leads more hydrodynamic action and so less shear at the interface. As the displacement of pin followed a sinusoidal trace, the rotation speed varied during each cycle. The climax speed took place at the zero angular displacement, where the lowest torque was produced on the interface.

## 5.5 Comparison between Simulation and Experiment

The average torque during each complete articulation was used for calculating the friction coefficient using Equation (5.2). The friction coefficient was then plotted against Sommerfeld number, rotation speed and load shown in Figure 5.15 to 5.17 respectively.

Figure 5.15 shows friction coefficient against Sommerfeld number for varying loads. Comparing simulation with experiment results, it is apparent that pin joint was working

in boundary lubrication regime on most occasions. The higher load cases showed a close agreement between the model simulations and experimental results. The friction coefficient for low speeds when there was negligible hydrodynamic lift was 0.117. This was close to the value of  $\mu_a$  that was assumed in the modelling. However, at lower loads, the agreement was somewhat imperfect. The onset of fluid film formation appeared to be occurring at lower speed. It was possible that at these lower loads the grease was not being squeezed out of the contact as effectively as at the higher loads. Also, grease thickeners could improve the friction property of pin joint because of the formation of films on the surface of the metal. This resulted in an improved film formation.

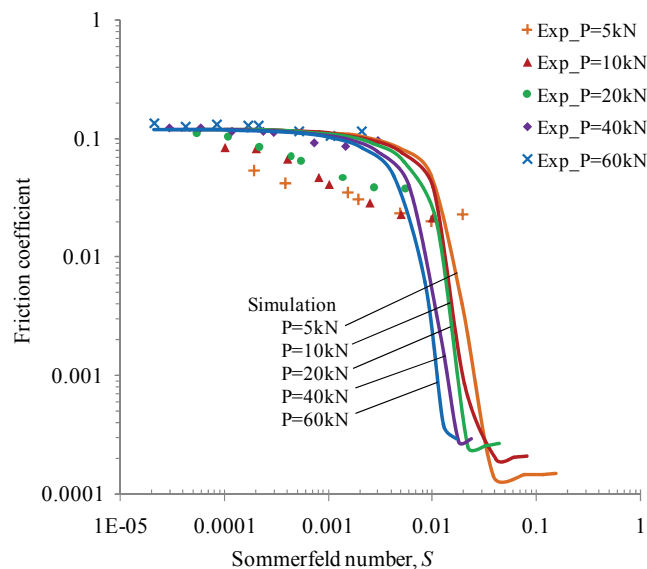


Figure 5.15. Fiction coefficient against Sommerfeld number with varying load.

The influence of pressure and velocity on friction is shown in Figure 5.16 and Figure 5.17. Model predictions and experimental results showed acceptable agreement. However, the comparison indicated by Figure 5.16 demonstrated that the effect of load was more pronounced than would be expressed by the theory. The simulation assumed the contact was fully flooded. In reality the joint articulating and the high load squeezes grease out of the contact. The greater the load and reciprocation frequency, the harder it was for the grease to flow back. This may be the reason why the higher loads show a higher friction coefficient.

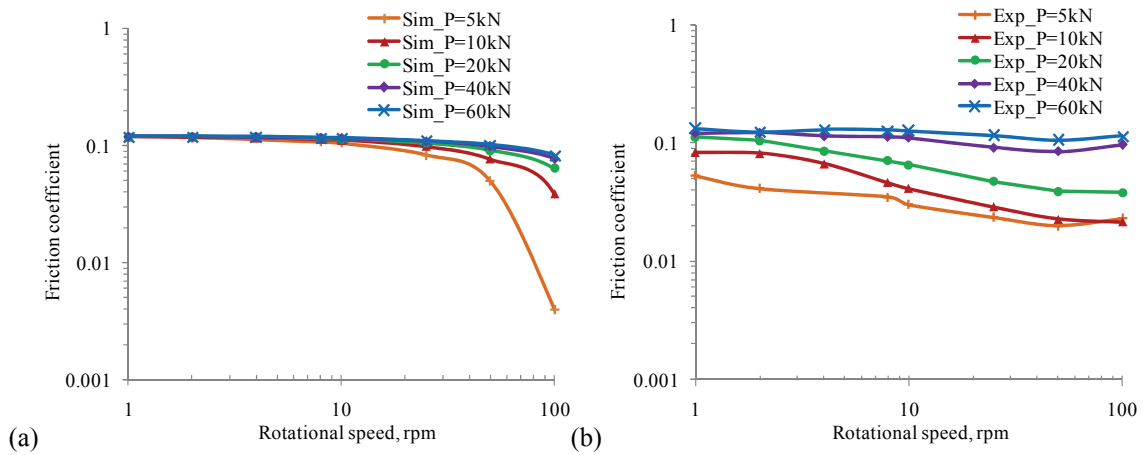


Figure 5.16. Friction coefficient against sliding speed, (a) simulation, and (b) experiment results.

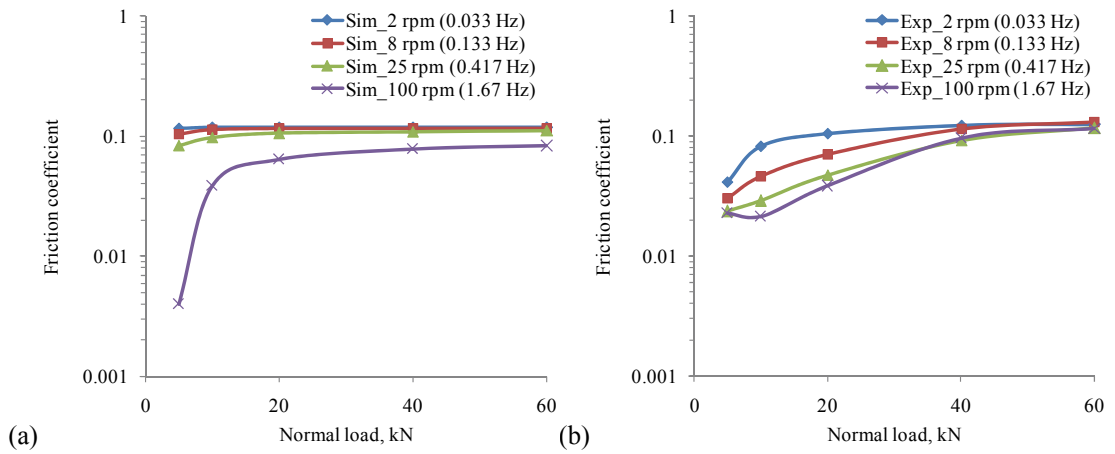


Figure 5.17. Friction coefficient against load, (a) simulation results, and (b) experiment results.

Figure 5.18 (a), Figure 5.19 (a) and Figure 5.20 (a) show the predicted torque cycle from the model for a full articulation of the pin joint. At lower speeds, the torque during rotation remained virtually constant (another indication that hydrodynamic was negligible). At higher speeds, there was a reduction in torque as the joint articulates at its maximum velocity. Figure 5.18 (b), Figure 5.19 (b) and Figure 5.20 (b) show the experiment measurement of the same cycle. The cycles have similar form and magnitude. At higher speeds there was some oscillation in the recorded torque (Figure 5.20 (b)). This was believed to be an effect of the hydraulic contact, as it could not respond quickly enough to the command signal.

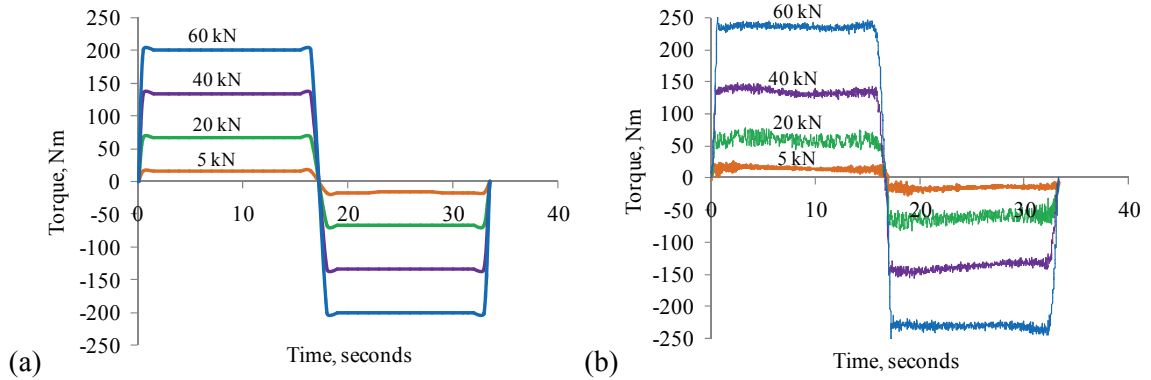


Figure 5.18. Frictional torque varying with time at  $f=0.03\text{Hz}$  (1.8rpm), (a) simulation result, and (b) experimental result.

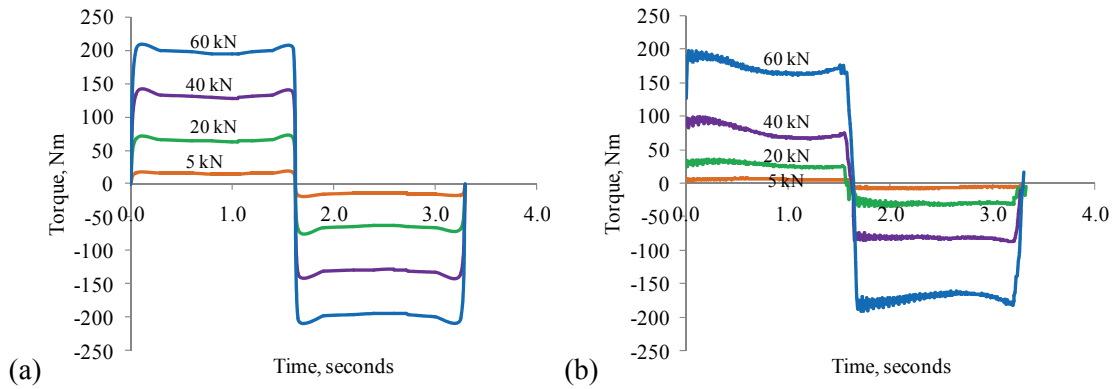


Figure 5.19. Frictional torque varying with time at  $f=0.3\text{Hz}$  (18rpm), (a) simulation result, and (b) experimental result.

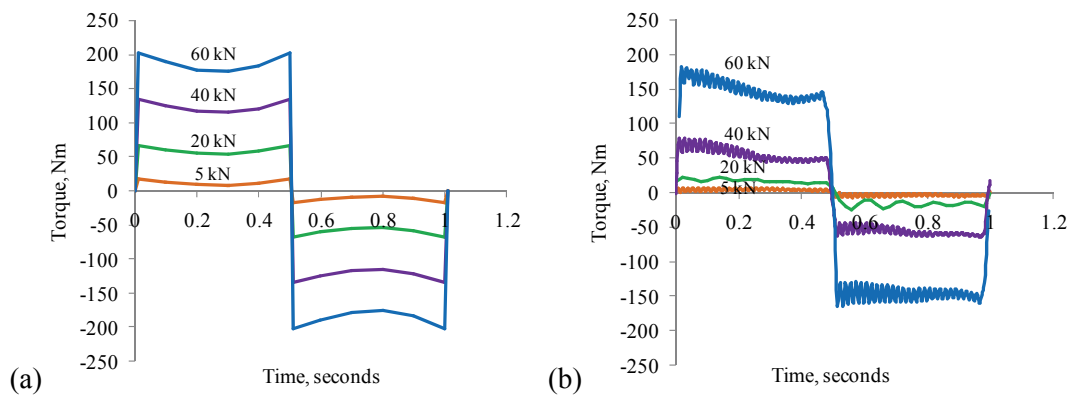


Figure 5.20. Frictional torque variation with time at  $f=1\text{Hz}$  (60rpm), (a) simulation result, and (b) experimental result.

## 5.6 Conclusions

The main lock stay pin joints on the landing gear were subjected to high load and slow

speed. These conditions were not conducive to the formation of a separating lubricant film and the joint operates with significant metallic contact. Experiments were performed on a purpose built apparatus to measure the torque during articulations of a pin and bush assembly under a range of load and speed condition.

A mixed lubrication model of the pin and bush contact was built to determine the friction coefficient and torque during articulation which can be used to assist in the joint design and actuator sizing. In this model, the proportions of asperity contact force and lubricant lifting action were predicted.

Under the operating conditions of pin joint, both the model and experiments demonstrated that, for all predicted purposes, the pin joint operated in a boundary regime. There was, however, little hydrodynamic effect on the overall friction. Most of the normal load was found to be supported by asperity interaction. On the interface full film lubrication did not form to any great extent.

# Chapter 6 Contact Pressure and Friction in a Landing Gear Pin Joint

This chapter is aimed at investigating the contact pressure distribution within a pin joint contact in a landing gear. Ultrasonic measurement has been used to determine contact pressure, contact size and friction torque. Simultaneously, two theoretical models, Hertzian model and Persson's model (Persson, 1964), were adopted for simulation of the pin joint contact. The findings were compared to experimental results. In addition, the real frictional torque taking place on the interface was analysed and compared to the nominal torque which was obtained through a traditional way ( $T = \mu RP$ ). The deviation between real friction torque/coefficient and nominal ones was quantified.

## 6.1 Introduction

Figure 6.1 (a) shows a pin contacting with bush, which is a typical example of a cylindrical conformal contact. Both the pin and bush have similar radii, the initial contact is similar to a non-conformal case as a line. However, the contact area increases dramatically with an increase in load, and may become comparable with the dimensions of the contacting bodies themselves (Johnson, 1985). From the cross section, the contact area is actually a segment which is strongly dependent on the applied load and radius difference between the contacting pin and bush (Persson, 1964). Half of the segment angle,  $\alpha$ , is known as the half contact angle (or wrap angle) for pin and bush contact. The contact pressure on the interface is a function of position, expressed as  $p(\phi)$ , shown in Figure 6.1 (b).



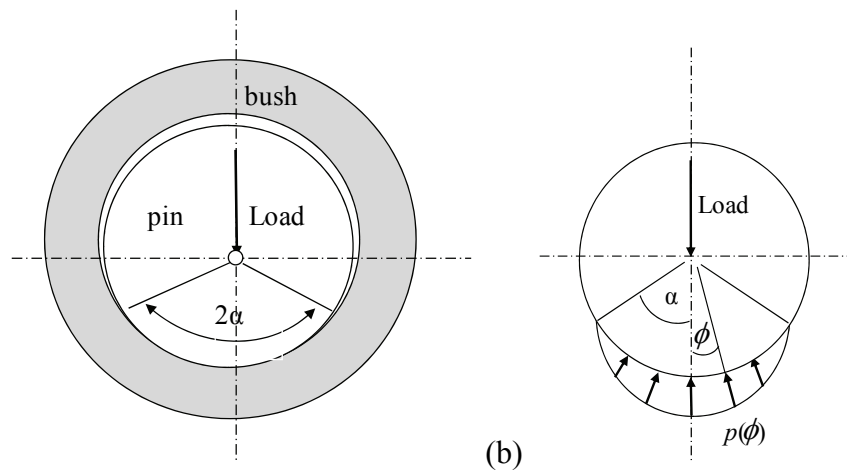


Figure 6.1. (a) Cylindrical contact between pin and bush, and (b) pressure distribution.

Contact pressure and friction at the interface are key factors affecting pin joint performance, material removal, failure and operating life. In this chapter, the contact pressure, friction torque and friction coefficient of a pin and four bushes from an actual upper to lower side-stay pin joint was investigated by using the ultrasonic method and theoretical models.

Ultrasound has previously been used as a technique to measure the contact stress between two surfaces (Marshall *et al.*, 2004, 2006, 2011; Lewis *et al.*, 2005). The concept is that an ultrasonic pulse is reflected back from an interface, and the proportion of the wave reflected is captured. This proportion of reflected signal is related to the contact stiffness and in turn to the contact stress. In this study, the ultrasonic reflection measurement was carried out by the Leonardo Centre for Tribology for a pin joint contact. Contact pressure was analysed using the ultrasonic measurements.

For theoretical modelling, the classic Hertzian theory of cylindrical contact and Persson's conformal contact model were adopted. Pressure distribution, contact size and friction on the pin and bush contact was simulated. The predictions were compared to experimental measurements.

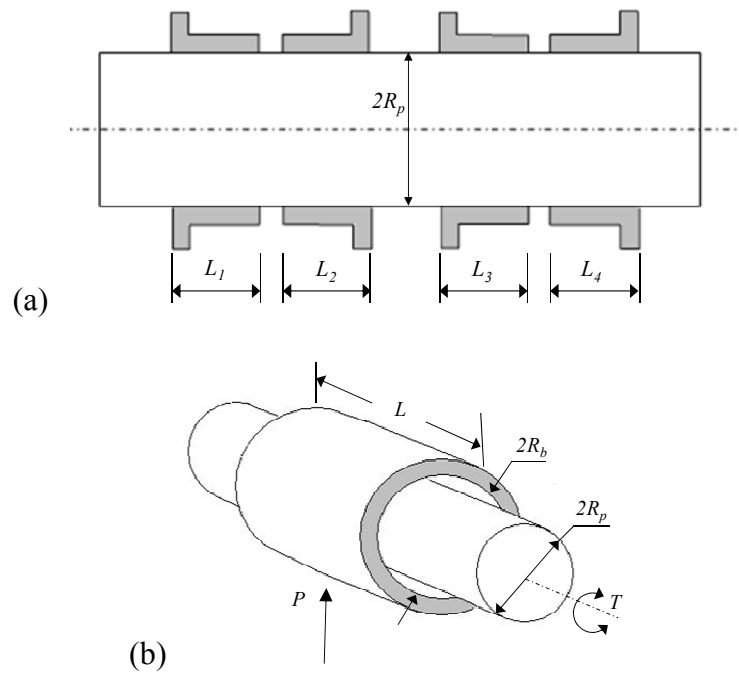


Figure 6.2. (a) Illustration of pin and bushing geometry, and (b) simplified contact model.

Figure 6.2 (a) shows the pin-bush contacting geometry, which is made up from one chromed 300M steel pin wrapped with four aluminum bronze bushes. All four bushes are of length  $L$ , with each bush of equal length,  $L_1=L_2=L_3=L_4$ . For simplicity, the total length of bush,  $L = L_1+L_2+L_3+L_4$ , was used in this study. Figure 6.2 (b) shows the dimensional relationship and application of load  $P$ . Radius  $s$  of pin and bush are expressed as  $R_p$  and  $R_b$  respectively.  $T$  is torque required to rotate the pin.

## 6.2 Experimental Measurement

In this section the ultrasonic reflection measurement carried out by the Leonardo Centre for Tribology for a pin joint contact was analysed. First, the ultrasonic reflection coefficient was used to determine contact stiffness by using the spring model. Then the contact pressure of pin and bush contacting interface was calculated from the obtained stiffness.

### 6.2.1 Ultrasonic Reflection and Contact Stiffness

A pin and four bushes were obtained from an actual upper to lower side-stay pin joint and

were used as the test specimens. Specimen details have been described in Chapter 5 and the picture of pin/bush contact was shown in Figure 5.3. The radial load was applied through a hydraulic cylinder which had a simple load cell read out.

Figure 6.3 shows a schematic layout of the instrumentation. A bespoke 25 MHz transducer was commissioned (from NDT Systems Ltd) for use with this test case. The transducer incorporates a focusing lens, a long stem and a mirror. In this way a focused beam can be made to strike the interface at a normal contact angle. The pin was filled with water and the transducer immersed in the water bath. The ultrasonic transducer was installed in the pin bore (submerged in a water bath) which scanned both vertically and radially to record reflection from the pin-bush interface. The ultrasonic reflection was recorded at each transducer position. This was then related to the interface stiffness and contact pressure. Full details of the experimental approach were given in (Dwyer-Joyce *et al.*, 2003).

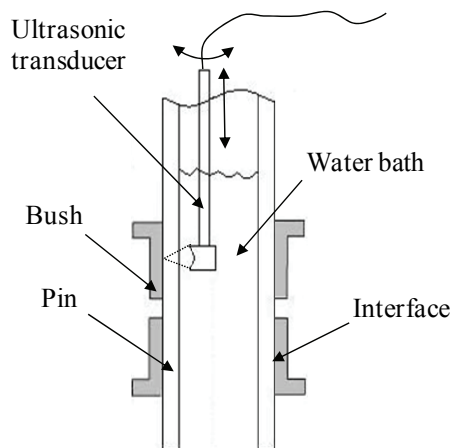


Figure 6.3. Schematic representation of ultrasonic measurement.

Figure 6.4 shows the reflection coefficient distributions with increasing load from 5 to 60 kN. The zero on the angular position axis corresponds to a position diametrically opposite to the joint loading direction. Reflection coefficients were measured in 10° increments, from -60° to 60°.

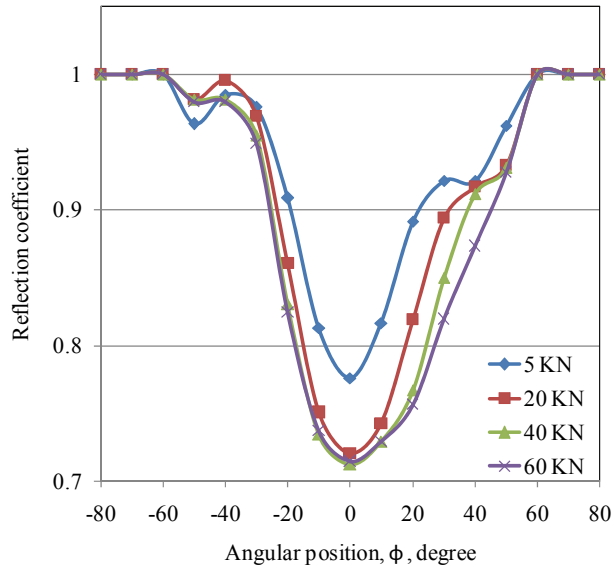


Figure 6.4. Ultrasonic reflection coefficient distributions under varying loads.

The plot shows the reflection coefficient was close to 1 for  $\phi < -60^\circ$  and  $\phi > 60^\circ$ . In this region the surface area was out of contact and the ultrasonic wave was fully reflected at the pin steel to air contact. In the region of  $-60^\circ < \phi < 60^\circ$  the reflection fell below 1. At this point, there was contact between the pin and bush surfaces and part of the wave was transmitted.

From the spring model, Equation (2.9), the stiffness,  $K$  can be determined through:

$$K = \sqrt{\frac{(\omega z_1 z_2)^2 (1 - R^2)}{R^2 (z_1 + z_2)^2 - (z_1 - z_2)^2}} \quad (6.1)$$

Figure 6.5 shows the contact stiffness varying with angular position on the pin joint. The peak stiffness was found in the middle of the pin and bush contact under a certain load. Under all load cases, the trend lines of contact stiffness gave approximate inverse funnel shapes. In the next section, the contact stiffness was used for the calculation of pressure distribution.

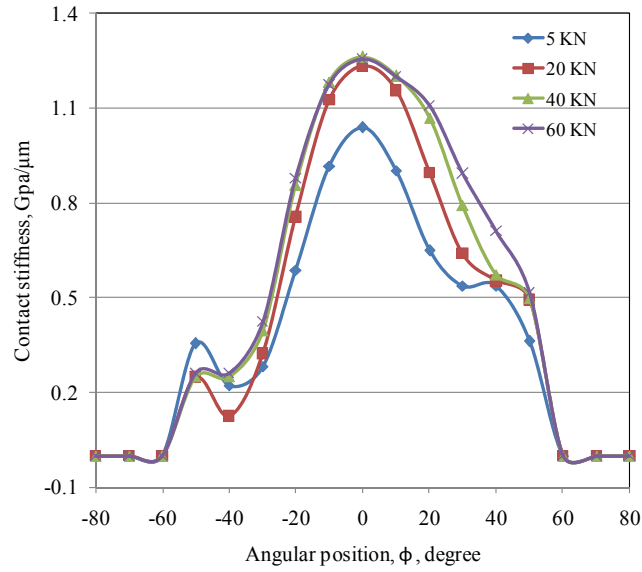


Figure 6.5. Contact stiffness distributions against angular position under varying loads.

## 6.2.2 Calculation of Contact Pressure

The interface stiffness  $K$  (expressed per unit area) is the change in nominal contact pressure,  $p_{nom}$  required to cause unit approach of the mean lines of the surfaces (Thomas and Sayles, 1977) (Equation (2.10)):

$$K = -\frac{dp_{nom}}{dh} \quad (6.2)$$

Where  $h$  is the separation of the mean lines of the roughness of the two surfaces.

From Figure 4.6 (a) it can be seen that the stiffness of an interface is approximately proportional to the contact pressure. As the surfaces are pressed together, more asperity contact occurs as the surfaces are in closer conformity. It then requires a greater pressure increase to push them closer together. It has been found that at mean pressure below bulk yield the relationship between contact pressure and interfacial stiffness may be approximated as linear with a constant  $m$  (Ito *et al.*, 1979; Arakawa, 1983; Hodson *et al.*, 2000). Experiments have been conducted and shown the same conclusion (Dwyer-Joyce and Drinkwater, 2003), which is expressed as:

$$p = mK \quad (6.3)$$

Equation (6.3) expresses the proportionality behavior between contact stiffness and contact pressure. As  $p$  varying across the interface, it is assumed at each point the following equation holds.

$$p_i = mK_i \quad (6.4)$$

Where  $p_i$  and  $K_i$  are the contact pressure and stiffness respectively at the  $i^{th}$  data point, using  $n$  as the number of data points. The contact pressure across the section of the interface,  $p(\phi)$ , is a function of the radial position shown in Figure 6.1 (b). It is assumed to be independent with axial position. Therefore, from Equation (6.4), the total normal load on the pin joint can be expressed as:

$$P = \frac{\pi R_p \alpha L}{90^\circ n} \sum_{i=1}^n p_i \cos(\phi_i) \quad (6.5)$$

Where  $\phi_i$  is the angle at the  $i^{th}$  data point from the line of the normal load shown in Figure 6.1. Therefore, combine equations (6.4) and (6.5), and get:

$$P = \frac{\pi m R_p \alpha L}{90^\circ n} \sum_{i=1}^n K_i \cos(\phi_i) \quad (6.6)$$

If the total load, dimensions of the pin and bush, and the contact stiffness are known it is then possible to deduce the constant of proportionality, and therefore the contact pressure distribution in a system.

In this study, the total length of the bushes,  $L$ , was 59.4 mm and the radius of the pin,  $R_p$ , was 28 mm. The loads in the tests were set to be 5, 20, 40 and 60 kN. For each of these load cases the constant  $m$  was obtained and shown in Table 6.1.

Table 6.1. Calculation of constant  $m$ .

<b>Load, kN</b>	<b>5</b>	<b>20</b>	<b>40</b>	<b>60</b>
$m, \times 10^{-9}$	3	10	18	26

The different load cases showed different contacts of proportionality between  $P$  and  $K$ .

These loads were applied to the same surface pair and therefore it was expected that linearity was retained across the whole loading range. However, this is restricted under the lower loads (Figure Figure 4.6 (a)). At higher loads, the linear relationship between contact stiffness and load doesn't hold. Therefore, the ratio,  $m$ , varies with loads.

Figure 6.6 shows the contact pressure distribution using Equation (6.6), calculated from the interference stiffness data of Figure 6.5 and the data from Table 6.1. It can be seen that an increase in load was accommodated by an increase in contact pressure, but not by an increase in the contact area. The pressure distribution was close to cosinusoidal. The 'bump' at  $-50^\circ$  was anomalous, but occurs on each load cycle. It is a possibility that this was due to a slight machining inaccuracy in the bush or pin. In the later section, the Hertzian model and Persson's model will be used to simulate the pin and bush contact. The prediction of pressure distribution was compared to the results calculated from ultrasonic measurement for varying loads

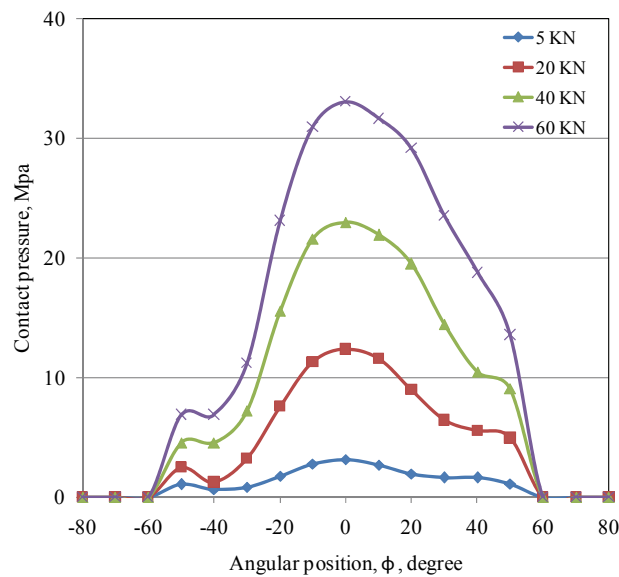


Figure 6.6. Radial pressure against angular position under varying loads.

## 6.3 Theoretical Modelling

### 6.3.1 Contact Pressure Distribution

When two cylinders coming to contact, the initial contact region is a line as there is no

bulk deformation taking place. If a slight normal load is applied, the two bodies deform along this line. The contact region spreads to form a long and narrow rectangle, which is known as the nominal contact area and increases with normal load. In this section, the Hertzian contact model and Persson's model were presented for determining the contact pressure for the contact between a pin and bush.

According to Hertzian theory, the contact pressure distribution is expressed as:

$$p(x) = \frac{1}{4R'} \sqrt{\frac{8P'R'E'}{\pi} - E'^2 x^2} \quad (6.7)$$

Where,  $E'$  is reduced elastic modulus,  $\nu_1$  and  $\nu_2$  are the Poisson's ratios of the contacting bodies 1 and 2 respectively,  $E_1$  and  $E_2$  are the elastic modulus of the contacting materials respectively,  $R'$  is reduced radius,  $\frac{1}{R'} = \frac{1}{R_1} + \frac{1}{R_2}$ ,  $R_1$  and  $R_2$  are the radius of the contacting bodies respectively,  $P'$  is the load per unit length (N/m), and  $x$  is the  $x$ -coordinate in meters, showing the direction of movement, expressed by  $R \sin(\phi)$ .

Hertzian contact theory is based on the assumption that the dimensions of the footprint area are small compared to the radii of curvature of the contacting surfaces. However, in this case, the contact surfaces are curved and closely conforming, having footprint dimensions nearly equal to their radii. Small radial clearance and a heavy application load result a conformal non-Hertzian type contact (Persson, 1964; Chen and Marshek, 1988).

Persson studied the elastic contact between two parallel cylinders which is a conformal case shown as Figure 6.1. (a). The following expression was deduced for conformal contact pressure distribution,  $p(\phi)$ , when  $E_1 = E_2 = E$  and  $\nu_1 = \nu_2 = \nu$ .

$$p(\phi) = \frac{P'}{R_1} \left( \frac{2}{\pi \sqrt{b^2 + 1}} \frac{\sqrt{b^2 - y^2}}{1 + y^2} + \frac{1}{2\pi b^2(1 + b^2)} \ln \frac{\sqrt{b^2 + 1} + \sqrt{b^2 - y^2}}{\sqrt{b^2 + 1} - \sqrt{b^2 - y^2}} \right) \quad (6.8)$$

Where  $-b \leq y \leq b$ ,  $-\alpha \leq \phi \leq \alpha$ ,  $y = \tan \frac{\phi}{2}$ ,  $b = \tan \frac{\alpha}{2}$ ,  $\phi$  and  $\alpha$  are shown in Figure 6.1.

The contact semi-width, the maximum contact pressure and the mean contact pressure



were obtained as:

Half contact width:

$$b \approx R_1 \sqrt{\frac{8}{\pi}} \sqrt{\frac{P'(1-\nu^2)}{E(R_2 - R_1)}} \quad (6.9)$$

Maximum contact pressure:

$$p_0 = \frac{1}{\sqrt{2\pi}} \sqrt{\frac{EP'(R_2 - R_1)}{(1-\nu^2)R_1^2}} \quad (6.10)$$

Mean contact pressure:

$$p_m = \frac{P'}{2b} \quad (6.11)$$

Based on Persson's theory, a closed form formula for pressure distribution and the relation between load and contact size for non-identical contacting materials,  $E_1 \neq E_2$  and  $\nu_1 \neq \nu_2$  was deduced (Ciavarella and Decuzzi, 2001):

$$p(\phi) = \frac{P'}{R_1} \left( \frac{2}{\pi \sqrt{b^2 + 1}} \frac{\sqrt{b^2 - y^2}}{1 + y^2} + \frac{1}{\pi} \left(1 - \frac{B_p}{2}\right) \ln \frac{\sqrt{b^2 + 1} + \sqrt{b^2 - y^2}}{\sqrt{b^2 + 1} - \sqrt{b^2 - y^2}} \right) \quad (6.12)$$

with  $B_p = \frac{2b^4 + 2b^2 - 1}{b^2(b^2 + 1)}$ ,  $b = \text{tg} \frac{\alpha}{2}$ .

A solution of two-dimensional contact for the contact pressure distribution and contacting dimensions was given. The relationship between load, the radial clearance and half contact angle was also determined. Figure 6.7 shows the dimensionless load varying with tangent of half-contact angle, which is compared with both Hertzian results.

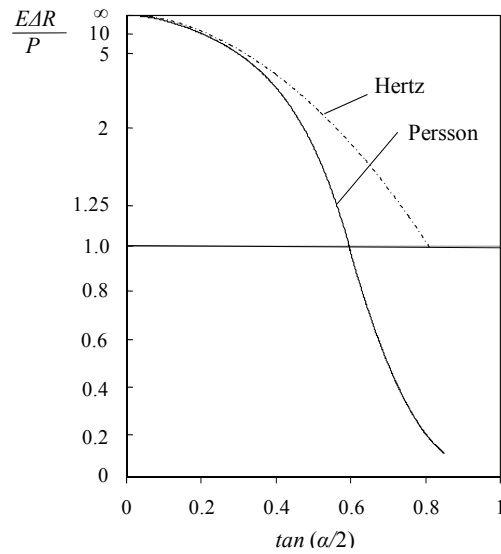


Figure 6.7. Dimensionless load varying with half contact angle.

Equations (6.7) and (6.12) were used to calculate the contact pressure distribution of pin joint for the Hertzian and Persson's model respectively. Figure 6.8 compares the contact pressure between these two models for varying loads. It is clear that the profiles of pressure from two models were approximately the same at 5kN. But with the increasing load, the difference also increased. Apparently, the shapes of pressure from Hertzian model seem to be wider and lower. It means that under the identical conditions, material deformation from Hertzian theory was greater than Persson's prediction.

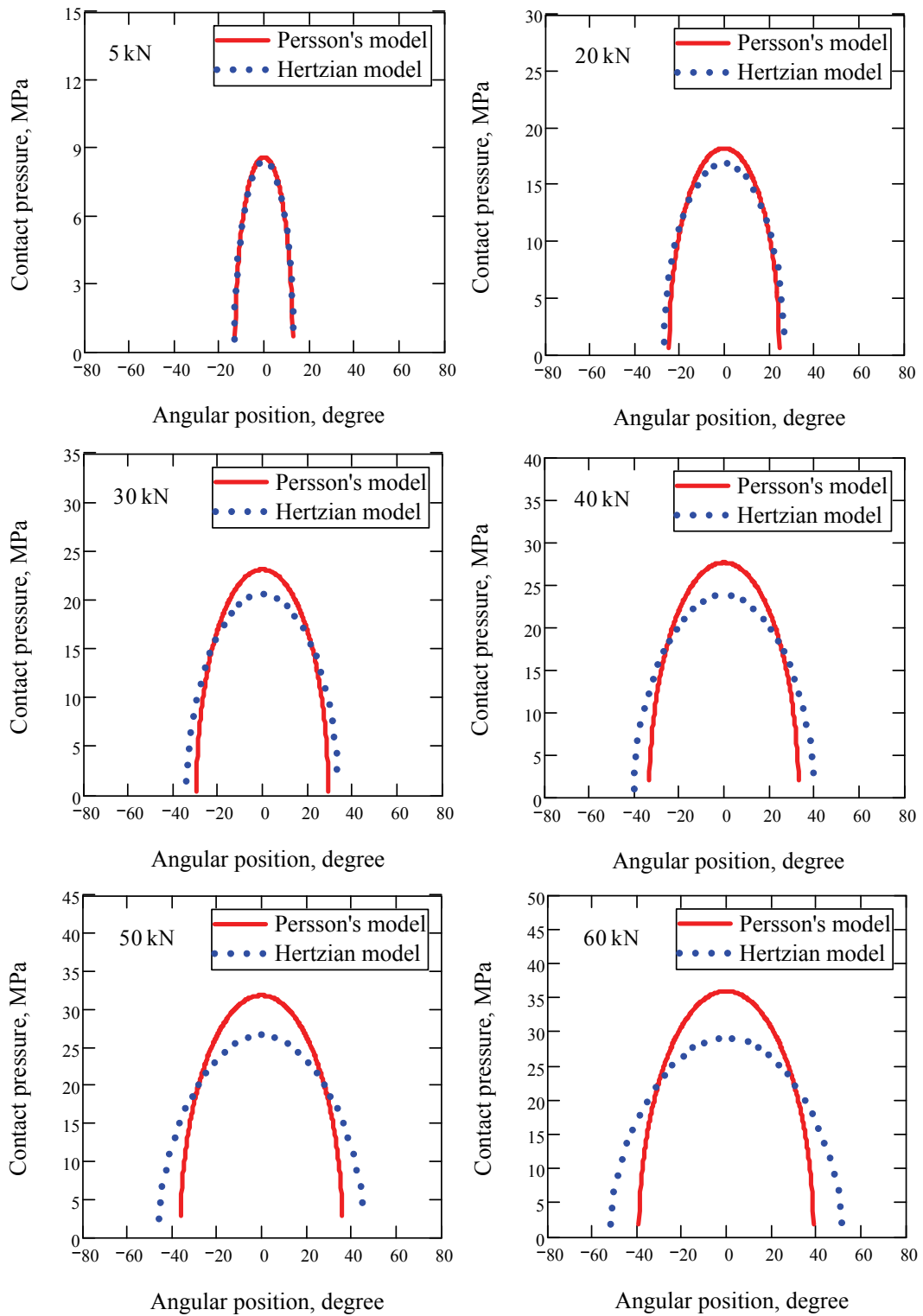


Figure 6.8. Comparison of pressure distribution between Persson's model and Hertzian model for varying normal loads 5 kN, 20 kN, 30 kN, 40 kN, 50 kN and 60 kN.

### 6.3.2 Contact Size

For cylindrical contact, the contact size is usually expressed by wrap angle,  $\alpha$ , shown in Figure 6.1. The amplitude of this angle depends on the radial clearance, normal applied load and material mechanical characteristics, which is known as load parameter,  $\frac{E_1^* \Delta R}{P'}$ .

The relationship between load parameter and contact angle is expressed as (Persson, 1964; Ciavarella and Decuzzi, 2001):

$$\frac{E_1^* \Delta R}{P'} = \frac{(\gamma - 1)(\ln(b^2 + 1) + 2b^4) + 2}{\pi(1 + \gamma)(b^2 + 1)b^2} \quad (6.13)$$

Where  $n^* = \frac{E_1^*}{E_2^*}$ ,  $\gamma = \frac{1 - n^*}{1 + n^*}$ ,  $E_i^* = \frac{E_i}{1 - \nu_i^2}$  ( $i = 1, 2$ , refer to contacting bodies respectively, in this study they refer to the pin and bush respectively).

Table 6.2 compares the half contact angle. It is evident that with lower load (higher load parameter  $\frac{E_1^* \Delta R}{P'}$ ), the angle difference from Hertz and Persson was as low as 0.1% for the same materials ( $n^* = \frac{E_1^*}{E_2^*} = 1$ ). At lower loads, the contacting size was small and there was no significant conformal contact, which could be treated as the case of Hertzian contact.

For pin joint studied here, the bronze bush and hard chromed steel pin give the material parameter,  $n^*$ , as 1.68. When the load range was 5-60kN, the load parameter  $\frac{E_1^* \Delta R}{P'}$  ranged from 66.1 to 5.5. Figure 6.9 compares the half contact angle for pin joint. It is clear that the difference of contact angle between two models was not significant at lower loads, but increases with load. The highest deviation of half wrap angle found in this study was within 15%.

Table 6.2. Half contact angle against load parameter  $\frac{E_1^* \Delta R}{P'}$  for varying materials.

			Half contact angle, $\alpha$ , degrees							
$\frac{E_1^* \Delta R}{P'}$			1	5	10	20	50	100	200	500
$n^* = \frac{E_1^*}{E_2^*}$	3	Hertz	129.3	57.8	40.9	28.9	18.3	12.9	9.1	5.8
		Persson	66.0	45.9	35.9	26.9	17.8	12.7	9.1	5.8
	2	Hertz	112.0	50.1	35.4	25.0	15.8	11.2	7.9	5.0
		Persson	64.2	41.9	32.1	23.8	15.5	11.1	7.9	5.0
	1	Hertz	91.4	40.9	28.9	20.4	12.9	9.1	6.5	4.1
		Persson	60.9	36.3	27.1	19.8	12.8	9.1	6.4	4.1
	1/2	Hertz	79.2	35.4	25.0	17.7	11.2	7.9	5.6	3.5
		Persson	58.1	32.5	23.9	17.3	11.1	7.9	5.6	3.5
	1/3	Hertz	74.7	33.4	23.6	16.7	10.6	7.5	5.3	3.3
		Persson	56.9	31.0	22.7	16.4	10.5	7.4	5.3	3.3

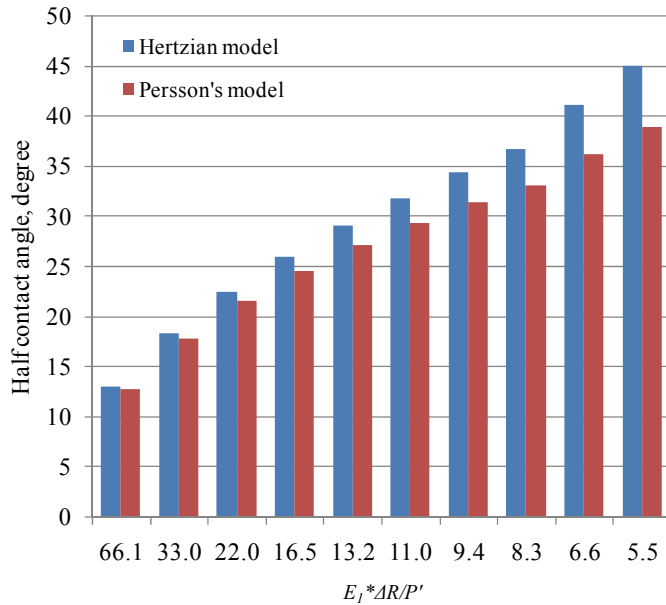


Figure 6.9. Comparison of half contact angle between Hertzian and Persson's model for the pin joint contact.

### 6.3.3 Nominal and True Frictional Torque in Pin Joint

Figure 6.10 (a) shows contact pressure distribution,  $p(\phi)$ , on a pin and bush contact under an applied load,  $P$ , over a half wrap angle,  $\alpha$ . The pressure,  $p(\phi)$ , acts normally to the surface at co-ordinate position,  $\phi$ . Thus, the infinitesimal force along the contact arc,  $d\phi$ , is expressed as:

$$dP = LR_p p(\phi) d\phi \quad (6.14)$$

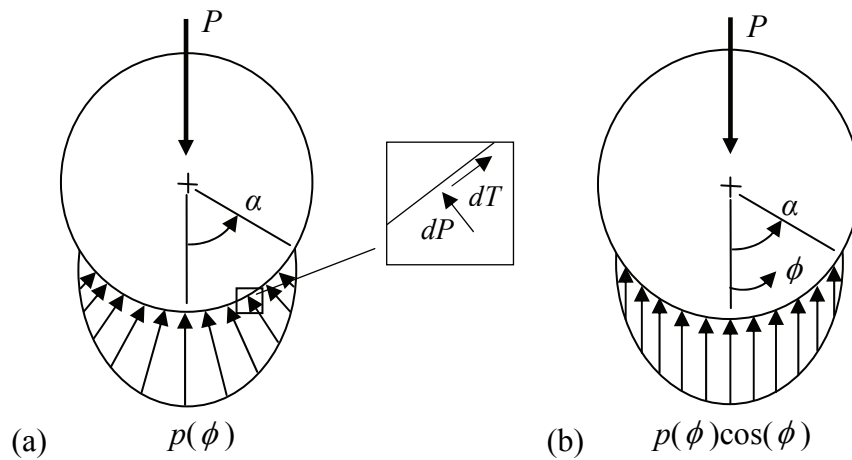


Figure 6.10. Pressure distribution on the pin, (a) illustration of pressure distribution, and (b) vertical component of pressure.

The application of a torque results in a traction distribution that is equal to the product of the pressure distribution and friction coefficient. Similarly, the infinitesimal torque is therefore given by:

$$dT = \mu LR_p^2 p(\phi) d\phi \quad (6.15)$$

If the pressure distribution is assumed to be constant along the axial direction, i.e. there are no edge effects caused by the bush, then:

$$T = \int_{-\alpha}^{\alpha} \mu p(\phi) LR_p^2 d\phi \quad (6.16)$$

Where  $\mu$  is the friction coefficient between pin and bush. Thus the friction torque can be calculated if the pressure distribution and friction coefficient are obtained. Or if the

torque can also be measured, the friction coefficient can be gained through:

$$\mu = \frac{T}{\int_{-\alpha}^{\alpha} p(\phi)LR_p^2 d\phi} \quad (6.17)$$

The component of the pressure that supports the applied load  $P$  is expressed as  $p(\phi)\cos(\phi)$  is shown in Figure 6.10 (b). Hence the formula for calculation of total normal load,  $P$ , is:

$$P = \int_{-\alpha}^{\alpha} p(\phi)\cos(\phi)LR_p d\phi \quad (6.18)$$

Traditionally, the simple method for calculating the torque on a body, called here the nominal torque  $T'$ , is to multiply the normal load by the friction coefficient with the half diameter.

$$T' = \mu PR_p \quad (6.19)$$

Substituting Equation (6.18) into Equation (6.19) gives,

$$T' = \int_{-\alpha}^{\alpha} \mu p(\phi)\cos\phi LR_p^2 d\phi \quad (6.20)$$

Defining a ratio of true torque,  $T$ , to nominal torque  $T'$  as  $T^* = T / T'$ . It can be seen from Figure 6.10 that there are antagonistic force components of the pressure distribution that do not support the normal force, hence, thus,  $T$  must always be greater than  $T'$ . The magnitude of the ratio,  $T^*$ , depends on the distribution of pressure wrap angle (Colbert *et al.*, 2010). Expressions of  $T$  and  $T'$  are given by equations (6.16) and (6.20). Thus  $T^*$  is as follows,

$$T^* = \frac{2 \int_{-\alpha}^{\alpha} \mu p(\phi)LR_p^2 d\phi}{2 \int_{-\alpha}^{\alpha} \mu p(\phi)\cos\phi LR_p^2 d\phi} = \frac{\int_{-\alpha}^{\alpha} p(\phi)d\phi}{\int_{-\alpha}^{\alpha} p(\phi)\cos\phi d\phi} \quad (6.21)$$

Figure 6.11 shows how the torque ratio,  $T^*$ , varies with the half wrap angle with the

assumption that the pressure over the interface, varies in a uniform and cosinusoidal way. Real torque on cylindrical contact interface was always higher than the nominal one. Its magnitude depended on the distribution of pressure, and therefore, the material properties and contact geometry (Colbert *et al.*, 2010). It became 1.57 times of nominal torque at  $\alpha = 90^\circ$  for uniform distribution at half wrap angle  $90^\circ$  and around 1.25 times for a cosinusoidal function of the pressure distribution.

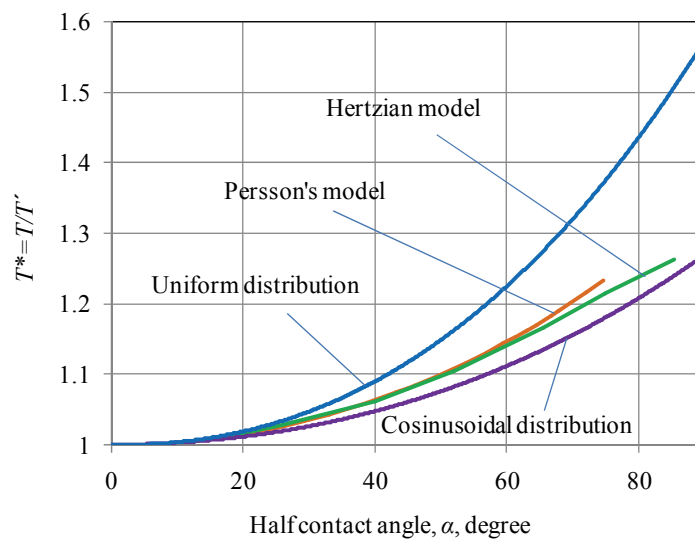


Figure 6.11. Torque ratios for different pressure distributions.

## 6.4 Comparison between Simulation and Experiment

### 6.4.1 Contact Pressure and Size

Table 6.3 shows the characteristics, dimensions of pin and bush contact. They were used in equations (6.7) and (6.12) for the determination of pressure distribution for pin joint by employing the Hertzian and Persson's model respectively. Figure 6.12 compares the theoretical simulation of pressure distribution with experiment results calculated from ultrasonic measurement.



Table 6.3. Characteristics and operating conditions of pin joint.

Parameter	Symbol	Value
Elastic modulus of pin	$E_p$	205 GPa
Elastic modulus of bush	$E_b$	117 GPa
Poisson's ratio of pin	$\nu_p$	0.28
Poisson's ratio of bush	$\nu_b$	0.34
Radius of pin	$R_p$	28 mm
Radius of bush	$R_b$	28.025 mm
Length of bush	$L$	59.4 mm
Total normal load	$P_t$	5,10,20,40 kN
Radial clearance	$\Delta R$	25 $\mu m$

From Figure 6.12 (a), it can be seen that Persson's model predicts a 'narrow' and 'high' pressure distribution compared to experimental results. For all loads, the peak pressures from Persson's model were higher than experimental values, especially under lower loads. Figure 6.12 (b) is the comparison between Hertzian model and experiment. Compared to Figure 6.12 (a), the Hertzian theory shows a better agreement to experimental measurements, especially under 40 N and 60 N.

However, even though the predicted contact size increased with normal load, both models predicted smaller half wrap angles than the experiment for all load cases. This may be because the predictions were based on a perfect smooth surface and standard surface geometry. The effect from the real rough engineering surface of pin and bush on contact parameters, such as pressure distribution and contact size, was ignored even though in the microscopic view the actual contact took place on these rough asperities distributed randomly on the surfaces. In addition, the constant contact angle from experiment implied some errors must exist during measurement as it was well known that contact size is mainly dependent on applied load. Despite this inaccuracy, it can be concluded that Hertzian theory was better in predicting contact pressure distribution and contact size, especially for heavier loads.

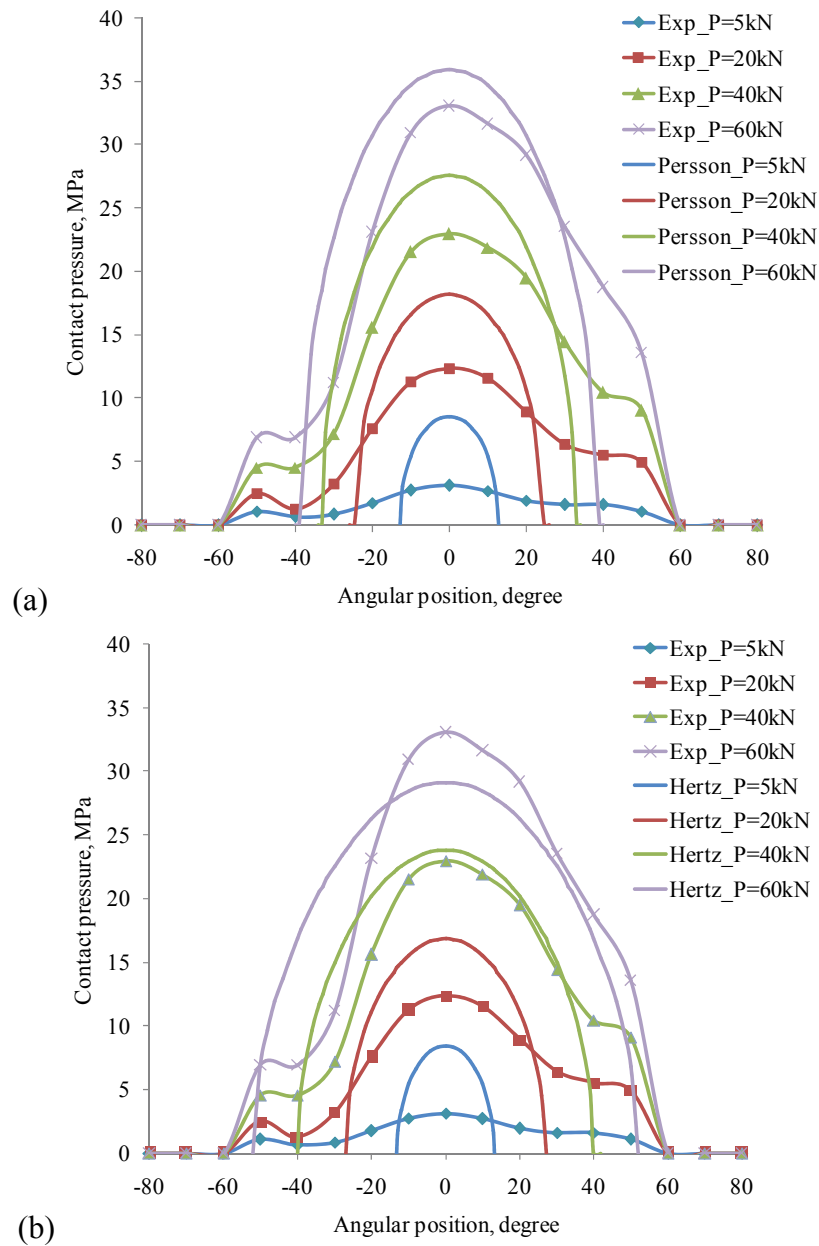


Figure 6.12. Comparison of experimental contact pressure distribution with, (a) Persson's model, and (b) Hertzian model.

In both cases the rapid reduction in pressure at the contact edges was observed for simulation results. This is because the models are for smooth surfaces. The experimental surfaces are rough and this would have tendency for spread of the load out slightly beyond the nominal contact area (Johnson, 1985), shown in Figure 6.13. This phenomenon is also shown in Figure 3.3.

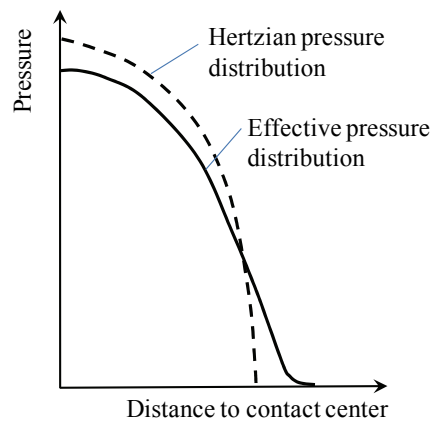


Figure 6.13. Contact pressure of a smooth elastic sphere with a nominally flat randomly rough surface.

Figure 6.14 shows the peak pressure under varying loads by these two models compared to experiment. From the theoretical simulations, it is clear that the deviation between them increased with the load. Persson’s model gave a sharper incremental curve. At the highest simulated load, 200N, peak pressure from Persson’s model was almost twice as high as Hertzian. The peak pressures from experiment, represented by data markers show good agreement to the prediction. Both models could be used for predicting peak pressure for practical application of pin joint design.

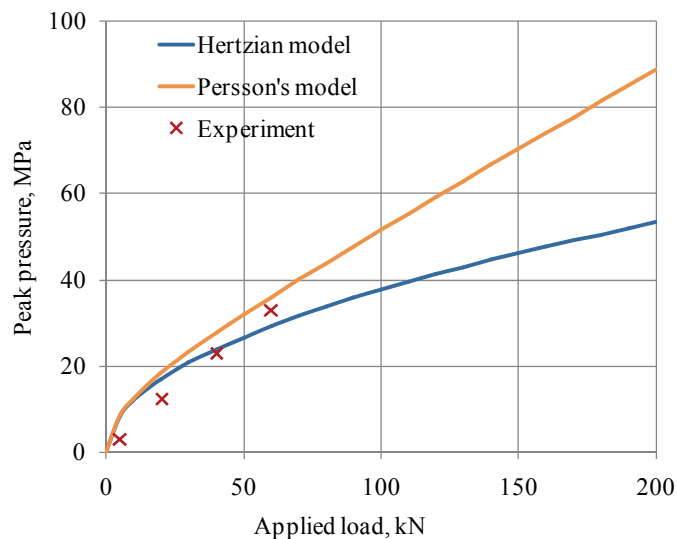


Figure 6.14. Peak pressure comparison among Hertzian model, Persson’s model and experiment.

## 6.4.2 Frictional Torque

From Chapter 5, it is known that the landing gear pin joint operates in the boundary

lubrication regime. The friction coefficient has been found in the range of 0.1-0.13 (Figure 5.16). The value of 0.12 was used for calculation of the friction torque from obtained pressure distribution shown by Figure 6.6 by applying Equation (6.16). Compare with Figure 5.18 (b), a good agreement of torque can be found. The consistency shows that in choosing the ‘dry’ friction coefficient for theoretical modelling, the value of 0.12 is reasonable. Figure 6.15 shows the calculated friction torques against normal applied load for Hertzian model, Persson’s model and the experiment data. The experimental torque showed a good agreement with theoretical simulations.

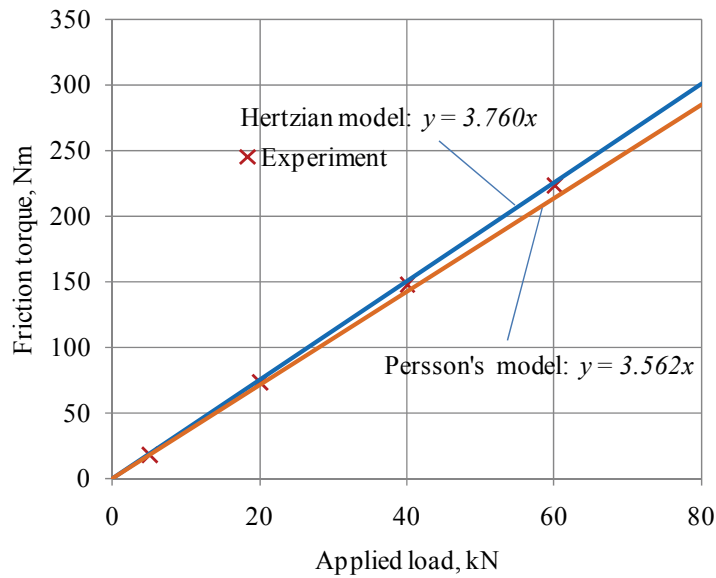


Figure 6.15. Friction torque varying with normal applied load.

Traditionally the friction torque was calculated from (Equation (6.19)):

$$T' = \mu PR_p \quad (6.22)$$

Therefore for the pin and bush contact, if the friction coefficient  $\mu$  is treated as 0.12, and the diameter of the pin is  $R_p = 28$  mm, the friction torque is then expressed as:

$$T' = 3.36P \quad (6.23)$$

Compared to calibrated equations in Figure 6.15, the traditional approach gives the smallest torque for the same load. Again, this was because on the pin and bush contact interface, the contribution of the tangential component of the pressure to the total friction

torque was neglected, which is shown in Figure 6.10. Normally, the torque obtained from Equation (6.23) is known as nominal friction torque.

The differences between nominal and true friction torque is now considered for the experiment data. From the pressure distribution calculated from ultrasonic reflection presented in section 6.2.2 and shown by Figure 6.6, the integration of  $\int_{-\alpha}^{\alpha} p(\phi)d\phi$  and

$\int_{-\alpha}^{\alpha} p(\phi)\cos\phi d\phi$  can then be obtained from calculated pressure separately. Table 6.4 shows the integration values for each load case and the ratio of true torque to nominal torque (Equation (6.21)).

Table 6.4. Ratio of true torque to nominal torque.

Load, kN	5	20	40	60
$\int_{-\alpha}^{\alpha} p(\phi)d\phi$	$1.92\times 10^7$	$7.57\times 10^7$	$1.52\times 10^8$	$2.29\times 10^8$
$\int_{-\alpha}^{\alpha} p(\phi)\cos\phi d\phi$	$1.72\times 10^7$	$6.88\times 10^7$	$1.38\times 10^8$	$2.07\times 10^8$
$T^*$	1.11	1.10	1.10	1.11

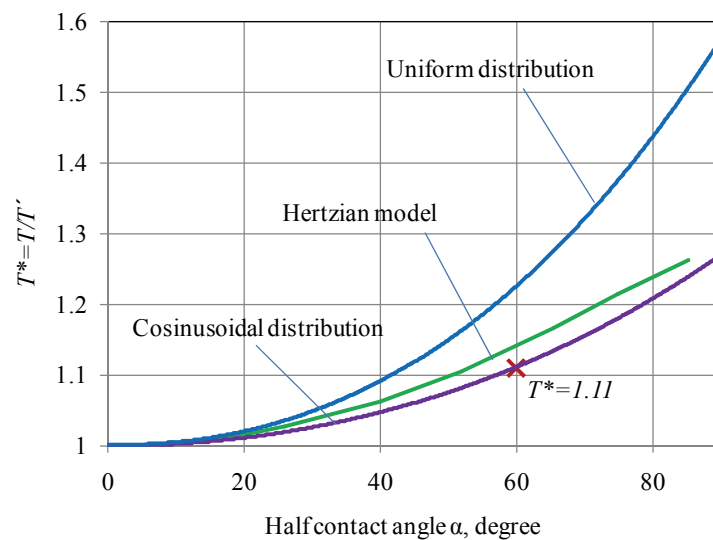


Figure 6.16. Torque ratios for uniform, cosinusoidal and Hertzian pressure distributions.

The values of  $T^*$  shown in Table 6.4 are stable and correlate with the case of

cosinusoidal pressure distribution, as indicated in Figure 6.16. The experimental pressure was proven to be close to the consinusoidal distribution.

### 6.4.3 Estimation of Friction Coefficient

The torque measurement obtained in Chapter 5 was used for the estimation of the real friction coefficient by dividing the measured torque by the ratio  $T^*$ :

$$T' = \frac{T}{T^*} = \mu PR_p \quad (6.24)$$

Thus the difference,  $\sigma_T$ , between the nominal torque,  $T'$ , and the real torque,  $T$ , is:

$$\sigma_T = T \left(1 - \frac{1}{T^*}\right) \quad (6.25)$$

The real friction coefficient in the contact is expressed as:

$$\mu = \frac{T}{T^* PR_p} \quad (6.26)$$

Similarly, the difference for friction coefficient is:

$$\sigma_\mu = \frac{T}{PR_p} \left(1 - \frac{1}{T^*}\right) \quad (6.27)$$

From the previous section, the torque ratio of 0.11 is used for the calculation of friction coefficient, torque difference and coefficient difference. The results for friction coefficient are given in Table 6.5 and Figure 6.17. The bar chart shows the friction coefficient,  $\mu$ , to the normal applied load,  $P$ . Friction coefficients varied from 0.1 to 0.114 on the pin joint as the load was increased. This indicated that the joint operates in a boundary lubrication regime. Both friction coefficient and torque were found to slightly increase with the load, but the friction coefficient deviation was shown to be independent of the load, shown in Figure 6.17.

Table 6.5. Measured torque, friction coefficient and deviation.

Load, $kN$	5	10	15	20	25	30	35	40
$T, Nm$	15.4	32.1	48.4	65.4	84	100.2	120.8	141.3
$\sigma_T, Nm$	1.5	3.2	4.8	6.5	8.3	9.9	12.0	14.0
$\mu$	0.099	0.103	0.104	0.105	0.108	0.107	0.111	0.114
$\sigma_\mu$	0.011	0.011	0.011	0.012	0.012	0.012	0.012	0.013

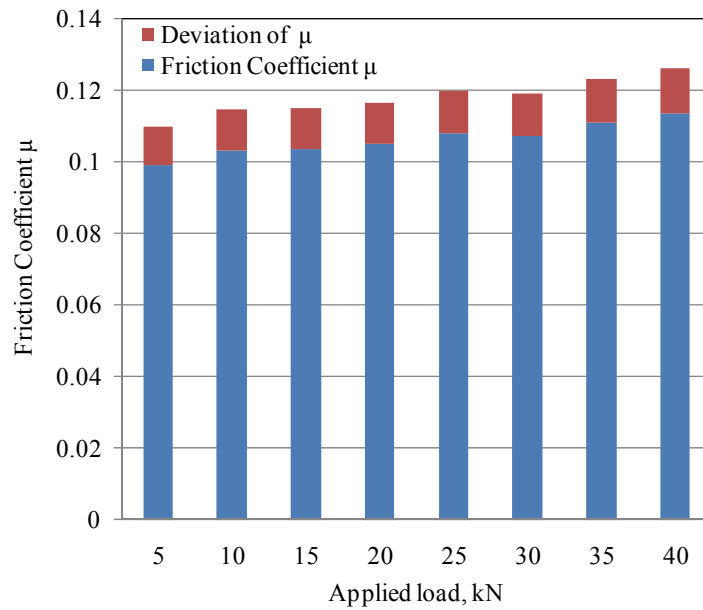


Figure 6.17. Friction coefficient and deviation varying with load.

## 6.5 Conclusions

Ultrasonic reflection coefficient data for a pin and bush contact has been analysed. The contact stiffness of the interface was calculated and then used for the determination of contact pressure distribution for a range of normal applied loads. The distribution was found to be close to a cosine function. In this way, the ultrasonic method was shown to be an effective method to analyse the radial contact pressure and contact size for pin joint contact.

Contact pressure distribution, half wrap angle and friction torque/coefficient of pin joint

were predicted using Hertzian theory and Persson's conformal contact model. Both models predict higher peak pressure and smaller contact size compared to the experimental results. The simulation torque was found to agree well with the experiment. By comparing the two models with the ultrasonic measurements, Hertzian theory was shown to be more accurate in determining the real contact pressure.

The torque used to rotate a pin is commonly calculated from  $\mu PD/2$ . This, however, underestimates the actual torque requirement because it neglects the tangential components of pressure that do not support normal load, but contribute to friction. The true torque can only be determined if the pressure distribution is known. In this study, the required torque during pin joint articulation was recorded, from which the ratio of true to nominal torque was found to be  $1.1 \pm 0.01$ .

The friction coefficient of pin joint contact was obtained from this torque data incorporating the ratio  $T^*$  determined from the measured pressure distribution. It was found to vary from 0.1 to 0.114 on the pin joint as the load increased. This indicates that the joint operates in a boundary lubrication regime.

From Chapter 3-6, the normal contact mechanics of engineering interfaces haven been investigated. Both theoretical model and experiments were carried out for the interfacial properties, including the normal pressure distribution, the contact size and the normal contact stiffness. In the next Chapter, how the micro-contact junctions deform along the tangential direction will be studied using the ultrasonic technique based on Perspex-Perspex and steel-steel contacts.



# Chapter 7 Shear Study on a Sliding Contact

In this chapter, the ultrasonic reflection coefficient of a shear wave from Perspex-Perspex and steel-steel interfaces has been measured under a range of nominal pressures, from which the interfacial shear stiffness was calculated by the spring model presented in Chapter 4. Firstly, the frequency-dependent reflection coefficient and hysteresis phenomenon of the interface were analysed. The second part was an ultrasonic and frictional study on the stick-slip process. The variation of reflection coefficient for a range of nominal pressures and sliding speeds has been recorded to study the evolution of interfacial shear stiffness. Finally, based on the elasto-plastic deformation theory of rough surface asperities, a formula relating shear stiffness and real contact area has been developed and used for prediction of real contact area. The real contact area variation in hysteresis cycles and the area evolution during the stick-slip process were investigated.

## 7.1 Introduction

Mechanical contact between solids generally consists of ‘rough’ surfaces, even though the surfaces are macroscopically considered to be ideally flat. The contact is taking place on these randomly distributed rough asperities. Interaction of asperities determines characteristics of the interface, such as the real contact area, shear property and material deformability. The deformability of a material is usually expressed as stiffness. Depending on the direction of the load, normal or tangential to the contact, the stiffness is characterised into normal stiffness and shear stiffness.

Shear stiffness is defined as the amount of shear stress per unit displacement required to deflect an elastic contact in tangential direction, with the unit of Pa/m.

$$K_s = dq / dx \quad (7.1)$$

Where  $q$  is shear stress, and  $x$  is the elastic tangential deformation.

As the characteristics of an interface are determined by properties of rough asperities on mating surfaces. The interfacial properties can be determined through studying the asperity interaction. This provides a method to analyse interfacial stiffness from microscopic interaction. Savkooor (1987) and Baumberger (1997) have studied microscopic interactions between asperities for plastic creep and adhesive friction individually. Therefore, based on the GW model, the interfacial shear stiffness can be calculated using the number of contact spots,  $N$ , and mean junction size,  $\langle a \rangle$ . The following expression for the interfacial shear stiffness was given as (Johnson, 1985):

$$K_s' \cong GN \langle a \rangle \quad (7.2)$$

Where  $G$  is the shear strength, the sign  $\cong$  stands for equality within a multiplicative geometry-dependent constant,  $K_s'$  has a unit of N/m, and the nominal contact area should be introduced if the stiffness is expressed per unit area (units of Pa/m).

The spring model described in Chapter 4 holds for the shear waves as well as longitudinal waves. So, the relation between the reflection coefficient,  $R$  and the stiffness of interface,  $K$  is:

$$R = \frac{z_1 - z_2 + i\omega(z_1 z_2 / K_s)}{z_1 + z_2 + i\omega(z_1 z_2 / K_s)} \quad (7.3)$$

where  $z_1$  and  $z_2$  refer to the acoustic impedance of the materials either side of the interface and  $\omega$  is the angular frequency ( $\omega=2\pi f$ ). For identical materials in contact ( $z_1=z_2=z'$ ) this equation reduces to:

$$|R| = \frac{1}{\sqrt{1 + (K_s / \pi f z')^2}} \quad (7.4)$$

In the above two equations, the shear stiffness  $K_s$  denotes the amount of nominal shear stress per unit displacement, has the unit of Pa/m.

Take Perspex for example, acoustic impedance is  $1629580 \text{ kg}/(\text{s}\times\text{m}^2)$  (1.63 MRayls). Figure 7.1 shows how reflection coefficient varies with frequency for certain shear stiffness,  $K_s$ . It was indicated that higher stiffness gives lower reflection coefficient, which means more ultrasound waves have transmitted through the bonded material.

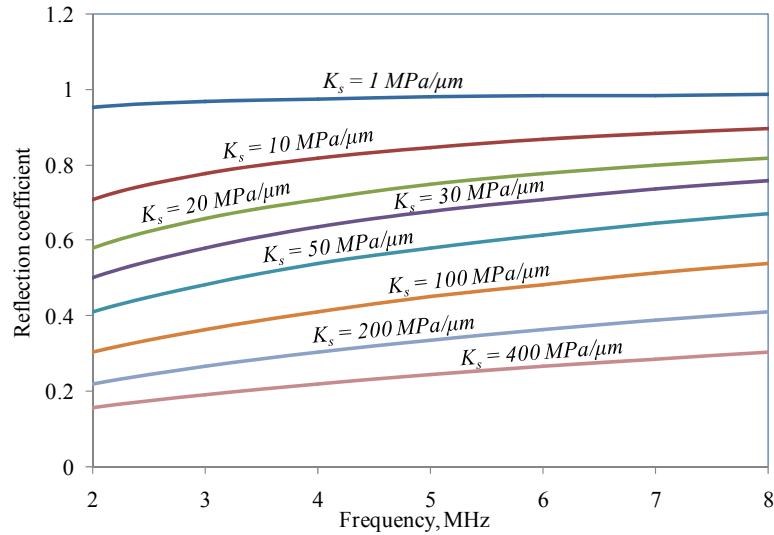


Figure 7.1. Reflection coefficient against frequency with varying shear stiffness.

Figure 7.2 shows a plot of shear wave reflection coefficient amplitude verses frequency for a sample pulse reflected from a dry sliding Perspex-Perspex contact under a pressure of 1.94 MPa (at a load of 98 N). Also shown was the amplitude spectrum fast Fourier transform (FFT) of the reflected signal and reference signal. Inspection of the amplitude spectrum shows the extent of the attenuation which has effectively reduced the centre frequency of the transducer from 5 MHz to 3.5 MHz. The reflection coefficient spectrum has been converted into the predicted shear stiffness using the spring model Equation (7.3). The shear stiffness calculated from ultrasonic reflection is also shown in Figure 7.2. Due to the fact that the interfacial shear stiffness is not varying with the measurement frequency for a certain interface, and only data in the 3 to 4 MHz region was independent of frequency, the data in this region known as measurable region will be chosen for further analysis in this study. In this region the reflection coefficient was close to being constant regardless of the measurement frequency selected. Interfacial shear stiffness can then be calculated from the measured reflection coefficient by the spring model Equation (7.3).

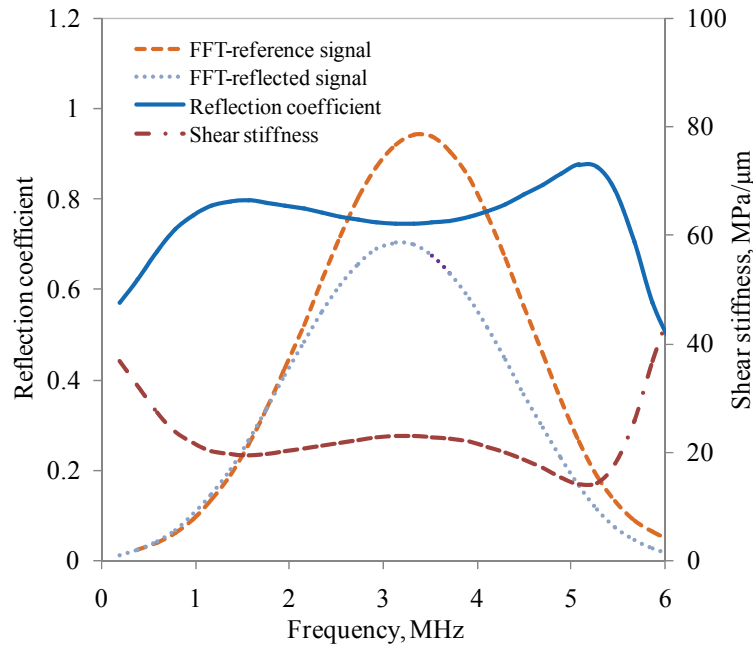


Figure 7.2. Reflection coefficient and shear stiffness plotted against ultrasonic frequency (in order to be shown on the same plot, the transducer output spectrum is plotted in arbitrary units).

In this chapter, the shear stiffness of steel-steel and Perspex-Perspex contacts were studied using the ultrasonic method. A 5 MHz shear transducer was mounted above the contact to record the reflection of ultrasound waves through the sliding process, including the threshold from static contact to kinetic sliding. Then the reflection coefficient,  $R$ , was obtained by comparing the reflection signal to the reference reflection signal. Applying the spring model, equation (7.3), the interfacial shear stiffness can then be calculated. A further analysis of the real contact area for both stationary contact and stick-slip process was processed using the shear stiffness. Simultaneously, during the sliding process, a load cell was used to record the friction force on the interface. Together with ultrasonic results, these friction measurements were then used to discern the point of transformation from static contact to kinetic movement.

## 7.2 Experimental Details

### 7.2.1 Specimen Preparation

The sliding contact interface in this study was composed of two nominally flat specimens,

shown in Figure 7.3. The top specimen was made of a cylindrical bar with a smaller cylindrical section extrusion machined at the end, which acted as one of the contacting surfaces. Its end surface was in contact with the plate made from the same material, which acted as the lower specimen. The lower plate was mounted to a guide track driven by a motor. The upper specimen, together with the ultrasonic transducer, was held in a housing, shown as the dashed square. The housing was mounted onto a two-arm cantilever, which enabled a weight application. The housing was stationary while the lower specimen was moving with the guide. This configuration made the sliding contact in the study. A photo with more details was shown in next section.

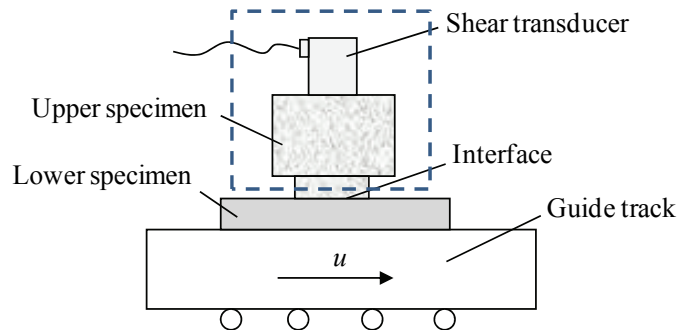


Figure 7.3. A sketch of the configuration of contact.

Perspex and steel were chosen as specimens, which represent two wide classes of materials, very different in their properties. Four sized Perspex specimens were prepared with end cylinder diameters of 5mm, 8mm, 12mm and 25mm. The contact surfaces were all ground except the lower plate, which remains in the original polished surface condition. Three EN24 steel specimens, 5mm, 8mm and 12mm diameter, were prepared for comparison with Perspex as they also have an excellent shear transmission property. However, as the steel has greater elastic modulus, much higher load was needed to get the same amount of surface approach as Perspex. In this test, due to the limitation of the loading condition, a dead weight load was applied. This restricts higher loads to be applied onto the interface. Furthermore, the steel specimens are more sensitive to alignment due to their high modulus. As a consequence, most of the ultrasonic reflection measurements for metal interface were much higher compared to Perspex specimens. Figure 7.4 shows the photo of specimens used in this study.

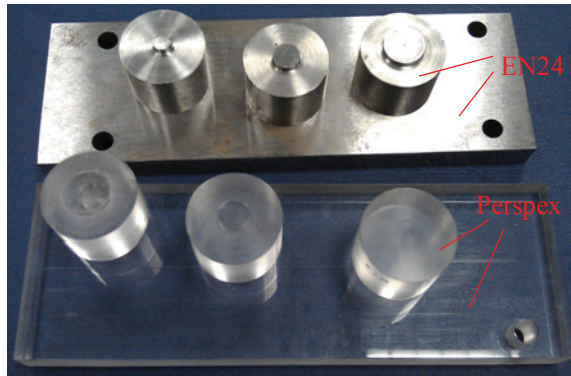


Figure 7.4. Photo of specimens used in the ultrasonic study.

Table 7.1 shows surfaces roughness,  $R_a$ , for tested specimens. Roughness measurements were carried out three times with different locations using a stylus profilometer (Model SV-602). Mean values of each measurement was used for further analysis.

Table 7.1. Surface roughness of specimens used in this study.

	Surface roughness, $R_a$ , $\mu m$				
	Upper specimen				Lower specimen
	$\phi 5mm$	$\phi 8mm$	$\phi 12mm$	$\phi 25mm$	
Perspex	1.01	0.57	0.44	0.63	0.05
Steel	3.85	2.54	2.06	--	0.69

Table 7.2. Mechanical and ultrasonic properties of specimens.

Property	Perspex	EN24 Steel
Young's modulus, $E$ , $GPa$	3.3	210
Hardness, $H$ , $GPa$	0.4	2
Yield stress, $\sigma_Y$ , $MPa$	84	472
Poisson's ratio, $\nu$	0.39	0.29
Shear modulus, $G$ , $GPa$	1.19	81.4
Density, $\rho$ , $kg/m^3$	1180	7850
Shear wave speed, $c$ , $m/s$	1381	3240

Table 7.2 shows mechanical properties of specimens. The material properties can vary with the manufacturing process, as well as test methods. Material properties quoted were based on common knowledge. Values in Table 7.2 were used in this study. The shear wave speeds in Perspex and steel were measured from ultrasonic reflection. According to the ultrasound travelling time and distance (thickness of specimen), so the wave speed equals to the distance divided by the travelling time.

### **7.2.2 Sliding Test Rig**

Figure 7.5 (a) and (b) show a sketch and photo of the sliding test rig. Basically, the test rig was composed of a two-arm cantilever, a load cell holder, and a sliding track driven by a motor. The free rotating lever was used for holding the upper specimen and applying a dead load at the end. A lower specimen was fixed onto the track and be driven with a certain speed. When the sliding was taking place between two specimen surfaces, the lever was dragged to touch the load cell. Therefore, the shear force on the interface was recorded.

In this test, a housing was designed to fix the shear sensor and hold the upper specimen, shown by Figure 7.5 (c). In the middle of the housing, a steel bar was mounted to two shafts using two small linear bearings. Two springs were used to balance the bar within the housing. At the early stage of sliding, they deformed and absorbed the interfacial shear force. So the upper specimen sticks on the lower one for a short while until the deformation limit of the spring was reached. Then the resilience energy releases and the interface undergo a slip movement. This process repeats so the stick-slip process was obtained for this study. A hole in the bar was machined for holding the ultrasonic sensor and the upper specimen. In this hole, the upper specimen was sitting on the sensor. In order to make a full face contact between the sensor and the end of the specimen, a small spring was added underneath of the sensor, shown in Figure 7.5 (c).

The housing was turned upside down and mounted to a two-arm cantilever through a pin. The cantilever was free to rotate along a vertical bar fixed on the foundation base. Next to it, a load cell was located on a fixed steel holder for recording the force from the rotating cantilever. The two-arm cantilever has freedom in the vertical and horizontal planes,

which makes possible to adjust the position of the specimen and measure the friction force from the interface. At the right end of the lever, dead weights were applied manually. The normal load applied on the interface in this study was up to 410 N, which makes a maximum nominal contact pressure of 104.5 MPa. The lower specimen (plate) was fixed to a guide track connected to a belt drive via a ball screw. The speed of the guide was in the range of 0-4.5 mm/s.

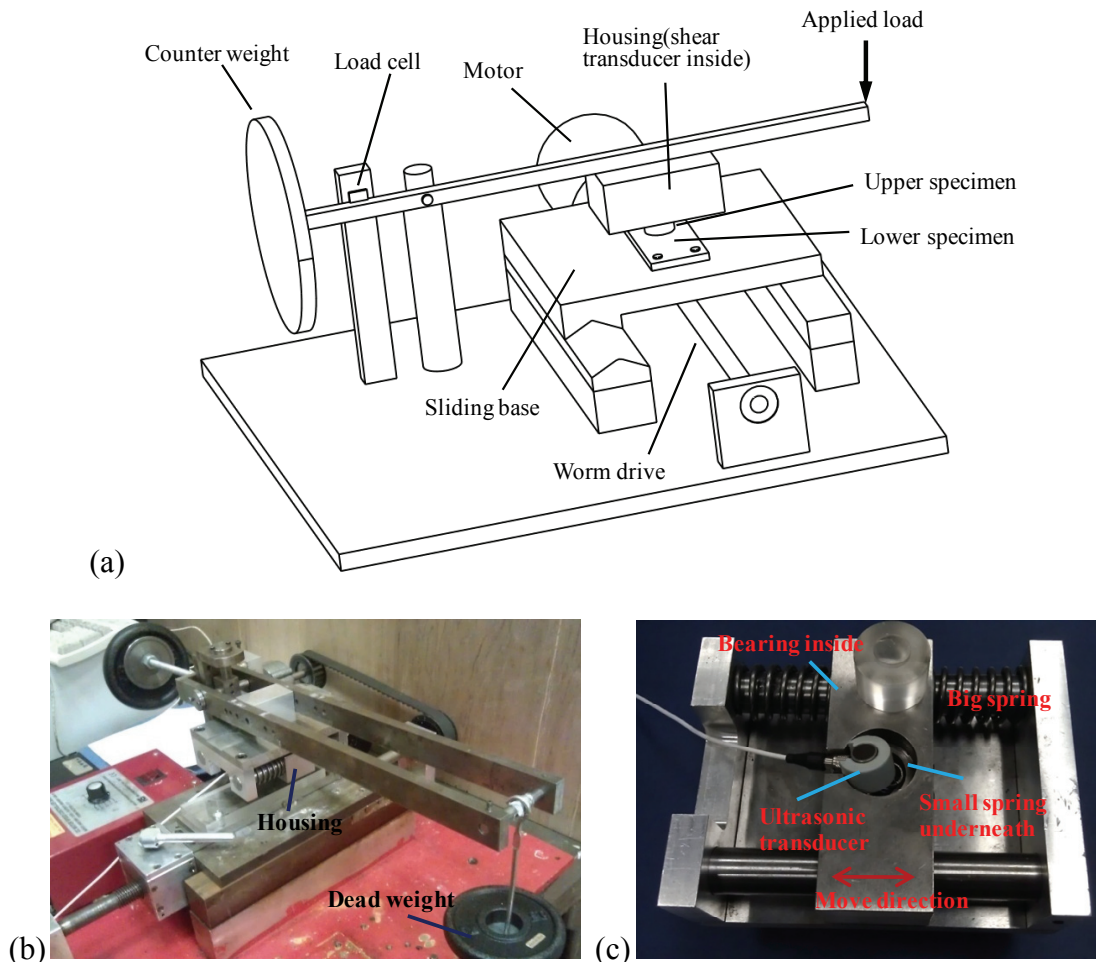


Figure 7.5. (a) sketch of test rig, (b) photo of sliding test rig, and (c) the housing for holding upper specimen and transducer.

### 7.2.3 Ultrasonic Apparatus and Data Processing

An ultrasonic unit consists of an ultrasonic-pulse receiver (UPR), a digital oscilloscope, a PC and ultrasound transducers. Figure 7.6 shows a sketch of the layout. The UPR generates a series of short duration voltage pulses that excite the piezoelectric transducer



causing it to resonate, thus sending the required ultrasonic pulse through the medium. A bespoke centre frequency 5 MHz piezoelectric shear transducer was commissioned (from NDT Systems Ltd) for this test case. The transducer was actuated by the UPR, which was controlled by a PC. The transducer operates in pulse-echo mode and so receives reflections back from the interface. Reflected pulses were stored on a digital oscilloscope and passed to a PC for data processing and analysis.

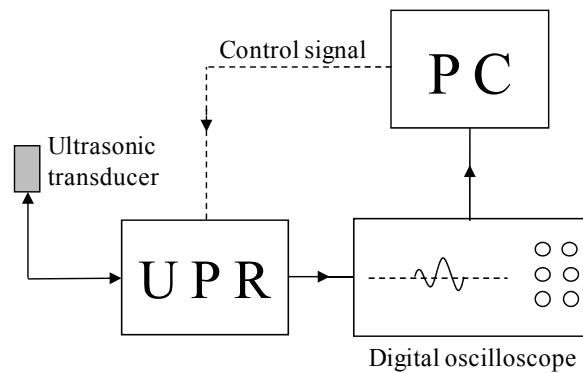


Figure 7.6. Sketch of ultrasonic unit used in this study.

The driver software was written in the software program LabView, which controls the sending and receiving of pulses, downloads reflected pulse waveforms, and performs the required signal processing. The ultrasonic reflection was recorded during sliding contact. This was then used for further analysis for the interface stiffness, contact pressure and the real contact area.

## 7.3 Ultrasonic Measurement

Ultrasonic measurements were carried out for both static and dynamic contacts. The spring model, equation (7.3), was then used for calculation of the shear contact stiffness. During the process of stick and slip, friction force was recorded. This allows real contact area, reflection coefficient, and shear stiffness variation to be analysed over the entire movement.

### 7.3.1 Reflection Dependence on Frequency

In early studies (Królikowski and Szczepek, 1993; Berthoud and Baumberger, 1998; Kim *et al.*, 2004), it has been proven to be difficult to measure the frequency dependence

of reflections as the studies were carried out using single frequency transducers. Aligning the contacting surfaces has also proved to be difficult (Drinkwater *et al.*, 1996). In this study, a 5MHz wide band shear transducer has been used which makes measuring frequency dependence possible.

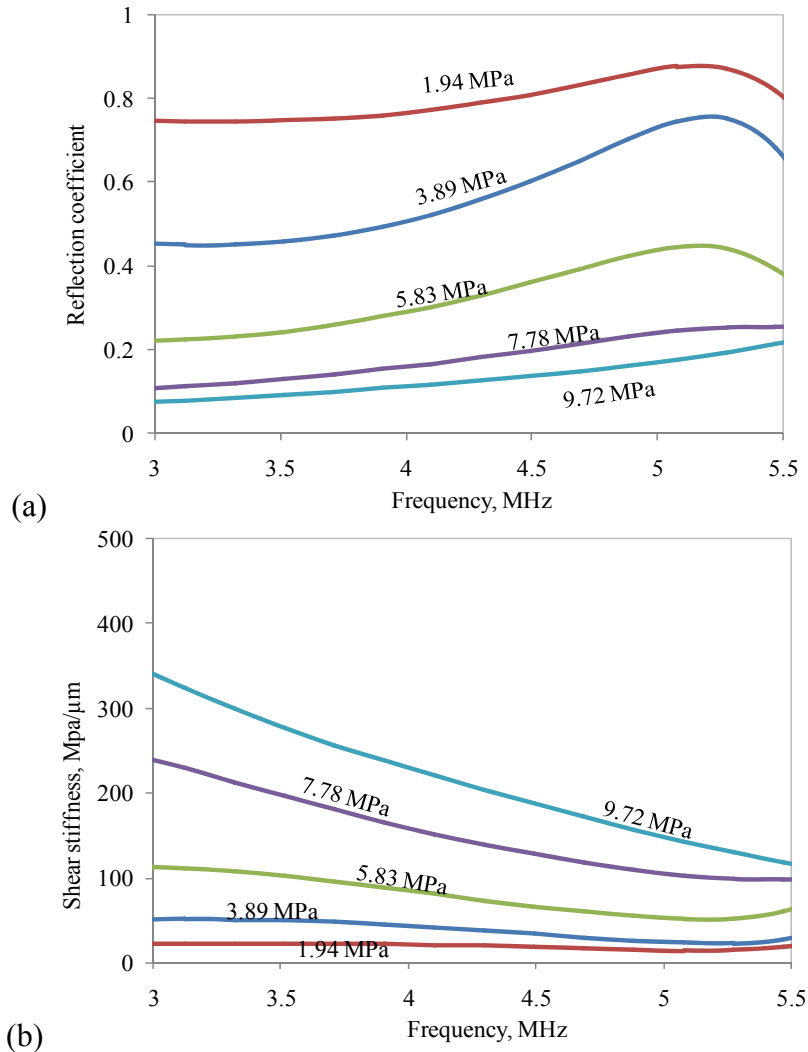


Figure 7.7. Ultrasonic reflection and shear stiffness varying with frequency for a range of nominal pressures for static Perspex-Perspex contact, (a) measured reflection coefficient, and (b) calculated shear stiffness from ultrasonic reflection.

Figure 7.7 (a) shows ultrasonic reflection coefficient varying with frequency over a range of nominal pressures for static Perspex-Perspex contact. The dependence of reflection coefficient on frequency can be seen clearly from the plot, especially for higher pressures (5-10MPa), where the reflection coefficient increases with frequency. Higher pressures causes well bonded interfaces, so more ultrasound waves transmitted through the material

into the second contacting body. The resulted reflection coefficient was therefore smaller compared to lower loads. Under pressure of 9.72 MPa, the reflection coefficient was found in the range of 0.05-0.14. With increasing pressure, it decreases to 0.05, rather than zero, which would be expected for the complete conformity.

The measured frequency dependence was then used for calculation of interfacial shear stiffness by using the spring model, Equation (7.3). Figure 7.7 (b) shows the obtained shear stiffness varying with frequency for a number of normal pressures. From Figure 7.7 (b), it can be seen that the shear stiffness shows independent from the frequency in the range of 3-4 MHz under lower loads. This agrees with Figure 7.2. Therefore, the stiffness in this region was used in this study. It should be noted that the stiffness was found to decrease with frequency under higher loads, 7.78 MPa and 9.72 MPa where the reflection coefficient varied from 0.07-0.25. Under higher loads, the interface is well bonded, reflected signals are too weak to characterise properties of the interface. In the application of ultrasonic film thickness measurement, a measurement zone was suggested by Gasni *et al.*, (2011) considering the measurement accuracy.

Figure 7.8 (a) shows the measured steel-steel reflection coefficient variation with frequency under a range of nominal pressures. Interfacial shear stiffness calculated from the reflection measurement is shown by Figure 7.8 (b). It is apparent that higher pressures resulted in greater shear stiffness. It can also be seen that in the frequency range of 3.5-5.5 MHz, the shear stiffness shows independence to frequency under all pressure cases. Therefore in the study, this frequency range was used for steel specimens. It has been suggested that a proper frequency range should be chosen in order to obtain useful information about a given contact (Drinkwater *et al.*, 1996). In studying a given contact using the ultrasonic method, attention must be drawn to the fact that if the frequency is too high, the reflected coefficient will be unity. This will result in the invalidation of the spring model. No information can be measured through ultrasonic method for the contact. The interface could be considered “too loose” to allow any ultrasound to transmit to the second body. Conversely, if the stiffness is too high as the interface is perfectly bonded together, all the ultrasound waves will pass through the interface and no reflection is obtained.

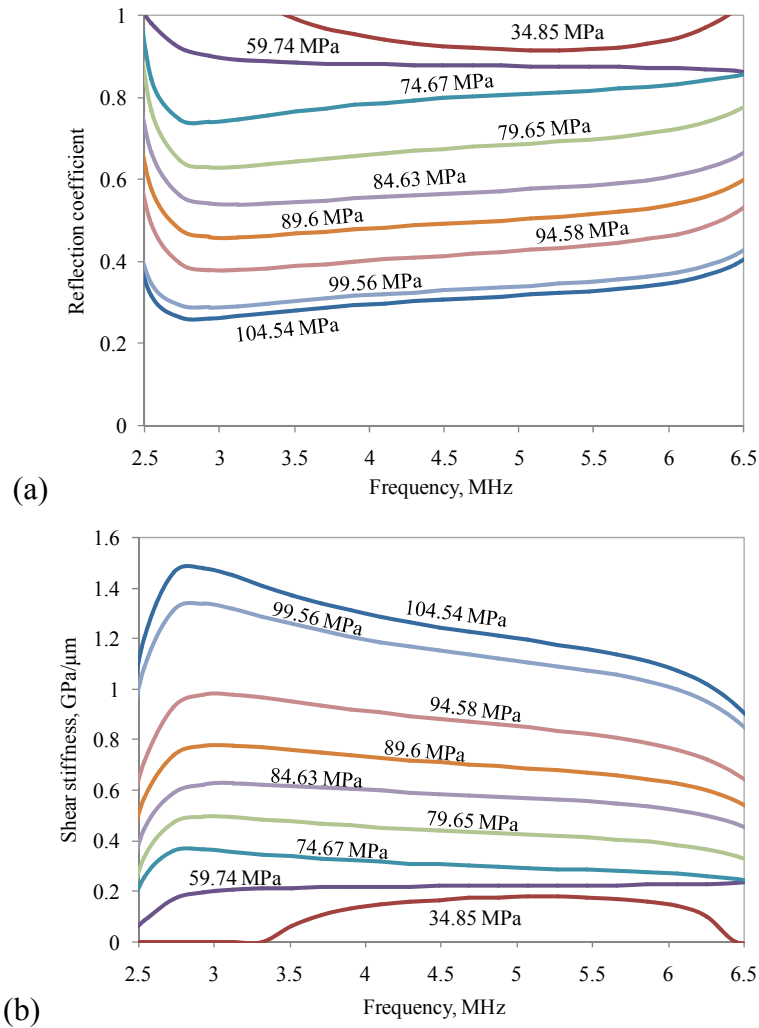


Figure 7.8. Ultrasonic reflection and shear stiffness varying with frequency for a range of nominal pressures for static steel-steel contact, (a) measured reflection coefficient, and (b) shear stiffness calculated from ultrasonic reflection.

### 7.3.2 Loading/Unloading Cycles

The shear ultrasonic response from a loading/unloading interface has been studied. Figure 7.9 (a) shows reflection coefficient measurement for two cycles of loading/unloading. Reflection coefficient decreases from unity as the pressure increased. It was found to increase and recover to the initial value as the pressure was gradually removed. The interfacial shear stiffness calculated from reflection measurement, Figure 7.9 (a), using spring model, Equation (7.3), was plotted against nominal normal pressure, shown by Figure 7.9 (b).

Looking at the single loading/unloading process, either 1<sup>st</sup> or 2<sup>nd</sup> cycle in Figure 7.9,

hysteresis behavior was exhibited as the reflection coefficient was lower in the unloading process than the loading at the same contact pressure. The different paths of loading and unloading cycle were caused by elasto-plastic deformation of asperities on the interface. From Figure 7.9 (a) it can be seen that the unloading lines show a similar path, but lower reflection coefficient, than loading ones. Hysteresis evolution presented by reflection coefficient was then displayed on the shear stiffness plot, shown by Figure 7.9 (b). Hysteresis loop was also studied by Konowalski (2009) through recording displacement of interface with varying pressure.

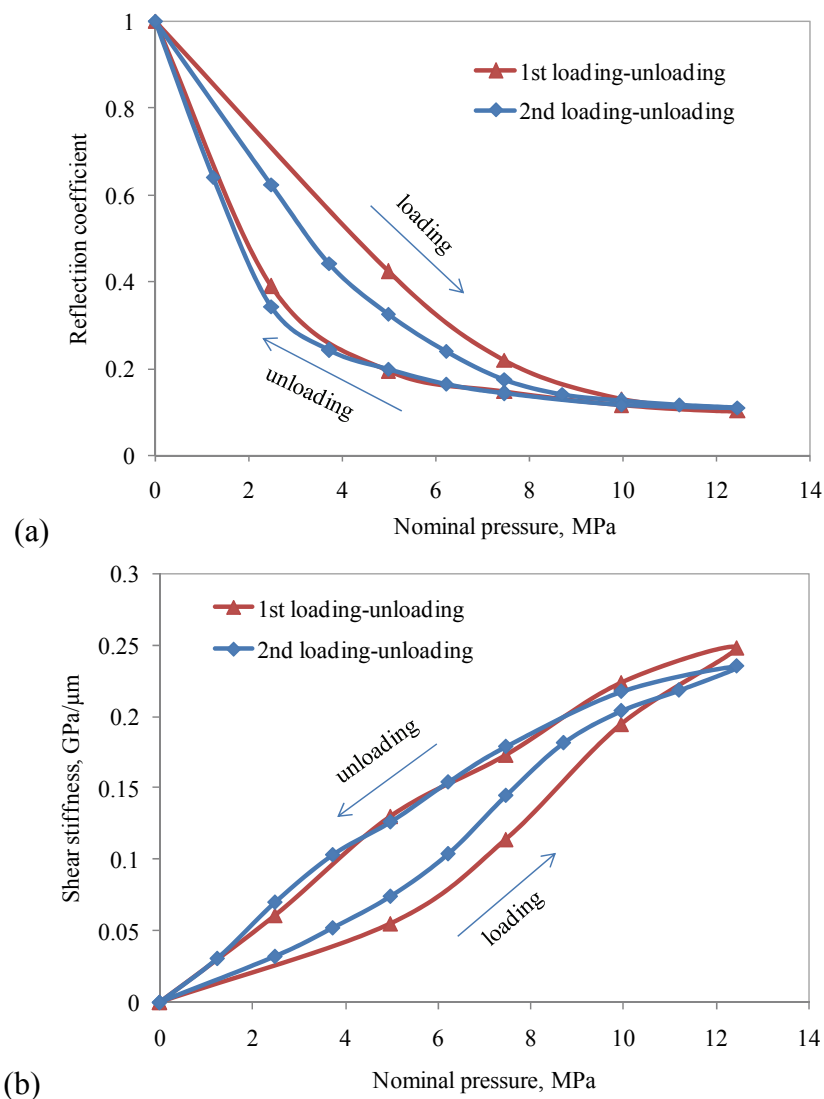


Figure 7.9. (a) Measured reflection coefficient varying with mean contact pressure for two load cycles for Perspex 5mm diameter specimen, and (b) shear stiffness calculated from measured reflection coefficient.

If we compare both reflection and shear stiffness curves in Figure 7.9 (a) and (b), it can be seen that the first loading path was different to the second. This indicates plastic deformation and partial elastic recovery of rough surface asperities took place during weight-loading, unloading and reloading. The real contact area in the subsequent loading cycle was greater. This leads to more ultrasound passing through the interface and less reflected back. As a result, the reflection coefficient in the second loading cycle is lower, which can be seen clearly from Figure 7.9 (a). It should be noted that the highest pressure in the test was 12.96 MPa, much lower than the bulk yield stress (84 MPa), shown in Table 7.2. Even though the bulk material was expected to be in elastic deformation state, asperities on the surfaces may have exceeded elastic deformation limit and undergo plastic deformation. Some confirmation has been made that, even for very light loads or nominal pressure applied onto a hard material, the asperities of a multi-contact interface must be treated as elasto-plastic (Baumberger, 1997; Berthoud and Baumberger, 1998). Therefore, the study of shear stiffness can be considered to be a probe for understanding the nature of an interface.

Figure 7.10 (a) shows ultrasonic reflection measurement for different nominal contact sizes, 5 mm, 8 mm and 12 mm. The interface of greatest nominal contact area shows most sensitivity to pressure. This can be seen from the sharp decrease of reflection coefficient with nominal contact pressure for 12mm diameter specimen. From Table 7.1, this specimen has the lowest surface roughness, 0.44  $\mu\text{m}$ . Lower reflection means more transmission of ultrasound and therefore higher shear stiffness. It can be concluded among these three interfaces, the stiffness and the real contact area this most 'smooth' surface increases most considerably with nominal pressure. This shows good agreement with the previous experimental result (Gonzalez-Valadez, 2006). Tattersal (1973) also found that the amount and size of roughness peaks mostly affect the contact parameters. Figure 7.10 (b) shows the calculated interfacial shear stiffness from reflection measurement. It confirms that the shear stiffness for 12 mm specimen shows highest shear stiffness at the same pressure. For all contacting sizes, hysteresis was clearly presented.

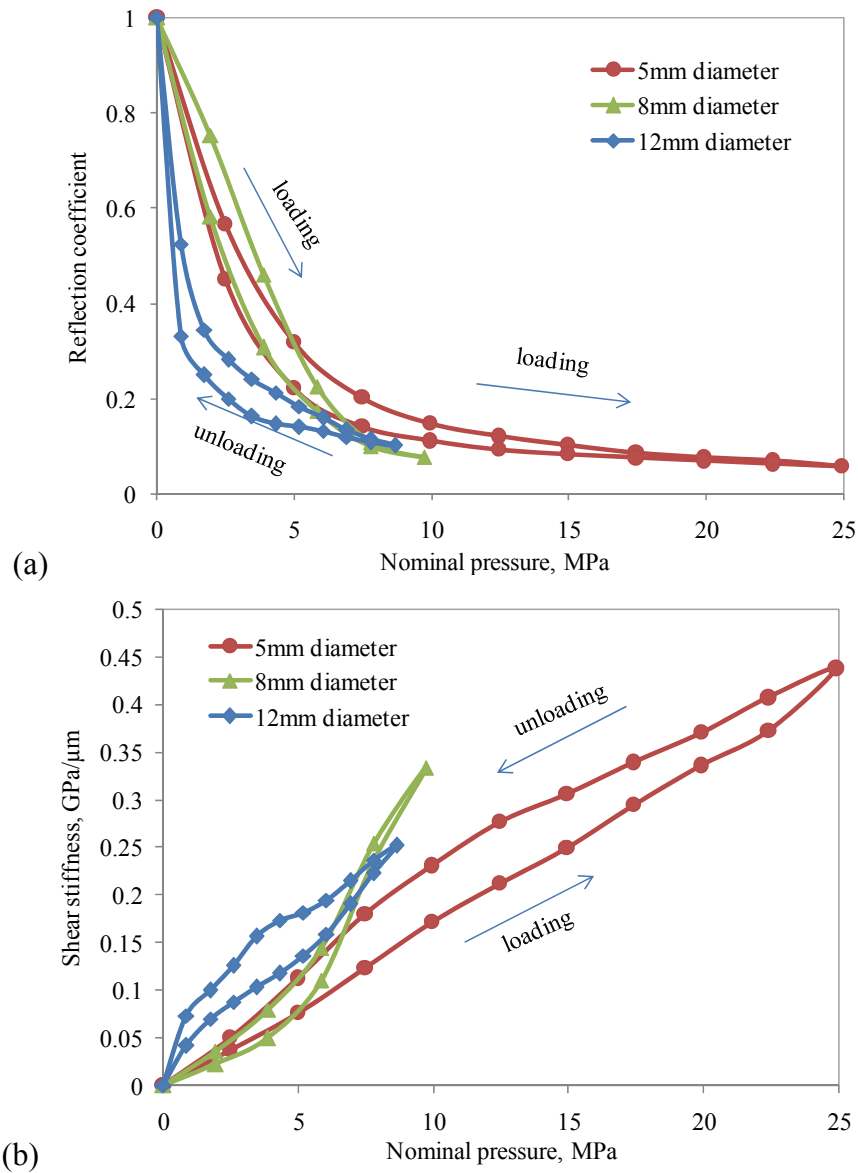


Figure 7.10. (a) Measured reflection coefficient varying with mean contact pressure for different contact size of Perspecx, and (b) shear stiffness calculated from measured reflection coefficient.

Figure 7.11 shows measured reflection coefficient and calculated shear stiffness varying with nominal contact pressure for the steel specimen. From 10.8 MPa to 21.6 MPa, the ultrasonic reflection decreases slightly in the loading process. The lowest reflection coefficient was found to be around 0.4. Królikowski and Szczepek (1993) found that under heavy pressure, reflection coefficient tended to be zero and consequently the interfacial shear stiffness becomes independent with pressure. In this test, due to the limitation of the load application, higher pressure tests were not performed.

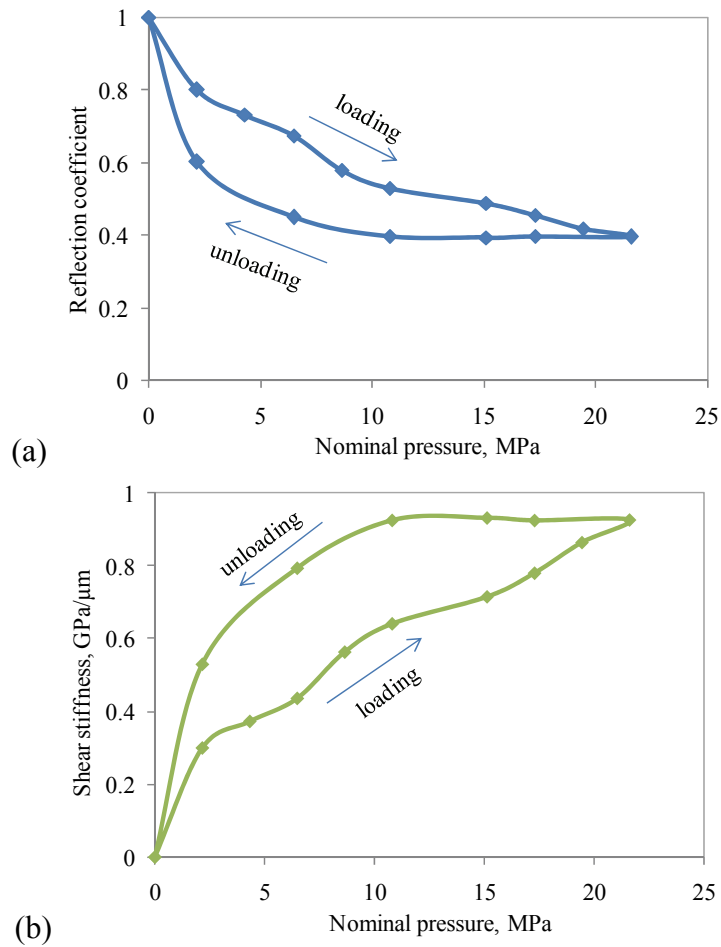


Figure 7.11. (a) Measured reflection coefficient varying with mean contact pressure for steel 12 mm diameter contact, and (b) shear stiffness calculated from measured reflection coefficient.

### 7.3.3 Reflection Measurement during Stick-slip

Figure 7.12 shows an example of measured friction force variation against time during a stick-slip process. Initially, the lower specimen starts moving with the guide together with the upper specimen due to static friction force under a certain normal load. The static friction increase in the stick stage and approaches a maximum value where the upper specimen escapes from contact and a slip takes place. The stick-slip process was replicated with a lattice spacing later on.



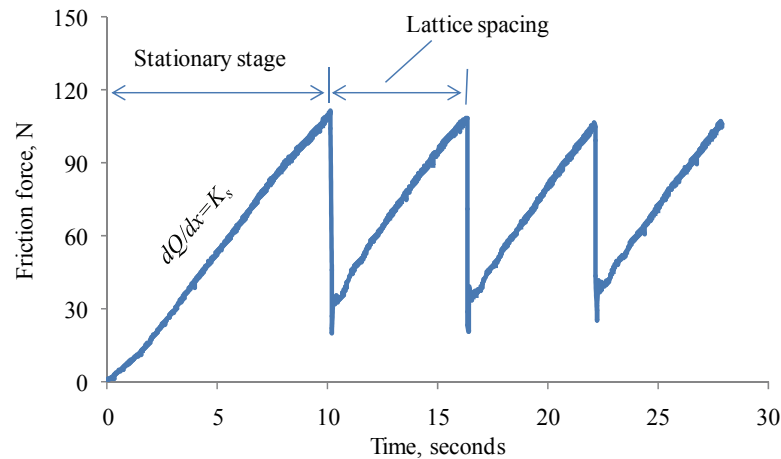


Figure 7.12. A typical experimental friction force varying with time during stick-slip process.

The ultrasonic reflection was recorded during this stick-slip process. By comparison with the reference reflection, the variation of reflection coefficient has been obtained and plotted against time. The interfacial shear stiffness,  $K_s$ , was calculated through the ultrasonic spring model, Equation (7.3). Figure 7.14 to Figure 7.16 show the reflection coefficient, interface friction force and obtained shear stiffness for 12mm diameter Perspex-Perspex contact at nominal contact pressure, 2.59 MPa (293 N), 3.46 MPa (391 N) and 4.32 MPa (489 N), all at the same sliding speed of 0.26m/s. It can be seen that with increasing friction force, the reflection coefficient was found to decrease slightly during the first stick-slip process. Therefore, the interfacial shear stiffness calculated from ultrasonic reflection measurement increases slightly before the first slip. Under the constant normal pressure, the increasing of static friction force brings a greater real contact area. According to the GW model, the mean separation of the rough contacting surfaces was determined by the normal load. Therefore the number of asperity contacts was expected to be constant during this sliding movement. Hence, the conclusion can be made that the increasing of the real contact area was from the growth of contacting junctions due to the shear deformation, shown in Figure 7.13. This could also be confirmed by looking at the shear stiffness property against the friction force, which was addressed in the section 7.3.4. Afterwards, the stick-slip repeats, the reflection coefficient was decreasing firstly and followed by a short increase before slip, this can be clearly seen from Figure 7.14.

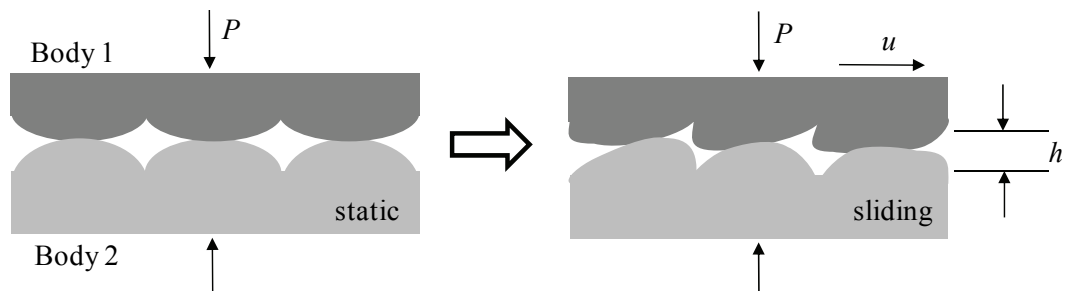


Figure 7.13. Sketch of junction growth from static contact to sliding.

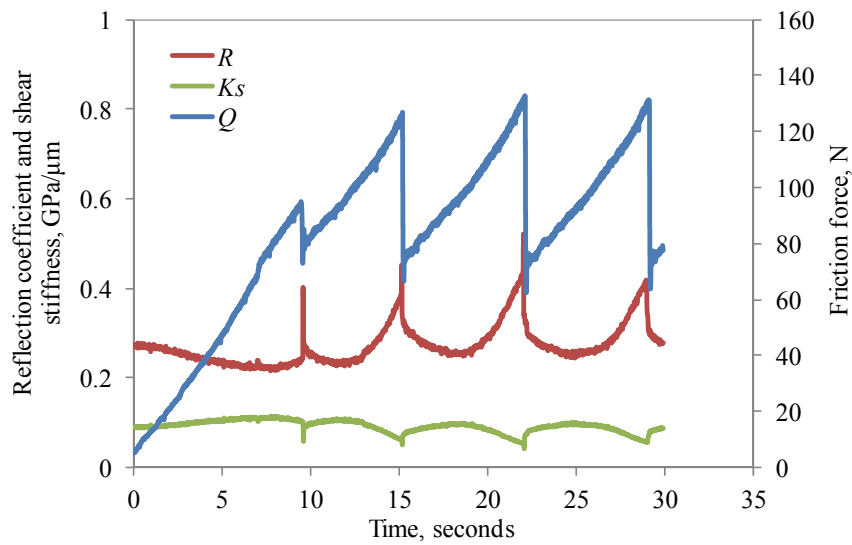


Figure 7.14. Measured friction force, reflection coefficient and calculated shear stiffness using the spring model (Equation (7.3)) at the nominal contact pressure of 2.59 MPa (293N) at sliding speed of 0.26m/s for Perspex 12mm diameter specimen.

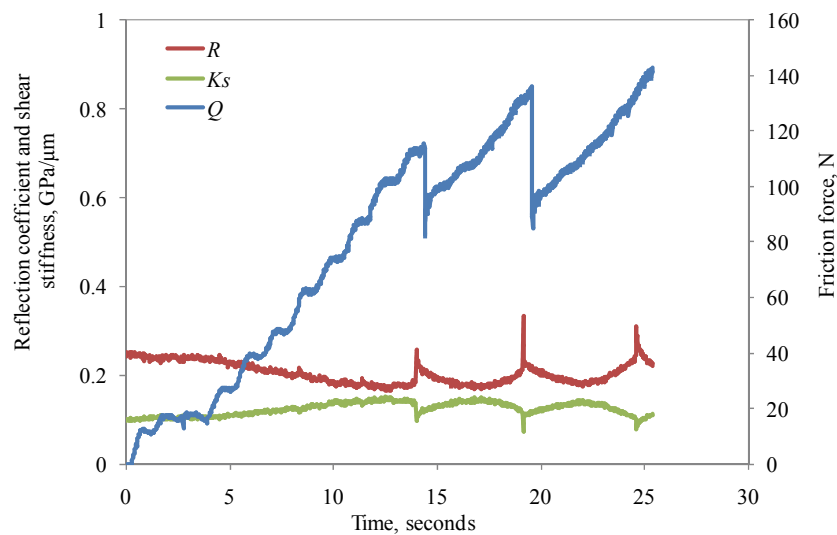


Figure 7.15. Measured friction force, reflection coefficient and calculated shear stiffness using the spring model (Equation (7.3)) at the nominal contact pressure of 3.46 MPa (391 N) at sliding speed of 0.26 m/s for Perspex 12mm diameter specimen.

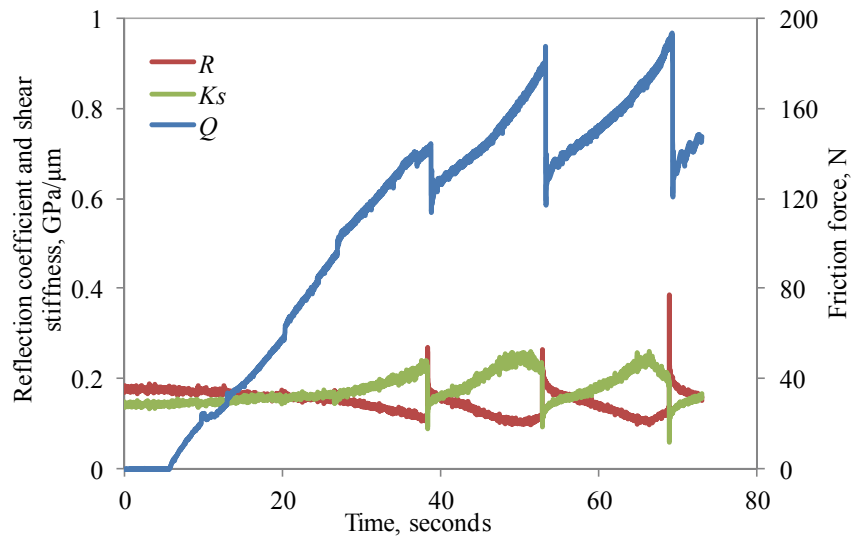


Figure 7.16. Measured friction force, reflection coefficient and calculated shear stiffness using the spring model (Equation (7.3)) at the nominal contact pressure of 4.32 MPa (489 N) at sliding speed of 0.26 m/s for Perspex 12mm diameter specimen.

From Figure 7.14 to Figure 7.16, the friction force was found to increase with the normal pressure. During the stick-slip process, it was found to be in the range of 63-133 N under 2.59 MPa and 112-194 N under 4.32 MPa. Lower reflection was recorded for higher normal pressures because of the greater real contact area. Accordingly, the interface under higher pressure was stiffer in shear direction, which was shown by the higher shear stiffness. More details can be seen from Figure 7.17 and Figure 7.18.

Figure 7.17 and Figure 7.18 show the friction force, reflection coefficient and interfacial shear stiffness varying during stick-slip process for the 8 mm and 5mm diameter Perspex specimens. For each specimen, the same dead weight range was applied, but, due to different apparent contact areas, the nominal pressure varies. The same conclusion can be obtained as: higher pressure produces higher friction force, more real contact area, lower reflection coefficient, and therefore more stiffer interface therefore (higher shear stiffness). A significant drop on shear stiffness was observed for both specimens under 7.78 MPa and 14.93 MPa respectively, shown in Figure 7.17 (c) and Figure 7.18 (c). It took place in the stationary stage before each sliding. This may be due to the bulk deformation of the top Perspex (low elastic modulus and shear modulus), which lead to a misalignment at the interface.

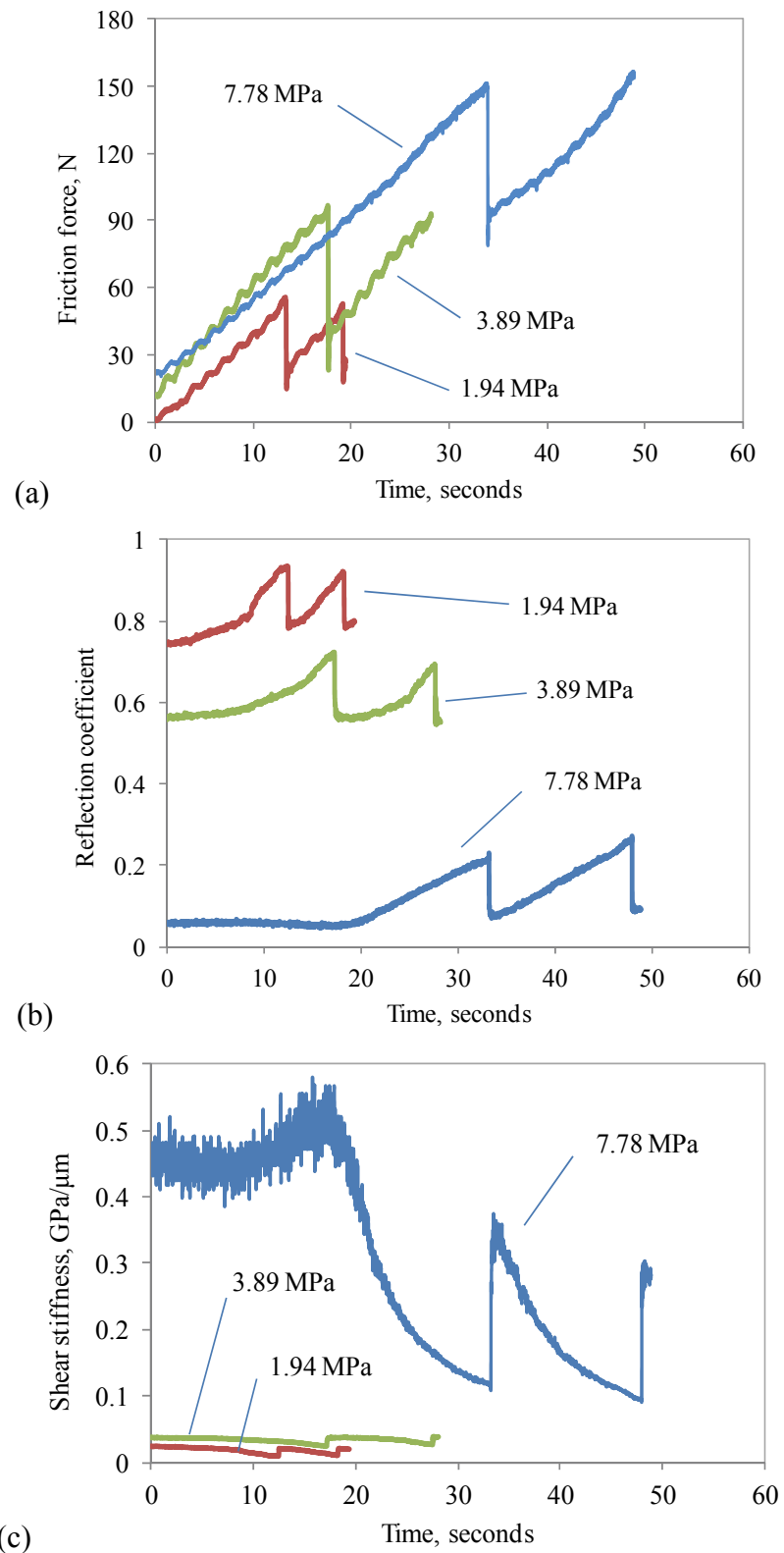


Figure 7.17. (a) Friction force, (b) measured reflection coefficient, and (c) interfacial shear stiffness calculated through spring model (Equation (7.3)) from measured reflection coefficient varying with time during stick-slip process at sliding speed of 0.26 m/s for Perspex 8 mm diameter specimen.

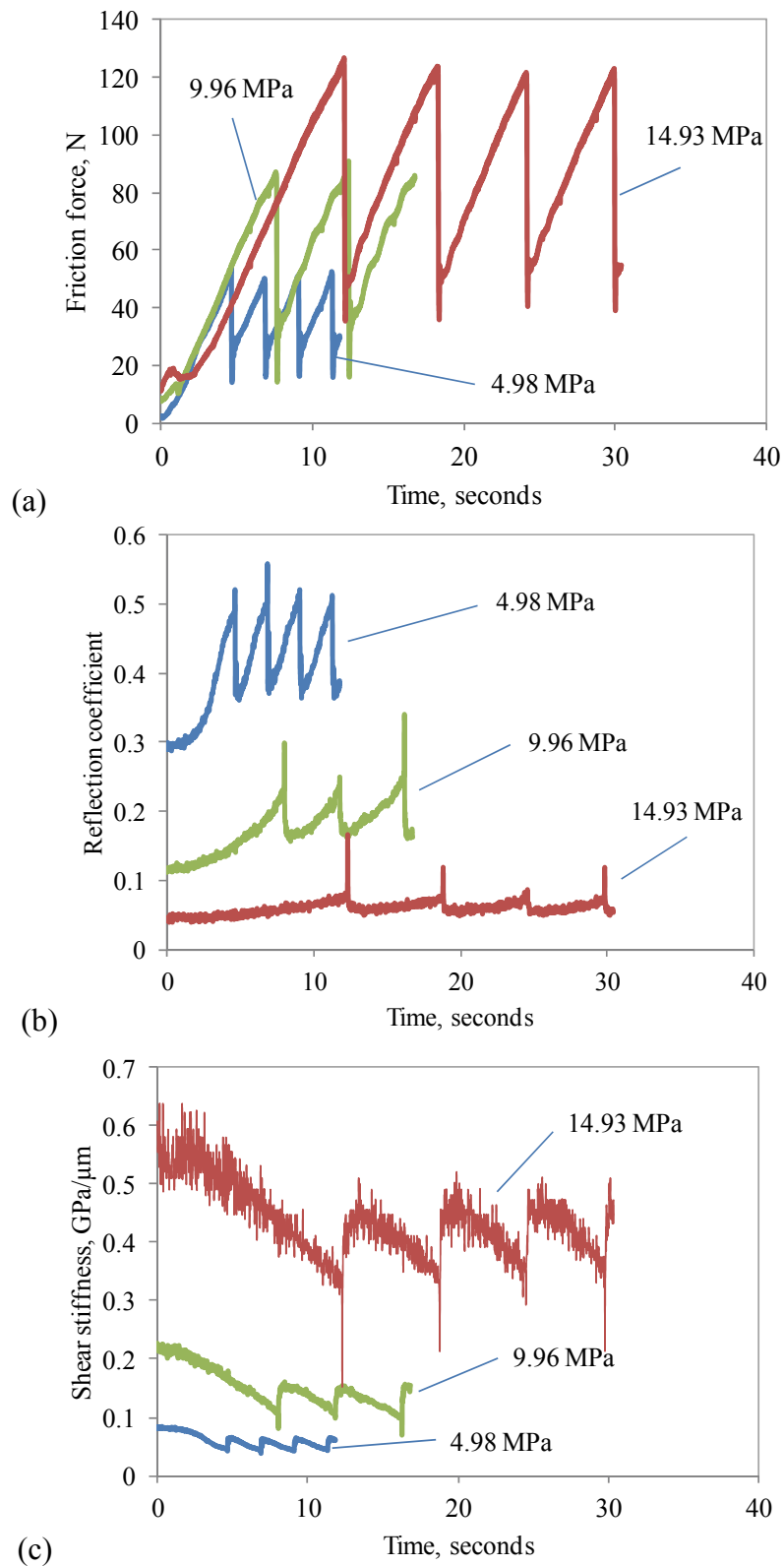


Figure 7.18. (a) Friction force, (b) measured reflection coefficient, and (c) interfacial shear stiffness calculated through spring model (Equation (7.3)) from measured reflection coefficient varying with time during stick-slip process at sliding speed of 0.26 m/s for Perspex 5 mm diameter specimen.

### 7.3.4 Interfacial Shear Stiffness Varying with Traction Force

The interfacial stiffness calculated from ultrasonic reflection was plotted against the traction force, shown in Figure 7.19-Figure 7.21.

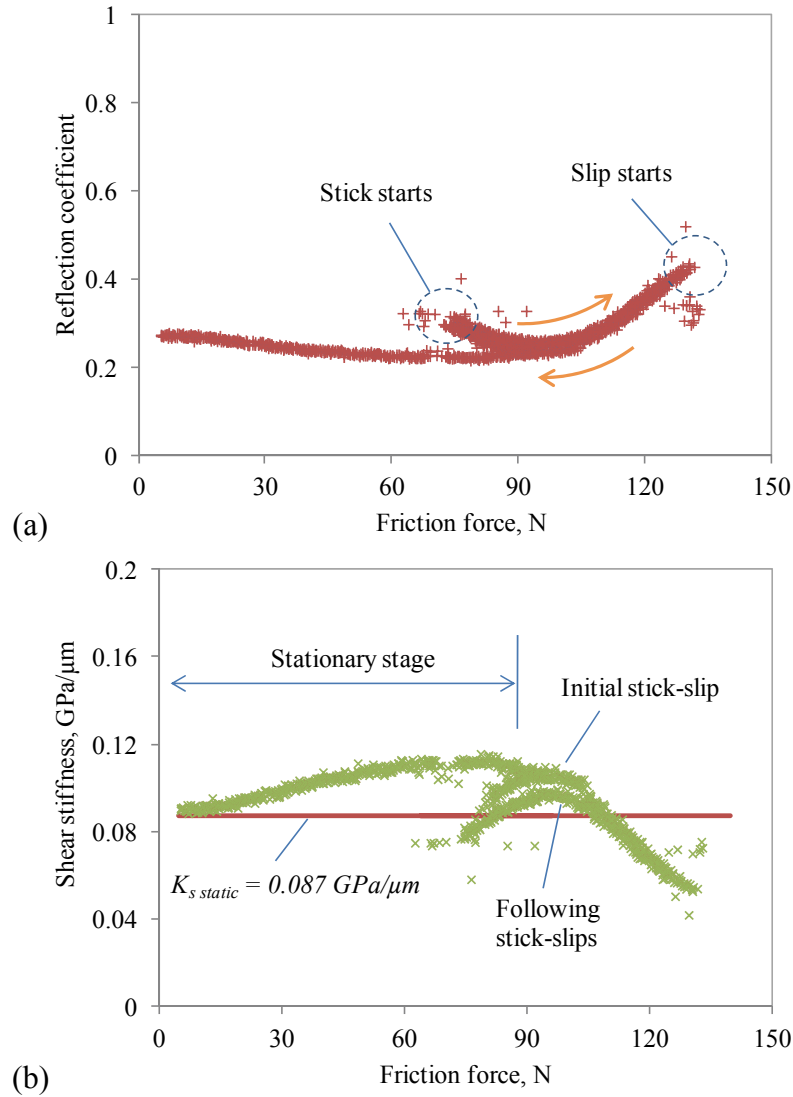


Figure 7.19. (a) Reflection coefficient, and (b) interfacial shear stiffness calculated through spring model (Equation (7.3)) varying with friction force during stick-slip process at the nominal contact pressure of 2.59 MPa (293 N) for Perspex 12 mm diameter specimen.

Figure 7.19 (a) shows the ultrasonic reflection against friction force during stick-slip process for a 12 mm Perspex specimen. It can be seen that the reflection coefficient decreases slightly and then increases significantly with friction force in the first stick phase. The friction force varying with time can be referred to Figure 7.14. The maximum

reflection was reached at the threshold of the first slip. The sliding then takes place, which was over a short period. The friction force restores to a low level and a new stick was built up, highlighted in Figure 7.19 (a). Afterwards, the reflection repeats along a same route.

The shear stiffness was calculated using measured reflection, shown in Figure 7.19 (b). In the stationary state, it increases from 0.087 GP/ $\mu\text{m}$ , which was the static shear stiffness tested at the same normal pressure (refer to Figure 7.10 (b)), to the maximum of 0.116 GP/ $\mu\text{m}$ . This shows the growth of real contact due to increasing traction force. In the first stick-slip process, the shear stiffness shows a slightly higher trace than the following repeats. Little difference can be observed for the later cycles. The following cycles overlap the second stiffness trace, as shown in Figure 7.19 (b). This indicates less conformity between the two surfaces in the following stick-slip process than the initial one. For each trace, with increasing shear force, the shear stiffness increased first due to the growth of asperity junctions and decreased as the slip released the junction growth. At the beginning of each stick and slip, a few irregular data points have been recorded. This was caused by the un-steady new start due to the alternation between stick and slip.

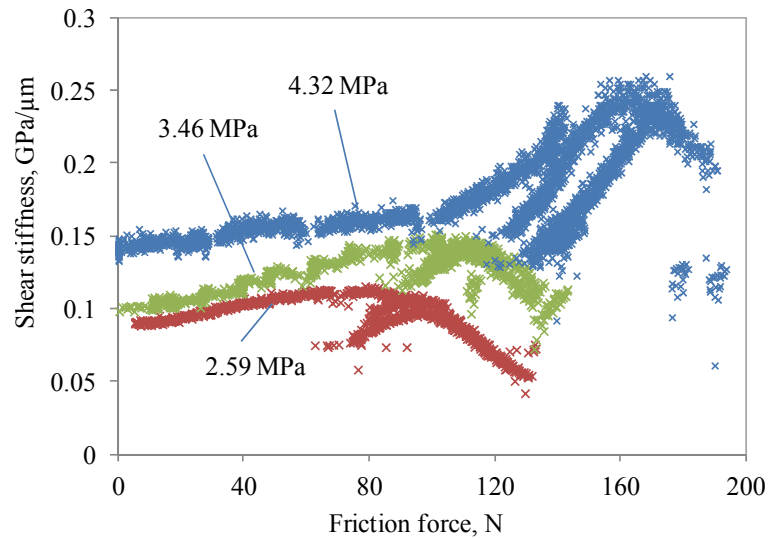


Figure 7.20. Interfacial shear stiffness calculated through spring model (Equation (7.3)) from measured reflection varying with friction force during stick-slip process under varying nominal contact pressures for Perspex 12 mm diameter specimen.

Figure 7.20 presents the effect of the normal pressure on the interfacial shear stiffness. Higher pressures produce greater shear stiffness as more asperities begin to interact. The real contact area increases and, therefore, the interface was stiffer. After the initial

stationary phase, a similar repeating route of the shear stiffness has been found for all three pressures. Shear force starts accumulating from the beginning of stick, approaches the climax at the slip and releases during the slip. This process repeats and forms traction cycles at the interface. Under 4.32 MPa, three shear stiffness cycles were observed, among which the latter show lower amplitude than the previous traction cycles. This indicates that the contact between two surfaces becomes less stiff afterwards. This observation was opposite to the hysteresis study in 7.3.2, where the tests focused on the shear stiffness in loading/unloading cycles, shown in Figure 7.9. The second normal loading leads to a higher shear stiffness due to plastic deformation of asperities. This is because in the loading/unloading test, the contact takes place at the same area. Asperities in this area were compressed into contact in the loading and released from interaction in the unloading. Plastic deformed peaks cannot get recovered and leads to higher stiffness. However, in the sliding test, the contact area changes with time. During the stick-slip process, asperity contact pairs were different from previous ones.

Figure 7.21 shows details occurring during the slip, which was found to be 0.05 seconds in this test. As the process was too short, only a few data points have been recorded and detailed in Figure 7.21 (b). A significant drop in friction force from 133 N to 72 N can be seen from the plot of friction force against time. However, little change was observed on the reflection coefficient and the shear stiffness. Both show an approximate constant trend and behave independently with the shear force. Even though, the slip process was very short, the sliding displacement of upper specimen against the lower plate was significant. During this sweeping process, the shear stiffness and the real contact area remains the same:

$$K_{s,stick} = K_{s,slip} \quad (7.5)$$

The interfacial shear stiffness at the sliding phase was found to be around 0.33 GPa/ $\mu\text{m}$ , which was clearly not zero that was expected at a sliding interface, at least on a micro-scale.



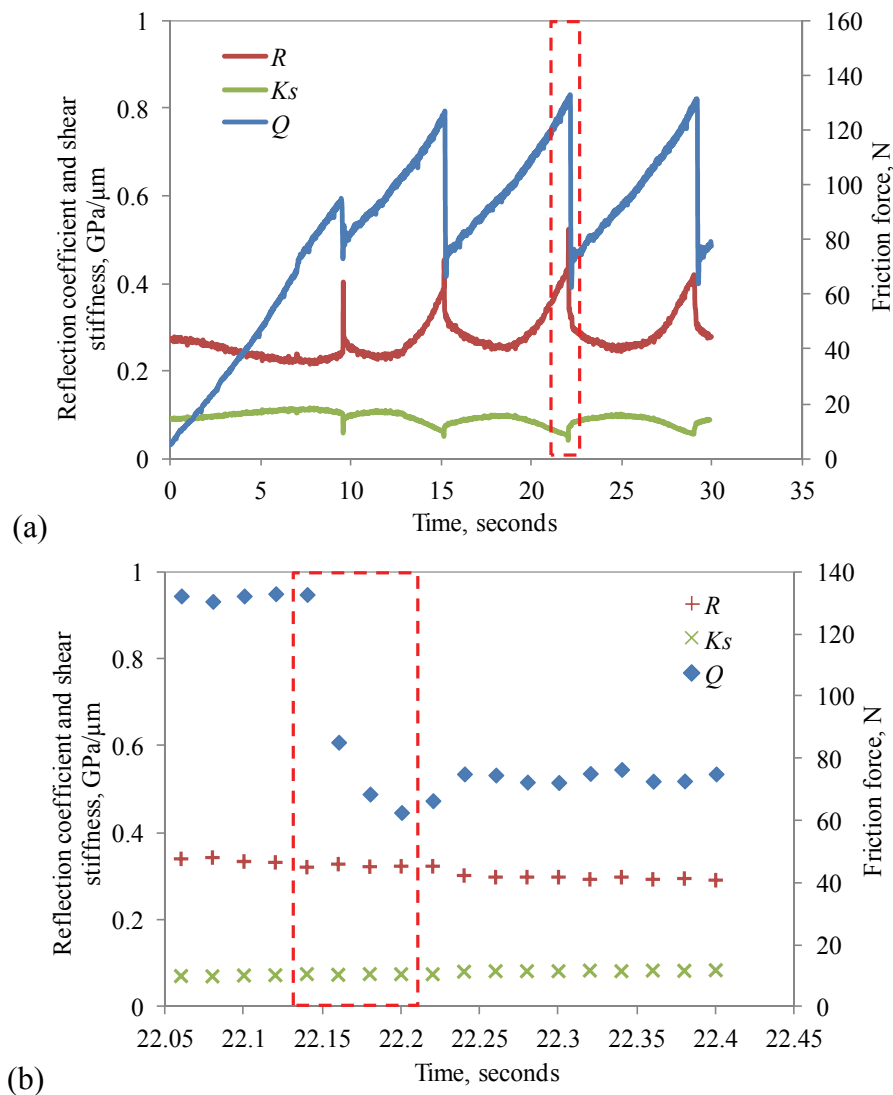


Figure 7.21. (a) Reflection coefficient, shear stiffness and friction force varying with time during stick-slip process at the nominal contact pressure of 2.59 MPa (293 N) for Perspex 12mm diameter specimen, and, (b) detailed information at slip phase.

### 7.3.5 Effect of the Sliding Speed

The start-up process of the sliding contact has been analysed in previous section. How the apparent reflection coefficient and friction force were influenced by the sliding speed and normal load during stick-slip stage was studied in this and the later section.

Table 7.3 shows the effect of sliding speed on ultrasonic reflection, shear stiffness, friction force and lattice spacing (expressed in seconds), under a nominal pressure of 4.98 MPa (98 N) for 5mm diameter Perspex specimens. It can be seen that the shear stiffness

slightly decreases with speed. It implies that under varying sliding speeds, the asperity interaction varies. Lower speed leads to stiffer interface due to higher real contact area caused by asperity interaction. Therefore, a conclusion might be obtained that under certain normal load, shorter interaction time of asperity spots causes less micro-spot junction growth (Figure 7.13).

For all speed cases, there is no significant effect of speed on friction force was observed from the recorded friction force curves, shown in the fourth row of Table 7.3. The same experiment has been carried out on 8mm diameter Perspex specimen as well, shown in Table 7.4. The maximum shear stiffness during the stick and slip process was found to be 76.1 MPa/ $\mu\text{m}$  at 0.639 m/s and 65.7 MPa/ $\mu\text{m}$  at 3.209 m/s. It shows that the shear stiffness decreases slightly with the sliding speed. When looking at the amplitude and span of the friction force, there was little effect of sliding speed on the friction force. More results on other Perspex specimens are shown in Appendix C.

Table 7.3. Influence of speed on reflection coefficient for Perspex 5mm diameter specimen at 4.98 MPa (98 N).

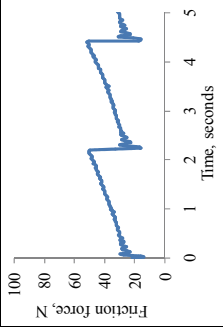
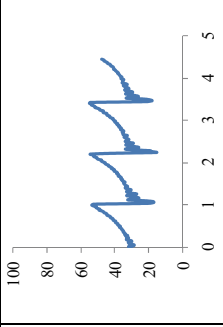
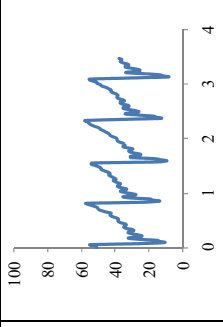
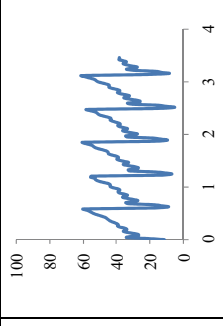
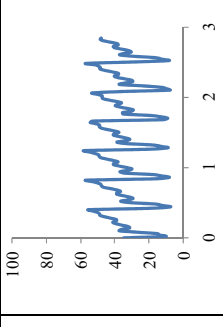
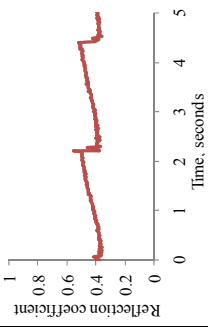
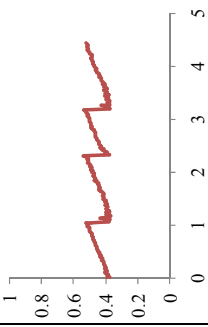
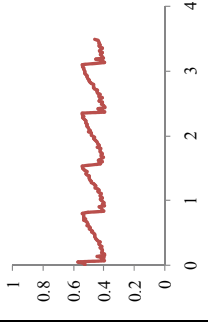
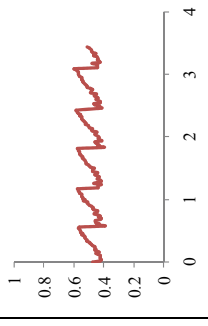
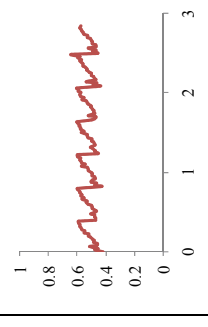
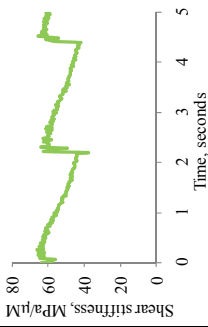
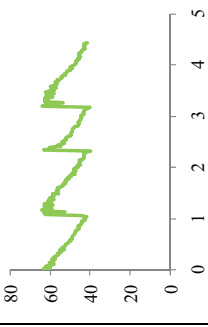
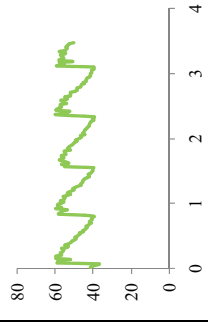
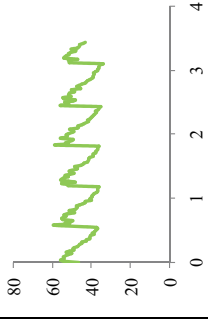
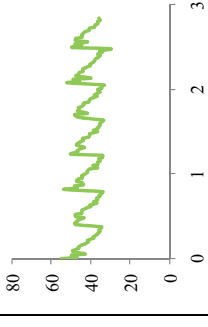
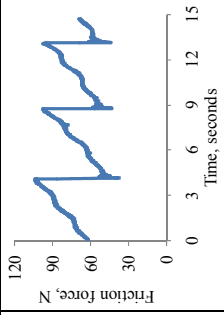
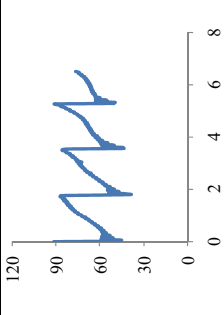
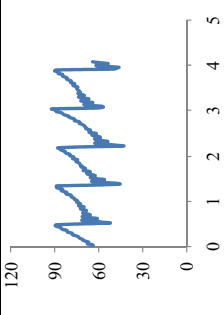
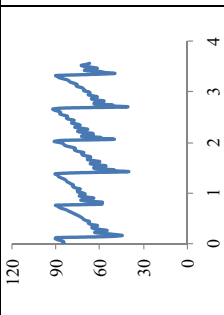
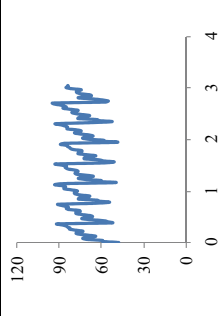
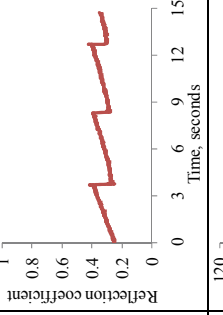
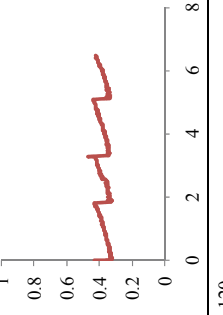
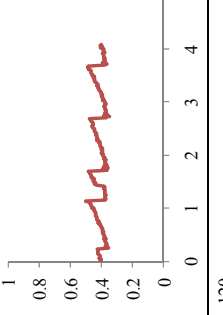
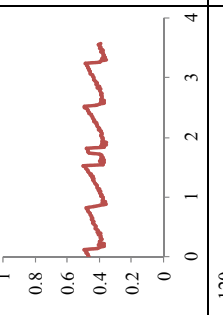
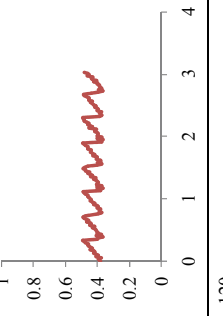
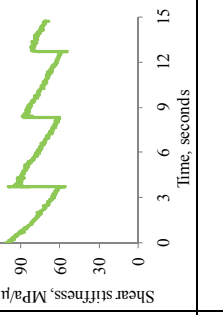
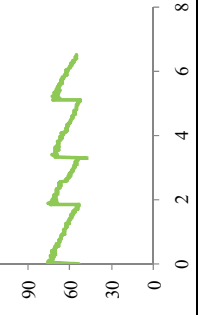
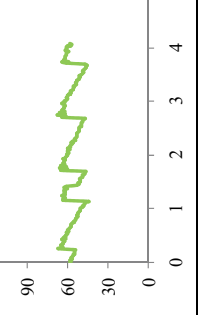
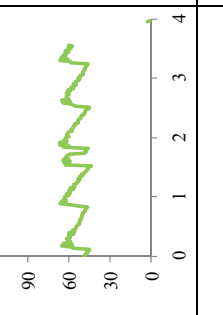
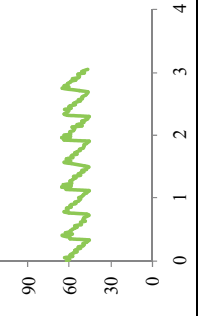
Sliding speed, $m/s$	0.264	0.639	1.154	1.83	3.029
Friction force, $N$					
Reflection coefficient					
Shear stiffness, $GPa/\mu m$					
Lattice spacing, seconds	2.24	1.20	0.76	0.63	0.42

Table 7.4. Influence of speed on reflection coefficient for Perspex 8 mm diameter specimen at 5.83 MPa (293 N).

Sliding speed, $m/s$	0.264	0.639	1.154	1.83	3.029
Friction force, $N$					
Reflection coefficient					
Shear stiffness, $GPa/\mu m$					
Lattice spacing, seconds	4.36	1.76	0.86	0.64	0.39

### 7.3.6 Effect of the Normal Load

Tables 7.5 and 7.6 show the effect of normal load on the ultrasound reflection, shear stiffness and friction force for 8mm and 12 mm diameter Perspex specimens at a sliding speed of 0.639m/s. It is clear that the normal load had a greater influence on the interfacial properties. The higher normal pressure leads to stiffer interface. Because more approaching of contacting surfaces is produced under higher loads. More asperities come into interact that consequently causes severe asperity interaction for existing contact spots, larger contact area and stiffer interface. In Figure 7.22,  $R$  and  $T$  in the figure refer to the ultrasonic reflection and transmission, respectively. A better bond was built under higher normal loads. This helps the transmission of ultrasound through to the second body (Figure 7.22). Thus less ultrasound was reflected back under higher loads, but the opposite trend for shear stiffness due to the spring model.

The total shear stress occurring on the interface is the integration of each interacting spot. Therefore more asperity interaction produces higher shear stress/friction force. The recorded friction force increases significantly with normal load. More ultrasonic measurements and friction forces recording for the other specimens are given in Appendix D.

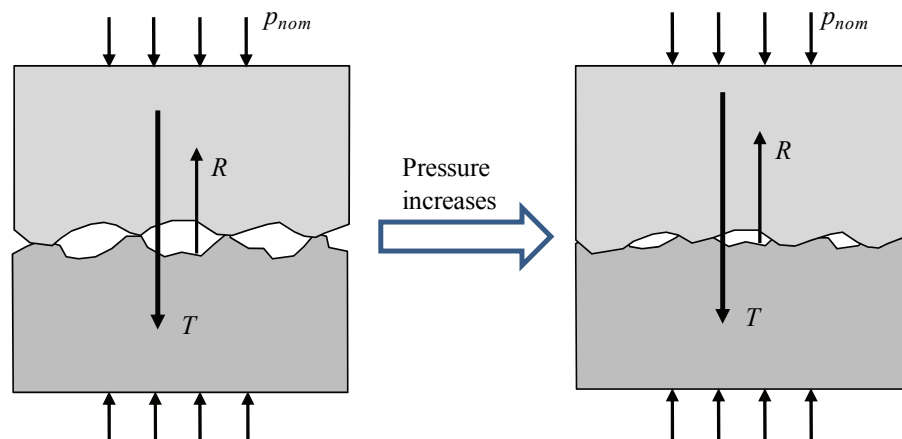


Figure 7.22. Sketch of approach of two contacting rough surfaces under a normal pressure.

Table 7.5. Influence of load on reflection coefficient for Perspex 8 mm diameter specimen at speed of 0.639 m/s.

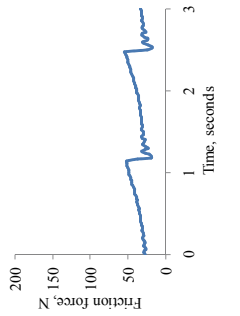
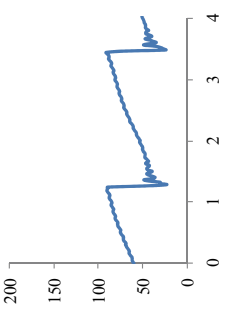
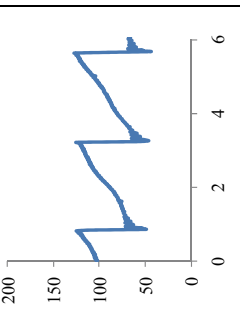
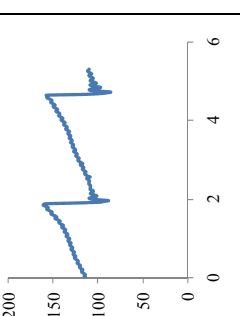
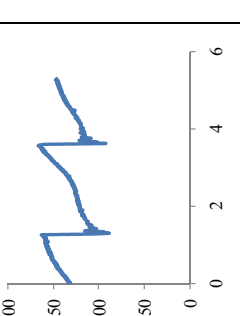
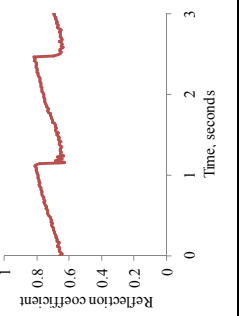
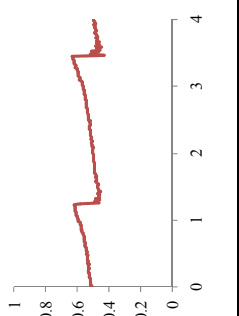
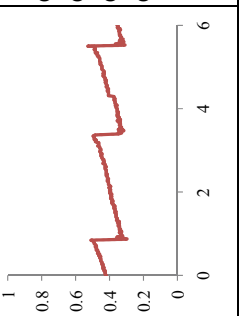
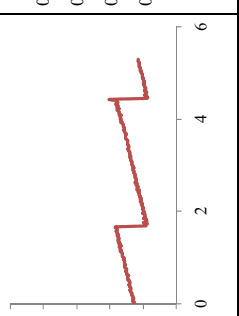
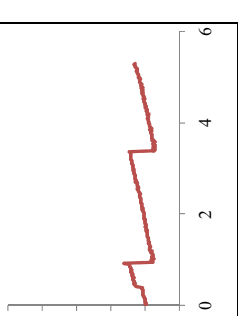
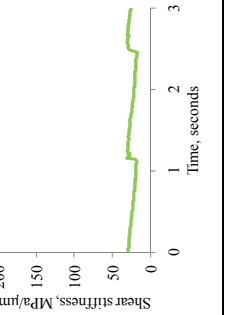
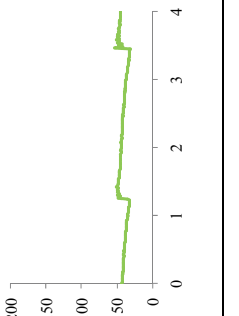
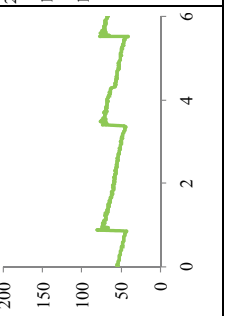
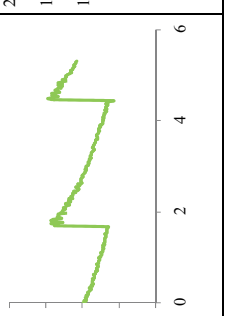
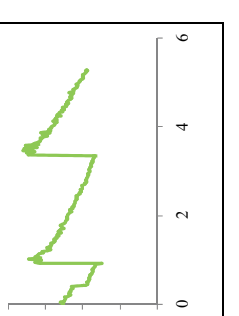
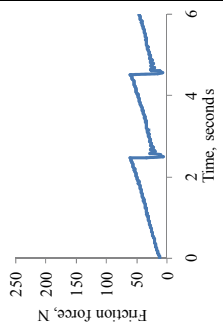
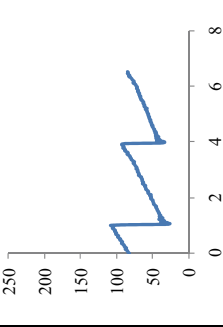
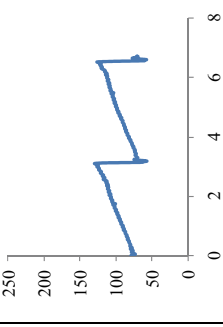
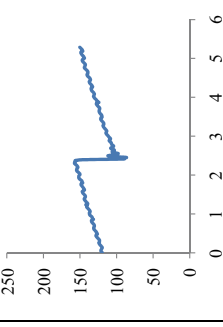
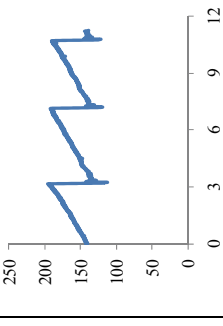
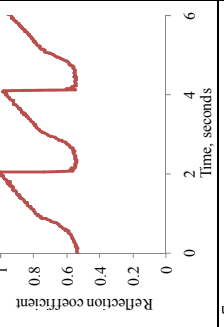
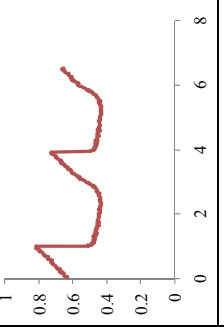
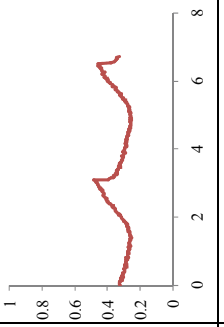
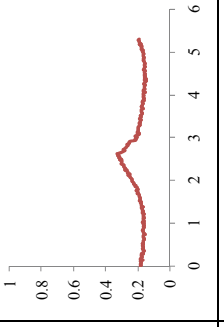
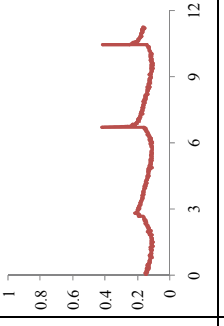
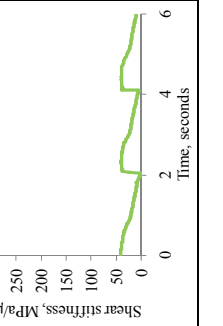
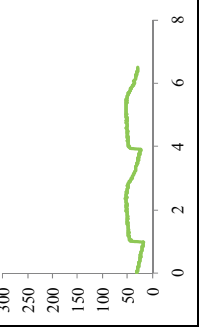
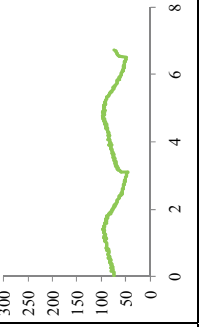
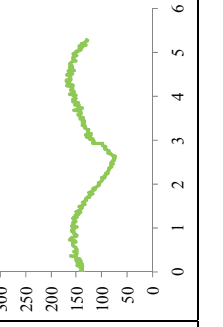
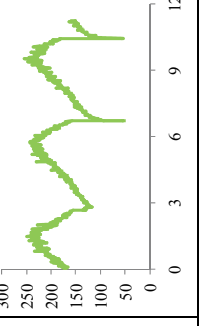
Nominal pressure, <i>MPa</i>	1.94	3.89	5.83	7.78	9.72
Friction force, <i>N</i>					
Reflection coefficient					
Shear stiffness, <i>GPa/μm</i>					

Table 7.6. Influence of load on reflection coefficient for Perspex 12 mm diameter specimen at speed of 0.639 m/s.

Nominal pressure, $MPa$	1.94	3.89	5.83	7.78	9.72
Friction force, $N$					
Reflection coefficient					
Shear stiffness, $GPa/\mu m$					

## 7.4 Real Contact Area from Ultrasonic Measurement

### 7.4.1 Formula Derivation

In order to fully understand the property of the interface it is necessary to study the real contact area. For the real engineering contact, the load is supported by random distributed asperities over the contact zone. The real contact area is significantly low compared to the nominal contact area and the stresses at the asperities are considerably higher than the average contact pressure (McCool, 1986; Drinkwater *et al.*, 1996). Kim *et al.* (2004) and Baltazar *et al.* (2006) calculated the real contact area using the statistical asperity micromechanical contact model for elasto-plastic materials. The real contact area found was mostly, less than 20% of the nominal area. As the real contact area is a very small proportion of the nominal contact area, plastic deformations of the load bearing asperities are considered to take place. This is recognised as an essential feature for sliding friction (Baumberger, 1997; Berthoud and Baumberger, 1998).

In this section a relationship between real contact area and interfacial shear stiffness was developed to disclose the real contact area for engineering interface. Under a certain normal load for an engineering interface, a number of asperities,  $N$ , interact. Assuming independent contacts, the distance from each contact spot is much greater than their average size. If the mean contact size of all contacting spots is assumed to be  $\langle a \rangle$ , the total real contact area becomes,

$$A = N\pi\langle a \rangle^2 \quad (7.6)$$

Considering most of the load bearing asperities are in a plastic pretrained state, the mean contact size, and the number of micro-contacts, are expressed as (Berthoud and Baumberger, 1998):

$$\langle a \rangle \cong \sqrt{\sigma_s R_s} \quad (7.7)$$

$$N \cong \frac{P}{H\sigma_s R_s} \quad (7.8)$$



Where  $P$  is the normal applied load and  $H$  is the bulk hardness, and  $\sigma_s$  and  $R_s$  are the standard deviation of asperity height distribution and the mean radius of asperity curvature based on GW model.

Combining equations (7.2) and (7.6)-(7.8), the interfacial shear stiffness becomes:

$$K_s = G \sqrt{\frac{pA}{\pi H A_0 \sigma_s R_s}} \quad (7.9)$$

Where  $p$  is the normal pressure. This expression shows the relationship between the interfacial shear stiffness,  $K_s$ , and the real contact area,  $A$ . It can be used to investigate the evolution of  $A$  during stick-slip process by using ultrasonic measurement of shear stiffness. Considering the simplicity of data, the real contact area is normalised with the apparent contact area  $A_0$  and given as,

$$A/A_0 = \frac{\pi K_s^2 H \sigma_s R_s}{p G^2} \quad (7.10)$$

Where  $R_s$  is the diameter of asperities, and  $\sigma_s$  is the standard deviation of the summit height distribution.  $R_s^{-1}$  was shown to behave as the RMS curvature of the profile (Berthoud and Baumberger, 1998; Williams, 2005). Therefore they are calculated through the following expression:

$$\sigma_s = \sqrt{\sigma_{s1}^2 + \sigma_{s2}^2} \quad (7.11)$$

$$\frac{1}{R_s^2} = \frac{1}{R_{s1}^2} + \frac{1}{R_{s2}^2} \quad (7.12)$$

Subscripts 1 and 2 refer to two contacting bodies, in this case they are upper Perspex pin and lower Perspex plate. The parameter  $R_s$  is obtained through the same principle by using surface profile measurements. For example, for the 12 mm diameter Perspex specimen,  $\sigma_s$  ( $\sigma_s = R_q$ ) and  $R_s$  were found to be 0.55 and 0.04  $\mu\text{m}$ , respectively.

## 7.4.2 Real Contact Area Evolution in Hysteresis Cycles

The shear stiffness,  $K_s$ , was calculated from the spring model, Equation (7.4). It was used

to determine the real contact area from Equation (7.10). Figure 7.23 shows the real contact area normalised with the apparent contact area versus nominal contact pressure for two loading/unloading cycles for the 5 mm diameter Perspex specimen. It can be seen that the normalised real contact area was within 22%, which was comparable to the observation of Kim *et al.* (2004), who reported a range of 0-0.23 for an aluminum contact. The real contact area for the second loading was higher than the first one, which again showed hysteresis lag.

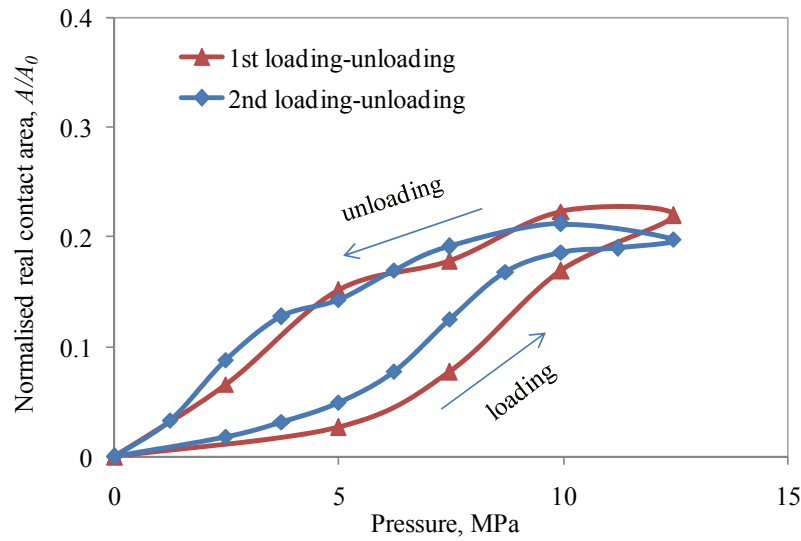


Figure 7.23. Normalised real contact area varying with nominal pressure for Perspex 5 mm diameter.

Analysis for loading/unloading cycle of the 8 mm diameter Perspex is shown in Figure 7.24, including shear stiffness, normalised real contact area and ultrasonic reflection coefficient. During the loading, a certain amount of asperities have undergone plastic deformation. This causes higher real contact area and less ultrasonic reflection in unloading. Therefore, higher shear stiffness in the unloading phase than in the loading process. At the normal pressure 5.83 MPa, the normalised real contact area was 5.4% during loading and 9.2% during unloading. If the real contact area increase was assumed to be caused by the plastic deformation of asperities, and all asperities have the same dimension, then it can be concluded that at 5.83 MPa in unloading at least 3.8% of the asperities on the nominal area were undergoing plastic deformation.

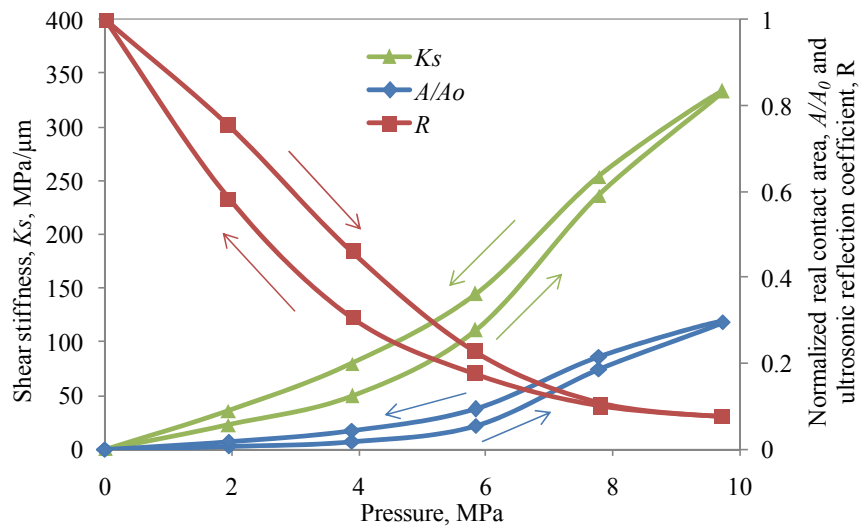


Figure 7.24. Normalised real contact area, ultrasonic reflection measurement and calculated shear stiffness varying with nominal pressure for Perspex 8 mm diameter.

### 7.4.3 Real Contact Area in Stick-slip Process

The properties of shear force and reflection coefficient have been discussed in the previous sections. Figure 7.25 shows the comparison of real contact area during stick-slip process for the 12 mm diameter Perspex contact under three normal pressures, 2.59 MPa, 3.46 MPa and 4.32 MPa.

A dimensionless real contact area was used for describing the variation of the real area during the stick-slip process. Comparing Figure 7.25 to Figure 7.14, it can be seen that under each pressure, the shear stiffness and the real contact area follow a similar wave profile, but the latter behaves with larger amplitude. This is because the normalised real contact area is linear with a square of the shear stiffness, shown by Equation (7.10).

The real contact area increases with the normal load. The climax ratio between the real contact area and the nominal area was found to be 0.1 at the normal pressure of 2.59 MPa (Figure 7.25 (a)) and 0.3 under 4.32 MPa (Figure 7.25 (c)). The real contact area increases much quicker than the normal pressure. Therefore, plastic deformation of the random distributed asperities was expected to take place without considering the effect from the traction action.

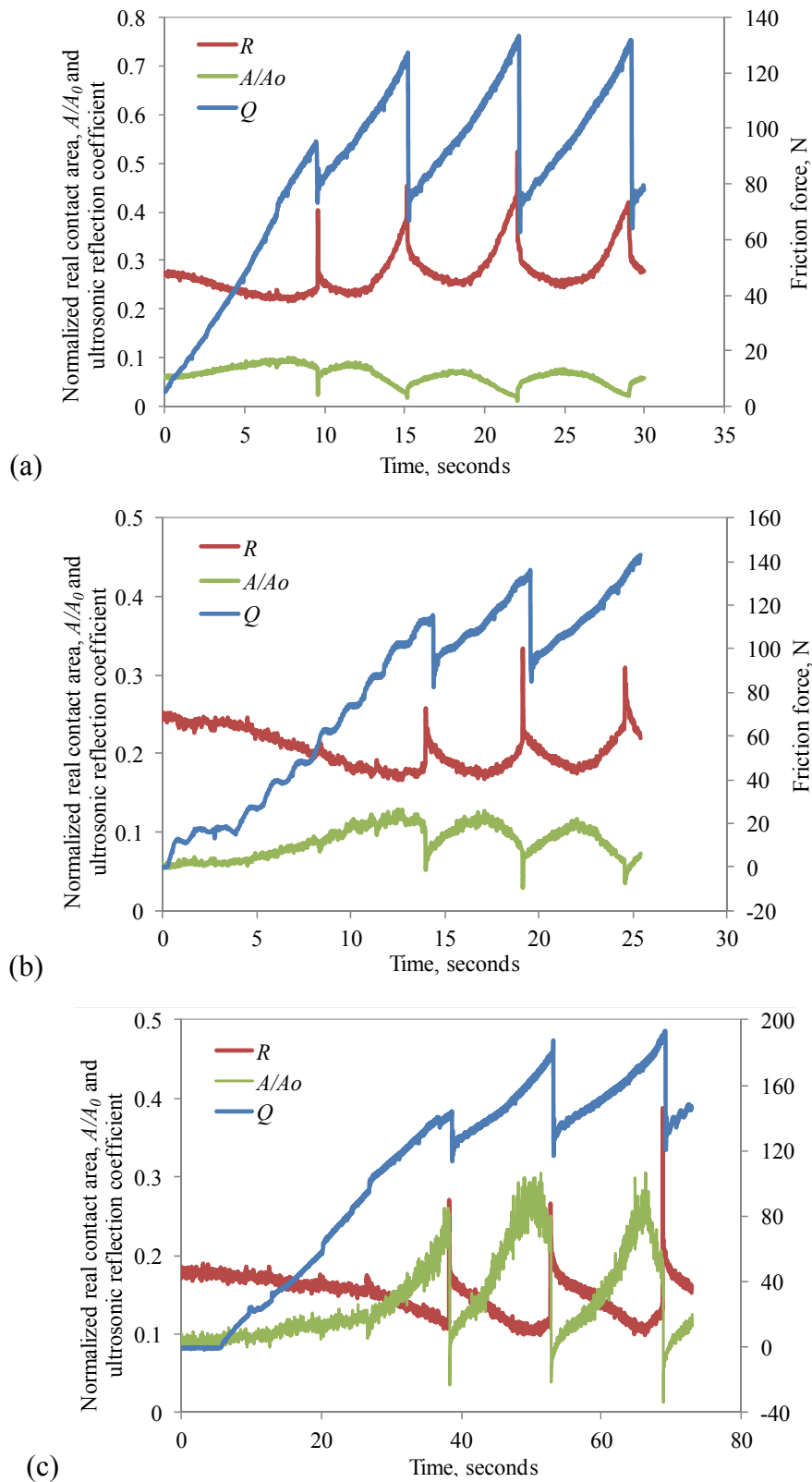


Figure 7.25. Normalised real contact area, ultrasonic reflection measurement and recorded friction force against time for Perspex 12 mm diameter at (a) 2.59 MPa (293 N), (b) 3.46 MPa (391 N), and (c) 4.32 MPa (489 N).

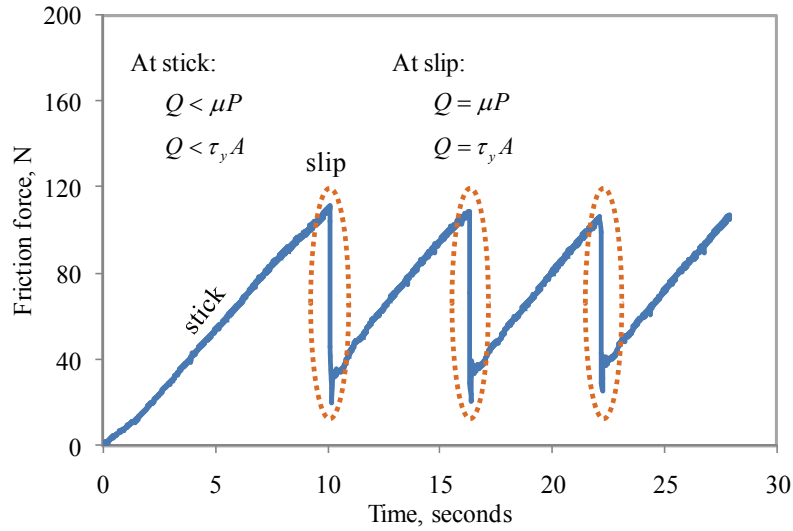


Figure 7.26. Friction force evolution during stick-slip process in a sliding contact.

From Figure 7.26, it can be seen that the shear force (friction force) increases in the stick phase. Assume Amontons's law of friction with a constant coefficient  $\mu$ , holds, the traction force on the interface,  $Q$ , is therefore lower than the product of the friction coefficient and the normal load,  $P$ :

$$Q < \mu P \quad (7.13)$$

The traction force on the interface increases with time in the stick phase and approaches the threshold where sliding takes place, which is marked by a dashed circle in Figure 7.26. Within the stick phase, the shear stress is lower the limiting value. While at slip, it reaches the limiting shear stress and the sliding takes place. Thus, the traction force on a single asperity is:

$$Q_i = \tau_{yi} A_i \quad (7.14)$$

Where  $A$  is the real contact area,  $i$  denotes the  $i^{th}$  contact spot. It is assumed that the limiting shear stress is the same for all contacting asperities. Limiting shear stress is denoted by  $\tau_y$ . Therefore, the total traction force becomes:

$$Q = \tau_y \sum A_i \quad (7.15)$$

As the real contact area is the integration of each single interacting asperity, the following equation is then used to express the relationship between the traction force and the real contact area:

$$Q = \tau_y A \quad (7.16)$$

Under a certain pressure, the real contact area can be obtained from the measured shear stiffness by using Equation (7.10). Thus the limiting shear stress,  $\tau_y$ , can be determined through above equation as the shear force,  $Q$ , has been recorded.

Simultaneously, Amonton's law of friction is applied to the sliding, therefore, Equation (7.13) becomes:

$$Q = \mu P \quad (7.17)$$

Figure 7.26 shows an example of the friction force varying with time in a stick and slip process. The threshold from stick to slip was high-lighted by a dashed circle. It can be seen that the highest shear force occurs just at the start of each 'slip'. Typically the sliding lasts less than one tenth of a second. This can be seen from Figure 7.21. It was dependent on the stiffness of the spring used in the housing for holding the specimen.

From Equation (7.16), it can be concluded that for a certain contact, a linear relationship between the traction force and the real contact area is expected. The traction force has been recorded during the stick and slip process. The real contact area can be determined from Equation (7.10), while the shear stiffness of the interface was obtained from the ultrasonic reflection measurement. Thus, the relationship between the shear force and the real contact area can be investigated. Figure 7.27 shows the normalised real contact area against the friction force from experimental measurement with the normal pressure from 0.87 MPa to 4.32 MPa. The ratio between the traction force and the real contact area and the normal pressures were shown next to the data markers. Under all pressure cases, the limiting shear force was found below 8 MPa, which was much lower than the bulk shear modulus,  $G = 1.19$  GPa (shown in Table 7.2). The distribution of the normalised real contact area along the trend line shows an approximate linear relationship between the real contact area and the shear force. Therefore, according to the experimental results in

this study, the shear force at the slip is expected to be proportional to the real contact area.

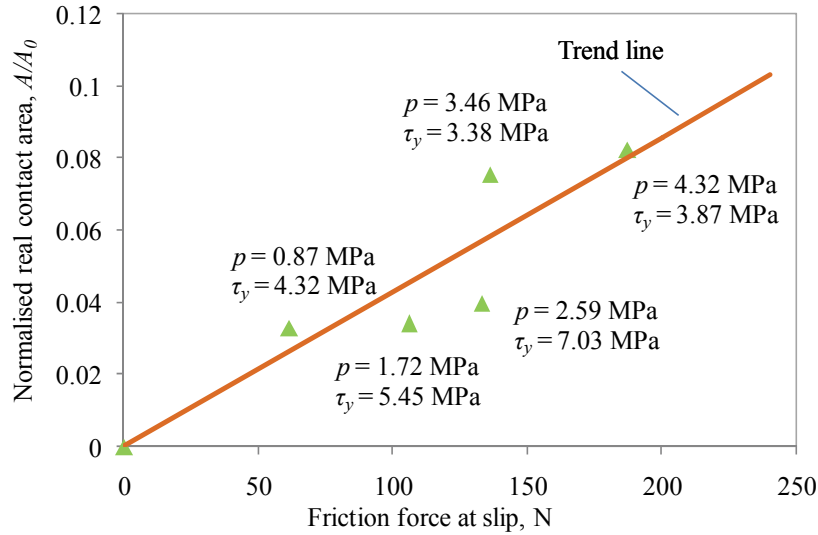


Figure 7.27. Normalised real contact area varying with friction force at slip for 12 mm Perspex specimen.

## 7.5 Conclusions

The aim of this study is to investigate characteristics for a sliding contact using the ultrasonic technique. Here are a few conclusions arisen from this work:

Firstly, the ultrasonic reflection was recorded with varying nominal load. Hysteresis phenomenon of the interface was investigated through loading/unloading cycles. This showed the occurrence of plastic deformation of asperities. For engineering rough surface contact, the elasto-plastic deformation of asperities should be taken into consideration.

The stick-slip of a Perspex-Perspex interface was studied by recording the shear ultrasonic reflection and the shear force, which were used for calculation of shear stiffness and real contact area. The reflection coefficient was found to decrease in the stationary stage before slip, and later fluctuating periodically with stick-slip cycles. The asperity interaction nature has not been understood completely, but the study of interfacial shear stiffness provides a new experimental method. The real contact area was estimated from the shear stiffness. For a stationary interface, the real contact area normalised by apparent contact area was found to be up to 30%, which shows good

agreement with other researchers' work. It confirms again that the feasibility of ultrasonic method in studying the interface in the microscopic scale. At slip where the limiting shear stress was reached, the relationship between the real contact area and the shear force was investigated. It was found that the shear force at the interface was linear to the real contact area.



# Chapter 8 General Discussion

## 8.1 Characterisation of an Engineering Interface

Engineering contacts can be divided into two categories: conformal or non-conformal contact. The Hertzian contact model is a classic theory for non-conformal contact based on a few key assumptions: smooth and frictionless bodies, semi-infinite elastic half spaces, non-conforming radii of curvature and so on. According to these rules, contact between the pin and bush on the landing gear is typically a conformal contact. Therefore, Persson's model, which was especially deduced for a conformal contact problem was adopted to analyse the pin joint contact. The contact pressure distribution and contact size were studied for the articulating pin joint. Hertzian model was also applied in order to compare with Persson's model (Chapter 6). Under lower pressures, little difference was observed between two models. However, with increasing pressure, the Persson's model predicted a 'high' and 'narrow' pressure distribution compared to Hertzian model. Greater deviation between the Persson's model and experimental results were found. Hertzian model gave a better simulation for this pin joint contact, even though the assumption of small footprint area was broken. Hence, in the modelling of articulating pin joint, the Hertzian contact analysis should be selected.

Parameters used for characterising engineering interface include contact stress, contact size, mean separation and so on. There is another useful parameter which can be used, known as contact stiffness. The normal interfacial stiffness describes the resistance to deformation in the vertical direction at the interface. Similarly, the shear interfacial stiffness indicates the resistance in the tangential direction.

The ultrasonic reflection technique is sensitive to the stiffness of the interface and

therefore in this study it was chosen for analysing static/dynamic engineering interface, with or without lubrication.

Firstly, static dry contact for a steel ball-on-disc configuration (Chapter 4) was analysed by means of normal contact stiffness. The simulation gave a dry contact stiffness of 5.6 GPa/ $\mu\text{m}$ , which was eight times lower than the ultrasonic measured value. The agreement between models of dry asperity contact and ultrasonic data was difficult to achieve. Poor agreement has also been observed in earlier work in this area (Królikowski and Szczepek, 1991; Drinkwater *et al.*, 1996). This might be caused by the input parameters of the simulation model, e.g., it is difficult to accurately measure surface roughness. Roughness parameters are dependent on the measurement scale used (Thomas, 1998) and it is likely that the measurement scale imposed by a stylus profilometer differs significantly from that of an ultrasonic wave striking the asperity. Meanwhile, the transmission of ultrasound waves relies on the elastic movement of material particles. Whether the microscopic deformation is elastic or plastic it is regulated by contact pressure and needs to be understood. The disagreement is an issue that remains to be resolved. Closer agreement with experimental data for this dry contact is observed using the modelling approach where roughness data is obtained by fitting ultrasonic data to model predictions (Baltazar *et al.*, 2002; Pecorari and Poznic, 2006). For static wet contact, a similar discrepancy between simulation and experiment was observed as well.

Secondly, the analysis of normal contact stiffness was applied to dynamic lubricated sliding contact between a steel ball and disc up to the speed of 2 m/s (Chapter 4). The interface composed of three media: two rough surfaces and a lubricant. In the mixed lubrication regime, the normal contact stiffness measured by ultrasonic method shows an integral value, contributed by both asperity interaction and lubricant layer. The concept of abstracting them from each other was firstly given by Dwyer-Joyce *et al.* (2011). By combining with the mixed lubrication model, the contribution from asperity contact and liquid layer were obtained for the mixed lubricated EHL problem. This method was also validated against Hamrock and Dowson theory (1976; 1977).

Finally, shear stiffness was used for representing the deformability in tangential direction

of the engineering interface. Ultrasonic study of shear stiffness on static and stick-slip contact was carried out. For the static contact, a clear hysteresis was found which was recently studied by many researchers (Drinkwater *et al.*, 1996; Kim *et al.*, 2004; Konowalski, 2009). The hysteresis was observed even when the applied pressure was 12.96 MPa for the Perspex contact, which was much lower than the bulk yield stress 84 MPa. This indicated that asperities on the rough surfaces might have plastically deformation, even though the bulk material was expected to be in elastic deformation state. This observation has been confirmed by other studies (Drinkwater *et al.*, 1996; Baumberger, 1997; Berthoud and Baumberger, 1998). Also, the shear stiffness was found to be effected by the relative movement speed between mating surfaces. It implies that the real contact area might depend on the interaction time of asperity junctions. Quicker movement reduces the interlock of asperities and brings a fast deflection of asperity tips. This is a thinking arisen from the study and more verification is needed. However, it does not prevent the use of shear stiffness becoming a tool for understanding the nature of a sliding interface.

## **8.2 Statistical Contact Model**

Hertzian elastic contact theory is based on the smooth and frictionless surfaces. However, for real engineering surfaces, contacting surfaces are rough with random distributed asperities with unknown height distribution which is usually considered as a Gaussian function. The nominal contact area is not always a small scale like plane contact. The actual characteristics of the interface are determined by the properties of these peaks. The approach of two matching surfaces is accompanied with deformation of micro-contact spots. In order to study the local contact stress or deformation state of asperities, a microscopic contact model should be adopted.

Theoretical models for interface analysis can be divided into two types based on how the roughness parameter is generated: stochastic models and deterministic models. The deterministic models are based on the geometric topography and surface profile of the real surface. But, due to the complex surface structure and limitations in duplicating topography of the real engineering surface, for large geometric contact problems it is

impossible to involve the full scale of texture in the computation, necessary simplification has to be made. Stochastic models use selected statistical parameters to represent the characteristics of rough surfaces. This provides a simplified mathematical tool to deal with rough surface contact, thus it has been widely adopted nowadays. One classic statistical rough contact model was developed by Greenwood and Williamson (1966) based on the stochastic theory. In this model, statistical parameters of rough surfaces are used to represent surface characteristics. Some improvement has been made to enlarge the application area (Whitehouse and Archard, 1970; Onions, 1973; Bush *et al.*, 1975; Chang *et al.*, 1987), such as compliance with elasto-plastic or plastic model deformation of asperities. This simple rough contact model still cannot provide detailed information about the distribution of local pressure at interaction junctions, film thickness fluctuations along the rough interface because of the local texture, and asperity deformation, which are usually considered to be critical for the study of lubrication breakdown and surface failure mechanisms. Since the rough surface lubrication is very complicated, it is difficult to capture the influence of surface topography satisfactorily with only a simple mathematical expression and a small number of stochastic parameters. Even though the statistical method has inevitable shortcomings, it has been successfully applied to a greased journal bearing and shows good agreement to experiments (Lu and Khonsari, 2007). The contact for a journal bearing is a typical conformal contact problem which has relatively large scale interface on which statistical model shows better applicability than deterministic theory. In this study, based on the statistical theory of surface parameters, the GW model has been adopted to develop a mixed lubrication model for engineering contact problems.

### **8.3 Ultrasonic Measurement**

In the past, for rough surfaces contact, the real contact area, along with contact size and pressure distribution, and how they vary with load, have been studied using techniques, such as optical, thermal and electrical conduction, none of which have proved satisfactory (Woo and Thomas, 1980). Ultrasonic technique has been proven to be a useful method in investigating engineering interfaces. In this study, the ultrasound technique has been

used to measure the contact parameters based on the measurement of the coefficient of reflection/transmission of ultrasonic waves from/through a contact interface. For a steel ball sliding on disc configuration, ultrasonic method provides an approach to study a mixed EHL problem. In studying the contact between the pin and bush on landing gear, it has been used to analyse the pressure distribution and real contact size. Finally, the method was applied to sliding contacts, Perspex-Perspex and steel-steel. The ultrasonic reflection and friction force were recorded to investigate the evolution of shear stiffness, real contact, and friction coefficient in the stick-slip process.

For the sliding contact between a steel ball and disc, the ultrasonic method was used for measuring the normal contact stiffness for static/dynamic and dry/lubricated cases. The ultrasonic reflection coefficient was found to be around 0.2 under a mean Hertzian pressure of 0.72 GPa, when the ball was stationary without lubricant on the interface. The normal contact stiffness was found to be of 40 GP/ $\mu\text{m}$  by using a simple ultrasonic spring model. In order to get a relative low ultrasonic reflection, the normal pressure was around four times than the study of Drinkwater *et al.* (1996) and two times higher than that of Królikowski and Szczepk's work (1991). Compared to theoretical stiffness, the experimental results showed much higher values. The error was believed to arise from the elastic micro-contact model, which underestimated the real contact area. The greater contact area in the tests was believed to be due to the deformation of asperities, which must undergo an elasto-plastic phase. A similar phenomenon was also observed for the static wet case, where the ball slide for a few cycles initially to wet the interface and then kept stationary for measurement. The ultrasound waves were reflected back from the filled lubricant in the asperity gaps and asperity junctions. The combined reflection coefficient presents a much lower value of around 0.07 while 0.2 for static dry contact.

For the problem of Perspex contact, the ultrasonic method shows a unique advantage in determining real contact area through the relationship between shear stiffness and contact area. It has been found that the real contact area is significantly low compared to the nominal contact area and the stresses at the asperities are considerably higher than the average contact pressure. The real contact area using the statistical asperity micromechanical contact model for elasto-plastic material has been theoretically

calculated by Kim *et al.* (2004) and Baltazar *et al.* (2006). In this study, the normalized real contact area (ratio of real contact area to nominal contact area) was found to be within 22%, which was comparable to the observation of Kim *et al.* (2004), who reported a range of 0-0.23 for aluminium contact.

Even though, the ultrasonic method has shown significant benefits in measuring interface parameters. There are still some limitations in applying this technique. For focusing transducer, the method is limited by the size of the focused spot. The obtained reflection measurement represents an average over the spot diameter. So, for the calculation of contact pressure, it is an average value also. It is therefore incapable of studying the pressure distribution for a relative small contact spot, such as those in a ball bearing. Besides, a couplant is required in application. It is not a problem for contact transducers, but is inconvenient when using focusing transducers as water bath is needed between the transducer and the component. The structure of the specimen or configuration of the interface does not always allow the installation of a water bath.

## **8.4 Mixed Solid-liquid Contact**

Two mixed solid-liquid contacts have been studied to investigate the effect from the liquid film and asperity interaction on interface properties, including contact stiffness, shear force, contact size, pressure distribution and so on. A mixed lubrication model was developed and used to predict interface characteristics and then compared with experimental measurements.

The load sharing proportions and film thickness were predicted for the ball-on-disc configuration in the speed range of 0-0.5 m/s under a nominal pressure up to 0.84 GPa (80 N), shown in Figure 4.11, Chapter 4. Over the whole speed range, full separation of mating surfaces did not occur as the load sharing proportion was found to be in the range of 80% - 93% when the sliding speed varied from 0.2 m/s to 0.5 m/s. Furthermore, the film thickness parameter was found below 1, which confirmed that solid contact existed and the asperity interaction could not be neglected. However, full film separation was not observed under any operating conditions in this study. Even though both liquid action

and asperity interaction shared the total load, it should be noted that most of the load was supported by the liquid layer.

The simulated film thickness at 0.5 *m/s* was about 0.3  $\mu\text{m}$ , which agrees well with the widely accepted EHL film thickness, 0.1-1 $\mu\text{m}$ . It is interesting to see that the lower loads lead to thicker film thickness but lower hydraulic load sharing percentage (expressed as  $1/\gamma_1$ ) from Figure 4.6. This is because the formation of elastohydrodynamic film is highly dependent on the pressure-viscosity of oil. It has been shown theoretically that under specific conditions of intense local contact pressure an EHL film can be formed. So the load needs to be high enough to compress the liquid layer and get improved viscosity.

Stiffness of both liquid layer and asperity contact for the ball and disc interface were predicted. The stiffness of the lubricant layer was found to be much higher than the asperity contact part for all loads and speeds. For example, at a pressure of 0.76 GPa and a speed of 0.3 *m/s*, the ratio between liquid stiffness to solid contact stiffness was found to be 58. This is because the liquid stiffness is more sensitive to film thickness according to Equation (2.13). Little change of thickness due to speed or load would make significant difference to stiffness. As a result, the total interface stiffness was mostly contributed by the liquid layer. Ultrasonic measurement for interface stiffness was carried out by Reddyhoff (2006) with the ball sliding speed varying from zero to 5 *m/s*. The comparison between experiment and simulation shows good agreement (Figures 4.15 and 4.17). The experiment method can only record the apparent properties of the interface; it cannot differentiate the lubricant layer component and asperity contact component. By using the theoretical scaling factors, the lubricant stiffness was extracted from the experimental stiffness. Therefore, the oil film thickness could be determined using Equation 2.13. It provides a method to separate the contribution from the lubricant layer and the asperity interaction at the interface.

The second mixed solid-liquid contact in this study was between a pin and bush on the landing gear (Chapter 5). This type of pin joint oscillates under low-speed and heavy-load. It is therefore considered to be operating in a boundary or mixed lubrication regime. A mixed lubrication model was developed and used for simulating the contact properties

for the pin joint. Parameters of working conditions, geometry, lubricant properties and pin/bush surface texture were used as inputs in the mixed lubrication model. Different from the ball-on-disc case, the load sharing proportion of asperity interaction was found to be around 99%, which was massively greater than hydraulic action, shown in Figures 5.10 and 5.11. The hydraulic effect tended to appear when the Sommerfeld number was above 0.001, which was beyond the typical operating condition of the joint. The lubricant thickness was assumed to be the mean separation of two mating rough faces. It was then used for the calculation of the film thickness parameter. In the pin joint operating regime, the film thickness parameter was found to be around 2, which indicated the severe lubrication condition on the pin joint interface.

In predicting friction coefficient, one critical parameter in this model is the “dry” friction coefficient,  $\mu_a$ , that represents the asperity contact points on the lubricated contact. From Figure 5.13 (b), it is clearly in the pin joint operation region the prediction of friction coefficient highly depended on the value selected for the dry friction coefficient,  $\mu_a$ . The data indicated that friction coefficients did not fall below 0.11 when  $\mu_a$  was 0.12. Actually, this parameter, and indeed the concept behind what actually is dry contact between asperities in a lubricated contact, are difficult to determine. It is difficult to know exactly the nature of the conditions are at the asperity-asperity contact. A surface coated with anti-wear or extreme pressure additive would have a friction coefficient in this area (Greenwood and Williamson, 1966). A similar value was used in the study of Gelinck and Schipper (2000) and Lu *et al.* (2006). As a further check the pin was rotated in the bush without any lubrication for a few cycles. The torque was measured for a range of applied loads and used to deduce the friction coefficient. Values in the range of 0.12 to 0.14 were recorded as the load varied from 5 to 35 kN. The lower bound of this range is in line with the value selected for the model. This is reasonable given that the dry case would not have any surface film that might be present in the boundary lubrication case.

Experiments were also performed on a purpose built apparatus to measure the torque during articulations of the pin and bush assembly under a range of load and speed. Under typical operating conditions, both the model and experiments showed that the pin joint operated in a boundary regime with hydrodynamic action having little effect on the



overall friction and load supporting. For practical purposes the agreement between model and experiment was good. The method shows validity of this model used for boundary lubrication problems.

# Chapter 9 Conclusions and Recommendation

## 9.1 Mixed Lubrication Model

A mixed lubrication model based on a concept that the total load on a lubricated contact is shared by asperity contact and liquid action has been established for a mixed EHL contact (a steel ball sliding on disc) and a conformal cylindrical contact (a pin sliding in a bush on the landing gear) in order to analyse load sharing factors, film thickness, friction force and friction coefficient at the interface.

Three equations were involved in the model. Input parameters include mating materials' mechanical properties, rough surfaces parameters, operating conditions and lubricant properties. A MathCAD program has been written for solving scaling factors (relating to load sharing proportions) and mean surfaces separation (relating to lubricant film thickness). Based on these simulations, friction force/friction coefficient/frictional torque (for pin joint) and lubricant layer stiffness/asperity contact stiffness were obtained for further analysis.

## 9.2 Mixed EHL Contact

By applying the mixed lubrication model, the contact between a sliding steel ball and disc was found operating in the mixed EHL regime under nominal load of 0.76 GPa and sliding speed 0-0.5 m/s. More than 50% of the normal load was found to be supported by the lubricating oil for all speeds. At the same sliding speed, the load sharing proportion was found to be greater at higher loads due to pressure-viscosity property of lubricant.

The GW model was applied to analyse stiffness for static dry and wet contacts. For dynamic lubrication, the predicted lubricant layer stiffness was found more than thirty times greater than asperity contact stiffness. The total interfacial normal stiffness was mostly contributed by lubricant layer. Simulation results were then compared to experimental stiffness determined from ultrasonic reflection coefficient. It shows good agreement for dynamic cases for all loads. But for static contact, theoretical prediction presented much lower stiffness compared to test results. It is therefore believed that the real contact area on the interface is greater than the prediction from the elastic-contact model.

Applying the scaling factors to experimental data, asperity stiffness and liquid stiffness were separated from the total interfacial stiffness. Film thickness was then calculated from the liquid stiffness. Under the nominal pressure of 0.72 GPa, the film thickness was found in the range of 0.08-0.45  $\mu\text{m}$ . It was then compared with Hamrock and Dowson's model, which showed a good agreement.

### **9.3 Pin Joint Contact**

An articulating pin joint on the landing gear has been chosen as a specimen for theoretical simulation and experimental study. A series of experiments have been carried out on the pin and bush assembly under a range of loads and speeds. Frictional torque was recorded for analysing the friction coefficient on the greased interface. Then the mixed lubrication model was built and a MathCAD program was written for solving the model. The load sharing proportions, mean surface separation and friction coefficient were determined. Under the typical operating region of the pin joint (very high load and slow speed), the lubrication was found to be in the boundary regime where asperity interaction is severe, the hydraulic action plays little effect on load sharing. Comparison between simulation results and experimental measurements has been made. The model has been shown to be an acceptable method for predicting friction performance of low speed and high load articulating contact.

The contact pressure distribution and contact size were also studied for a pin joint using

theoretical models and ultrasonic measurements. By using an experiential linear relationship between ultrasonic stiffness and contact pressure, the contact stress and friction torque on the interface were obtained through analysing ultrasonic measurements. Under all load cases, the pressure was found distributed over the wrap angle from  $-60^\circ$  to  $60^\circ$ . The peak pressure under 40 kN was found to be 23 MPa. Classic Hertzian theory and Persson's conformal contact model were adopted for analysing the pressure distribution and contact size as well. Both models predicted a higher peak pressure and a smaller contact size compared to experimental results. But, Hertzian predictions were shown to be more close to the ultrasonic measurements. The simulation torque was found to agree very well with the experiment recording. It was also found that the traditional way for calculating frictional torque underestimates the real torque occurring on the interface as the tangential components of pressure that do not support normal load but contributes to friction. The ratio between the true torque and the nominal torque was found to be  $1.1 \pm 0.01$ . Therefore, it is suggested that 110% of the nominal torque should be considered in the pin joint design.

## **9.4 Ultrasonic Investigation for Static/Dynamic Interfaces**

Ultrasonic measurements have been used for studying the properties of interfaces in both normal and tangential directions. For the mixed EHL contact, the normal stiffness was calculated from the ultrasonic measurements for a start-up process. The comparison between theoretical simulations and experimental results were made. A good agreement between predictions and experimental observations was found for the dynamic contact. But for static contacts, the models underestimated the contact stiffness. A large deviation was found between simulations and experimental results.

The ultrasonic reflections were also used for analysing the pin joint contact. The contact size was found from  $-60^\circ$  to  $60^\circ$  for all load cases. The normal contact stiffness was determined from the ultrasonic reflection using the spring model. Based on the linear relationship between the contact pressure and the stiffness, the contact pressure distribution was then presented against the wrap angle. The pressure distribution was found to be close to a cosinusoidal distribution.

A shear study on Perspex-Perspex and steel-steel contacts has been carried out using an ultrasonic 5 MHz shear transducer. For static contact cases, the hysteresis phenomenon at the interface was studied through loading/unloading cycles. A clear hysteresis lag was observed, which indicated the plastic deformation of asperities. Therefore in the characterisation of the interface, the deformation state of rough asperities should be considered.

In the stick-slip process of the Perspex-Perspex sliding contact, the ultrasonic reflection was recorded to investigate the shear stiffness evolution at the interface. The interfacial shear stiffness was found to increase in the stick phase and fluctuate periodically with stick-slip repeats. The relationship between the shear stiffness and the real contact area was deduced. Based on the shear stiffness calculated from ultrasonic reflection, the real contact area at the interface was then determined and found to show a similar varying trend to the shear stiffness. The normalised contact area was found to be up to 30% of the apparent area, which showed a good agreement with other researchers' work. It shows the feasibility of the ultrasonic method in determining the interfacial stiffness and the real contact area. In the slip phase, the relationship between the real contact area and the shear force was analysed. The real contact area was found to increase with the shear force. An approximate linear relation was observed between them.

## **9.5 Future Work**

The work in this thesis contained three parts, the first part stressed how the mixed lubrication mode was established and applied to engineering interfaces. The second is the investigation of the pressure distribution, contact size, and the real friction torque/coefficient. The third piece of the work is the study of the shear properties of a stick-slip interface. From the work undertaken, a series of recommendations can be summarized for further investigation.

One of the areas for further study is the determination of input parameters for the mixed lubrication model. The density of asperity distribution, the average radius and the standard deviation of asperity height were calculated as an average value from

two-dimensional measurement data of the mating surfaces using MathCAD. This could only give an approximate value. A three-dimensional reproduction of the real rough surfaces should be carried out, which represents the real properties of the interface. More accurate simulations can therefore be obtained for the analysis of the interface.

The second work that should be further considered is the 'dry' friction coefficient. It is the friction coefficient of a single junction of a pair asperity. In the current model it is assumed to be the same for all asperity junctions, known as the dry friction coefficient in the mixed lubrication regime. This parameter can only be obtained from experiment, but it is very difficult to measure, especially in the presence of a lubricant, where all the asperity peaks have been 'wetted'. More theoretical understanding and experimental work represent the further study.

Another recommendation arises from the prediction of the static interfacial stiffness. In the present study, it has been found that there is little agreement between ultrasonic measurements and model predictions. Further investigation of the numerical model for static contact stiffness is required.

The final recommended for further work comes from the interface nature of engineering contacts. The first method has been addressed in this study by using ultrasonic method to analyse the friction and real contact area evolution during the static and dynamic process. Shear stiffness and normal stiffness are two important parameters in disclosing the interface properties. If they can be obtained through the ultrasonic method at the same time, it will be helpful in understanding the local stress distribution, real contact area, and friction and wear on the interfaces. So the work recommended is to build a test rig by applying both the normal and shear transducers. This rig can also be used for studying the lubricated interface. This also provides a method to separate liquid layer stiffness from asperity contact stiffness.

## 9.6 Publications Arising from this Work

### Journal papers:

Zhu, J., Pugh, S., and Dwyer-Joyce, R.S., 2011, "Model and Experiments to Determine Lubricant Film Formation and Frictional Torque in Aircraft Landing Gear Pin Joints", *Proceedings of the Institution of Mechanical Engineers, Part J: Journal of Engineering Tribology*, Vol.226(4), pp 315-327.

Dwyer-Joyce, R.S., Reddyhoff, T., and Zhu, J., 2011, "Ultrasonic Measurement for Film Thickness and Solid Contact in Elastohydrodynamic Lubrication", *ASME, Journal of Tribology*, Vol.133(3), (doi:10.1115/1.4004105).

Zhu, J., Pugh, S., Dwyer-Joyce, R.S., Beke, A., Cumner, G., and Ellaway, T., 2010, "Experiments on the Pressure Distribution and Frictional Torque in Articulating Pin Joints", *Proceedings of the Institution of Mechanical Engineers, Part J: Journal of Engineering Tribology*, Vol.224(10), pp 1153-1162.

### Conference papers:

Zhu, J., Pugh, S., and Dwyer-Joyce, R.S., 2010, "Model and Experiments to Predict Lubricant Film Formation and Frictional Torque in Articulating Pin Joints", *Proceedings of the STLE/ASME 2010 International Joint Tribology Conference (IJTC 2010)*, San Francisco, California, USA, Paper no. IJTC2010-41061.

Dwyer-Joyce, R. S., Zhu, J., and Reddyhoff, T., 2010, "Ultrasonic Measurement for Film Thickness and Solid Contact in Elastohydrodynamic Lubrication", *Proceedings of the STLE/ASME 2010 International Joint Tribology Conference (IJTC 2010)*, San Francisco, California, USA, Paper no. IJTC2010-41080.

Pugh, S., Zhu, J., and Dwyer-Joyce, R.S., 2010, "Experiments on Grease Performance in Aircraft Landing Gear Pin Joints", *Proceedings of the STLE/ASME 2010 International Joint Tribology Conference (IJTC 2010)*, San Francisco, California, USA, Paper no. IJTC2010-41101.

## Reference

- Ai, X. and Cheng, H.S., 1996, "The Effects of Surface Texture on EHL Point Contacts", *Journal of Tribology*, Vol.118(1), pp 59-66.
- Arakawa, T., 1983, "A Study on the Transmission and Reflection of an Ultrasonic Beam at Machined Surfaces Pressed against Each Other", *Materials Evaluation*, Vol.41, pp 714-719.
- Baik, J.M. and Thompson, R.B., 1984, "Ultrasonic Scattering from Imperfect Interfaces: a Quasi-Static Model", *Journal of Nondestructive Evaluation*, Vol.4(3), pp 177-196.
- Bair, S. and Winer, W.O., 1979, "A Rheological Model for Elastohydrodynamic Contacts Based on Primary Laboratory Data", *ASME, Journal of Lubrication Technology*, Vol.101, pp 258-265.
- Bair, S. and Winer, W.O., 1990, "The High Shear Stress Rheology of Liquid Lubricants at Pressures of 2 to 200 MPa", *Journal of Tribology*, Vol.112(2), pp 246-252.
- Bair, S., 2007, *High Pressure Rheology for Quantitative Elastohydrodynamics*, Elsevier Science, Oxford.
- Baltazar, A., Kim, J.Y., and Rokhlin, S.I., 2006, "Ultrasonic Determination of Real Contact Area of Randomly Rough Surfaces in Elastoplastic Contact", *Revista Mexicana de Fisica*, Vol.52, pp 37-47.
- Baltazar, A., Rokhlin, S.I., and Pecorari, C., 2002, "On the Relationship between Ultrasonic and Micromechanical Properties of Contacting Rough Surfaces", *Journal of the Mechanics and Physics of Solids*, Vol.50(7), pp 1397-1416.
- Baumberger, T., 1997, "Contact Dynamics and Friction at a Solid-Solid Interface: Material versus Statistical Aspects", *Solid State Communications*, Vol.102(2-3), pp 175-185.
- Berthoud, P. and Baumberger, T., 1998, "Shear Stiffness of a Solid--Solid Multicontact Interface", *Proceedings of the Royal Society of London, Series A: Mathematical*,



*Physical and Engineering Sciences*, Vol.454, pp 1615-1634.

Bush, A.W., Gibson, R.D., and Thomas, T.R., 1975, "The Elastic Contact of a Rough Surface", *Wear*, Vol.35(1), pp 87-111.

Cameron, A. 1971, *Basic lubrication theory*, Longman, Harlow.

Chang, W.R., Etsion, I., and Bogy, D.B., 1987, "An Elastic-Plastic Model for the Contact of Rough Surfaces", *Journal of Tribology*, Vol.109(2), pp 257-263.

Chen, H.H. and Marshek, K.M., 1988, "Effect of Clearance and Material Property on Contact Pressure in Two-Dimensional Conforming Cylinders", *Mechanism and Machine Theory*, Vol.23(1), pp 55-62.

Christensen, H., 1969, "Stochastic Models for Hydrodynamic Lubrication of Rough Surfaces", *Proceedings of the Institution of Mechanical Engineers*, Vol.184, pp 1013-1026.

Ciavarella, M. and Decuzzi, P., 2001, "The State of Stress Induced by the Plane Frictionless Cylindrical Contact. I. The Case of Elastic Similarity", *International Journal of Solids and Structures*, Vol.38(26-27), pp 4507-4523.

Colbert, R.S., Alvarez, L.A., Hamilton, M.A., Steffens, J.G., Ziegert, J.C., Burris, D.L., and Sawyer, W.G., 2010, "Edges, Clearances, and Wear: Little Things that Make Big Differences in Bushing Friction", *Wear*, Vol.268(1-2), pp 41-49.

Cook, R.L., King, H.E., Herbst, C.A., and Herschbach, D.R., 1994, "Pressure and Temperature Dependent Viscosity of Two Glass Forming Liquids: Glycerol and Dibutyl Phthalate", *The Journal of Chemical Physics*, Vol.100(7), pp 5178-5189.

Dowson, D., 2001, "New Joints for the Millennium: Wear Control in Total Replacement Hip Joints", *Proceedings of the Institution of Mechanical Engineers, Part H: Journal of Engineering in Medicine*, Vol.215, pp 335-358.

Drinkwater, B.W., Dwyer-Joyce, R.S., and Cawley, P., 1996, "A Study of the Interaction between Ultrasound and a Partially Contacting Solid--Solid Interface", *Proceedings of the Royal Society of London, Series A: Mathematical, Physical and Engineering Sciences*, Vol.452(1955), pp 2613-2628.

Dwyer-Joyce, R.S., Drinkwater, B.W., and Quinn, A.M., 2001, "The Use of Ultrasound in the Investigation of Rough Surface Interfaces", *Journal of Tribology*, Vol.123(1), pp 8-16.

Dwyer-Joyce, R.S. and Drinkwater, B.W., 2003, "In Situ Measurement of Contact Area and Pressure Distribution in Machine Elements", *Tribology Letters*, Vol.14(1), pp 41-52.

Dwyer-Joyce, R.S., Drinkwater, B.W., and Donohoe, C.J., 2003, "The Measurement of Lubricant--Film Thickness Using Ultrasound", *Proceedings of the Royal Society of London, Series A: Mathematical, Physical and Engineering Sciences*, Vol.459(2032), pp 957-976.

Dwyer-Joyce, R.S., Reddyhoff, T., and Zhu, J., 2011, "Ultrasonic Measurement for Film Thickness and Solid Contact in Elastohydrodynamic Lubrication", *ASME, Journal of Tribology*, Vol.133(3), (doi:10.1115/1.4004105).

Dwyer-Joyce, R.S., Reddyhoff, T., and Drinkwater, B.W., 2004, "Operating Limits for Acoustic Measurement of Rolling Bearing Oil Film Thickness", *Tribology Transactions*, Vol.47(3), pp 366-375.

Elrod, H., 1973, "Thin-Film Lubrication Theory for Newtonian Fluids with Surfaces Possessing Striated Roughness or Grooving", *ASME Journal of Lubrication Technology*, Vol.93, pp 324-330.

Fakhreddine, Y.A. and Zoller, P., 1990, "The Equation of State of a Polydimethylsiloxane Fluid", *Journal of Applied Polymer Science*, Vol.41(5-6), pp 1087-1093.

Fein, R., 1997, *High Pressure Viscosity and EHL Pressure-Viscosity Coefficients*, *Tribology Data Handbook*, CRC Press, Boca Raton, FL, pp 638-644.

Gasni, D., WanIbrahim, M.K., and Dwyer-Joyce, R.S., 2011, "Measurements of Lubricant Film Thickness in the Iso-viscous Elastohydrodynamic Regime", *Tribology International*, Vol.44, pp 933-944.

Gelinck, E.R.M. and Schipper, D.J., 1999, "Deformation of Rough Line Contacts", *Journal of Tribology*, Vol.121(3), pp 449-454.

Gelinck, E.R.M. and Schipper, D.J., 2000, "Calculation of Stribeck Curves for Line Contacts", *Tribology International*, Vol.33(3-4), pp 175-181.

Glaeser, W.A. and Dufrane, K.F., 1977, "Performance of Heavily-loaded Oscillatory Journal Bearings", *ASLE Transactions*, Vol.20(4), pp 309-314.

Gonzalez-Valadez, M., 2006, *Ultrasonic Investigation of Contacts in Dry and Mixed Lubrication Regimes*, PhD Thesis, The University of Sheffield.

Greenwood, J.A. and Williamson, J.B.P., 1966, "Contact of Nominally Flat Surfaces", *Proceedings of the Royal Society of London, Series A: Mathematical and Physical Sciences*, Vol.295, pp 300-319.

Haines, N.F., 1980, "The Theory of Sound Transmission and Reflection at Contacting Surfaces", *CEGB Report RD/B/N4744*.

Hamrock, B.J. and Dowson, D., 1976, "Isothermal Elastohydrodynamic Lubrication of Point Contacts. I - Theoretical Formulation", *Journal of Lubrication Technology*, Vol.98(2), pp 223-229.

Hamrock, B. J. and Dowson, D., 1977, "Isothermal Elastohydrodynamic Lubrication of Point Contacts. III - Fully Flooded Results", *Journal of Lubrication Technology*, Vol.99(2), pp 264-276.

Hamrock, B. J., Schmid, S.R., and Jacobson, B., 2004, *Fundamentals of Fluid Film Lubrication*, Marcel Dekker, Inc, New York.

Harper, P., Dwyer-Joyce, R.S., Sjödin, U., and Olofsson, U., 2005, "Evaluation of an Ultrasonic Method for Measurement of Oil Film Thickness in a Hydraulic Motor Piston Ring", *Tribology and Interface Engineering Series*, Vol.48, pp 305-312.

Hertz, H., 1885, *Gesammelte Werke*, Vol.1, Leipzig.

Hirschfelder, J.O., Curtiss, C.F., and Bird, R.B., 1954, *Molecular Theory of Gases and Liquids*, John Wiley, New York.

Hisakado, T., 1969, "On the Mechanism of Contact between Solid Surfaces, 3rd Report", *Bulletin of JSME*, Vol.12, pp 1519-1527.

Hisakado, T., 1970, "On the Mechanism of Contact between Solid Surfaces, 4th Report", *Bulletin of JSME*, Vol.13, pp 129-139.

Hodson, K., Dwyer-Joyce, R.S., and Drinkwater, B.W., 2000, "Ultrasound as an Experimental Tool for Investigating Engineering Contacts", *Proceedings of the 9th Nordic Symposium on Tribology*, Nordic, Vol.2, pp 377-386.

Holmes, M.J.A., Evans, H.P., and Snidle, R.W., 2005, "Analysis of Mixed Lubrication Effects in Simulated Gear Tooth Contacts", *Journal of Tribology*, Vol.127(1), pp 61-69.

Hornig, J.H., 1998, "An Elliptic Elastic-Plastic Asperity Micro-contact Model for Rough Surfaces", *Journal of Tribology*, Vol.120(1), pp 82-88.

- Hosten, B., 1991, "Bulk Heterogeneous Plane Waves Propagation through Viscoelastic Plates and Stratified Media with Large Values of Frequency Domain", *Ultrasonics*, Vol.29(6), pp 445-450.
- Hu, Y.Z. and Zhu, D., 2000, "A Full Numerical Solution to the Mixed Lubrication in Point Contacts", *Journal of Tribology*, Vol.122(1), pp 1-9.
- Ichimaru, K., 2005, "A New Implementation of Reynolds Equation for Analyzing Mixed EHL", *ASME Conference Proceedings, World Tribology Congress III*, Vol.1, pp 499-500.
- Ito, Y., Toyoda, J., and Nagata, S., 1979, "Interface Pressure Distribution in a Bolt-Flange Assembly", *Journal of Mechanical Design*, Vol.101(2), pp 330-337.
- Jacobson, B. and Vinet, P., 1987, "A Model for the Influence of Pressure on the Bulk Modulus and the Influence of Temperature on the Solidification Pressure for Liquid Lubricants", *Journal of Tribology*, Vol.109, pp 709-714.
- Jacobson, B. and Kalker, J.J., 2000, *Rolling Contact Phenomena*, Springer, New York.
- Jacobson, B., 2006, "High-Pressure Chamber Measurements", *Proceedings of the Institution of Mechanical Engineers, Part J: Journal of Engineering Tribology*, Vol.220(3), pp 199-206.
- Jiang, X., Hua, D.Y., Cheng, H.S., Ai, X., and Lee, S.C., 1999, "A Mixed Elastohydrodynamic Lubrication Model with Asperity Contact", *Journal of Tribology*, Vol.121(3), pp 481-491.
- Johnson, K. L., 1985, *Contact Mechanics*, Cambridge, Cambridge University Press.
- Johnson, K.L., Greenwood, J.A., and Poon, S.Y., 1972, "A Simple Theory of Asperity Contact in Elastohydro-Dynamic Lubrication", *Wear*, Vol.19(1), pp 91-108.
- Kendall, K. and Tabor, D., 1971, "An Ultrasonic Study of the Area of Contact Between Stationary and Sliding Surfaces", *Proceedings of the Royal Society of London, Series A: Mathematical and Physical Sciences*, Vol.323(1554), pp 321-340.
- Khonsari, M.M. and Hua, D.Y., 1993, "Generalized Non-Newtonian Elastohydrodynamic Lubrication", *Tribology International*, Vol.26(6), pp 405-411.
- Kim, J.Y., Baltazar, A., and Rokhlin, S.I., 2004, "Ultrasonic Assessment of Rough Surface Contact Between Solids from Elastoplastic Loading–Unloading Hysteresis Cycle", *Journal of the Mechanics and Physics of Solids*, Vol.52(8), pp 1911-1934.

- Kogut, L. and Etsion, I., 2002, "Elastic-Plastic Contact Analysis of a Sphere and a Rigid Flat", *Journal of Applied Mechanics*, Vol.69(5), pp 657-662.
- Kondo, S., Sayles, R.S., and Lowe, M.J.S., 2006, "A Combined Optical-Ultrasonic Method of Establishing the Compressibility of High-Pressure Oil and Grease Films Entrapped in a Ball on Flat Contact", *Journal of Tribology*, Vol.128(1), pp 155-167.
- Konowalski, K., 2009, "Experimental Research and Modelling of Normal Contact Stiffness and Contact Damping of Machined Joint Surfaces", *Advances in Manufacturing Science and Technology*, Vol.33(3), pp 53-68.
- Królikowski, J. and Szczepek, J., 1991, "Prediction of Contact Parameters Using Ultrasonic Method", *Wear*, Vol.148(1), pp 181-195.
- Królikowski, J. and Szczepek, J., 1993, "Assessment of Tangential and Normal Stiffness of Contact between Rough Surfaces Using Ultrasonic Method", *Wear*, Vol.160(2), pp 253-258.
- Kweh, C.C., Evans, H.P., and Snidle, R.W., 1989, "Micro-Elastohydrodynamic Lubrication of an Elliptical Contact With Transverse and Three-Dimensional Sinusoidal Roughness", *Journal of Tribology*, Vol.111(4), pp 577-584.
- Lewis, R., Marshall, M.B., and Dwyer-Joyce, R.S., 2005, "Measurement of Interface Pressure in Interference Fits", *Proceedings of the Institution of Mechanical Engineers, Part C: Journal of Mechanical Engineering Science*, Vol.219(2), pp 127-139.
- Liu, G., Zhu, J., Yu, L., and Wang, Q.J., 2001, "Elasto-Plastic Contact of Rough Surfaces", *Society Tribologists and Lubrication Engineers, Annual Meeting No56*, Orlando, Florida, Vol.44(3), pp 437-443.
- Longuet-Higgins, M.S., 1957, "The Statistical Analysis of a Random, Moving Surface", *Philosophical Transactions of the Royal Society of London, Series A: Mathematical and Physical Sciences*, Vol.249(966), pp 321-387.
- Lu, X., Khonsari, M.M., and Gelinck, E.R.M., 2006, "The Stribeck Curve: Experimental Results and Theoretical Prediction", *Journal of Tribology*, Vol.128(4), pp 789-794.
- Lu, X. and Khonsari, M.M., 2007, "An Experimental Investigation of Grease-Lubricated Journal Bearings", *Journal of Tribology*, Vol.129(1), pp 84-90.
- Lunn, B., 1957, "Friction and Wear Under Boundary Lubrication: A Suggestion", *Wear*, Vol.1(1), pp 25-31.

- Manolov, N.T., 1970, *Acoustical Method of Investigation of Contact of Solids*, PhD Thesis, Moscow.
- Marshall, M.B., Lewis, R., Drinkwater, B.W., and Dwyer-Joyce, R.S., 2004, "An Ultrasonic Approach for Contact Stress Mapping in Machine Joints and Concentrated Contacts", *The Journal of Strain Analysis for Engineering Design*, Vol.39(4), pp 339-350.
- Marshall, M.B., Lewis, R., and Dwyer-Joyce, R.S., 2006, "Characterisation of Contact Pressure Distribution in Bolted Joints", *Strain*, Vol.42(1), pp 31-43.
- Marshall, M.B., Lewis, R., Dwyer-Joyce, R.S., Demilly, F., and Flament, Y., 2011, "Ultrasonic Measurement of Railway Wheel Hub–Axle Press-Fit Contact Pressures", *Proceedings of the Institution of Mechanical Engineers, Part F: Journal of Rail and Rapid Transit*, Vol.225(3), pp 287-298.
- McCool, J.I., 1986, "Comparison of Models for the Contact of Rough Surfaces", *Wear*, Vol.107(1), pp 37-60.
- Millat, J., Dymond, J.H., and Nieto de Castro, C.A., 1996, *Transport Properties of Fluids Their Correlation, Prediction and Estimation*, IUPAC (International Union of Pure and Applied Chemistry), Cambridge.
- Minakuchi, Y., Yoshimine, K., Koizumi, T., and Hagiwara, T., 1985, "Contact Pressure Measurement by Means of Ultrasonic Waves (on a Method of Quantitative Measurement)", *Bulletin of JSME*, Vol.28(235), pp 40-45.
- Moes, H., 1992, "Optimum Similarity Analysis with Applications to Elastohydrodynamic Lubrication", *Wear*, Vol.159(1), pp 57-66.
- Nayak, P.R., 1971, "Random Process Model of Rough Surfaces", *ASME, Journal of Lubrication Technology*, Vol.93(3), pp 398-407.
- Nayak, P.R., 1973, "Random Process Model of Rough Surfaces in Plastic Contact", *Wear*, Vol.26(3), pp 305-333.
- Nuri, K.A. and Halling, J., 1975, "The Contact of Surfaces in Sliding", *Wear*, Vol.32(1), pp 95-113.
- O'Callaghan, P.W. and Probert, S.D., 1987, "Prediction and Measurement of True Areas of Contact between Solids", *Wear*, Vol.120(1), pp 29-49.
- Onions, R.A. and Archard, J.F., 1973, "The Contact of Surfaces Having a Random

Structure", *Journal of Physics D: Applied Physics*, Vol.6(3), pp 289-304.

Patir, N. and Cheng, H.S., 1978, "An Average Flow Model for Determining Effects of Three-Dimensional Roughness on Partial Hydrodynamic Lubrication", *ASME, Journal of Lubrication Technology*, Vol.100, pp 12-17.

Pecorari, C. and Poznic, M., 2006, "On the Linear and Nonlinear Acoustic Properties of Dry and Water-Confining Elasto-Plastic Interfaces", *Proceedings of the Royal Society, Series A: Mathematical, Physical and Engineering Science*, Vol.462(2067), pp 769-788.

Pei, L., Hyun, S., Molinari, J.F., and Robbins, M., 2005, "Finite Element Modelling of Elasto-Plastic Contact between Rough Surfaces", *Journal of the Mechanics and Physics of Solids*, Vol.53(11), pp 2385-2409.

Persson, A., 1964, *On the Stress Distribution of Cylindrical Elastic Bodies in Contact*, PhD Thesis, Chalmers University.

Pullen, J. and Williamson, J.B.P., 1972, "On the Plastic Contact of Rough Surfaces", *Proceedings of the Royal Society of London, A: Mathematical and Physical Sciences*, Vol.327(1569), pp 159-173.

Raimondi, A.A. and Szeri, A.Z., 1984, *Journal and thrust bearings*, in *CRC Handbook of Lubrication, Vol.2*, Booser, E.R. (Ed.), CRC Press, New York.

Reddyhoff, T., 2006, *Ultrasonic Measurement Techniques for Lubricant Films*, PhD Thesis, the University of Sheffield.

Reddyhoff, T., Dwyer-Joyce, R.S., and Harper, P., 2008, "A New Approach for the Measurement of Film Thickness in Liquid Face Seals", *Tribology Transactions*, Vol.51(2), pp 140-149.

Redlich, A.C., Bartel, D., and Deters, L., 2003, "Calculation of EHL Contacts in Mixed Lubrication Regime", *Tribology Series*, Vol.41, pp 537-547.

Roelands, C.J.A., 1966, *Correlational Aspects of the Viscosity-Temperature-Pressure Relationship of Lubricating Oils*. PhD Thesis, Technische Hogeschool Delft, The Netherlands.

Rokhlin, S.I. and Wang, L., 2002, "Ultrasonic Waves in Layered Anisotropic Media: Characterization of Multidirectional Composites", *International Journal of Solids and Structures*, Vol.39(16), pp 4133-4149.

Savkoor, A.R., 1987, *Dry Adhesive Friction of Elastomers: A Study of the Fundamental*

*Mechanical Aspects*, PhD Thesis, Delft University of Technology.

Schoenberg, M., 1980, "Elastic Wave Behavior Across Linear Slip Interfaces", *The Journal of the Acoustical Society of America*, Vol.68(5), pp 1516-1521.

Soda, N., 1978, "Effect of Bearing Area and Surface Roughness in Fluid and Mixed Lubrication", *Journal of Japanese Society of Lubrication Engineers*, Vol.23, pp 22-30.

Soda, N., 1985, "Effect of Abbott Bearing Area on Characteristics of Stribeck Curve", *Journal of Japanese Society of Tribologists*, Vol.31, pp 637-642.

Stachowiak, G.W. and Batchelor, A.W., 2005, *Engineering Tribology (Third edition)*, Elsevier Butterworth-Heinemann, USA.

Ståhl, J. and Jacobson, B., 2003, "A Non-Newtonian Model Based on Limiting Shear Stress and Slip Planes--Parametric Studies", *Tribology International*, Vol.36(11), pp 801-806.

Stribeck, R., 1901, "Kugellager für beliebige Belastungen (Ball Bearings for any Stress)", *Zeitschrift des Vereins Deutscher Ingenieure* Vol.45.

Stribeck, R., 1902, "Die wesentlichen Eigenschaften der Gleit- und Rollenlager (Characteristics of Plain and Roller Bearings)", *Zeitschrift des Vereins Deutscher Ingenieure*, Vol.46.

Tallian, T.E., 1967, "On Competing Failure Modes in Rolling Contact", *ASLE Transactions*, Vol.10(4), pp 418 - 439.

Tallian, T.E., 1972, "The Theory of Partial Elastohydrodynamic Contacts", *Wear*, Vol.21(1), pp 49-101.

Tattersall, H.G., 1973, "The Ultrasonic Pulse-Echo Technique as Applied to Adhesion Testing", *Journal of Physics D: Applied Physics*, Vol.6(7), pp 819-832.

Temple, J.A.G., 1985, "The Effects of Stress and Crack Morphology on Time-of-Flight Diffraction Signals", *International Journal of Pressure Vessels and Piping*, Vol.19(3), pp 185-211.

Thomas, T.R. and Sayles, R.S., 1977, "Stiffness of Machine Tool Joints: A Random-Process Approach", *ASME, Journal of Engineering for Industry*, Vol.99(1), pp 250-256.

Thomas, T.R., 1998, *Rough Surfaces*, Imperial College Press, London.



Timoshenko, S.P. and Goodier, J.N., 1982, *Theory of Elasticity, Third Edition*, Singapore, Singapore: McGraw-Hill.

Tsao, Y.H. and Tong, K.N., 1975, "A Model for Mixed Lubrication", *ASLE Transactions*, Vol.18(2), pp 90-96.

Tsukada, T., Anno, Y., and Kamahora, F., 1972, "An Analysis of the Deformation of Contacting Rough Surfaces : 2nd Report, Estimation of the Initial Contact Positions", *Bulletin of JSME*, Vol.15, pp 989-995.

Tsukada, T. and Anno, Y., 1972, "An Analysis of the Deformation of Contacting Rough Surfaces : 3rd Report, Introduction of a New Contact Theory of Rough Surfaces ", *Bulletin of JSME*, Vol.15, pp 996-1003.

Tsukizoe, T. and Hisakado, T., 1965, "On the Mechanism of Contact between Metal Surfaces-the Penetrating Depth and the Average Clearance", *ASME, Journal of Basic Engineering*, Vol.87(3), pp 666-674.

Tsukizoe, T. and Hisakado, T., 1968, "On the Mechanism of Contact between Metal Surfaces: Part 2-The Real Area and the Number of Contact Points", *Journal of Tribology*, Vol.90, pp 81-88.

Uppal, A.H. and Probert, S.D., 1972, "Considerations Governing the Contact Between a Rough and a Flat Surface", *Wear*, Vol.22(2), pp 215-234.

Venner, C.H. and Lubrecht, A.A., 1996, "Numerical Analysis of the Influence of Waviness on the Film Thickness of a Circular EHL Contact", *Journal of Tribology*, Vol.118(1), pp 153-161.

Wang, Q.J., Zhu, D., Cheng, H.S., Yu, T., Jiang, X., and Liu, S., 2004, "Mixed Lubrication Analyses by a Macro-Micro Approach and a Full-Scale Mixed EHL Model", *Journal of Tribology*, Vol.126(1), pp 81-91.

Wang, Q.J. and Zhu, D., 2005, "Virtual Texturing: Modelling the Performance of Lubricated Contacts of Engineered Surfaces", *Journal of Tribology*, Vol.127(4), pp 722-728.

Whitehouse, D.J. and Archard, J.F., 1970, "The Properties of Random Surfaces of Significance in their Contact", *Proceedings of the Royal Society of London, Series A: Mathematical and Physical Sciences*, Vol.316(1524), pp 97-121.

Williams, J., 2005, *Engineering Tribology*, Cambridge, Cambridge University Press.

Woo, K.L. and Thomas, T.R., 1980, "Contact of Rough Surfaces: a Review of Experimental Work", *Wear*, Vol.58(2), pp 331-340.

Yamaguchi, A. and Matsuoka, H., 1992, "A Mixed Lubrication Model Applicable to Bearing/Seal Parts of Hydraulic Equipment", *Journal of Tribology*, Vol.114(1), pp 116-121.

Yarwood, T.M., 1953, *Acoustics*, McMillan, London.

Zhang, J. and Drinkwater, B.W., 2008, "Thin Oil-film Thickness Distribution Measurement Using Ultrasonic Arrays", *NDT & E International*, Vol.41(8), pp 596-601.

Zhao, J., Sadeghi, F., and Hoeprich, M.H., 2001, "Analysis of EHL Circular Contact Start Up: Part I--Mixed Contact Model With Pressure and Film Thickness Results", *Journal of Tribology*, Vol.123(1), pp 67-74.

Zhao, Y., Maietta, D.M., and Chang, L., 2000, "An Asperity Micro-contact Model Incorporating the Transition from Elastic Deformation to Fully Plastic Flow", *Journal of Tribology*, Vol.122(1), pp 86-93.

Zhu, D. and Ai, X., 1997, "Point Contact EHL Based on Optically Measured Three-Dimensional Rough Surfaces", *Journal of Tribology*, Vol.119(3), pp 375-384.

Zhu, D. and Cheng, H.S., 1988, "Effect of Surface Roughness on the Point Contact EHL", *Journal of Tribology*, Vol.110, pp 32-37.

Zhu, J., Pugh, S., Dwyer-Joyce, R.S., Beke, A., Cumner, G., and Ellaway, T., 2010, "Experiments on the Pressure Distribution and Frictional Torque in Articulating Pin Joints", *Proceedings of the Institution of Mechanical Engineers, Part J: Journal of Engineering Tribology*, Vol.224(10), pp 1153-1162.

# Appendix

## Appendix A: MathCAD Program for Ball on Disc Contact

### A.1 Formulation and Solution

$$D := 0.019 \text{ m} \quad R1 := \frac{D}{2} \text{ m} \quad E_d := 195 \cdot 10^9 \text{ Pa} \quad \nu_d := 0.31 \quad E_b := 195 \cdot 10^9 \text{ Pa} \quad \nu_b := 0.31$$

$$PT := 40 \text{ N} \quad u := 0.7 \text{ m/s} \quad D_s := 1.966 \cdot 10^{10} \text{ m}^2 \quad R_s := 2.703 \cdot 10^{-6} \text{ m} \quad \sigma_s := 0.2975 \cdot 10^{-6} \text{ m} \quad \eta_0 := 0.0952 \text{ Pa}\cdot\text{s}$$

$$\alpha := 2.51 \cdot 10^{-8} \text{ Pa}^{-1}$$

$$E1 := \frac{2}{\frac{1 - \nu_d^2}{E_d} + \frac{1 - \nu_b^2}{E_b}} \text{ Pa} \quad a := \left( \frac{3 \cdot PT \cdot R1}{2E1} \right)^{\frac{1}{3}} \text{ m}$$

$$P :=$$

	0
0	10
1	20
2	30
3	40
4	50
5	60
6	70
7	80

$$u_{\text{avg}} :=$$

	0
0	2·10 <sup>-3</sup>
1	5·10 <sup>-3</sup>
2	7·10 <sup>-3</sup>
3	0.01
4	0.05
5	0.07
6	0.1
7	0.15
8	0.2
9	0.25
10	0.3
11	0.35
12	0.4
13	0.45
14	0.5

$$m_{\text{avg}} := \frac{2}{3} \cdot \pi \cdot D_s \cdot E1 \cdot R_s^{\frac{1}{2}} \cdot \sigma_s^{\frac{3}{2}} \cdot \left( \frac{3PT \cdot R1}{2E1} \right)^{\frac{2}{3}}$$

$$h := 0.0001 \quad \gamma_1 := 10 \quad \gamma_2 := 10.001$$

Given

$$\frac{1}{\gamma_1} + \frac{1}{\gamma_2} = 1$$

$$\frac{h}{R1} = 1.899 \cdot \left( \frac{\eta_0 \cdot u \cdot \gamma_1}{E1 \cdot R1} \right)^{0.67} \cdot \left( \frac{\alpha \cdot E1}{\gamma_1} \right)^{0.53} \cdot \left( \frac{PT}{E1 \cdot R1^2} \right)^{-0.067}$$

$$m \cdot \frac{1}{\sqrt{2\pi}} \cdot \int_{\frac{h}{0.2975 \cdot 10^{-6}}}^{\infty} \left( t - \frac{h}{0.2975 \cdot 10^{-6}} \right)^{1.5} \cdot e^{-0.5 \cdot t^2} dt = \frac{PT}{\gamma_2}$$

$$v := \text{Find}(\gamma_1, \gamma_2, h)$$

$$v = \begin{pmatrix} 1.143725 \\ 7.957725 \\ 0 \end{pmatrix}$$

$$\gamma_1_{\text{avg}} :=$$

	0
0	1.878
1	1.824
2	1.796
3	1.761
4	1.519
5	1.453
6	1.379
7	1.295
8	1.237
9	1.194
10	1.161

$$\gamma_2_{\text{avg}} :=$$

	0
0	2.139
1	2.214
2	2.256
3	2.314
4	2.928
5	3.209
6	3.636
7	4.387
8	5.216
9	6.144
10	7.193

$$h_{\text{avg}} :=$$

	0
0	8.375·10 <sup>-9</sup>
1	1.541·10 <sup>-8</sup>
2	1.927·10 <sup>-8</sup>
3	2.44·10 <sup>-8</sup>
4	7.026·10 <sup>-8</sup>
5	8.748·10 <sup>-8</sup>
6	1.103·10 <sup>-7</sup>
7	1.434·10 <sup>-7</sup>
8	1.728·10 <sup>-7</sup>
9	1.997·10 <sup>-7</sup>
10	2.248·10 <sup>-7</sup>

## A.2 Stribeck Parameter and Friction Coefficient

$$f := \frac{Ff}{FT} = \frac{FfH + FfC}{FT} = \frac{FfH + fc \cdot Fc}{FT} \quad FfC := fc \cdot Fc \quad \tau L := \tau L0 + \beta0 \cdot pm \quad fc := 0.12 \quad pm := \frac{FT}{\gamma1 \pi \cdot a^2}$$

$$\eta := \eta0 \cdot \left( \frac{\eta\infty}{\eta0} \right)^{1 - \left( 1 + \frac{pm}{Cp} \right)^z} \quad FfH := \tau L \cdot \left( 1 - e^{-\frac{\eta \cdot u}{h \cdot \tau L}} \right) \cdot \pi \cdot a \cdot a \quad \eta_{uht} := \frac{-\eta \cdot u}{h \cdot \tau L}$$

u :=

	0
0	2·10 <sup>-3</sup>
1	5·10 <sup>-3</sup>
2	7·10 <sup>-3</sup>
3	0.01
4	0.05
5	0.07
6	0.1
7	0.15
8	0.2
9	0.25
10	0.3

h :=

	0
0	8.648·10 <sup>-9</sup>
1	1.59·10 <sup>-8</sup>
2	1.986·10 <sup>-8</sup>
3	2.514·10 <sup>-8</sup>
4	7.211·10 <sup>-8</sup>
5	8.969·10 <sup>-8</sup>
6	1.13·10 <sup>-7</sup>
7	1.467·10 <sup>-7</sup>
8	1.766·10 <sup>-7</sup>
9	2.04·10 <sup>-7</sup>
10	2.295·10 <sup>-7</sup>

γ1 :=

	0
0	2.057
1	1.984
2	1.947
3	1.9
4	1.593
5	1.513
6	1.425
7	1.327
8	1.26
9	1.211
10	1.174

γ2 :=

	0
0	1.946
1	2.016
2	2.056
3	2.111
4	2.686
5	2.951
6	3.353
7	4.063
8	4.849
9	5.733
10	6.736

$$pm := \frac{FT}{\gamma1 \pi \cdot a^2}$$

	0
0	294221455.11709994
1	305071441.3058959
2	310890761.6637178
3	318500512.67009455
4	379938273.59999686
5	400160350.8365524
6	424744571.46844244
7	456294563.5496868
8	480447590.5515473
9	499700233.76869845
10	515416648.29162806

$$\eta := \eta0 \cdot \left( \frac{\eta\infty}{\eta0} \right)^{1 - \left( 1 + \frac{pm}{Cp} \right)^z}$$

	0
0	8.400737054467893
1	9.61843218302976
2	10.336734320030683
3	11.350838455183421
4	23.61452101499067
5	29.806193640945068
6	39.36067198206089
7	55.81219202747155
8	72.52337417282727
9	89.0764766422048
10	105.14182825239246

$$\tau L := \tau L0 + \beta0 \cdot pm$$

$$Fc := \frac{FT}{\gamma2} \quad FfC := Fc \cdot fc$$

	0
0	16108408.390503697
1	16618357.741377108
2	16891865.798194736
3	17249524.09549444
4	20137098.85919985
5	21087536.48931796
6	22242994.859016795
7	23725844.48683528
8	24861036.755922724
9	25765910.987128828
10	26504582.46970652

	0
0	1.850074305407974
1	1.785538166641877
2	1.750930260006121
3	1.705667878499632
4	1.340258009145363
5	1.219983900740006
6	1.073765866991985
7	0.886118665988608
8	0.74246360523222
9	0.627956449818467
10	0.534477809637746

$$\eta_{uht} := \begin{cases} r \leftarrow \text{rows}(u) \\ \text{for } i \in 0..r-1 \\ \eta_{uht_{i,0}} \leftarrow \frac{-\eta_{i,0} \cdot u_{i,0}}{h_{i,0} \cdot \tau_{i,0}} \\ \eta_{uht} \end{cases}$$

	0
0	-0.120610634740763
1	-0.182037174530043
2	-0.215635159640174
3	-0.261729533159937
4	-0.813146492680144
5	-1.103168749879226
6	-1.566662028937274
7	-2.404787922187229
8	-3.302895157652681
9	-4.236655116605355

$$FfH := \begin{cases} r \leftarrow \text{rows}(u) \\ \text{for } i \in 0..r-1 \\ FfH_{i,0} \leftarrow \tau_{i,0} \cdot (1 - e^{\eta_{uht_{i,0}}}) \cdot \pi \cdot a^2 \\ FfH \end{cases}$$

	0
0	0.090714276320174
1	0.137082894662242
2	0.162397066081342
3	0.196878982136391
4	0.555465827559151
5	0.698369250283202
6	0.872321361229078
7	1.069773105411326
8	1.18689078047574
9	1.258595135881572
10	1.306313053572625

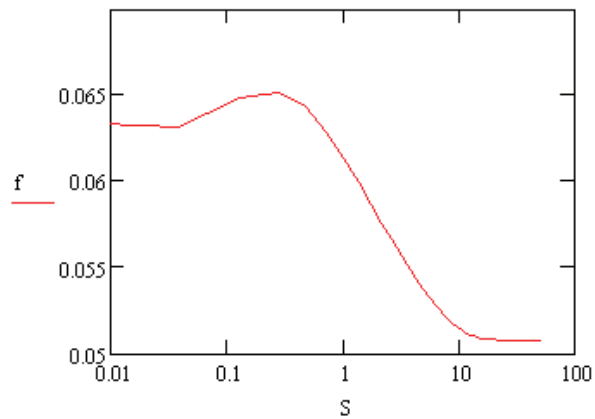
Stribeck parameter and friction coefficient

$$S_{\frac{S}{FT}} := \frac{\eta \cdot u}{FT} \quad f := \frac{FfH + FfC}{FT}$$

$$S := \begin{cases} r \leftarrow \text{rows}(u) \\ \text{for } i \in 0..r-1 \\ S_{i,0} \leftarrow \frac{\eta_{i,0} \cdot u_{i,0}}{FT} \\ S \end{cases}$$

	0
0	0.000560049136965
1	0.001603072030505
2	0.002411904674674
3	0.003783612818394
4	0.039357535024984
5	0.069547785162205
6	0.131202239940203
7	0.279060960137358
8	0.483489161152182
9	0.742303972018373
10	1.051418282523925
11	1.405616640858946

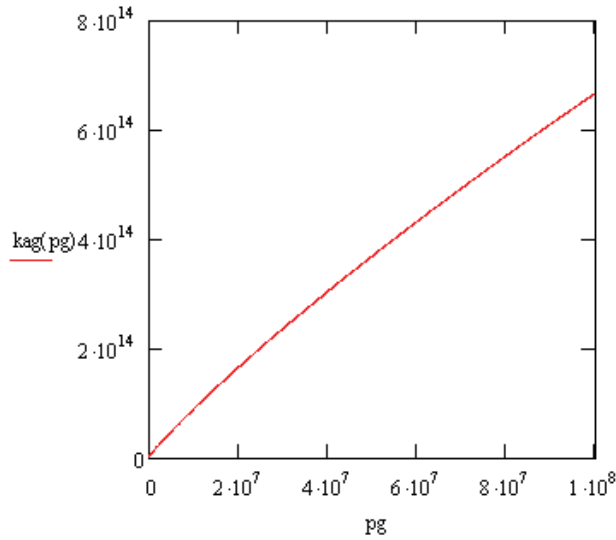
	0
0	0.064692952724272
1	0.064087368710137
2	0.063777577536249
3	0.063418228687867
4	0.063190794556817
5	0.063945105034107
6	0.064869574274035
7	0.065196392379998
8	0.064311812856932
9	0.062885052856668
10	0.061359695440346
11	0.059935735078756
12	0.058676231014408



### A.3 Calculation of Static Contact Stiffness

Greenwood-Williamson model

$$k_{ag}(p_g) := \frac{p_g}{\sigma_s} \cdot \left( 2.05 - 1.24 \cdot \ln \left( \frac{1.74 \cdot p_g}{n \cdot E1 \cdot \beta^{0.5} \cdot \sigma_s^{1.5}} \right) \right)^{0.5}$$



$$p_g = 200 \times 10^6$$

$$k_{ag}(p_g) = 1175992322823835.8$$

contact stiffness ka and surface separation

$$u_g := \frac{\sigma_s}{0.62} \cdot \left( \sqrt{2.05 - 1.24 \cdot \ln \left( \frac{1.74 \cdot p_g}{n \cdot E1 \cdot \beta^{0.5} \cdot \sigma_s^{1.5}} \right)} - 1.43 \right)$$

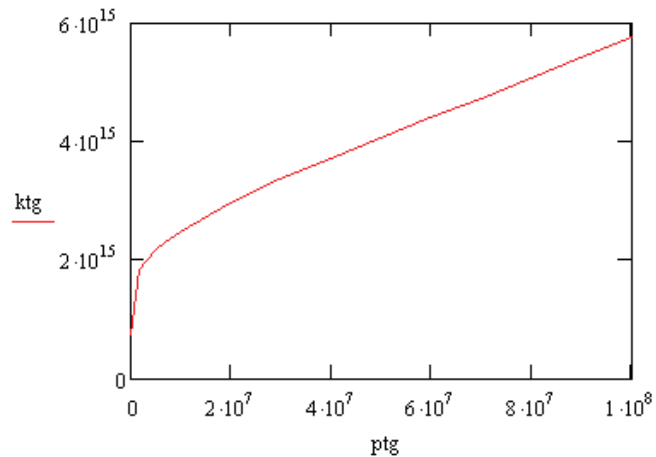
ptg :=	0	ug :=	0
0	0	0	1.796-10-6
1	2-106	1	7.349-10-7
2	5-106	2	6.396-10-7
3	7-106	3	6.029-10-7
4	1-107	4	5.628-10-7
5	2-107	5	4.809-10-7
6	3-107	6	4.302-10-7
7	4-107	7	3.927-10-7
8	5-107	8	3.628-10-7

Stiffness of lubricant under static condition Kf :

kgf =	0	kag :=	0
0	7.45508298582-1014	0	1.739-107
1	1.82209594104-1015	1	1.991-1013
2	2.09339774557-1015	2	4.644-1013
3	2.2209616316-1015	3	6.321-1013
4	2.37930660715-1015	4	8.749-1013
5	2.7846116413-1015	5	1.635-1014
6	3.11280247536-1015	6	2.346-1014
7	3.40934552788-1015	7	3.023-1014
8	3.69069800774-1015	8	3.674-1014
9	3.96515167668-1015		
10	4.23775750153-1015		
11	4.51200280357-1015		
12	4.79057769573-1015		
13	5.07573804794-1015		
14	8.73980953873-1015		
15	5.2245503141-1016		

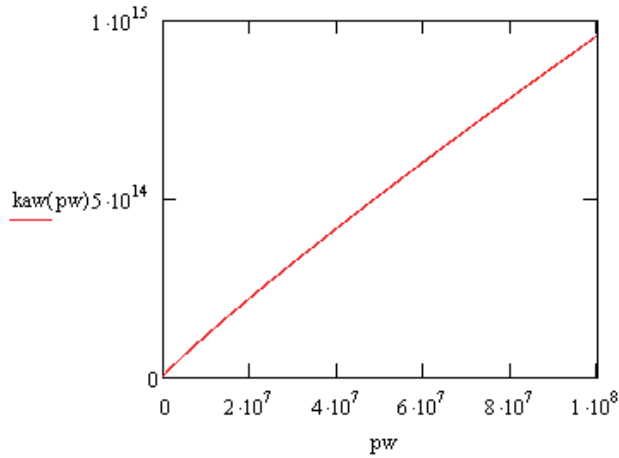
Total contact stiffness kt:

ktg =	0
0	7.455083159706-1014
1	1.84200514104-1015
2	2.139834845572-1015
3	2.284172131602-1015
4	2.466796607151-1015
5	2.948115641299-1015
6	3.347404475364-1015
7	3.711663527876-1015
8	4.05810900774-1015
9	4.395489676676-1015
10	4.729166501527-1015



Whitehouse-Archard-Onions model

$$k_{aw}(pw) := \frac{pw}{\sigma_s} \cdot \left( 1.7 - 1.6 \cdot \ln \left( \frac{2.7 \cdot pw}{n^{0.5} \cdot E1 \cdot \sigma_s} \right) \right)^{0.5}$$



$$pw := 1210.561288 \cdot 10^6$$

$$k_{aw}(pw) = 8214510527253056$$

Nominal pressure and stiffness Ka:

$$uw := \frac{\sigma_s}{0.8} \cdot \left( \sqrt{1.69 - 1.6 \cdot \ln \left( \frac{2.74 \cdot pw}{n^{0.5} \cdot E1 \cdot \sigma_s} \right)} - 1.3 \right)$$

ptw :=

	0
0	0
1	2·10 <sup>6</sup>
2	5·10 <sup>6</sup>
3	7·10 <sup>6</sup>
4	1·10 <sup>7</sup>
5	2·10 <sup>7</sup>
6	3·10 <sup>7</sup>
7	4·10 <sup>7</sup>

uw :=

	0
0	1.794·10 <sup>-6</sup>
1	9.224·10 <sup>-7</sup>
2	8.483·10 <sup>-7</sup>
3	8.201·10 <sup>-7</sup>
4	7.894·10 <sup>-7</sup>
5	7.277·10 <sup>-7</sup>
6	6.901·10 <sup>-7</sup>
7	6.626·10 <sup>-7</sup>

Stiffness of lubricant under static condition Kf:

$$B_w := 1.339 \cdot 10^9$$

$$k_{fw} := \frac{B_w}{uw}$$

kfw =

	0
0	746389293020507.63
1	1451695089822956.3
2	1578432412679327.3
3	163280735559349.3
4	1696160520882155.5
5	1840069260261924.8
6	1940410978755470.5
7	2020766049923032.8
8	2089314632298090.3
9	2150002408516514.3
10	2204986332048875
11	2255613766150632.5
12	2302784322492992
13	2347228552396311.5
14	2705050505050505
15	3240483047360906

kaw =

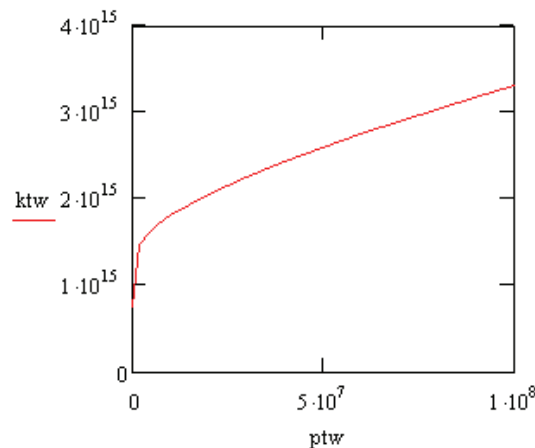
	0
0	2.059·10 <sup>7</sup>
1	2.544·10 <sup>13</sup>
2	6.027·10 <sup>13</sup>
3	8.259·10 <sup>13</sup>
4	1.152·10 <sup>14</sup>
5	2.193·10 <sup>14</sup>
6	3.188·10 <sup>14</sup>
7	4.151·10 <sup>14</sup>
8	5.091·10 <sup>14</sup>
9	6.011·10 <sup>14</sup>
10	6.915·10 <sup>14</sup>

Total contact stiffness kt:

$$k_{tw} := k_{fw} + k_{aw}$$

ktw =

	0
0	746389313614963.63
1	1477138889822956.3
2	1638698912679327.3
3	171539535559349.3
4	1811378520882155.5
5	2059360260261924.8
6	2259161978755470.5
7	2435862049923033
8	2598373692298090
9	2751083408516514
10	2896442332048875
11	3036012766150632.5
12	3170855322492992
13	3301827552396311.5
14	4478130505050505
15	6491693047360906



+

### Bush-Gibson-Thomas model

$$m4 := \left( \frac{0.375}{\beta} \right)^2 \cdot \pi \quad (\text{Longuet-Higgins, 1957})$$

$$m2 := \frac{m4}{n \cdot (6\pi \cdot \sqrt{\beta})} \quad (\text{Nayak, 1971})$$

pb := 1210.561288 · 10<sup>6</sup>    tb := 5  
Given

$$pb = \frac{E1}{2\pi} \cdot \left( \frac{m2}{2} \right)^{0.5} \cdot \frac{1}{tb} \cdot e^{-\frac{tb^2}{2}}$$

Dimensionless separation t :

$$stb := \text{Find}(tb)$$

$$stb = 2.47252440721$$

Separation of contacting surfaces h :

$$hb := stb \cdot \sigma_s$$

$$hb = 0.00000073558$$

Stiffness of solid asperity contact Ka :

$$kab := \frac{1}{\sigma_s} \cdot pb \cdot \left( stb + \frac{1}{stb} \right)$$

$$kab = 11706715043966185$$

$$ptb :=$$

0	
0	0
1	2·10 <sup>6</sup>
2	5·10 <sup>6</sup>
3	7·10 <sup>6</sup>
4	1·10 <sup>7</sup>
5	2·10 <sup>7</sup>
6	3·10 <sup>7</sup>
7	4·10 <sup>7</sup>
8	5·10 <sup>7</sup>

$$ub :=$$

0	
0	2.016·10 <sup>-6</sup>
1	1.257·10 <sup>-6</sup>
2	1.195·10 <sup>-6</sup>
3	1.171·10 <sup>-6</sup>
4	1.145·10 <sup>-6</sup>
5	1.094·10 <sup>-6</sup>
6	1.063·10 <sup>-6</sup>
7	1.041·10 <sup>-6</sup>
8	1.023·10 <sup>-6</sup>

$$kab :=$$

0	
0	2.328·10 <sup>7</sup>
1	3·10 <sup>13</sup>
2	7.167·10 <sup>13</sup>
3	9.858·10 <sup>13</sup>
4	1.381·10 <sup>14</sup>
5	2.655·10 <sup>14</sup>
6	3.886·10 <sup>14</sup>
7	5.088·10 <sup>14</sup>
8	6.269·10 <sup>14</sup>

Stiffness of lubricant under static condition Kf :

$$Bb := 1.339 \cdot 10^9$$

$$kfb := \frac{Bb}{ub}$$

$$kfb =$$

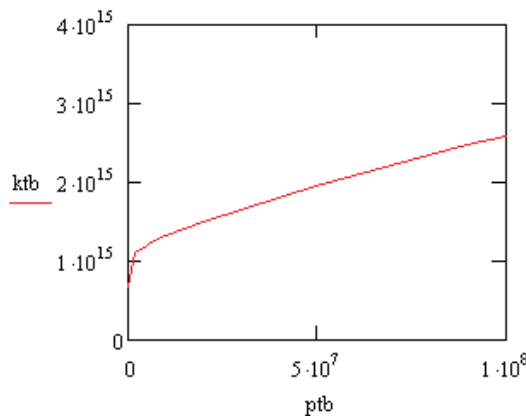
0	
0	664150269578544.88
1	1065217737187952.5
2	1120933581127463.3
3	1143603846745127.5
4	1169136201311458.3
5	1223814572441779.8
6	1259405568096313
7	1286522737535910.3
8	1308741887559621.8
9	1327727592737657.3
10	1344404506114580.8
11	1359349461437722.5
12	1372924976160936.8
13	1385396943642590.3
14	1476246651158175.5
15	1586079457961195

Total contact stiffness kt:

$$ktb := kfb + kab$$

$$ktb =$$

0	
0	664150292853837.5
1	1095214100325283
2	1192602917437580.5
3	1242186491186922.8
4	1307270030442112
5	1489334652943646.5
6	1648003329312441.8
7	1795334690249873.3
8	1935604425612898.5
9	2070895062273078
10	2202410440349380
11	2330927623944627
12	2456960009088682.5
13	2580891402375283
14	3746382674802745
15	5875301148376094





## Appendix B: MathCAD Program for Pin Joint

### Parameters:

$$R_a := 0.028 \text{ m} \quad R_b := 0.028025 \text{ m} \quad B := 0.0594 \text{ m} \quad E := 205 \cdot 10^9 \text{ Pa} \quad \nu := 0.28 \quad E_b := 117 \cdot 10^9 \text{ Pa} \quad \nu_b := 0.34$$

$$F_T := 20000 \text{ N} \quad n := 10 \text{ rpm} \quad \dot{n} := 7.15 \cdot 10^9 \text{ m}^{-2} \quad \beta := 3.405 \cdot 10^{-6} \text{ m} \quad \sigma_s := 1.0885 \cdot 10^{-6} \text{ m} \quad \eta_0 := 0.01245 \text{ Pa} \cdot \text{s}$$

$$\alpha := 1.69 \cdot 10^{-8} \text{ Pa}^{-1} \quad Z := 0.634 \quad \beta_0 := 0.047 \quad \eta_{\infty} := 6.315 \cdot 10^{-5} \text{ Pa} \cdot \text{s} \quad C_p := 1.962 \cdot 10^8 \text{ Pa}$$

$$\tau_{L0} := 2.28 \cdot 10^6 \text{ Pa} \quad a_1 := 1.558 \quad a_2 := 0.0337 \quad a_3 := -0.442 \quad a_4 := -1.7$$

$$\tau_{L0} := 2.28 \cdot 10^6 \text{ Pa} \quad a_1 := 1.558 \quad a_2 := 0.0337 \quad a_3 := -0.442 \quad a_4 := -1.7$$

$$R_1 := \frac{R \cdot R_b}{R_b - R} \text{ m} \quad E_1 := \frac{2}{\frac{1 - \nu^2}{E} + \frac{1 - \nu_b^2}{E_b}} \text{ Pa} \quad u := \frac{n \cdot 2 \cdot \pi \cdot R}{60} \text{ m/s} \quad a := \left( \frac{8 \cdot F_T \cdot R_1}{\pi \cdot E_1 \cdot B} \right)^{0.5} \text{ m}$$

$$\frac{2}{3} \cdot n_1 \cdot \sigma_{s1} \cdot \sqrt{\sigma_{s1}} \cdot F_T \cdot F(t) = \left[ 1 + \left( a_1 \cdot n_1 \cdot a_2 \cdot \sigma_{s1} \cdot a_3 \cdot W^{a_2 - a_3} \cdot \gamma_2^{a_2} \right)^{a_4} \right]^{\frac{1}{a_4}} \cdot \frac{1}{\gamma_2} \quad n_1 := n \cdot R_1 \cdot \sqrt{\beta \cdot R_1}$$

$$\sigma_{s1} := \frac{\sigma_s}{R_1} \quad F_{T1} := \sqrt{\frac{2 \cdot \pi \cdot B \cdot R_1 \cdot E_1}{F_T}} \quad dd := 1.15 \cdot \sigma_s \quad d_{d1} := \frac{dd}{R_1} \quad hc_1 := \frac{hc}{R_1}$$

$$\frac{2}{3} \cdot n_1 \cdot \sigma_{s1} \cdot \sqrt{\sigma_{s1}} \cdot F_{T1} = 98.47020764012366$$

$$\frac{W}{\sigma_{s1}} = \frac{F_T}{E_1 \cdot R_1 \cdot B} \quad a_1 \cdot n_1 \cdot a_2 \cdot \sigma_{s1} \cdot a_3 \cdot W^{a_2 - a_3} = 2.429293258504701$$

$$U\Sigma := \frac{\eta_0 \cdot u}{E_1 \cdot R_1} \quad G_{\omega} := \alpha \cdot E_1 \quad M := W \cdot U\Sigma^{-0.5} \quad L_{\omega} := G \cdot U\Sigma^{0.25} \quad \frac{W}{\sigma_{s1}} = \frac{F_T}{E_1 \cdot R_1 \cdot B}$$

$$H_{R1} := 3 \cdot M^{-1} \quad H_{E1} := 2.621 \cdot M^{-0.2} \quad H_{R2} := 1.287 \cdot L^{\frac{2}{3}} \quad H_{E2} := 1.311 \cdot M^{\frac{-1}{8}} \cdot L^{\frac{3}{4}}$$

$$U\Sigma^{-0.5} \cdot \frac{1}{R_1} = 3805213.7695417413 \quad -2 \cdot \frac{H_{E1}}{H_{R1}} = -8.96544063076557$$

$$H_{R1}^{\frac{7}{3}} = 0.110123063917525 \quad H_{E1}^{\frac{7}{3}} = 3.648733302511443 \quad \frac{H_{R2}^{-7}}{2} + \frac{H_{E2}^{-7}}{2} = 43.58741644278391$$

### Formulation and solution

$$hc := 0.0001 \quad \gamma_1 := 100 \quad \gamma_2 := 10.001 \quad s := 3$$

Given

$$\frac{1}{\gamma_1} + \frac{1}{\gamma_2} = 1$$

$$s = \frac{1}{5} \cdot \left( 7 + 8 \cdot e^{-8.96544063076557 \cdot \gamma_1^{-0.4}} \right)$$

$$3805213.7695417413 \cdot hc = \left[ \gamma_1^{0.5 \cdot s} \cdot \left( 0.110123063917525 + \gamma_1^{\frac{-14}{15}} \cdot 3.648733302511443 \right)^{3 \cdot \frac{s}{7}} + \gamma_1^{\frac{-s}{2}} \cdot 43.58741644278391 \right]^{\frac{1}{s}} \cdot \gamma_1^{0.5}$$

$$98.47020764012366 \cdot \frac{1}{\sqrt{2 \cdot \pi}} \int_{\frac{hc - 1.251775 \cdot 10^{-6}}{1.0885 \cdot 10^{-6}}}^{\infty} \left( t - \frac{hc - 1.251775 \cdot 10^{-6}}{1.0885 \cdot 10^{-6}} \right)^{1.5} \cdot e^{-0.5 \cdot t^2} dt = \left[ 1 + \left( 2.429293258504701 \cdot \gamma_2^{0.0337} \right)^{-1.7} \right]^{\frac{-1}{1.7}} \cdot \frac{1}{\gamma_2}$$

v := Find( $\gamma_1, \gamma_2, hc, s$ )

$$v = \begin{pmatrix} 20.32299104971231 \\ 1.051751794143938 \\ 0.000003328516917 \\ 1.508862423685698 \end{pmatrix}$$

$\underline{hc} := 0.000003328516917$      $\underline{\gamma_2} := 1.051751794143938$      $fc := 0.12$

### Friction coefficient:

$$f := \frac{Ff}{FT} = \frac{FfH + FfC}{FT} = \frac{FfH + fc \cdot Fc}{FT}$$

$$pm := \frac{FT}{2 \cdot a \cdot B} \quad \tau L := \tau L_0 + \beta_0 \cdot pm \quad \eta := \eta_0 \cdot \left( \frac{\eta_{\infty}}{\eta_0} \right)^{1 - \left( 1 + \frac{pm}{C_p} \right)^z} \quad Fc := \frac{FT}{\gamma^2} \quad FfH := \tau L \cdot \left( 1 - e^{-\frac{\eta \cdot u}{hc \cdot \tau L}} \right) \cdot 2 \cdot a \cdot B \quad FfC := fc \cdot Fc$$

So

$$FfH = 0.20739247601915 \quad FfC = 2281.907207920148$$

$$f := \frac{FfH + FfC}{FT}$$

$$f = 0.114105730019808$$

### Sommerfeld number:

$$NT := \frac{nn}{60} \text{ rps} \quad C := 25 \cdot 10^{-6} \text{ m} \quad \eta = 0.015560235369406 \quad PL := \frac{FT}{2 \cdot R \cdot B}$$

$$S := \frac{\eta \cdot NT \cdot \left( \frac{R}{C} \right)^2}{PL}$$

$$S = 0.000541060006337$$

## Appendix C: Influence of Speed on Reflection

Table C.1. Influence of speed on reflection coefficient for Perspex 5mm diameter specimen at 14.93 MPa (293 N).

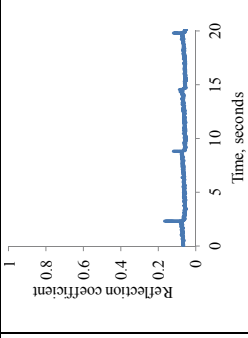
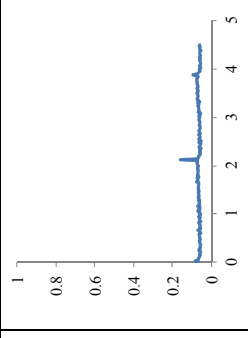
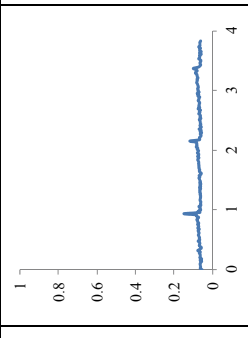
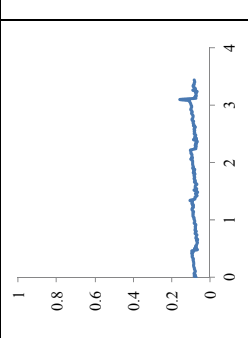
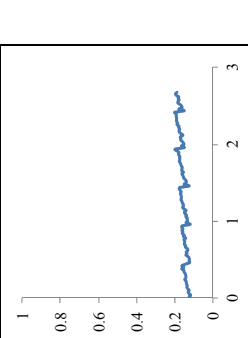
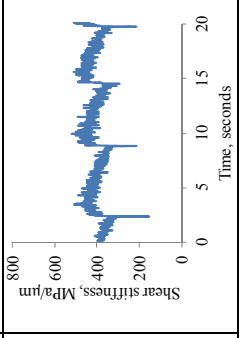
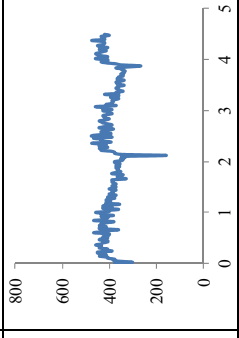
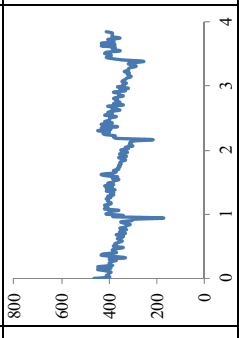
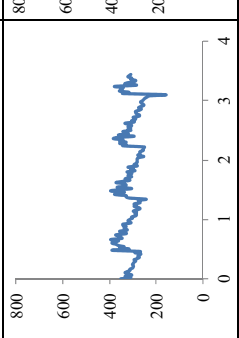
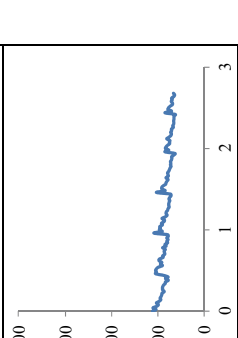
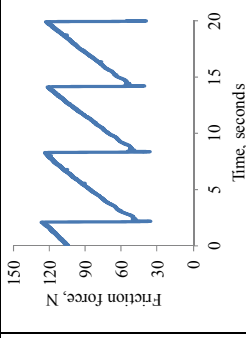
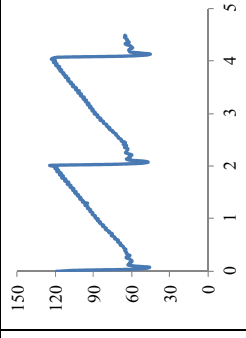
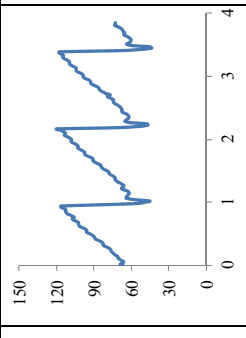
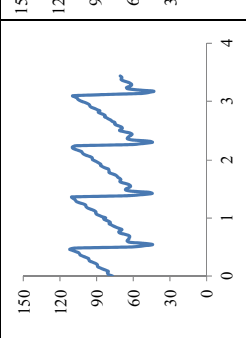
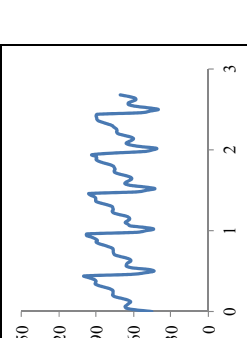
Sliding speed, $m/s$	0.264	0.639	1.154	1.83	3.029
Reflection coefficient					
Shear stiffness, $GPa/\mu m$					
Friction force, $N$					

Table C.2. Influence of speed on reflection coefficient for Perspex 8 mm diameter specimen at 3.89 MPa (195 N).

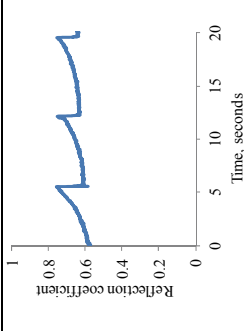
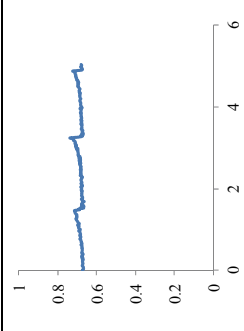
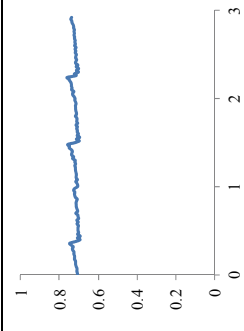
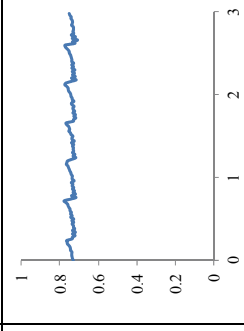
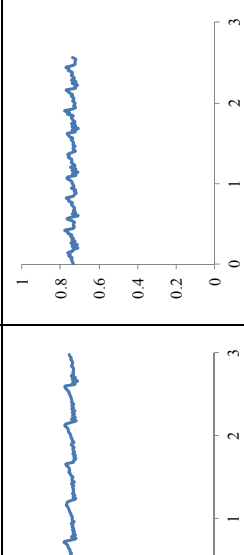
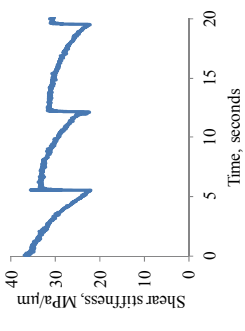
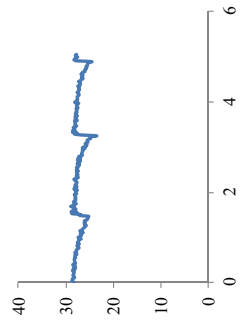
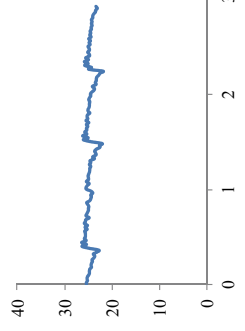
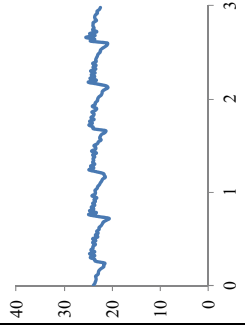
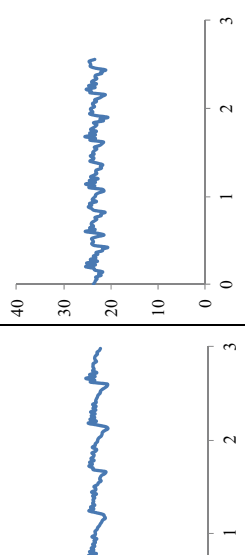
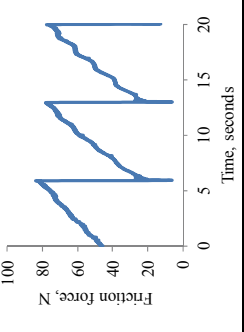
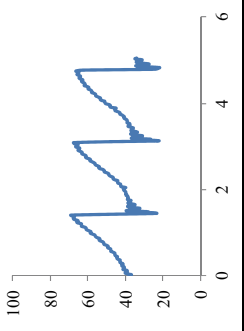
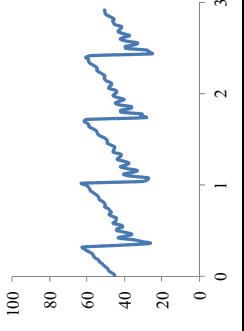
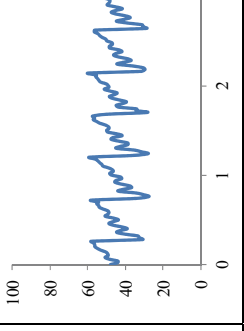
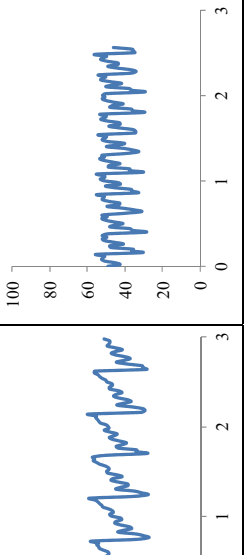
Sliding speed, $m/s$	0.264	0.639	1.154	1.83	3.029
Reflection coefficient					
Shear stiffness, $GPa/\mu m$					
Friction force, $N$					

Table C.3. Influence of speed on reflection coefficient for Perspex 12 mm diameter specimen at 2.59 MPa (293 N).

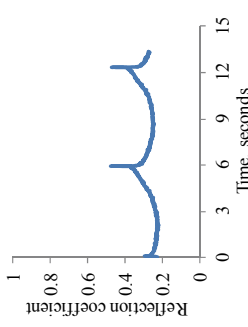
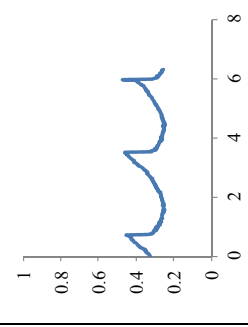
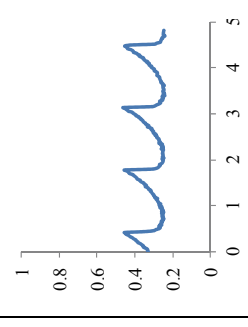
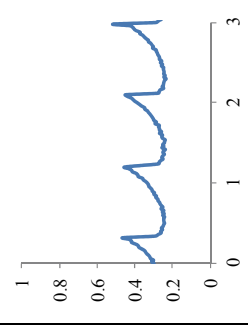
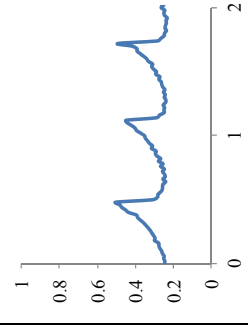
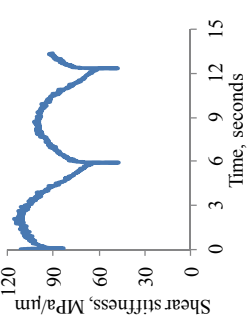
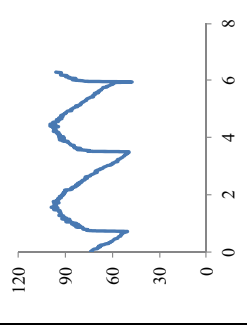
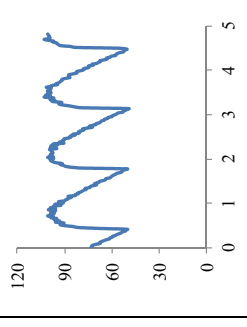
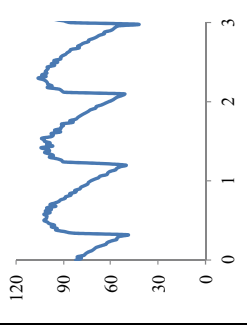
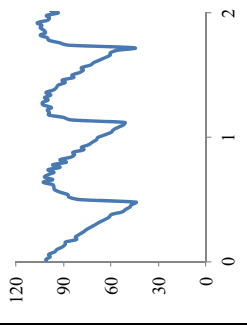
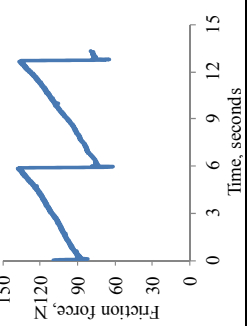
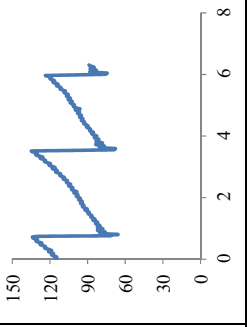
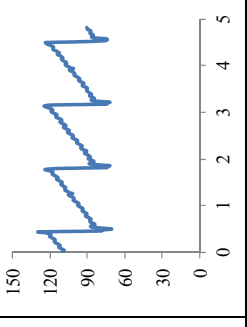
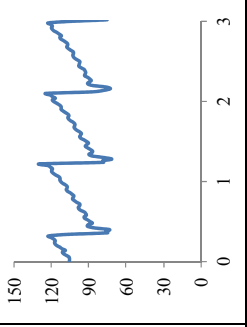
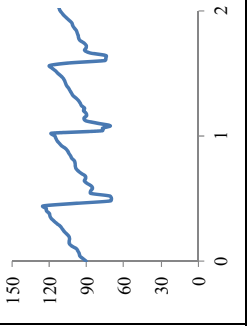
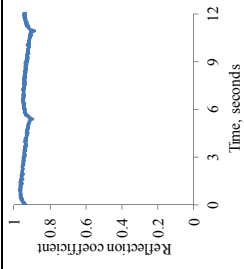
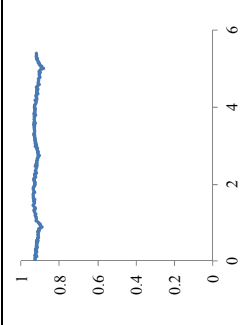
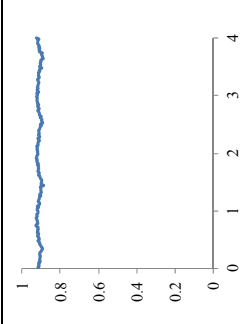
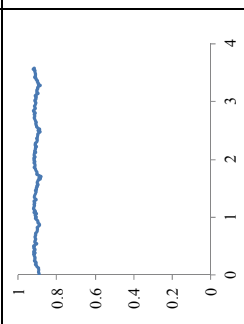
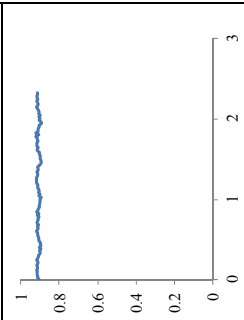
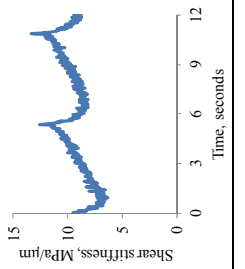
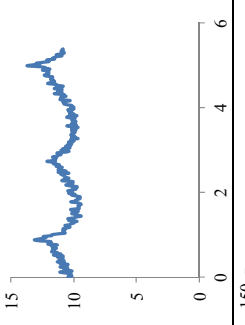
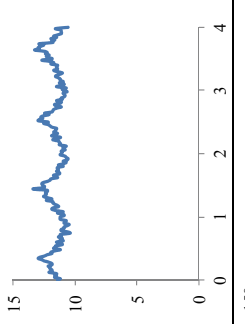
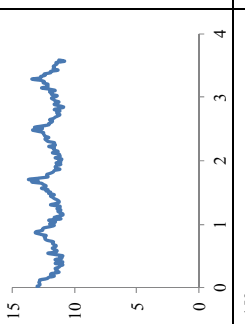
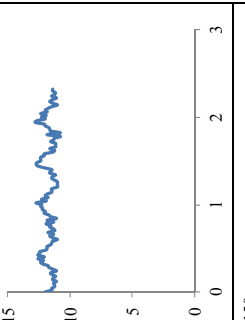
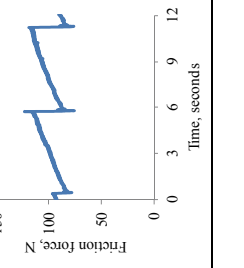
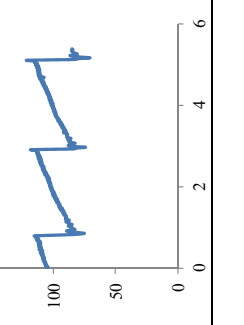
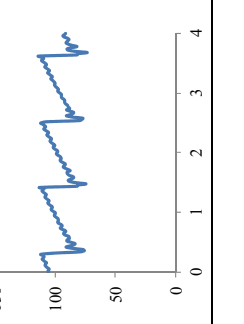
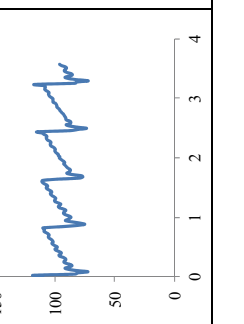
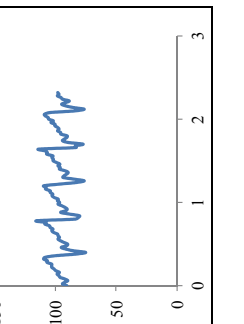
Sliding speed, $m/s$	0.264	0.639	1.154	1.83	3.029
Reflection coefficient					
Shear stiffness, $GPa/\mu m$					
Friction force, $N$					

Table C.4. Influence of speed on reflection coefficient for Perspex 25 mm diameter specimen at 0.6 MPa (293 N).

Sliding speed, $m/s$	0.264	0.639	1.154	1.83	3.029
Reflection coefficient					
Shear stiffness, $GPa/\mu m$					
Friction force, $N$					

## Appendix D: Influence of Load on Reflection

Table D.1. Influence of load on reflection coefficient for Perspex 5 mm diameter specimen at speed of 0.639 m/s.

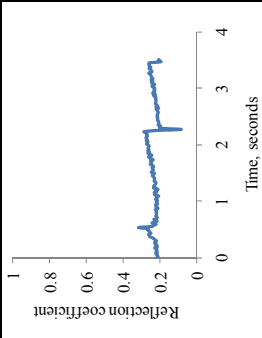
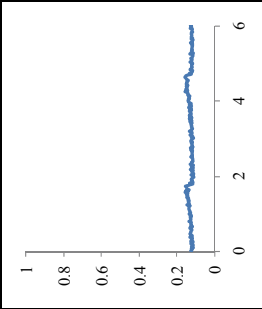
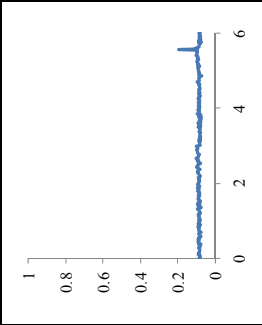
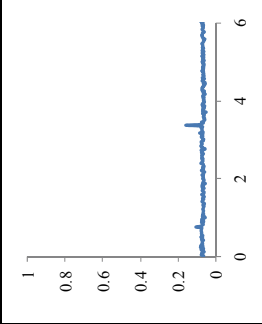
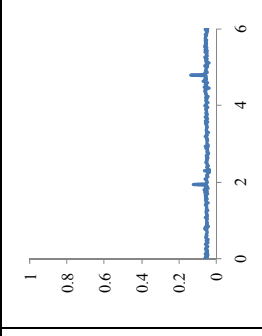
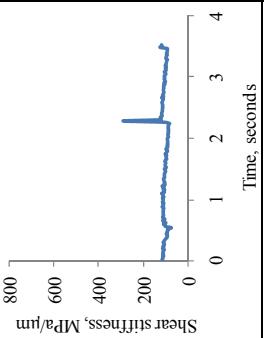
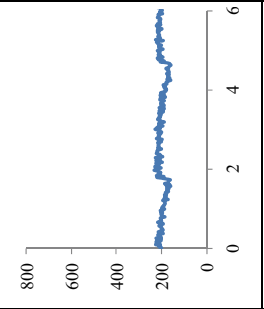
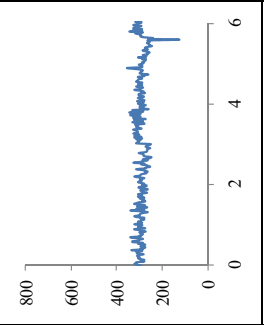
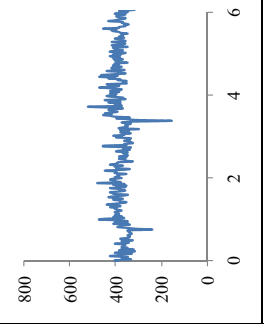
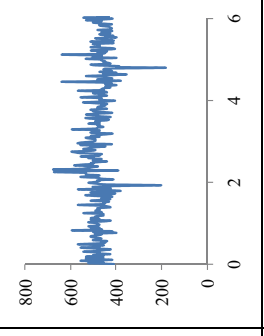
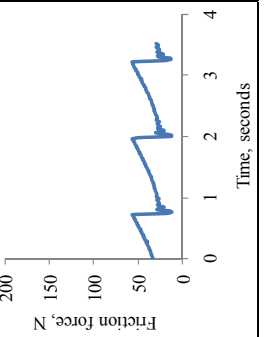
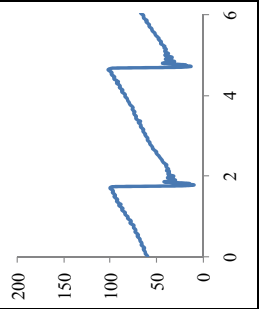
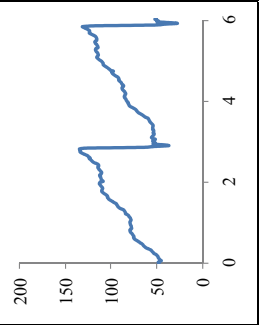
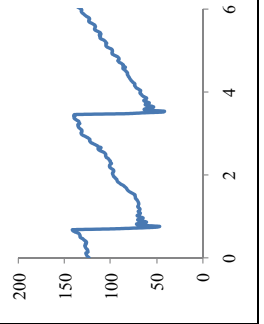
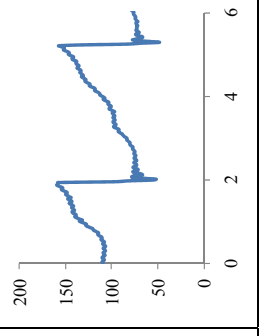
Nominal pressure, $MPa$	1.94	3.89	5.83	7.78	9.72
Reflection coefficient					
Shear stiffness, $GPa/\mu m$					
Friction force, $N$					

Table D.2. Influence of load on reflection coefficient for Perspex 8 mm diameter specimen at speed of 1.83 m/s.

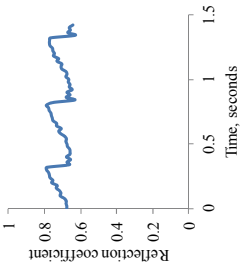
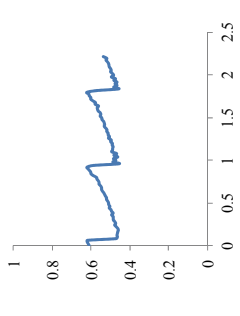
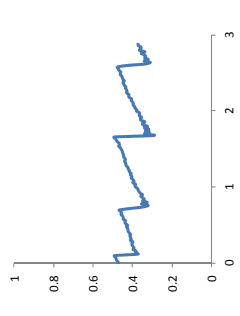
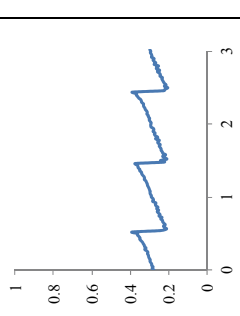
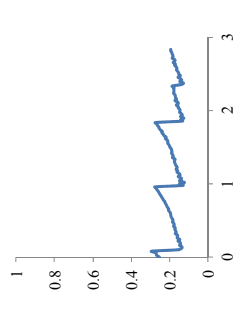
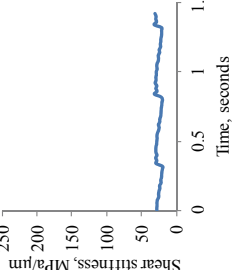
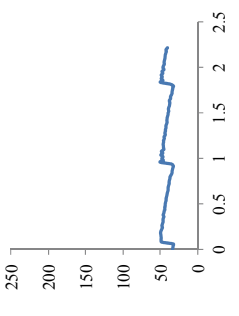
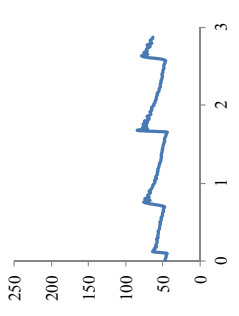
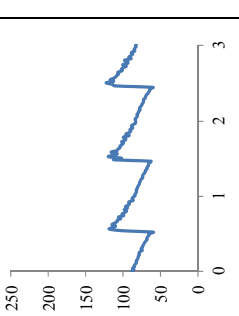
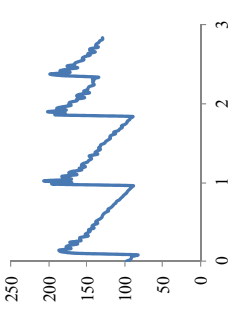
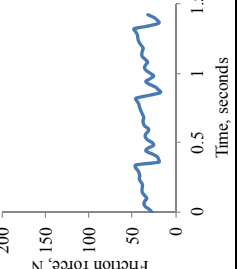
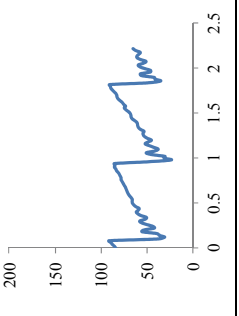
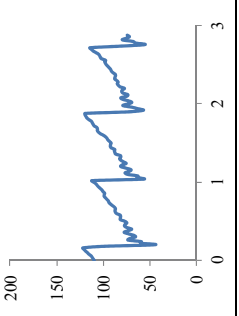
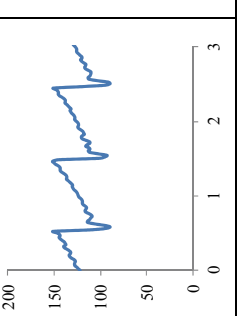
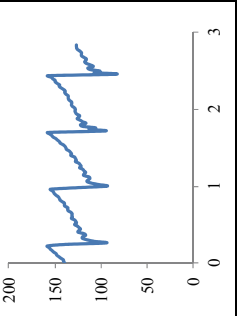
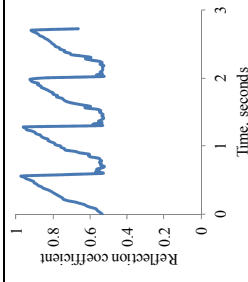
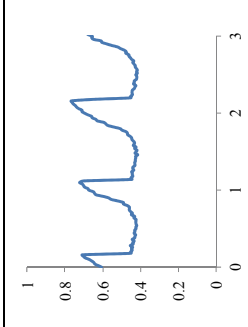
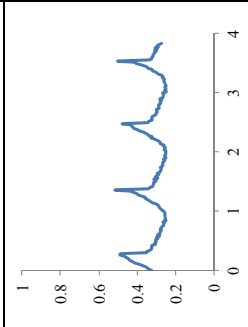
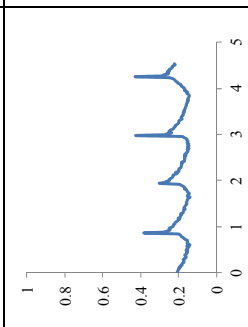
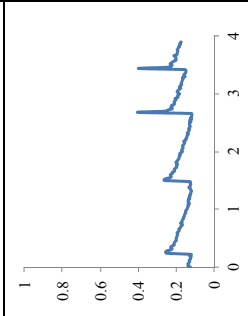
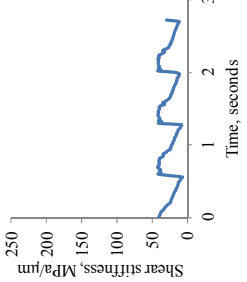
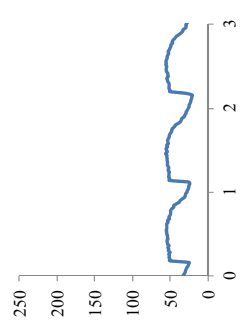
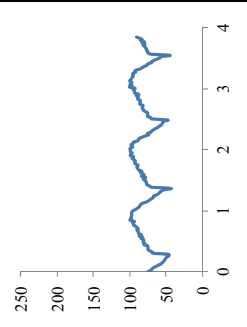
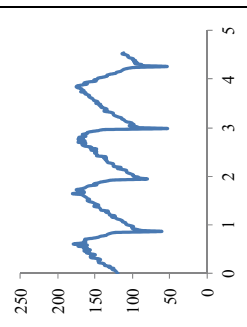
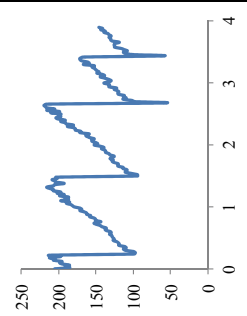
Nominal pressure, $MPa$	1.94	3.89	5.83	7.78	9.72
Reflection coefficient					
Shear stiffness, $GPa/\mu m$					
Friction force, $N$					



Table D.3. Influence of load on reflection coefficient for Perspex 12 mm diameter specimen at speed of 1.83 m/s.

Nominal pressure, $MPa$	0.86	1.73	2.59	3.46	4.32
Reflection coefficient					
Shear stiffness, $GPa/\mu m$					
Friction force, $N$	